Function of Reelin Signaling in the Tangential Migration of Dopaminergic Neurons

Dissertation

Zur

Erlangung des Doktorgrades (Dr. rer. Nat.)

Der

Mathematisch-Naturwissenschaftlichen Fakultät

der Rheinischen Friedrich-Wilhelms-Universität Bonn

vorgelegt von

Ankita Ravi Vaswani

aus Ghataprabha, Karnataka, India

Bonn, 2020

Angefertigt mit Genehmigung der Mathematisch-Naturwissenschaftlichen Fakultät der Rheinischen Friedrich-Wilhelms-Universität Bonn

1. Gutachter: Prof. Dr.Sandra Blaess

2. Gutachter: Prof. Dr. Walter Witke

Tag der Promotion: 29.01.2020
Erscheinungsjahr: 2021

“It does not matter how slowly you go as long as you do not stop.”

Confucius

TABLE OF CONTENTS

ABBREVIATIONS

3D	three dimensions (x,y,z in space)
4D	3D over time
A(8-10)	Aminergic group (8-10)
ADF	Actin depolymerizing factor
AES	anterior extramural stream
AKT	Protein kinase B
ALDH1A1	Aldehyde dehydrogenase 1 family member A1
ANOVA	Analysis of Variance
AP	Alkaline phosphatase
ApoER2	Apolipoprotein E receptor
ARP2/3	Actin related proteins 2/3
ASCL1	Achaete-scute homolog
ATP	Adenosine tri-phosphate
BABB	Benzyl alcohol/benzyl benzoate
bp	Base pair
BSA	Bovine serum albumin
C3G	Rap guanine nucleotide exchange factor 1
Calbindin	Ca^{2+} binding protein
CDF	cumulative density function
CDH2	Cadherin 2
CDK5	Cyclin-dependent kinase 5
cDNA	complementary DNA
CGE	caudal ganglionic eminence
CKO	conditional knockout
CNS	Central nervous system
CP	Cortical plate
CR	Cajal-Retzius cell
Cre	Causes recombination
CreER	Cre Estrogen receptor fusion protein
CRK	Adaptor molecule crk
CRKL	crk-like
Cx	Cortex
CXCL12	Chemokine (C-X-C motif) Ligand 12
CXCR4	Chemokine (C-X-C motif) Receptor 4
DAB1	Disabled-1
DAPI	4'-6-Diamidino-2-phenylindole
DAT	Dopamine transporter
DCC	Deleted in colorectal carcinoma
DCX	Doublecortin
DG	Dentate gyrus
DLS	Dorsolateral striatum
DMEM	Dulbecco's Modified Eagle Medium
DMS	Dorsomedial striatum
DMSO	Dimethylsulfoxide
DNA	Deoxyribonucleic acid
DNAse	Deoxyribonuclease
dNTP	Deoxynucleotidetriphosphate
DRF1,2	Diaphanous related formin 1,2
E	embryonic day
EB3	End binding protein 3
ECM	Extracellular matrix
ECN	external cuneate nucleus
EDTA	Ethylenediaminetetraacetic acid

EGFP	Enhanced green fluorescent protein
EGL	External granule layer
EN1/2	Engrailed 1 and 2
ENA/VASP	Vasodilator-stimulated phosphoprotein
EphBs	Ephrin receptor tyrosine kinases
EtBr	Ethidium bromide
FGF8	Fibroblast growth factor 8
FOXA2	Forkhead box protein A2
GBX2	Gastrulation Brain homeobox 2
GE	Ganglionic eminences
GFAP	Glial fibrillary acidic protein
GIRK2	G-protein regulated inward rectifier potassium channel-2
GLI2	Gli family zinc finger 2
GTPase	Guanosine triphosphatase
HEM	Hematopoetic protein 1
HRP	horse raddish peroxidase
Ig	Immunoglobulin
IO	Inferior olive nucleus
ISH	In situ hybridization
IZ	Intermediate zone
LAP	linear assignment problem
LB	Lauria Bertani
LGE	Lateral ganglionic eminence
LIMK1	LIM domain kinase 1
LMX1A/B	LIM homeodomain transcription factors A/B
LMO3	LIM domain only protein 3
LoG	Laplacian of Gaussian
LP	leading process
LRN	Lateral reticulate nucleus
LUT	lookup table
mDA	midbrain dopaminergic
MGE	Medial ganglionic eminence
MHB	midbrain-hindbrain boundary
MZ	marginal zone
NEUROG2	Neurogenin 2
NURR1	Nuclear receptor subfamily 4, group A, member 2
OB	Olfactory bulb
OTX2	Orthodenticle homeobox 2
P	postnatal day
p-	phosphorylated-
PAR3/6	Partitioning defective 3/6 homolog
PBS	Phosphate buffer saline
PCR	Polymerase chain reaction
PES	posterior extramural stream
PFA	Paraformaldehyde
PI3K	Phosphatidylinositol- 3-kinase
PITX3	Paired like homeodomain 3
PN	Pontine neuron
POA	preoptic area
r	rhombic lip
RAP1	Ras-proximate-1
RN	Red nucleus
RNAse	Ribonuclease
RRF	Retrorubral field
RT	room temperature
SEM	Standard error of the mean

SHH	Sonic hedgehog
SN	Substantia nigra
SNT	simple neurite tracer
SOX6	Sex determining region Y-box6
SPN	Sympathetic preganglionic neuron
SRC/FYN	Src family tyrosine kinases
SVZ	subventricular zone
TH	Tyrosine hydroxylase
TM	Tamoxifen
VLDLR	very low density lipoprotein receptor
VTA	Ventral tegmental area
VZ	ventricular zone
WNT1	wingless-related MMTV integration site 1
YFP	Yellow fluorescent protein

SUMMARY

Midbrain dopaminergic neurons (mDA neurons) are involved in the regulation of voluntary movement, reward behavior and cognitive processes. mDA neurons are born in the floor plate of the ventral midbrain, from where they migrate to form three anatomically distinct structures: the laterally positioned substantia nigra (SN), the medially positioned ventral tegmental area (VTA), and the posterior retrorubral field (RRF). Previous studies of the developing mDA system have shown that both SN- and VTA-mDA neurons undergo radial migration between embryonic (E) day 9.5-13.5. Between E12.5 and E15.5, SN-mDA neurons migrate tangentially to separate from the VTA-mDA neurons and take up a more lateral position. However, while the tangential migration of SN-mDA neurons is important for the correct anatomical positioning of the dopaminergic system, little is known about the extracellular signaling cues and dynamic cell morphologies that underlie this process.

The first step in studying migration is visualizing cell movements at high resolution. To provide easy visual access to the neuronal population under investigation, migration is often studied in organotypic slice culture preparations. Migrating mDA neurons form dense clusters in the developing ventral midbrain. In order to study mDA migration in detail, it is therefore essential to mosaically label mDA neurons. Furthermore, to characterize mDA migration, data-analysis protocols need to be developed for tracking a large number of migrating mDA neurons and tracing their cell morphologies in 3D. This study establishes an imaging pipeline for high-resolution 2-photon microscopy of migrating mDA neurons in organotypic slices. Using time-lapse 2-photon images, this study tracks the trajectories, neuronal speeds and cell morphologies of migrating mDA neurons in 3D.

Reelin, an extracellular matrix protein and a well-established regulator of neuronal migration, is known to be important for SN-mDA tangential migration. However, the exact role of Reelin signaling in this process is not completely understood. Disabled 1 (DAB1) is the intracellular mediator of the Reelin signal. The binding of Reelin to its receptors apolipoprotein E receptor 2 (ApoER2) and very low density lipoprotein receptor (VLDLR) activates DAB1 (via phosphorylation). By activating the downstream effectors of Reelin, phosphorylated DAB1 brings about changes.in cell adhesion properties and cytoskeletal stability thereby regulating cell migration. In this study, *Dab1* was specifically inactivated in differentiated mDA neurons. This resulted in an ectopic medial localization of parts of the SN and an intermingling of SN and VTA-mDA neurons. These data indicate that Reelin signaling is directly required in mDA neurons for their correct localization. Applying the image acquisition and data-analysis pipeline developed in this study to mDA neurons in embryonic organotypic slices from control and *Dab1*$^{-/-}$ (*Dab1* knockout) mice, the speeds, trajectories and underlying cell morphologies of mDA neurons were examined in the presence and absence of Reelin signaling. Using these techniques, this study characterizes the migratory modes and morphological changes

underlying SN-mDA tangential migration and demonstrates that Reelin promotes laterally-biased movements in mDA neurons during their slow migration mode. Furthermore, Reelin stabilizes leading process morphology and increases the probability of fast, laterally-directed migration of mDA neurons.

Overall, this study characterizes in detail the migratory and cell morphological characteristics of developing mDA neurons and elucidates the complex role of Reelin in modulating mDA neuronal speed, migratory trajectory and dynamic cell morphology.

ZUSAMMENFASSUNG

Dopaminerge Neuronen des Mittelhirns (mDA-Neurone) sind an der Regulation von extrapyramidaler Motorik, Belohnungsverhalten und kognitiven Prozessen beteiligt. mDA-Neurone entstehen in der Bodenplatte des ventralen Mittelhirns, von wo aus sie zu drei anatomisch unterschiedlichen Strukturen wandern: der seitlich positionierten Substantia Nigra (SN), dem medial positionierten ventralen Tegmentalbereich (VTA) und dem posterioren Retrorubralfeld (RRF). Frühere Studien des sich entwickelnden mDA-Systems haben gezeigt, dass sowohl SN- wie auch VTA-mDA-Neurone eine radiale Migration zwischen dem embryonalen Tag (E) 9,5-13,5 durchlaufen. Zwischen E12,5 und E15,5 wandern SN-mDA-Neurone tangential, um sich von den VTA-mDA-Neuronen zu trennen und eine lateralere Position einzunehmen. Über die extrazellulären Signalstoffe und dynamischen Zellmorphologien, die der mDA-Migration zugrunde liegen, ist jedoch wenig bekannt.

Der erste Schritt zur Untersuchung der Migration ist die Visualisierung von Zellbewegungen mit hoher Auflösung. Um einen einfache Visualisierung der zu untersuchenden neuronalen Population zu ermöglichen, wird die Zellmigration oft in organotypischen Schnittkulturpräparaten untersucht. Migrierende mDA-Neurone sind im sich entwickelnden ventralen Mittelhirn dicht gedrängt. Um die mDA-Migration im Detail zu untersuchen, ist es daher unerlässlich, mDA-Neuronen mosaikartig zu markieren. Darüber hinaus müssen zur Charakterisierung der mDA-Migration Protokolle zur Datenanalyse entwickelt werden, um eine große Anzahl von migrierenden mDA-Neuronen verfolgen und deren Zellmorphologien dreidimensional charakterisieren zu können. Die vorliegende Studie nutzt die hochauflösende 2-Photonen Mikroskopie zur dreidimensionalen Bildgebung migrierender mDA-Neurone in organotypischen Schnittkulturen. Anhand der gewonnenen Zeitraffer-2-Photonen-Bildern werden die Bewegungsbahnen, neuronalen Geschwindigkeiten und Zellmorphologien migrierender mDA-Neurone in 3D analysiert.

Reelin ist ein extrazelluläres Matrixprotein, das neuronale Migration in verschiedenen Gehirnbereichen regelt. Für die tangentiale SN-mDA-Migration ist Reelin ebenfalls wichtig, aber die genaue Rolle des Reelin-Signalwegs in diesem Prozess ist nicht vollständig verstanden. Disabled 1 (DAB1) ist der intrazelluläre Effektor des Reelin-Signals. Die Bindung von Reelin an seine Rezeptoren Apolipoprotein E Receptor 2 (ApoER2) und Very Low Density Lipoprotein Receptor (VLDLR) aktiviert DAB1 durch Phosphorylierung. Durch die Aktivierung von nachgeschalteten Effektoren bewirkt phosphoryliertes DAB1 Veränderungen der Adhäsionseigenschaften und der zytoskelettalen Stabilität der Zelle und reguliert so die Zellmigration. In dieser Dissertation wurde *Dab1* in differenzierten mDA-Neuronen spezifisch inaktiviert. Dies führte zu einer ektopischen medialen Lokalisation von Teilen der SN und einer teilweisen Vermischung von SN- und VTA-mDA-Neuronen. Diese Daten deuten darauf hin, dass die Aktivierung des Reelin-Signalwegs in SN-mDA-Neuronen für ihre korrekte

Lokalisierung erforderlich ist. Unter Anwendung der in dieser Studie entwickelten Protokolle für die Bildgebung und Datenanalyse von mDA-Neuronen in embryonalen organotypischen Schnittkulturen von Kontroll- und *Dab1-/-* (*Dab1* Knockout)-Mäusen wurden die Geschwindigkeiten, Bewegungsbahnen sowie die zugrunde liegenden Zellmorphologien von mDA-Neuronen in Gegenwart und Abwesenheit von Reelin-Signalen untersucht. Mit diesen Techniken charakterisiert diese Studie die Migrationsmodi und morphologischen Veränderungen, die der SN-mDA tangentialen Migration zugrunde liegen, und zeigt, dass Reelin lateral orientierte Bewegungen in mDA-Neuronen während ihres langsamen Migrationsmodus fördert. Darüber hinaus stabilisiert Reelin die Morphologie des Leitsaums und erhöht die Wahrscheinlichkeit einer schnellen, lateral gerichteten Migration von mDA-Neuronen.

Insgesamt charakterisiert diese Studie im Detail die migratorischen und zellmorphologischen Eigenschaften der sich entwicklenden mDA-Neuronen und verdeutlicht die komplexe Rolle von Reelin bei der Modulation der neuronalen Geschwindigkeit, den migratorischen Bewegungsbahnen und der dynamischen Zellmorphologie dieser Neurone.

1. INTRODUCTION

The brain is an intricately structured arrangement of many diverse and specialized cell types. Neural development refers to the cohort of spatiotemporally coordinated processes by which a monolayer of embryonic neuroepithelium transforms into complex brain structures. To achieve this transformation the generation, cell positioning and axon guidance of distinct groups of neurons must be precisely orchestrated. By various modes of cell movement, neuronal cells undergo substantial rearrangement within the developing nervous system and settle in brain regions often far away from their place of origin. These modes of cell movements are collectively termed as neuronal migration. To reach their correct final positions, diverse neuronal cell types must migrate by responding to specific extracellular cues and modulating their membrane trafficking and cytoskeleton assembly.

The study of neuronal migration is essential for a comprehensive understanding of brain development. Delineating the diverse mechanisms of migration involved in correct segregation and positioning of distinct neuronal populations may result in the design of assays/ genetic tools to target specific groups of neurons. The study of neuronal migration is also of clinical interest. In humans, genetic mutations that cause incorrect or misdirected neuronal migration result in structural abnormalities in the brain such as lissencephaly and microgyria (Portes et al. 1998; Sheen et al. 2006; Ganeshwaran and Mochida 2009).

1.1. Modes of neuronal migration

Radially arranged fibers, running from the ventricular zone to the pial surface in brains and spinal cords of mammalian fetuses, were first observed with Golgi staining in the 19th century, and it was reported by Magini and Cajal that neuronal cells were juxtaposed to these fibers (García-Marín, García-López, and Freire 2007; Bentivoglio and Mazzarello 1999). With the advent of immunohistochemical stains, it was established that these fibers arise from glial fibrillary acidic protein (GFAP) expressing cells in the ventricular zone (VZ) (Levitt and Rakic 1980). We now know that these cells, called radial glia cells due to their appearance and astrocytic marker identity, are the major neuronal progenitors in the central nervous system (Malatesta, Hartfuss, and Gotz 2000; Noctor et al. 2002; Anthony et al. 2004). Radial glia cells in the ventricular zone of the developing brain generate neurons by asymmetric division, each division resulting in a radial glia cell, that inherits radial fibers from its parent, and a neuronal precursor (Miyata et al. 2001). Neuronal precursors migrate away from the cell-dense ventricular zone either independently, or by using radial glia fibers as scaffolds (Noctor et al. 2001; Nadarajah et al. 2001). Radial migration refers to cell movement along the radial axis of the neural tube, while tangential migration refers to cell movements orthogonal to the axis of radial glia (Walsh and Cepko 1988; Austin and Cepko 1990). Both radial and tangential migration, are events coordinated by changes in cellular polarity, which dictate the direction

along which a neuron migrates by modulating cytoskeletal stability and adhesion properties of migrating cells (Marin et al. 2010).

1.1.1 Radial migration

Radial migration may be directed towards the pial surface, as in the case of cortical projection neurons, or away from the pial surface, as seen in granule cells of the cerebellum, or early born neurons of the pontine nucleus in the hindbrain (Watanabe and Murakami 2009; Hatanaka et al. 2016; Kratochwil, Maheshwari, and Rijli 2017).

1.1.2. Tangential migration

Directed tangential migration in response to specific extracellular cues is seen, among other regions, in cortical interneurons as they migrate from the ganglionic eminence (GE) to the cortex, and in neuronal clusters of the precerebellar system, as they migrate rostroventrally from their birthplace in the developing hindbrain (Anderson et al. 1997; Marin et al. 2001; Watanabe and Murakami 2009; Kratochwil, Maheshwari, and Rijli 2017). Tangential migration may also be non-directed, as seen in cortical interneurons migrating in the marginal zone (MZ) (Tanaka 2006; Tanaka et al. 2009).

1.2 Examples of neuronal migration

Radial and tangential migrations are seen in many brain areas and result either in the formation of laminar structures, or the formation of neuronal clusters. A schematic of some examples of long distance migration in diverse brain regions at E13.5 is presented in Figure 1. Usually, in both the formation of clusters and laminae, neurons switch between radial and tangential migration (Hatanaka et al. 2016) .

1.2.1 Neuronal migration in laminar structures

Examples of neuronal migration resulting in laminar structures include the cortex, hippocampus and cerebellum. Cortical migration involves radial migration of excitatory pyramidal neurons born in the ventricular zone of the cortex, and tangential migration of interneurons born in the lateral (LGE) and medial (MGE) ganglionic eminences (**Figure 1A**). Radial and tangential modes of cortical migration are described in detail in sections 1.2.3 and 1.2.4.

Hippocampal migration, which occurs postnatally, is similar to cortical migration: excitatory neurons (pyramidal and granule cell neurons) are born in the dorsal telencelphalon and migrate radially, while interneurons are born in the ganglionic eminences (GE) and migrate tangentially (Förster, Zhao, and Frotscher 2006; Bagri et al. 2002; Nery, Fishell, and Corbin

2002). Hippocampal granule cells can also undergo a short step of tangential migration before switching to radial migration (Wang et al. 2018).

Cerebellar Purkinje cells, migrate radially for a short distance in the periventricular region of the fourth ventricle, after which they switch to tangential migration towards anterior regions, before resuming radial migration to form the cerebellar preplate (Miyata et al. 2010; Hatanaka et al. 2016). Cerebellar granule cells, first carry out a tangential migration in the external granule layer (EGL, the place of last mitotic division) during which they show bipolar morphology (Rakic 1971). After 24-48 hours, they extend a third process in a radial direction, and switch to glia guided migration along Bergman glia fibers, across the molecular layer to settle in the inner granule layer of the cerebellum (Rakic 1971; Edmondson et al. 1988; Komuro et al. 1998; Komuro et al. 2001; Schilling 2018).

1.2.2 Migration resulting in neuronal clusters

Neuronal migration is relatively less well characterized in the formation of non-laminar clusters of the ventral CNS. Midbrain dopaminergic neurons (mDA neurons), neuronal clusters of the precerebellar system, and autonomous nuclei of the spinal cord are a few examples of the numerous neuronal clusters that form in the ventral CNS (Vaswani and Blaess 2016; Kratochwil, Maheshwari, and Rijli 2017) (**Figure 1A**). Of these, mDA neuronal migration is described in Section 2.3.

Neuronal clusters of the precerebellar system are the best studied examples of tangentially migrating ventral populations (Kratochwil, Maheshwari, and Rijli 2017). They include pontine neurons (PN), external cuneate nucleus (ECN), lateral reticulate nucleus (LRN) and inferior olive nucleus (IO) among other nuclei (Chedotal and Rijli 2009). PN, ECN and LRN are born in a specialized neurogenic zone in the dorsal hindbrain called the rhombic lip, and migrate circumferentially just beneath the pia in a distinct mode of migration defined as extramural migration (Hatanaka et al. 2016). Of these nuclei, PNs give out long processes and migrate in the anterior extramural stream (AES) first in a ventral, and then in a rostroventral direction, to settle in the region between rhombomere (r) 3 and 5 in the adult (Kratochwil, Maheshwari, and Rijli 2017) (**Figure 1A, C**). Early born PNs also undergo a subsequent, small step of radial migration to settle in the dorsal core of the pontine nucleus (Watanabe and Murakami 2009; Hatanaka et al. 2016) (**Figure 1C**). In contrast to the PNs, neurons of the LRN and ECN migrate ventrally in the posterior extramural stream (PES) to settle in r7-8 (**Figure 1 A, D**). Of these nuclei, neurons of the IO settle in the same side (ipsilateral) of the midline as their birthplace, while ECNs and LRNs traverse the developing ventral midline to settle on the contralateral side (Hatanaka et al. 2016).

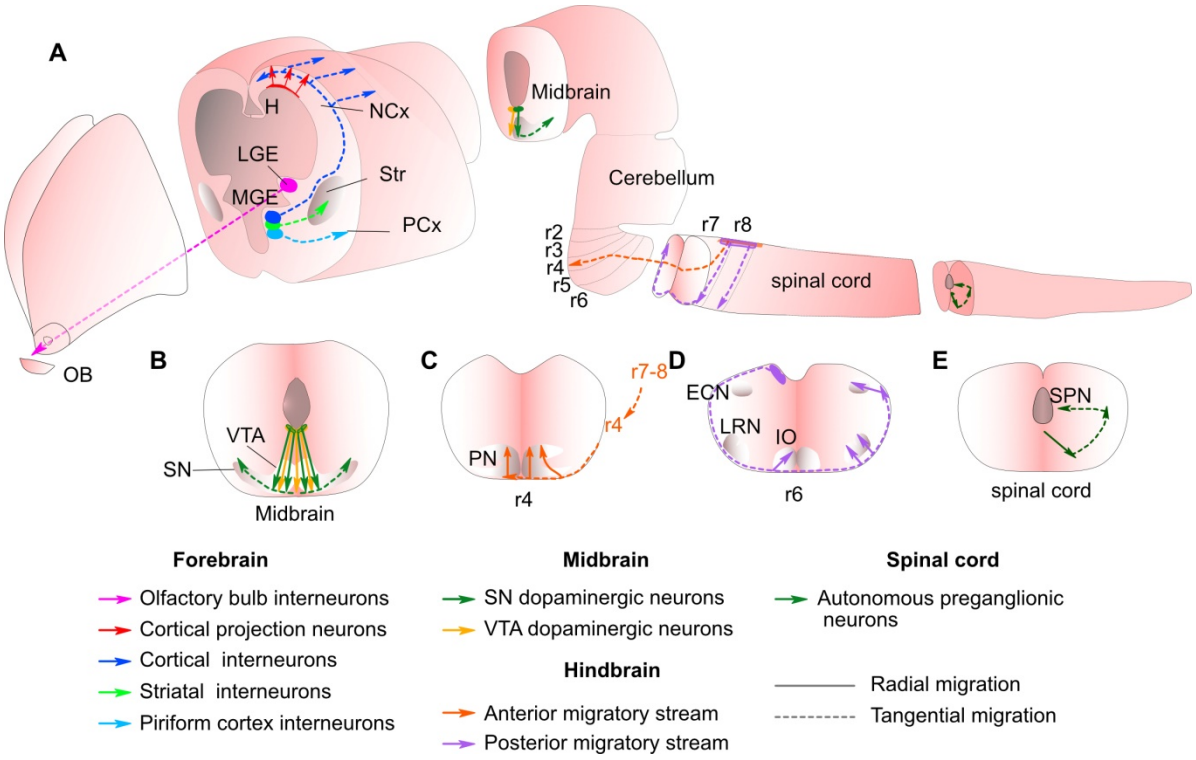

Figure 1: Examples of neuronal migration in the developing CNS. (A) Schematic indicating various migrating neuronal populations in mouse. Dashed arrows indicate tangential migratory mode, solid arrows represent radial migration. In the forebrain: red solid arrows indicate location and direction of radially cortical projection neurons migrating from the ventricular zone of the cortex to varius cortical layers. Dark blue dashed arrows represent migratory path of cortical interneurons from the medial ganglionic eminence (MGE) to the cortex. Magenta dashed arrow depicts final destination of interneurons that are born in the lateral ganglionic eminence (LGE) and settle in the olfactory bulb (OB). Cyan and light blue dahed arrows indicate migration of striatal (Str) and piriform cortical (PCx) interneurons, respectively. (B) Coronal section at the level of the midbrain in (A) shows detailed radial and tangential migratory routes of midbrain dopaminergic (mDA) neurons. Both substantia nigra (SN, dark green arrows) and ventral tegmental area (VTA, light green arrows) mDA neurons undergo radial migration from the ventricular zone to reach the pial surface. SN-mDA neurons undergo an extra tangential migration step (dark green dashed arrow) to segregate and settle lateral to VTA-mDA neurons. (C) Pontine neurons (PN) migrate tangentially in the anterior migratory stream (AES, dashed orange arrow) just below the pial surface from rhombomeres (r) 7-8 to r4 before switching to radial migration (orange solid arrow). (D) External cuneate nucleus (ECN) and lateral reticular nucleus (LRN) migrate in the posterior migratory stream (PES) to reach the ventral r7-8. These neurons then cross the midline to settle on the contralateral side in the regions indicated in (D). Inferior olive (IO) neurons migrate in the precerebellar intramural migratory stream (shown along with PES in purple for simplicity) and settle on the ipsilateral side of the midline. (E) Sympathetic preganglionic neurons (SPNs) of the spinal cord first migrate radially (solid dark green arrow in E), before migrating tangentially (dashed dark green arrow in E) to settle in the intermediolateral nucleus of the spinal cord. A few SPNs undergo and extra migratory step to settle in the more medial central autonomic region of the spinal cord. Figure concept adapted from (Marin et al. 2010).

Autonomous preganglionic nuclei are born in the VZ neuroepithelium of the spinal cord. From their birthplace, they migrate ventrolaterally along with spinal motor neurons towards the intermediate lateral region of the developing spinal cord (Phelps, Barber, and Vaughn 1991; Yip, Capriotti and Yip 2003; Vaswani and Blaess 2016). Then, in a second step they migrate dorsolaterally and thus form the intermediolateral column of the spinal cord, from where a small

number migrate towards the central canal to settle in regions medial to the intermediolateral column (Yip, Capriotti, and Yip 2003).

Though this section gives several examples for dorsal and ventral, radial and tangential migration, the best studied examples of radial and tangential migration are cortical pyramidal neurons and cortical interneurons respectively. These are described in detail in the following sections.

1.2.3 Radial migration of cortical projection neurons

The mammalian neocortex is a laminar structure consisting mainly of excitatory projection neurons and inhibitory interneurons arranged in six layers. The laminar fate of projection neurons is birth-date dependent as early neurons settle in deep layers while later born neurons settle in superficial layers (Evsyukova, Plestant and Anton 2013; He et al. 2015).

Cortical projection neurons are born in the dorsal ventricular zone (VZ) of the telencephalic lateral ventricles (**Figure 2A,B**). Early born cortical neurons migrate radially, independent of glia fibers, in a process described as somal translocation, while late born cortical neurons migrate by adhering to the radial glia scaffold (Nadarajah et al. 2001). During somal translocation, early born projection neurons extend a long process, along radial glia fibers, that traverses the intermediate zone (IZ) and branches shortly before entering the marginal zone (MZ) (**Figure 2B,a**) (Nadarajah et al. 2001; Kawauchi et al. 2015). The soma of these neurons then moves rapidly, along this long leading process, into the cortical plate (Nadarajah et al. 2001; Nadarajah et al. 2002).

Late born neuronal precursors migrate radially from the VZ to the subventricular zone (SVZ), where they detach from radial glia and temporarily adopt a multipolar morphology (**Figure 2B**) (Noctor et al. 2004; Cooper 2014). These cells migrate short distances in the SVZ, in random directions and at slower speeds than observed during somal translocation or glia dependent locomotion (Tabata and Nakajima 2003; Noctor et al. 2004). At this time, they may divide symmetrically to form two neurons that inherit multipolar morphology (**Figure 2B**) (Noctor, Martínez-Cerdeño, and Kriegstein 2008). These neurons extend multiple processes in random directions and some give rise to a horizontally oriented process which usually becomes the axon (Hatanaka and Yamauchi 2012; de Anda et al. 2010; Namba et al. 2014). After a day or more in this multipolar phase, they repolarize in response to various extracellular cues, reorient their centrosomes to face the pia, and resume glia mediated locomotion across previously generated neuronal cell layers (**Figure 2B**) (de Anda et al. 2010; Cooper 2014; Namba et al. 2014). In the last phase of their migration, known as terminal translocation, late born neurons migrate similar to somal translocation in early neurons: the leading process anchors in the marginal zone, followed by rapid movement of the cell along this

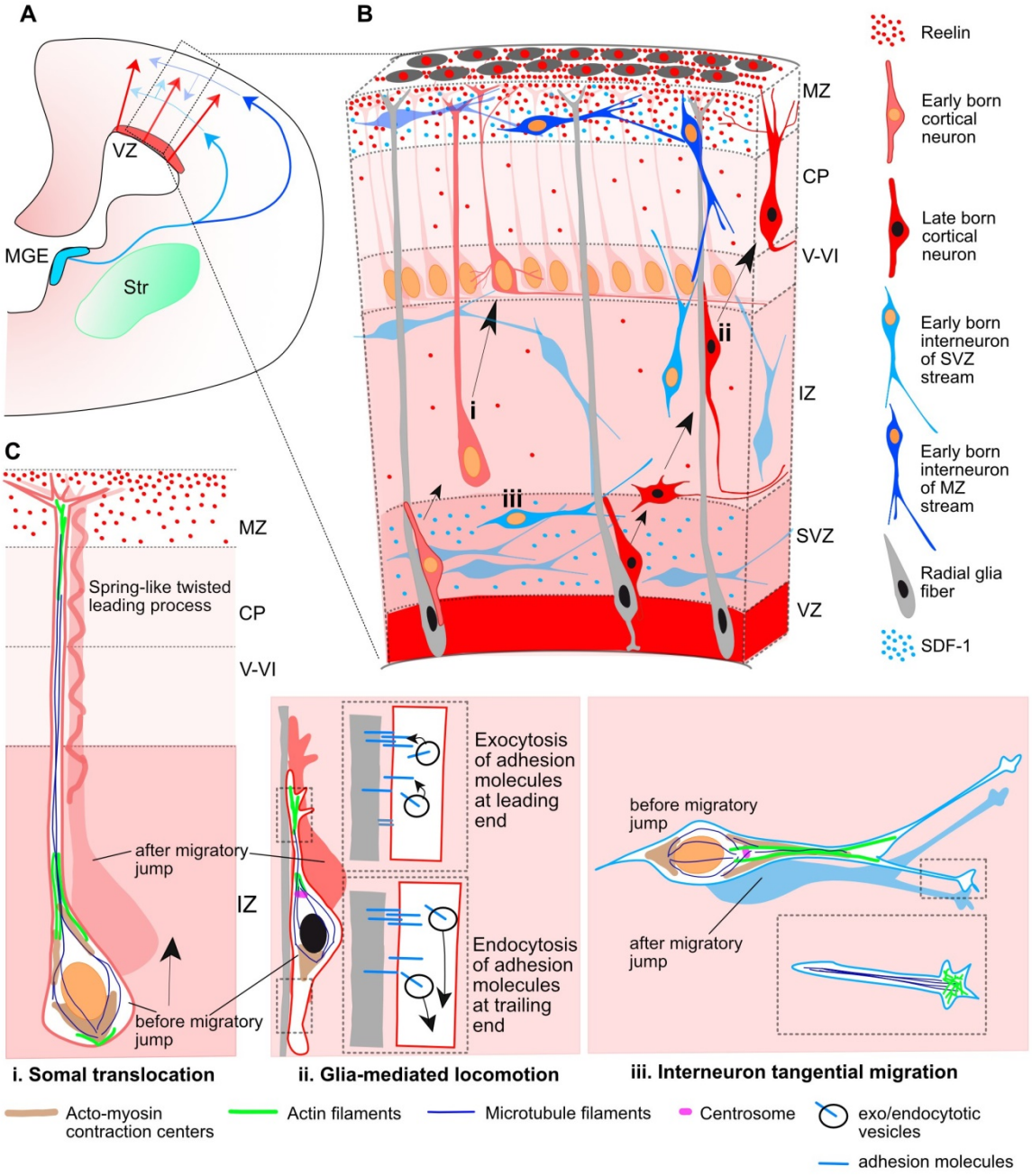

Figure 2. Neuronal migration in the cortex. (A) Radial migratory paths of cortical projection neurons (red arrows) and tangential migratory paths of cortical interneurons (light and dark blue). (B) Early born cortical projection neurons (light red, orange nucleus) migrate by somal translocation (i). Late born projection neurons (dark red, black nucleus) adopt a multipolar morphology in the SVZ before switching to glia mediated locomotion (ii). Tangentially migrating interneurons disperse through the cortex and settle in the same layers as contemporaneous projection neurons (iii, early born projection neurons and interneurons indicated by orange nucleus, Marín and Rubenstein 2003). For simplicity migratory modes (i) (ii) and (iii) are shown in the same schematic but occur at different times. (C) Cellular mechanisms underlying the three migratory modes indicated in (B): (i) Mechanism of somal translocation involves actin (green strokes) and microtubule filaments (dark blue strokes) that generate a spring-like force in the LP. (ii) Glia-mediated locomotion differs from somal translocation as these cells adhere to glia cells by expressing adhesion molecules on their surface. Migration is achieved by polarized exo- and endocytotic regulation; adhesion molecules are endocytosed in the trailing process and upregulated in the LP. (iii) Interneuron migration occurs with a branched LP; actin filaments accumulate at process ends to form small environment-sensing protrusions. Acto-myosin contraction centers (light brown regions), and the peri-nuclear microtubule cage are important for nucleokinesis (Ci-iii). CP: cortical plate, IZ: intermediate zone, MGE: medial ganglionic eminence, MZ: marginal zone, Str: striatum, SVZ: sub-ventricular zone, VZ: ventricular zone, V-VI: layer V and VI. Adapted from (Marin et al. 2010; Evsyukova, Plestant, and Anton 2013).

leading process (Nadarajah et al. 2001). The leading process begins to mature into dendrites as the neuron terminates its migration (Hatanaka and Murakami 2002). The correct radial migration of cortical neurons, through the intermediate zone and beyond earlier-born cortical layers, is essential for the inside-out layering of the cortex (Marín and Rubenstein 2003; Cooper 2008).

Neurons rarely follow a single mode of migration. Especially when traveling long distances, neurons switch between radial and tangential migration. This switching brings about a change or randomization of the direction of movement and facilitates the exposure of neurons to diverse extracellular cues in a spatiotemporally regulated manner (Cooper 2008).

1.2.4 Tangential migration of cortical interneurons

Cortical interneurons are a heterogenous population that mainly arise in the medial ganglionic eminence (MGE), caudal ganglionic eminence (CGE) or preoptic area (POA) of the ventral telencephalon (Lavdas et al. 1999; Nery, Fishell and Corbin 2002; Wichterle et al. 1999; Gelman et al. 2009). Migrating cortical interneurons are born in the GEs and POA along with amygdalar, hippocampal and striatal interneurons (**Figure 1A ,2A**) (Nery, Fishell, and Corbin 2002; Wichterle et al. 1999). They segregate from these populations, and avoiding the striatum, migrate over long distances to reach the cortical plate (Marín et al. 2001; Wichterle et al. 2001). This necessitates divergent transcription factor and molecular expression profiles that enable cortical interneurons to avoid the striatum and follow distinct routes to the cortex (**Figure 1A, 2A**) (Sussel et al. 1999; NobregaPereira et al. 2008; Nobrega-Pereira and Marín 2009; Guo and Anton 2014). Furthermore, cortical interneurons are a highly diverse group, both during development and in the adult brain (Sultan and Shi 2017). Based on spatiotemporal differences in their generation, and diverse transcription factor profiles during development, adult interneurons derived from distinct regions in the GE differ in morphology, molecular marker expression, laminar identity, electrophysiological properties and cell connectivity profiles (**Figure 2B**) (Butt et al. 2005; Fogarty et al. 2007; Gelman and Marín 2010; Corbin and Butt 2011; Sultan and Shi 2017).

Migrating cortical interneurons reach the cortex by distinct routes: MGE interneurons migrate in a deep migratory stream dorsomedial to the striatum, while POA interneurons migrate in a superficial stream around the striatum (Marín et al. 2001; Zimmer et al. 2011; Guo and Anton 2014). Furthermore, upon reaching the cortex, MGE interneurons further diverge into three separate streams: at the level of the MZ above the CP, at the level of the subplate just below the CP, and at the level of the lower IZ/SVZ (**Figure 2B**) (Marín et al. 2001; Anderson et al. 1997; Marín 2013; Evsyukova, Plestant and Anton 2013). Interneurons from the CGE follow a separate caudal migratory stream to migrate into the cortex (Yozu 2005; Ruiz-Reig and Studer 2017).

In the next phase of their migration, interneurons in various dorsoventral cortical zones disperse into the cortex by various migratory maneuvers (Guo and Anton 2014). Interneurons in the MZ disperse tangentially to cover the mediolateral extent of the cortex by multidirectional migration steps during which they contact several radial glia end feet (Tanaka 2006; Tanaka et al. 2009; Yokota et al. 2007; Guo and Anton 2014). During this phase of tangential dispersion, interneurons extend highly branched leading processes (LP), and dynamically stabilize and retract branches to facilitate frequent changes in direction (**Figure 2B, C**) (Martini et al. 2008; Lysko et al. 2011; Lysko, Putt and Golden 2014). While this random migratory behavior is believed to expose interneurons to extracellular cues (Tanaka et al. 2009), it has also been suggested that contact inhibition between interneurons during this process might result in more effective tangential dispersion (Marín 2013). In the lower IZ/SVZ regions interneurons disperse tangentially from lateral regions towards the midline (Hatanaka et al. 2016; Sultan and Shi 2017). The final mediolateral position of interneurons does not seem to be linked topographically to their birthplace in the GE, rather earlier born MGE interneurons in any specific layer tend to occupy more medial positions than younger interneurons (Lourenço et al. 2012; Bartolini, Ciceri and Marín 2013).

After tangential dispersion, interneurons transition to radial migration to disperse into the appropriate laminar layer (Nadarajah et al. 2002; Yokota et al. 2007). This switch from tangential to radial migration is believed to be mediated by signaling from the primary cilium that typically docks to the leading process in these interneurons (Baudoin et al. 2012). During their radial migration, they either move directly towards the pial surface, or first towards the ventricle before moving towards the pia (Nadarajah et al. 2002). Radially migrating interneurons require dynamic interactions with radial glia cells or with thalamocortical projections to transition from tangential to radial migration (Yokota et al. 2007; Bartolini, Ciceri and Marín 2013; Zechel, Nakagawa and Ibáñez. 2016). The current view is that ventricle-directed radial migration, and interactions with multipolar cortical projection neurons and radial glia cells in the SVZ, provide important cues for correct laminar dispersion of interneurons (Ayala et al. 2007; Yokota et al. 2007). The correlation between birthdate of interneurons and their laminar fate, with contemporaneous interneurons and projection neurons sharing the same laminar fate (**Figure 2B**), is hypothesized to be the result of cues from contemporary projection neurons (Lodato et al. 2011; Bartolini, Ciceri and Marín 2013).

Having described the two modes of migration and the various migratory behaviors of neuronal subpopulations, I will now focus on the morphology and underlying cytoskeletal changes that are important for these various migratory behaviors.

1.3. Cellular mechanisms of neuronal migration

Neuronal migration is achieved by a dynamic regulation of actin and microtubule assembly. With the exception of neurons that extend and maintain a large leading process during their migration phase, one cycle of neuronal migration consists of three phases: (1) leading process extrusion, (2) nucleokinesis and (3) retraction of trailing end (Marín et al. 2010). Typically, a neuron polarizes in response to physical or chemical cues and gives out a process, called the leading process (LP), by modifying its actin cytoskeleton (Tsai and Gleeson 2005; Graziano and Weiner 2014; Tsujita, Takenawa and Itoh 2015; Schelski and Bradke 2017). The LP may be stabilized or destabilized by local regulation of microtubule assembly in response to extracellular cues (**Figure 2C, i-iii**) (Martini et al. 2008; Yanagida et al. 2012). When the LP comes into contact with the appropriate cues, it stabilizes by a characteristic thickening of the process (Solecki et al. 2004). Cell organelles, and finally the nucleus are transported into this LP by coordination of the centrosome and perinuclear microtubule skeleton (**Figure 2a-c**) (Solecki et al. 2004; Tsai and Gleeson 2005). This process is called nucleokinesis.

Neurons typically migrate in spurts: a phase of rapid cell locomotion is followed by a phase of rest. During both, the rest and motion phases, the neuron constantly extends and retracts processes and senses its extracellular environment (Edmondson et al. 1988). This saltatory cell movement is accompanied by periodic changes in cell morphology that are regulated by cyclic changes in the actin cytoskeleton (Graziano and Weiner 2014). Similar patterns of periodic actin cytoskeletal regulation are seen in other motile eukaryotic cells. The following section briefly describes the general features of cell migration.

1.3.1 Mechanisms of eukaryotic cell motility

Directed eukaryotic cell movement has been extensively studied in various cell-types and organisms, including *Dictyostelium*, fibroblasts, keratinocytes, neutrophils and cultured neurons (Da Silva and Dotti 2002; Allard and Mogilner 2013; Graziano and Weiner 2014). Based on these studies, the steps of neuronal migration described in the previous section are regulated by the following coordinated changes in the cytoskeleton: (1) characteristic protrusions which result in the formation of a leading edge, (2) strong adhesion contacts in the front end of a cell, (3) cytoskeletal contraction that brings about the movement of organelles, (4) release of contact sites at the trailing end, (5) recycling of cytoskeletal proteins and membrane receptors from the trailing end to the leading end (**Figure 2C. i-iii)**) (Friedl and Bröcker 2000; Friedl and Wolf 2009; Allard and Mogilner 2013).

Actin cytoskeleton in the periphery of a cell (called cortical actin) regulates formation of protrusions by a modulation of membrane tension (Allard and Mogilner 2013; Flynn 2014; Zhang et al. 2016). Actin polymerization can be stabilized by formins, such as the diaphanous related formin 1,2 (DRF1,2) and actin related proteins 2/3 (ARP2/3), that cap the barbed ends

of growing actin filaments, or destabilized by anti-capping proteins such as Ena/VASP proteins (EVH-1) (Shinohara et al. 2012; Devreotes and Horwitz 2015). Actin polymerization in chemotactic cells has been described as an oscillatory excitable system (Graziano and Weiner 2014). Local fluctuations in the concentration of actin nucleators or stimulators — such as hematopoetic protein 1 (HEM-1) of the SCAR/WAVE complex, or Rho family GTPases — generate periodic oscillations in levels of cortical actin in the cell periphery (Weiner et al. 2007; Allard and Mogilner 2013). In a stationary cell, these oscillations are randomly and locally generated, and do not result in net movement of the soma (Graziano and Weiner 2014).

When this excitable system is faced with polarizing cues, actin nucleators such as Hem-1 organize into wave-like patterns at the leading edge of the cell (Weiner et al. 2007). The recruitment and release of these actin polymerizing factors propagates towards the cell membrane and results in a corresponding wave-like organization of polymerized actin (Huang et al. 2013; Graziano and Weiner 2014). Furthermore, the velocity and stability of actin waves increases with increasing proximity to the plasma membrane (Weiner et al. 2007). When propagating Hem-1 waves reach the plasma membrane, they stabilize and induce local actin polymerization. Actin aggregation at the plasma membrane results in the formation of a leading process (Steffen et al. 2004; Graziano and Weiner 2014; Zhang et al. 2016). While leading edge formation increases stabilization of actin polymerization locally, it also results in an overall increase in cell membrane tension (Tsujita, Takenawa, and Itoh 2015). This increased membrane tension globally suppresses formation of new protrusions on the cell membrane (Flynn 2014; Tsujita, Takenawa, and Itoh 2015; Schelski and Bradke 2017). The combination of fast, local excitation and slow global inhibition of actin polymerization results in the generation of wave like patterns in the cortical actin facilitating cell movement (Huang et al. 2013; Graziano and Weiner 2014). The self-organization of actin polymerizing complexes into wave-like patterns, aided by myosin-mediated actin contraction, are responsible for the dynamic behavior of lamellopodia in motile cells (Allard and Mogilner 2013). Having described here the basic mechanisms of actin regulation in cell motility, the next section focuses on neuron-specific cellular migratory mechanisms.

1.3.2 Leading edge dynamics of migratory neurons

Similar to other motile cell types, extracellular or intrinsic cues cause neurons to polarize, defining an orientation and direction for migration. These cues may be chemical ligands, such as motogenic, chemoattractant or chemorepellant cues, physical factors like cell plasma membrane tension, or intrinsic fluctuations in actin aggregates at the cell cortex (Ghashghaei, Lai, and Anton 2007; Tsujita, Takenawa, and Itoh 2015; Zhang et al. 2016). After its formation, further stabilization and extension of a leading process is facilitated by microtubules that run

from the cell soma into the process, allowing for structural stability and intracellular communication (Shim et al. 2008; Valiente and Marín 2010).

Leading edges of neurons display complex morphologies and process dynamics. Leading edge morphologies have also been reported to be different depending upon the type of neuron, complexity of extracellular environments and type of migratory behavior involved (Valiente and Marín 2010). Early born cortical projection neurons extend a long leading process that branches just before ending in the MZ (**Figure 2C.i**) (Nadarajah et al. 2001; Noctor et al. 2004). The end of the leading process remains stationary as the soma translocates along the process, and stops upon reaching the branch-point. One of the branches is retracted before the neuron migrates along the remaining branch (Nadarajah et al. 2001). Migration force for somal translocation has been proposed to be generated by a twisting and stretching of intermediate filaments in the leading process that pulls the nucleus and soma forward (Miyata and Ogawa 2007). Based on this observation, it is hypothesized that production of cell-type dependent intrinsic cytoskeletal modulators and extrinsic factors like tissue tension and crowding combinatorically regulate somal translocation in projection neurons (Miyata and Ogawa 2007; Evsyukova, Plestant and Anton 2013).

Late born cortical projection neurons have short and unbranched leading process as they exit the VZ by radial migration (Noctor et al. 2004). In their multipolar phase, they display thin, transient leading processes before forming a horizontal or ventricle oriented process that goes on to become the axon (**Figure 2B**) (Tabata and Nakajima 2003; de Anda et al. 2010). This process trails behind the soma when the cell resumes glia-mediated locomotion with an unbranched leading process that moves, along with the soma, towards the pia (**Figure 2C.ii**) (Nadarajah et al. 2001; Tabata and Nakajima 2003; de Anda et al. 2010; Cooper 2014).

During tangential migration, the leading edge of neurons is frequently branched (**Figure 2C.iii**) (Martini et al. 2008; Lysko, Putt, and Golden 2011; Yanagida et al. 2012). How exactly branching of the leading edge process is regulated in response to extracellular cues is unclear. However, it has been shown that when interneurons migrate without change in direction, branch angle remains constant, left and right branches are equally likely and the nucleus translocates into the left or the right branch with equal probability (Martini et al. 2008). When a neuron decides to choose between one of two branches, it stabilizes one and retracts the other and the nucleus translocates to the branch point before the next cycle begins (Martini et al. 2008). It has been hypothesized that local intracellular Ca^{2+} levels mediate frequency and orientation of branching in response to extracellular cues (Martini et al. 2008; Valiente and Marín 2010).

Leading process (LP) stabilization and dynamics are intimately linked to the subsequent phase of nucleokinesis and cell soma movement. Cell adhesion mechanisms seem to be important for LP stabilization (Evsyukova, Plestant, and Anton 2013). Interfering with the

interactions between radial glia and radially migrating projection neurons results in abnormal branching of radially migrating projection neurons, suggesting that glial interactions may be responsible for stable, unbranched leading processes in these neurons (Marin et al. 2010). This hypothesis is further strengthened by evidence uncovering regulatory feedback loops between adhesion, actin polymerization and myosin mediated contraction (reviewed in (Devreotes and Horwitz 2015)). Especially in glia dependent locomotion, gap junctions between radial glia fibers and translocating neurons provide transient adhesive contacts that are important for the stabilization of the LP and proper nuclear translocation (Elias, Wang, and Kriegstein 2007). While the formation of these gap junctions has shown to be dispensable for the tangential migration of interneurons, it is required for their transition to radial migration and correct laminar positioning (Elias et al. 2010).

The forward flow of F-actin into the LP seems to be important for coordinated nucleokinesis following LP stabilization (Solecki et al. 2009; He et al. 2010; Trivedi and Solecki 2011; Trivedi et al. 2014). Regulated by myosin II activity, this forward flow of F-actin is believed to act as a traction providing contractile centre at the proximal leading process in migrating neurons (He et al. 2010; Jiang et al. 2015). Furthermore, the F-actin rich tip of the leading process has been compared to growth cones in axon guidance, where F-actin dynamics at the tip of the leading process seem to be important for exploratory behaviors of growth cones (Dent, Gupton, and Gertler 2011).

Misregulated leading process dynamics and stabilization can have profound impact on migratory behaviors of a cell. Multiple ligands have been reported to affect leading process stability. Branching of leading process is correlated with a decrease in migratory speed. For example, stromal cell derived factor 1 (SDF-1) acts through its receptor the chemokine (C-X-C motif ligand) 12 (CXCR4) and causes an increase in leading process branching in migrating interneurons and slows down their tangential migration (Lysko, Putt, and Golden 2011; Lysko, Putt, and Golden 2014).

1.3.3 Nucleokinesis

Leading edge formation is followed by translocation of the centrosome, mitochondria, rough endoplasmic reticulum and Golgi apparatus into the leading edge, which causes a characteristic thickening of this process (Solecki et al. 2004; Schaar and McConnell 2005; Bellion et al. 2005). The centrosome is a microtubule organizing center, consisting of two non-membranous centrioles (Sanchez and Feldman 2017). The centrosome in migrating neurons organizes and remains connected to a microtubule network that envelopes the nucleus in a cage-like assembly of diverse types of microtubules (**Figure 2C.i-iii**) (Rivas and Hatten 1995; Solecki et al. 2004; Higginbotham and Gleeson 2007). Microtubules surrounding the nucleus are highly dynamic due to tyrosine modifications, while those around the centrosome are more

stable due to acetylation (Baudoin et al. 2007; Umeshima et al. 2007). In migrating interneurons, the centrosome is typically located in the front of the nucleus (in the direction of migration), and microtubules emanating from it run posteriorly around the nucleus and forwards into the leading edge (Solecki et al. 2004).

It is believed that the translocation of the centrosome into the leading process pulls the nucleus into the leading process, while the nucleus receives a push from the rear end by a myosin II mediated contraction (**Figure 2C. i-iii**) (Bellion 2005; Higginbotham and Gleeson 2007; Tsai, Bremner, and Vallee 2007; Trivedi and Solecki 2011). Movement of the centrosome and nucleus along microtubules is regulated by the motor protein dynein, and its regulator lissencephaly 1 (LIS1) (Tsai, Bremner, and Vallee 2007). Dynein is enriched in the leading edge swelling and has been hypothesized to pull the centrosome into this region by acting on the microtubules running from the centrosome to the leading edge. LIS1 and dynein act on microtubules, independent of myosin II motors that act on the actin cytoskeleton (Bellion 2005; Tsai, Bremner, and Vallee 2007). LIS1 and dynein pull on the nucleus from the proximal leading edge, while myosin II accumulates at the rear end of the cell and provides a contractile push from behind the nucleus (Tsai, Bremner, and Vallee 2007).

However, while this type of behavior explains the tangential migration of interneurons, radially migrating cerebellar granule cells frequently undergo a different type of nucleokinesis during which the nucleus moves faster than the centrosome and overtakes it. During the subsequent rest phase of the nucleus, the centrosome reestablishes cell polarity by moving back to the front of the cell (Umeshima, Hirano, and Kengaku 2007; Trivedi and Solecki 2011). Hence mechanisms of nucleokinesis may differ in radial and tangentially migrating cells (Evsyukova, Plestant, and Anton 2013).

Other microtubule associating proteins, such as double cortin (DCX) and kinesin are important for proper nucleokinesis (Marin et al. 2010; Evsyukova, Plestant, and Anton 2013). Cell polarity-influencing molecules, such as partition defective (PAR) 1, and PAR6 are important for the proper alignment of the centrosome and nucleus and hence indirectly influence nucleokinesis (Solecki et al. 2004; Reiner and Sapir 2009; Valiente and Marín 2010; Hansen et al. 2017).

1.3.4. Trailing process dynamics

Reflecting differences in nucleokinesis, tangentially or radially migrating neurons display distinct types of trailing processes (Evsyukova, Plestant, and Anton 2013). Enrichment of myosin II is observed at the rear end of tangentially migrating interneurons, while in radially migrating projection neurons or cerebellar granule cells, myosin II is highly concentrated at the proximal end of the leading process (Bellion 2005; Trivedi and Solecki 2011). In interneurons, contractile action of myosin II is believed to propel the nucleus and soma forward, while in

radially migrating neurons, it is thought to bring about the forward translocation of the centrosome, which then mediates nucleokinesis (Bellion 2005; Solecki et al. 2009; He et al. 2010).

As neuronal migration involves the coordinated activity of various cytoskeletal compartments, *in vivo* regulation of this process is achieved by diverse signaling pathways that differently converge on, and regulate cytoskeletal and adhesion dynamics (Ayala et al. 2007). As this study focusses on the role of Reelin in the tangential migration of midbrain dopaminergic neurons, the following section will discuss the molecular mechanisms by which Reelin modulates neuronal migration.

1.4. Reelin signaling pathway

Reelin, a large extracellular matrix molecule, binds to receptors apolipoprotein E receptor 2 (APOER2 also known as LRP8) and very low density lipoprotein receptor (VLDLR), bringing about the phosphorylation of the intracellular downstream effector disabled homolog (DAB1) (Hiesberger et al. 1999; Trommsdorff et al. 1999; Howell et al. 1997). In addition to APOER2 and VLDLR, Reelin has been reported to bind α3β1-integrin (Dulabon et al. 2000). Also, DAB1 phosphorylation is mediated by the Src family tyrosine kinases, FYN and SRC, and because APOER2 and VLDLR both lack intrinsic kinase activity required to activate FYN and SRC, it has been debated whether Reelin signaling requires other coeffectors such as Ephrin-B (Sentürk et al. 2012; Pohlkamp et al. 2016).

The downstream effects of DAB1 phosphorylation have been primarily studied in cortical projection neurons. DAB1 phosphorylation can recruit several signaling pathways such as the CRK/CRKL-RAP1-CDH2 pathway to promote cell adhesion, and the LIMK1-Cofilin 1 pathway to stabilize the cytoskeleton (CRK: adapter molecule crk; CRKL: Crk-like; C3G: Rap guanine nucleotide exchange factor 1; RAP1: Ras-proximate-1; CDH2: Cadherin 2; LIMK1: LIM domain kinase 1) (**Figure 3**) (Ballif, Arnaud, and Cooper 2003; Ballif et al. 2004; Park and Curran 2008; Voss et al. 2008; Chai et al. 2009; Franco et al. 2011; Jossin and Cooper 2011; Gil-Sanz et al. 2013).

Reelin is expressed in the developing cortex in the Cajal-Retzius (CR) cells of the MZ, while APOER2/VLDLR and DAB1 expression are seen in radially migrating cortical projection neurons (D'Arcangelo et al. 1995; Trommsdorff et al. 1999; Howell et al. 1997). Early studies established the importance of Reelin for correct inside-out cortical lamination (D'Arcangelo et al. 1995). The *reeler* mouse mutant (a homozygous spontaneous mutation of *Reln* gene), *Apoer2/Vldlr* double knockout mice and *Dab1* mutant mice (*scrambler* and *yotari* with a spontaneous mutation of *Dab1*, and the genetically engineered knockout line *Dab1*$^{-/-}$), all show similar lamination defects in the cortex, hippocampus and cerebellum; and various migratory defects in dorsal and ventral structures in the brain and spinal cord (Falconer 1951;

D'Arcangelo et al. 1995; Hiesberger et al. 1999; Trommsdorff et al. 1999; Howell et al. 1997; D'Arcabgelo 2014; Krüger et al. 2010). Based on studies in the cortex, several roles for Reelin signaling have been hypothesized. In an attempt to elucidate the complexity of Reelin function, the following sections describe the well-established roles of Reelin in the formation of laminar structures.

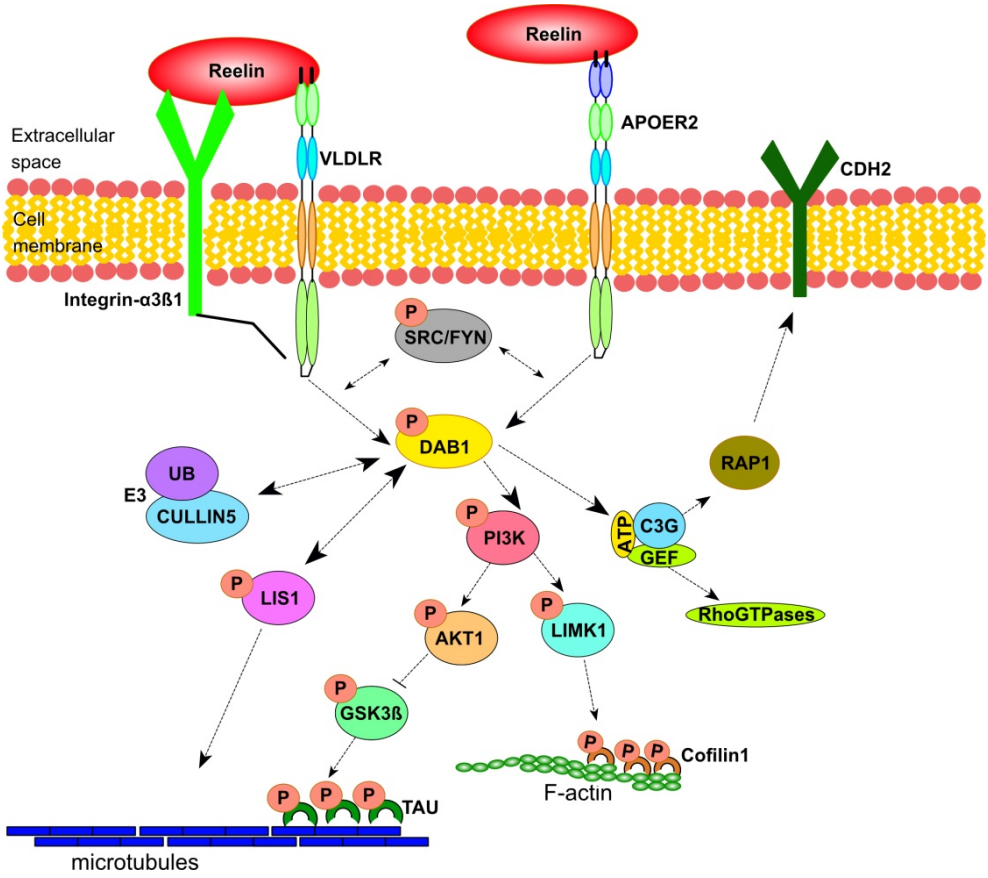

Figure 3. Cannonical Reelin signaling pathway. Reelin binds its receptors APOER2 and VLDLR resulting in the phosphorylation of DAB1 through SRC/FYN kinases. The phosphorylation of DAB1 can effect microtubule stability via LIS1 or through the inhibition of GSK3ß. Phosphorylation of DAB1 also modulates F-actin stability through LIMK1 and Cofilin1, and can modulate cell adhesion properties of cells by membrane localization of CDH2 via the C3G-RAP1 pathway. APOER2: apolipoprotein E receptor 2, VLDLR: very low density lipoprotein receptor, DAB1: disabled homolog 1, SRC/FYN: Src family tyrosine kinases, CRK/CRKL: adapter molecule crk/ Crk-like, C3G: Rap guanine nucleotide exchange factor 1, RAP1: Ras-proximate-1, CDH2: Cadherin 2, LIMK1: LIM domain kinase 1, LIMK1: LIM domain kinase 1, LIS1: lissencephaly 1, AKT1: serine/threonine kinase 1, GEF: Guanine exchange factor, GSK3ß: glycogen synthase kinase 3ß, UB: ubiquitin ligase.

1.4.1. Diverse roles for Reelin in the regulation of neuronal migration

Over the years, various hypothesis have been proposed for the roles of Reelin in cortical neuronal migration: Reelin as a repellant (Ogawa et al. 1995), a chemoattractant (Gilmore and Herrup 2000), a stop signal (Dulabon et al. 2000; Jossin et al. 2004) and a regulator of cell orientation/polarization (Miyata et al. 2010; Jossin and Cooper 2011; Cooper 2014). Other proposed roles include promotion of cytoskeletal stability (Chai et al. 2009), leading process stability through regulation of neuronal cell adhesion properties (Franco et al. 2011; Sekine et al. 2012) and the promotion of microtubule assembly (Meseke, Cavus and Förster 2013).

Some of these proposed roles have gained credibility in light of recent findings, while others have been ruled out. In the following sections, the accepted roles of Reelin signaling in neuronal migration are discussed.

1.4.2. Reelin stabilizes the leading process of migrating cortical projection neurons

Reelin signaling pathway has been shown to cell autonomously regulate somal translocation in deep layer neurons and terminal translocation in upper layer neurons by stabilizing their leading processes in the MZ and facilitating their subsequent translocation in a glia-independent manner (Franco et al. 2011). The CRK/CRKL-C3G-RAP1 pathway has been implicated downstream of DAB1 (**Figure 3**) in the stabilization of neuronal apical processes (Park and Curran 2008; Voss et al. 2008; Franco et al. 2011; Sekine et al. 2012). However, while Reelin signaling results in the membrane localization of CDH2 (Cadherin 2, of the cadherin superfamily) downstream of RAP1 during somal translocation, the role of CDH2 in terminal translocation is not straightforward, as its overexpression does not rescue the effects of Rap1 knockdown (Franco et al. 2011; Sekine et al. 2012; Gil-Sanz et al. 2013). Moreover, CDH2 is involved in glia-dependent locomotion, making its role in terminal translocation even more difficult to dissect (Kawauchi et al. 2010; Kawauchi 2015). Other factors can also be activated downstream of RAP1; the knockdown of integrinα5ß1, also affects apical process stability in terminal translocation suggesting that additional adhesion molecules may be recruited by Reelin signaling (Sekine et al. 2012). It has been hypothesized that both CDH2 and Integrin α5ß1 act downstream of Reelin, with Integrin α5ß1 anchoring the leading tip of terminally translocating neurons in the MZ and N-cadherin regulating the subsequent cell movements (Sekine, Kubo, and Nakajima 2014). Hence Reelin signaling seems to modulate the stability of leading processes during migration by altering cell adhesion properties of the processes.

Reelin signaling by phosphorylating Cofilin 1 via LIMK1 (**Figure 3**) has been shown to stabilize leading processes of migrating neurons (Chai et al. 2009; Flynn et al. 2012). Reelin signaling results in the activation (phosphorylation) of PI3K (Phosphatidylinositol-4,5-bisphosphate 3-kinase) through DAB1 (Hiesberger et al. 1999). PI3K activates LIMK1 (Lim domain kinase 1) via Rac1/Cdc42 and PAK1. P-LIMK1 in turn inactivates Cofilin 1 by phosphorylation. Cofilin 1 is a regulator of actin polymerization (Bellenchi et al. 2007). Along with actin depolymerizing factor (ADF), non-phosphorylated Cofilin 1 regulates the dynamic actin cytoskeleton by severing F-actin to generate barbed F-actin ends and new G-actin available for polymerization (Lappalainen and Drubin 1997; Ichetovkin et al. 2000; Andrianantoandro and Pollard 2006; Flynn et al. 2012; Chai et al. 2016). Phosphorylation of Cofilin 1 by LIMK1, prevents actin binding activity and stabilizes F-actin structures (Bravo-Cordero et al. 2013; Kanellos et al. 2015). While Franco et al. showed that the knockdown of

LIMK1, AKT1 or Cofilin 1 does not affect somal/ terminal translocation cell autonomously, regulation of cytoskeleton stability downstream of Reelin via the LIMK1-AKT1-Cofilin 1 pathway has not been completely ruled out as the overexpression of pseudophosphorylated Cofilin 1 seems to partially rescue the *reeler* phenotype (Chai et al. 2009; Sekine, Kubo, and Nakajima 2014). Hence, it is possible that Reelin mediates leading process stability, directly and indirectly, by regulating several downstream pathways.

1.4.3. Reelin is important for neuronal polarity and correct orientation of leading process

Reelin is a large protein (size ~ 385 kDA) and upon its secretion into the extracellular environment, it is cleaved into three major proteolytic fragments (D'Arcangelo 2014). Upon Reelin secretion by the Cajal Retzius (CR) cells, these cleavage products have been shown to diffuse to the bottom of the CP (Jossin and Goffinet 2007). Additionally, a low level of Reelin, the source of which is yet to be identified, has been reported in the SVZ (Uchida et al. 2009). Reelin signaling through RAP1 brings about the correct orientation of multipolar neurons in the IZ, thereby facilitating a transition from multipolar to bipolar morphology and enabling their entry into the cortical plate (CP) for their subsequent radial migration (Jossin and Cooper 2011). More specifically, RAP1 activation by Reelin signaling enhances CDH2 localization at the membranes of multipolar neurons (**Figure 3**). By unknown mechanisms (Rho and Ras-related protein family GTPases might be involved), CDH2 membrane localization sensitizes these neurons to external cues that then result in their proper orientation (Jossin and Cooper 2011). Hence, a dual role for the Reelin-mediated RAP1-CDH2 signaling has been proposed in the neuronal migration in the neocortex: surface localization of CDH2, downstream of Reelin, orients multipolar neurons in the IZ allowing them to begin glia dependent locomotion, while the same signaling pathway facilitates glia-independent, somal translocation of deep layer neurons (Franco et al. 2011; Jossin and Cooper 2011). How CDH2 mediates these distinct functions is unclear.

Polarity defects in *reeler* mice and reelin receptor knock-outs also appear in the dentate gyrus (DG) of the hippocampus (Drakew et al. 2002). In the absence of Reelin signaling, granule cells migrate along aberrant trajectories, do not laminate the suprapyramidal zone of the DG, but tend to be scattered in the hilus (Wang et al. 2018) In the DG, neurons continue to be generated in adulthood, and Reelin has been shown to be required not just for guiding late born hippocampal neurons, but also for the maintenance of their positions: reduced Reelin is associated with motility and dispersion of these neurons (Chai et al. 2013; Förster 2014).

Radially migrating cortical neurons have a thick leading process in the direction of migration, while at the other end of the cell, a thinner process distinguishes the future axon (de Anda et al. 2010). A recent study shows that overexpression of phosphorylated Cofilin results in

indistinguishable processes of equal thickness, suggests that Reelin dependent phosphorylation may influence polarity of migrating neurons (Chai et al. 2016). Hence, Reelin can influence the polarity and orientation of neurons by sensitizing neurons to other signals or by direct actin cytoskeleton regulation.

1.4.4. Reelin as a stop signal for neuronal migration

Reelin has been suggested to function as a stop signal for migrating cortical neurons by regulating their adhesion to radial glia: Reelin induces detachment of migrating neurons from radial glia cells in vivo and inhibits neuronal migration in vitro (Dulabon et al. 2000; Tissir and Goffinet 2003). *Scrambler* mutants have also been reported to show abnormal adhesion to radial glia (Sanada, Gupta, and Tsai 2004). However, ectopic expression of Reelin in the ventricular zone (VZ) in a transgenic mouse line does not result in premature detachment of neurons from their radial glia (Magdaleno, Keshvara, and Curran 2002). This model also fails to explain the partial recovery of inverted layering by application of exogenous Reelin to cortical slices (Jossin 2004). Recently, it has been proposed that Reelin acts as a stop signal by inducing neuronal aggregation via the CDH2 pathway, and thus the fine tuning of proper lamination in the cortex might be mediated by homophilic aggregation of layer specific neurons (Matsunaga et al. 2017).

While the stabilization of the cytoskeleton via the LIMK1-Cofilin 1 pathway is thought to stabilize the leading process anchoring in the marginal zone (see section 1.3.1.), it has also been suggested that termination of migration is mediated through Reelin-dependent, Cofilin 1 stabilization (Krüger et al. 2010). This seems to be true in the spinal cord, where Reelin has been shown to prevent the aberrant tangential migration of neurons of the autonomous nervous system by stabilizing the actin cytoskeleton by signaling through LIMK1 and phosphorylating Cofilin 1 (Krüger et al. 2010).

1.4.5. Indirect roles for Reelin signaling

While the functions of Reelin discussed so far have focused on direct effects of Reelin signaling, indirect effects on neuronal migration due to affected radial glia morphology or misplaced cues due to inverted layering cannot be ruled out. Reelin has been shown to regulate radial glia cell morphology and maturation (Hartfuss et al. 2003). Reelin also acts, apparently via binding of Notch1 to DAB1, to promote process extension of radial glia (Keilani and Sugaya 2008). It is also believed that altered radial glia morphology may cause inefficient neuronal migration in the hippocampus (D'Arcangelo 2014). Indirect effects of improper cortical layering, such as abnormal dendritogenesis of early cortical projection neurons, may also be responsible for the ectopic localization of late cortical projection neurons and interneurons (Jossin and Goffinet 2007; Yabut et al 2007; Nichols and Olson 2010). As multiple nuclei are

affected in the absence of the Reelin signaling pathway in the brain, it is essential to generate conditional knockouts specific to the neuronal population being assessed to rule out indirect effects. In this study, we generate conditional knockouts for *Dab1* specific to the midbrain dopaminergic (mDA) neurons, to dissect out the role of Reelin in the correct positioning and migratory behaviors of SN-mDA neurons. The last part of this introduction is a general description of mDA neurons, their development, with a focus on their migration, connectivity and function.

1.5. Midbrain dopaminergic neurons

Pioneering studies classified all monoamine-producing neurons in the brain according to the 'A' (for aminergic) group nomenclature: groups A1-A7 consist of noradrenergic neurons, while A8-A14 are dopaminergic (Dahlström and Fuxe 1964). Acccording to this classification, midbrain dopaminergic (mDA) neurons are comprised of three dopaminergic groups: the retrorubral field (RRF, A8), substantia nigra (SN, A9), ventral tegmental area (VTA, A10) (**Figure 4D**) (Falck et al. 1962; Dahlström and Fuxe 1964; Björklund and Dunnett 2007a).

mDA neurons, located in the ventral midbrain, are the largest source of dopamine in the mammalian CNS, with diverse, long distance, stereotypically arranged connectivity patterns. Anatomically, early studies distinguished the substantia nigra (from Latin, means 'black substance') from neighboring VTA, as the SN appears dark, in humans, primates and rats, due to the neuromelanin that accumulates in the cell bodies of these neurons (Scherer 1939; Mann and Yates 1974). While recent studies have highlighted many differences within and across the anatomically defined SN and VTA subdivisions, the historical division of mDA neurons into these three groups has been extensively used to characterize and define these subpopulations and hence, remains indispensable in describing them (Anderegg, Poulin, and Awatramani 2015).

Correlated with their distinct anatomical positions, SN and VTA mDA neurons predominantly project to distinct target areas and modulate different aspects of behavior (**Figure 4B**) (Lammel et al. 2008; Lammel et al. 2012; Lammel et al. 2014). Laterally-located SN-mDA neurons project predominantly to the dorsal striatum and form the mesostriatal pathway that regulates voluntary movement (Albin, Young, and Penney 1989). Their degeneration causes the motor symptoms of Parkinsons disease (Weisenhorn, Giesert, and Wurst 2016; Przedborski 2017). VTA-mDA neurons, made up of heterogeneous subpopulations, project to diverse cortical and subcortical regions and are important for the modulation of reward behavior, motivation, addictive and depressive behaviors (**Figure 4B,D**) (Wise 2004; Bromberg-Martin et al. 2010; Lammel et al. 2012; Beier et al. 2015; Morales and Margolis 2017). Hence the laterally-located SN and medially-located VTA approximately define a stereotypic pattern in connectivity and underlie distinct functions of these subpopulations.

The diversity of mDA connectivity and function has received increasing attention in the recent years and we are beginning to understand the underlying complexity of the system and its implications for behavior (Morales and Margolis 2017).

1.5.1. Midbrain dopaminergic neuron diversity and function

mDA neurons of the SN make expansive axonal arbors innervating the matrix and patch components of the striatum (Matsuda et al. 2009; Gerfen 1985). Based on their predominant projections to the striatum (**Figure 4B**), SN-mDA neurons are believed to mostly contribute to the mesostriatal pathway involved in the regulation of voluntary movement, action selection, and exploration (Roeper 2013). Recently, it has been suggested that different populations of SN-mDA neurons project to the dorsolateral (DLS) and dorsomedial striatum (DMS). Furthermore, these different populations appear to have distinct input-output patterns, different electrophysiological properties and appear to encode dopamine release in separate streams implicated in different behaviors (Lerner et al. 2015). Specifically, SN-mDA neurons projecting to the DLS are located in the lateral SN, receive inputs from the DLS and DMS, and encode salience detection. SN-mDA neurons projecting to the DMS are located in the medial SN and are activated in response to reward (Lerner et al. 2015). Another recent study defined an anatomically distinct class of laterally located SN-mDA neurons projecting to the posterior striatum. It has been proposed that this population, which receives distinctively strong inputs from the subthalamic nuclei may be one of the subpopulations that degenerates in Parkinson's disease (Menegas et al. 2015).

VTA-mDA neurons mainly project to the prefrontal cortex, ventral striatum (core and shell of nucleus accumbens, olfactory tubercle), and basolateral amygdala (Björklund and Dunnett 2007a). The lateral VTA-mDA neurons project to the ventrolateral striatum i.e. the lateral shell of the nucleus accumbens (Lammel et al. 2008; Ikemoto 2007). Medial VTA-mDA neurons, posteromedial neurons along with the medial PN neurons, innervate the olfactory tubercle and nucleus accumbens shell of the ventromedial striatum, basolateral amygdala, and prefrontal cortex (Lammel et al. 2008; Ikemoto 2007). VTA-mDA neurons are involved in distinct reward prediction behaviors: some medial VTA-mDA neurons are activated in response to unexpected reward and their activity is decreased when expected reward is omitted, while others, especially in the lateral VTA, are activated in response to unpredicted reward (Schultz 1997; Matsumoto and Hikosaka 2009; Cohen et al. 2012; Morales and Margolis 2017). Furthermore, VTA neurons are extremely heterogenous and contribute to various microcircuits (Lammel et al. 2014). For example, a specific circuit involving inputs to VTA-mDA neurons from the anterior cortex and VTA-mDA output to the lateral shell of the nucleus accumbens is believed to be reinforcing (Beier et al. 2015).

The topographic relationship between the laterally-located SN and the medially located VTA and the distinct function carried out by these two populations of mDA neurons stresses the need to understand mDA development and formation of mDA anatomy. Identification of factors that specifically lead to the setup of this anatomy could provide subpopulation specific genetic handles to dissect out circuitry and function. In the following section I will summarize mDA development and describe the events that at least in part setup mDA neuronal diversity of SN and VTA-mDA neurons allowing for their wide-ranging functions.

1.5.2. Midbrain dopaminergic neuron development

Early in development, morphogen gradients along the anteroposterior and dorsoventral axes establish a coordinate matrix, conferring a unique topographic, transcription factor based identity to each region of the developing neural tube (Jessell and Sanes 2000; Smidt and Burbach 2007). The intersection of orthodenticle homeobox 2 (OTX2), a transciption factor expressed by the anterior neural tube; and gastrulation brain homeobox 2 (GBX2), expressed in the hindbrain region of the neural tube defines the correct position of the isthmus, also known as the midbrain-hindbrain boundary (MHB) (Liu and Joyner 2001). Mis-expression of these factors along the anterior-posterior axis results in an altered positioning of the MHB (Smidt and Burbach 2007; Bodea and Blaess 2015). In addition, OTX2 is important for the expression of the wingless-related MMTV integration site 1 (WNT1) at the level of the midbrain (Joyner, Liu and Millet 2000). WNT1 in turn is important for MHB formation (McMahon and Bradley 1990) and for the generation of mDA neurons by regulating the expression of *Engrailed 1/2 (EN1/2)* genes (Danielian and McMahon 1996; Arenas 2014). At embryonic day (E) 8, the midbrain floorplate that gives rise to mDA neurons is defined by the coincidence of the FGF8, secreted by the isthmus, and sonic hedgehog (SHH), a neural tube ventralizing signal, secreted from the notochord (Ye et al. 1998; Smidt and Burbach 2007; Bodea and Blaess 2015). SHH secreted from the notochord induces expression of zinc finger transcription factor GLI2 and forkhead box A1/2 (FOXA1/2) in the cells of the floor plate (Blaess, Corrales, and Joyner 2006; Mavromatakis et al. 2011). FOXA1/2 in turn are required to turn on SHH expression in the floor plate (Mavromatakis et al. 2011). FGF8, SHH, WNT1, EN1/2, OTX2 and FOXA1/2 are important for the induction of the neurongenic midbrain floor plate (reviewed in (Blaess and Ang 2015)).

Induction of the floorplate is followed by the specification of mDA progenitor pool (E9): transcription factors are necessary for activation and maintenance of gene expression patterns required for specification of mDA precursors from floor plate cells, and their differentiation into mDA neurons (reviewed in (Ang 2006; Blaess and Ang 2015)). Along with the above-mentioned inducers of the floor plate, expression of transcription factors LMX1A/B (LIM homeodomain transcription factors), NEUROG2 (Neurogenin 2) and achaete-scute homolog

1 (ASCL1) are important for the transition between proliferation and differentiation (Andersson et al. 2006; Kele et al. 2006; Nakatani et al. 2010; Yan et al. 2011; Blaess and Ang 2015).

Neurogenesis and differentiation of mDA neurons occur over several days (E10.5-E14.5) (**Figure 4A**). mDA progenitors predominantly give rise to SN-mDA and lateral VTA neurons between E10.5 and E11.5, medial VTA-mDA neurons are born later (E12.5) (Bayer et al. 1995; Bye, Thompson and Parish, 2012). Dynamic spatiotemporal domains of *Shh* expression define distinct mDA progenitor pools that contribute differentially to the forming mDA subpopulations (Blaess et al. 2011). *Shh*-expressing progenitor domain first appears at E8 in the medial most floor plate cells, and this expression domain broadens between E8.5 and E10.5. There is a shift in *Shh* expression from medial to lateral floor plate cells by E11 (Joksimovic et al. 2009; Blaess et al. 2011; Hayes et al. 2011). Using an inducible CreER system under the *Shh* promoter and administering tamoxifen (TM) at time-points between E8.5-E11.5, it was shown that *Shh* expressing progenitors at E8.5 give rise predominantly to the SN and dorsolateral VTA, while those expressing *Shh* at E11.5 give rise predominantly to medial VTA-mDA neurons (Blaess et al. 2011; Hayes et al. 2011; Panman et al. 2014; Bodea et al. 2014).

As the CreER system applied in Blaess et al. 2011 and Bodea et al. 2014 was used in this study , this method of genetic inducible fate-mapping is explained here in detail. Mice with CreER sequence inserted into the *Shh* locus (Harfe et al. 2004) were crossed with a reporter line $ROSA^{loxP\text{-}STOP\text{-}loxP\text{-}YFP}$ (*R26YFP*) expressing enhanced yellow fluorescent protein (YFP) (Srinivas et al. 2001). Upon Cre-mediated recombination, the *STOP* sequence is excised resulting in permanent YFP expression in Cre-expressing cells and their progeny. CreER (Cre Estrogen Receptor) is a fusion protein of Cre and a modified human estrogen receptor. This CreER fusion protein can only enter the nucleus upon binding with tamoxifen (TM). Hence, Cre-mediated recombination in is only possible after an injection of TM at the desired time-point. Blaess et al. 2011; Bodea et al 2014 used this system and administered TM at E8.5 and observed that YFP expressing cells, descended from the medial progenitor domain *expressing Shh* at E8.5, were predominantly found in the SN. When TM was administered at E9.5, SN and VTA-mDA neurons were labeled. TM at 11.5 resulted in predominant YFP expression in the VTA. Hence, Blaess et al. 2011; Bodea et al. 2014 could show that midbrain floor plate progenitors expressing *Shh* in distinct regions at distinct time-points differentially give rise to the SN or VTA-mDA neurons. An added advantage of this genetic inducible fate-mapping system is the mosaic labeling of *Shh*-expressing progenitors as only cells in which the CreER protein successfully binds TM are labeled. Hence in this study, this system of labeling was used to sparsely label SN-mDA neurons (TM administered at E8.5) making visualization of an otherwise dense population of migrating SN-mDA neurons possible (Results section 4.4).

As proliferating mDA progenitors exit the mitotic cell cycle they begin to differentiate into mDA neurons. NEUROG2 and ASCL1 push mDA progenitors towards differentiation. SHH

and WNT signalling pathways induce FOXA2 and LMX1A, which in turn cooperate to induce nuclear receptor related 1 (NURR1) expression around E10.5 in differentiating mDA neurons. NURR1 is required for the activation of TH (Tyrosine hydroxylase), DAT (Dopamine transporter), ALDH1A1 (Aldehyde dehydrogenase 1 family member A1) and paired like homeodomain 3 (PITX3) expression (reviewed in Blaess and Ang 2015). EN1/2 are also required for proper differentiation and survival of mDA neurons as they also regulate TH, DAT and PITX3 expression (Veenvliet et al. 2013). TH^+ cells first appear in the ventral midbrain at E10.5. As mDA neurons differentiate, they begin to migrate from the ventricular zone towards the pial surface (**Figure 4A,E**).

Differentiated SN-mDA neurons are distinguished from VTA-mDA neurons by subtype specific expression of the potassium chanel GIRK2 (G-protein-regulated inward-rectifier potassium channel 2) and the transcription factor SOX6 (sex determining region Y-box6) (Björklund and Dunnett 2007b; Poulin et al. 2014; Panman et al. 2014; Poulin et al. 2018). In addition, a small population of mDA neurons in the region of the lateral VTA and SN, expresses the LIM domain protein LMO3 (LIM domain only protein 3) (La Manno et al. 2016; Bifsha et al. 2017). In contrast, VTA-mDA neurons express the calcium binding protein Calbindin and the transcription factor OTX2 (Orthodenticle homeobox 2) (Poulin et al. 2014; Panman et al. 2014; DiSalvio et al. 2009).

1.5.3. Midbrain dopaminergic neuron migration

Early work, using thymidine-H^3 labelling to birth-date ventral midbrain neurons at different time points, suggested that mDA precursors first follow a radial path through the mantle zone and then move laterally to take up their final positions in the adult brain (Hanaway, McConnell, and Netsky 1971). Alignment of TH-expressing cells along radial glial fibres, which run from the ventricle towards the pial surface, suggests that these glial cells provide a scaffold for migrating mDA neurons when they leave the ventricular zone and migrate into the mantle layer of the ventral mesencephalon (**Figure 4E**) (Shults et al. 1990; Kawano et al. 1995). Direct observation of mDA neuron migration *in vitro* has been hindered due to the early development of ventrally migrating mDA, and dense clustering of mDA neurons at early embryonic stages, preventing the visualization of individual neurons. Electroporation of a few mDA neurons to observe migration is challenging as differentiated neurons do not take up electroporated DNA easily and mDA differentiation starts at E10.5. Due to the technical difficulties of *in utero* electroporations at early time points (E10.5), this method is not suitable for mosaic labeling of mDA neurons. By mosaic labelling of medial or lateral *Shh*-expressing mDA progenitor domains, it is possible to label precursors that predominantly contribute to either the SN or VTA neurons (Blaess et al. 2011; Bodea et al. 2014). Monitoring migratory behaviour of these mosaically labelled mDA neurons in organotypic slice cultures, shows that intermingled SN

and VTA-mDA precursors migrate radially towards the medial pial surface, after which, mDA neurons destined for the SN segregate from the VTA-mDA neurons, before migrating tangentially to reach their lateral positions (**Figure 4E**) (Bodea et al. 2014).

Radial migration of mDA neurons is modulated by the chemokine (C-X-C motif ligand) 12 (CXCL12, also known as SDF-1) and its receptor CXCR4 (Yang et al. 2013; Bodea et al. 2014). CXCL12 is expressed in the meninges of the pial surface of the ventral midbrain while CXCR4 is expressed in migrating mDA neurons. When this signalling pathway is disrupted in migrating mDA neurons, they transiently accumulate dorsally and away from the midline. However, differences between *Cxcl12*$^{-/-}$ and *Cxcr4*$^{-/-}$ mice, with the latter showing an off-midline, ventral accumulation of mDA neurons suggests a complex regulation of mDA radial migration which is yet to be unravelled (Bodea et al. 2014).

Reelin signalling has been shown to regulate the long-distance tangential migration of SN-mDA neurons. In the absence of Reelin signaling, SN-mDA neurons fail to occupy their lateral positions (**Figure 4F**), and though they separate from the VTA-mDA neurons (as assessed by the distribution of GIRK2- and Calbindin^{+} mDA neurons), they are located in an ectopic medial position (Nishikawa et al. 2003; Kang et al. 2010; Sharaf et al. 2014; Bodea et al. 2013; Vaswani and Blaess 2016).

Delineating migratory routes and mechanisms of mDA neurons is important to understand how mDA anatomy and circuitry is setup. In contrast to other brain areas, little is known about the cell behaviors and the molecular mechanisms that underlie mDA neuronal migration and anatomical arrangement. In contrast to migrating neuronal populations in the cortex, migrating mDA neurons have so far not been visualized in 3D, at a resolution that would allow the characterization of their precise mode(s) of migration. The following section outlines the goals of this study.

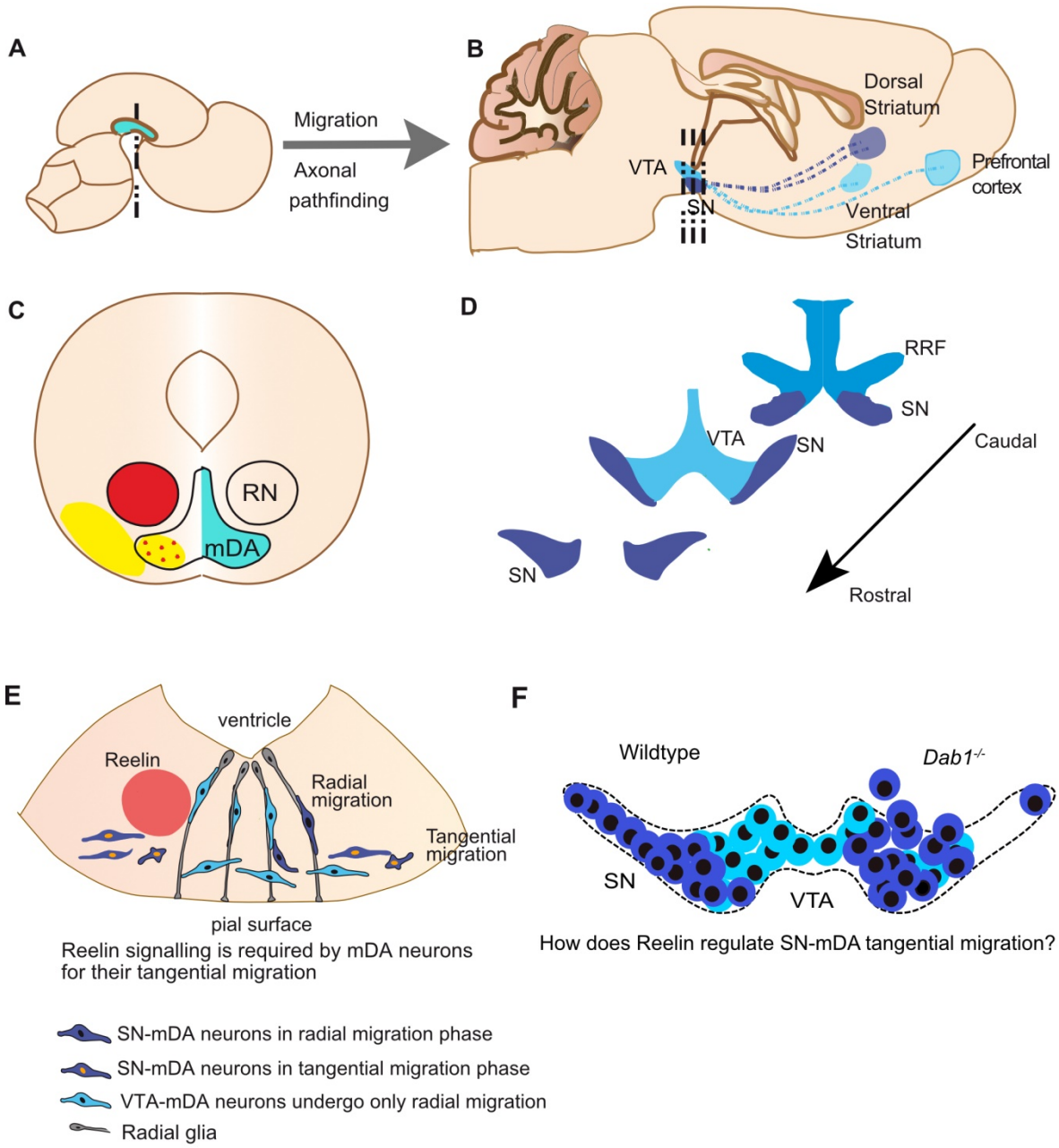

Figure 4. mDA neuronal migration during development: (A) Schematic of E13.5 mouse brain. Cyan region represents the developing mDA domain. Neurons from this region migrate and give out axons to form distinct SN and VTA populations in the adult dopaminergic system (B). (B) mDA neurons in adult mice can be distinguished as the substantia nigra (SN, dark blue) and VTA (light blue). In addition to different anatomical positions due to distinct migratory routes, these mDA populations have different forebrain targets enabling them to carry out diverse functions. (C) Coronal section of the rostrocaudal level indicated by dashed line in (A) shows the developing mDA domain (cyan, right side of schematic). Regions of Reelin (red) and DAB1 expression (yellow) are shown on the left side of the schematic (black outline on the left side delineates developing mDA domain). Red dots indicate region of the developing mDA domain that could be potentially responding to Reelin signaling. (D) Anatomy of the adult dopaminergic system. Rostrocaudal level of (D) is indicated by dashed lines in (B). (E) Schematic showing the radial and tangential migration of SN and VTA-mDA neurons at E13.5. VTA-mDA neurons undergo only radial migration, while SN-mDA neurons undergo an extra step of tangential migration after their radial migration to settle in more lateral positions. Red circle represents Reelin expression in the region of the red nucleus (RN). (F) In the absence of Reelin signaling, SN-mDA neurons fail to migrate tangentially to take up lateral positions and instead settle medially in the region of the VTA. How Reelin regulates tangential migration of SN-mDA neurons is the focus of this study. Figure adapted from (Vaswani and Blaess 2016).

2. OBJECTIVES OF THE STUDY

2.1. Investigate whether Reelin acts directly on mDA neurons

Reelin signaling is important for the tangential migration of mDA neurons but how it regulates their migration is unknown. Inactivating Reelin pathway components (complete knockouts of *Reelin* or *Dab1* or *ApoER2/VLDLR* double knockouts) prevents SN-mDA neurons from reaching their final position in the ventrolateral midbrain and results instead in their accumulation in the lateral VTA (Nishikawa et al. 2003; Kang et al. 2010; Sharaf et al. 2013; Bodea et al. 2014; Vaswani and Blaess 2016). However, whether Reelin plays a direct role in tangential mDA neuronal migration, or whether the absence of Reelin signaling in glia fibers or neighboring neuronal populations results in the ectopic SN phenotype has not been explored. Hence, the first objective of the study was to inactivate *Dab1*, the intracellular transducer of Reelin signaling, specifically in tangentially migrating mDA neurons and compare the distribution of TH^+ dopaminergic neurons in control brains, conditional knockouts and complete knockouts of *Dab1*. By this strategy, the direct action of Reelin signaling on mDA neurons was investigated.

2.2. Visualize tangential migration and dynamic cellular morphology of mDA neurons

While the migratory routes of mDA neurons have been characterized, the accompanying changes in cell morphology remain unexplored. This is due to the early development and differentiation of mDA neurons, which makes it difficult to achieve mosaic labeling of mDA neurons by *in utero* electroporation. Thus challenges in achieving sparse labeling of mDA neurons have prevented the observation of their morphological changes during tangential migration. Using a genetically inducible fate-mapping system that predominantly labels SN-mDA neurons in combination with 3D time-lapse imaging of organotypic slices, tangential migration and associated cell morphologies of mDA neurons were visualized. Then, using a semi-automated tracking plugin, the speeds and trajectories of a large population of mDA neurons were tracked. Using manual segmentation of 3D cell morphology on a subset of tracked mDA neurons, the relationship between speed, migratory direction and morphology of mDA neurons was examined.

2.3 Dissect out the precise effect of Reelin signaling on the migration and morphology of mDA neurons

While it has been shown that blocking Reelin in organotypic slices results in decreased migratory speeds of mDA neurons, the precise role of Reelin signaling in the regulation of mDA migration remains unclear. This study, having established a system for visualizing mDA

tangential migration in 3D, compares migratory speeds, trajectories and morphological characteristics of mDA neurons in the presence and absence of Reelin signaling and thereby uncovers a host of interconnected processes that are regulated by Reelin during the tangential migration of mDA neurons.

3. MATERIALS AND METHODS

3.1. Materials

3.1.1. Table 1: Technical equipment

Appliance	Model/Cat. No.	Manufacturer	Registered Office
2-Photon laser	Chameleon Ultrall	Coherent	Dieburg, DE
2-Photon microscope	LSM710NLO	Carl Zeiss	Jena, DE
10x objective (ApoTome)	EC PlnN 10x/0.3 DICI 1.11µm	Carl Zeiss	Jena, DE
10X objective (Leica SP8)	HCX PL APO 10x/0.40 CS	Leica	Wetzlar, DE
20x objective (ApoTome)	EC PlnN 20x/0.5 DIC II 0.67 µm	Carl Zeiss	Jena, DE
32X objective (LSM-710)	C-Achroplan 32x/0.85 W Corr M27	Carl Zeiss	Jena, DE
40x objective (ApoTome)	Pln Apo 40x/1.3 Oil DIC III 0.26 µm	Carl Zeiss	Jena, DE
40X objective (Leica SP8)	HC PL APO 40x/1.1 Water CORR CS2	Leica	Wetzlar, DE
63x objective (ApoTome)	Pln Apo 63x/1.4 Oil DIC II 0.24µm	Carl Zeiss	Jena, DE
63X objective (Leica SP8)	HC PL APO 63X/1.3 Gly CORR CS2	Leica Microsystems	Wetzlar, DE
Autoclave	DX-150 benchtop	Systec	Wettenberg, DE
Balance	AC211S	Sartorius	Göttingen, DE
Balance	ATL-822-1	Sartorius	Göttingen, DE
Centrifuge	Pico 17	Thermo Fisher Scientific	Schwerte, DE
Centrifuge	Labofuge 400R 75008-162	Thermo Fisher Scientific	Schwerte, DE
Chemiluminiscent imager	Chemidoc XRS+	BioRAD	München, DE
Confocal microscope	Leica TCS-SP8	Leica Microsystems	Wetzlar, DE
Cryostat	Leica CM 3050S	Leica	Wetzlar, DE
Fluorescence Lamp	Illuminator HXP120C	Carl Zeiss	Jena, DE
Gel chambers	Model 41-1525 Model 40-1515	Peqlab	Erlangen, DE
Heating Block	Dry bath Typ15103	Thermo Fisher Scientific	Schwerte, DE
Heating Plate	flattening table OTS 40 01 - 4002 - 00	Medite	Burgdorf, DE
Hot plate	Hi1220	Leica Microsystems	Wetzlar, DE
Hybridization oven	InSlide Out 241000	Boekel Scientific	Feasterville, USA
Incubator (bacteria)	AL01-07	Advantage-Lab	Schilde, BE
Magnetic stirrer	AGE 1200 rpm	VELP Scientifica	Usmate, IT

Micro-centrifuge	Corning LSE Mini Microcentrigure 120V	Thermo Fisher Scientific	Schwerte, DE
Microscope Camera (Leica)	DMC6200	Leica Microsystems	Wetzlar, DE
Microscope Camera (ApoTome)	AxioCam MRm	Carl Zeiss	Jena, DE
Microscope Color Camera (ApoTome)	AxioCam MRc	Carl Zeiss	Jena, DE
Microscope (ApoTome)	AxioObserver Z1 SIP66732	Carl Zeiss	Jena, DE
Microwave	MW7809	Severin	Sundern, DE
Mini-centrifuge	3722L	Thermo Fisher Scientific	Schwerte, DE
pH Meter	FE20 FiveEasy	Mettler Toledo	Giessen, DE
Pipette-boy Accu-jet pro	26300	Brand	Wertheim, DE
Pipettes (10, 20, 200, 1000µL)	FA10002M FA10003M FA10005M FA10006M	Gilson	Middleton. USA
Power supply electrophoresis	EV231	Peqlab	Erlangen, DE
Power Units (microscope)	Power supply 231	Carl Zeiss	Jena, DE
Refridgerators Freezers 4°C, -20°C, -80°C	G 2013 Comfort HERAfreeze	Liebherr Kendro	Lindau Hanau, DE
Rocking Platform	4440148	VWR	Darmstadt , DE
Spectrophotometer	Nanodrop 1000	Peqlab	Erlangen, DE
Stereomicroscope with fluorescence	MZ10F 10446377	Leica Microsystems	Wetzlar, DE
Thermoblock	230-1.00AT	Peqlab	Erlangen, DE
Thermocycler	DANN engine PTC-200	BioRAD	München, DE
Thermocycler	Biometra TRIO	analytikjena	Jena, DE
Vacuum pump	Vacuubrand	Brand	Wertheim, DE
Vibratome	HM650V	Microm	Walldorf, DE
Vortexer	Vortex genius	IKA	Staufen, DE
Water bath	10679808	GFL	Burgwedel, DE

3.1.2. Table 2: Data acquisition and data analysis

Computing	**Software**	**Producer**	**Registered Office**
Gel documentation	Quantity One	BioRAD	München, DE
Image acquisition	Zen Blue 2012	Carl Zeiss	Jena, DE
Image acquisition	Zen Black 2012	Carl Zeiss	Jena, DE

Image acquisition	Leica Application Suite X 4.13	Leica microsystems	Wetzlar, DE
Image editing	Affinity Designer 1.5.5	Serif	Nottingham, UK
Image processing	Fiji/ImageJ 1.51n	Wayne Rasband, National Institutes of Health	Bethesda, USA
Image processing	Adobe Photoshop CS3	Adobe Systems	München, DE
Image processing	Affinity Photo1.5.5	Serif	Nottingham, UK
Image processing	Imaris 8.3.1	Bitplane	Zürich, CH
Image processing and data analysis	MatLab R2017b	MathWorks	Ismaning, DE
Immunoblot quantification and analysis	Image Lab 6.0	BioRAD	München, DE
Statistical analysis	GraphPad Prism 7.0	GraphPad Software	San Diego USA

3.1.3. Table 3: Laboratory consumables

Consumables	**Model/Cat. No.**	**Manufacturer**	**Registered Office**
12-well culture plate	353043	BD Biosciences	Heidelberg, DE
24-well culture plate	353047	BD Biosciences	Heidelberg, DE
6-well culture plate	353046	BD Biosciences	Heidelberg, DE
Autoclave tape	SteriClin sticky tape	VP group	Feuchtwangen, DE
Blades	Apollo	Apollo Herkenrath GmbH & Co KG	Solingen, DE
Bis-Tris gels (4 – 12%)	NP0335BOX	NuPAGE	Darmstadt, DE
Cover slips	LAME110071	Labomedic	Bonn, DE
Culture dishes 100X20mm	831802003	Sarstedt	Sarstedt, USA
DermaClean gloves	PFC 4303971	Ansell	München, DE
Embedding molds	Peel-A-Way	Polysciences Inc.	Eppelheim, DE
Eppendorf tubes 1.5mL	72690	Sarstedt	Nümbrecht, DE
Filter tips	ART 100/200/1000 Barrier tips	Thermo Fischer Scientific	Schwerte, DE
Forceps Dumont (#5)	11252 – 30	Fine Science Tools	Heidelberg, DE
Graefe Forceps (0.8mm)	11050-10	Fine Science Tools	Heidelberg, DE
Imaging dishes (µ-dish 50mm. low)	81136	Ibidi GmbH	Martinsreid, DE

Iris scissors (11 cm)	14060-11	Fine Science Tools	Heidelberg, DE
Iris scissors (9 cm)	14060-09	Fine Science Tools	Heidelberg, DE
Lens Cleaning Tissue 105	2105841	Whatman	Dassel, DE
Liquid scintillation vials	Z190527	Merck	Darmstadt, DE
Microcentrifuge tubes 1.5mL	780400	BIO-CERT	Werthein, DE
Cryostat blades	819	Leica	Wetzlar, DE
Millicell membrane insert	PIGMORG 50	Merck Millipore	Darmstadt, DE
Perforated spoon	Moria MC17BIS 10370-18	Fine Science Tools	Heidelberg, DE
Noyes Spring Scissors (14mm)	15012-12	Fine Science Tools	Heidelberg, DE
Parafilm	PM-996	Bemis	Köln, DE
Pasteur plastic pipettes 1mL	2655181	VWR	Darmstadt, DE
PCR strip tubes	732-0551	VWR	Darmstadt, DE
PCR tubes with individual caps	732-0545	VWR	Darmstadt, DE
Petri dishes 100x15mm	351029	BD Biosciences	Heidelberg, DE
Polypropylene conical tubes 15mL	352096	BD Biosciences	Heidelberg, DE
Polypropylene conical tubes 50mL	352070	BD Biosciences	Heidelberg, DE
Razor blades	121-6	Plano GmbH	Wetzlar, DE
Rein Rotmarder Brush 770	149-2120	VWR	Darmstadt, DE
Round bottom tubes	352059	BD Biosciences	Heidelberg, DE
Serological pipettes	4487 (5mL) 4488 (10mL) 4489 (25mL)	Corning Life Sciences	Kaiserslautern, DE
Single-use feeding needle	18061-20	Fine Science Tools	Heidelberg, DE
Slide boxes	HS15994E	Carl Roth GmbH	Karlsruhe, DE
Steriflip Sterile disposable vacuum	9479650	Merck	Darmstadt, DE
Student surgical scissors	91401-12	Fine Science Tools	Heidelberg, DE
Surgical Blade No.10	0201000010	Feather Safety Razor Co. ltd.	Köln, DE
Syringes – 1mL	300013	BD Biosciences	Heidelberg, DE
Tissue Wipes	05511	KimTech	Surrey, UK
Winged Needle	P295A05	Venisystems	Hospira, USA

3.1.4. Table 4: Chemical reagents

Chemicals	Catalog no.	Manufacturer	Registered Office
Acetic anhydride	1.00639.1000	VWR	Darmstadt, DE
Ampicillin	A5354	Merck	Darmstadt, DE
Agarose	16500-500	Thermo Fischer Scientific	Darmstadt, DE
AMD3100 octahydrochloride	A5602	Merck	Darmstadt, DE
Ampuwa water	40676.00.00	Ampuwa, Fresenius	Bad Homburg, DE
Aqua-PolyMount	18606	Polysciences Inc.	Eppelheim, DE
Ascorbic acid	A4403	Merck	Darmstadt, DE
Benzyl alcohol	402834	Merck	Darmstadt, DE
Benzyl benzoate	B6630	Merck	Darmstadt, DE
Bisbenzimide H33258 10mg/mL	B2883	Merck	Darmstadt, DE
BM purple AP substrate	11442074	Roche	Penzberg, DE
Bromphenol blue	A1120.005	AppliChem	Darmstadt, DE
CaCl	22322.295	VWR	Darmstadt, DE
Chlorophorm	22711.260	VWR	Darmstadt, DE
Corn Oil	C8267	Merck	Darmstadt, DE
Denhardt's Solution 50x concentrate	D2532	Merck	Darmstadt, DE
Dextran sulfate	A4970.0250	AppliChem	Darmstadt, DE
Digoxigenin-labeled NTPs	11277073910	Roche	Penzberg, DE
DMEM	41966-029	Thermo Fischer Scientific	Darmstadt, DE
DMSO	D8418	Merck	Darmstadt, DE
DNA ladder (1kb)	10787-018	Thermo Fischer Scientific	Darmstadt, DE
DNAse I	LS002138	Cell Systems	Kirkland, USA
dNTPs (100mM)	28-4065-52	GE Healthcare	Dornstadt, DE
EDTA	E6511	Merck	Darmstadt, DE
Ethanol	20821.321	VWR	Darmstadt, DE
Ethidium bromide	2218.2	Carl Roth	Karlsruhe, DE
Formamide	155-15026	Thermo Fischer Scientific	Darmstadt, DE
Glucose	G7528-250g	Merck	Darmstadt, DE
Glue	Roti coll 10258.1	Carl Roth	Karlsruhe, DE
Goat serum	G9023519	Merck	Darmstadt, DE
Halt protease and phosphatase inhibitor	78442	Thermo Fisher Scientific	Darmstadt, DE
Hanks'Balanced Salt solution	H9394-100mL	Merck	Darmstadt, DE
Hexane	21390.293	VWR	Darmstadt, DE
Histoacryl glue	BRAU9381104	Braun Aesculap	Tuttlingen, DE
Horse Serum	26050-088	Thermo Fischer Scientific	Darmstadt, DE
Immersol	TM518F	Carl Zeiss	Jena, DE

Isoflurane	Forane 2594.00.00	Abbott	Wiesbaden, DE
Isopropanol	P/7500/15	Thermo Fisher Scientific	Schwerte, DE
Propidium Iodide	P4864	Merck	Darmstadt, DE
KCl	26764.260	VWR	Darmstadt, DE
Luria-Bertani-Medium	A0954	AppliChem	Darmstadt, DE
MgCl	25108.260	VWR	Darmstadt, DE
Na_2HPO4	28028.298	VWR	Darmstadt, DE
NaCl	27808.297	VWR	Darmstadt, DE
NaH_2PO4	28013.264	VWR	Darmstadt, DE
$NaHCO_3$	27775.293	VWR	Darmstadt, DE
NaOH	31627.290	VWR	Darmstadt, DE
Normal donkey serum	017-000-121	Jackson ImmunoResearch	Suffolk, UK
Paraffin Remover	41-5600-00	Medite	Burgdorf, DE
Paraformaldehyde	0335.2	Carl Roth	Karlsruhe, DE
PBS tablets	18912-014	Thermo Fischer Scientific	Darmstadt, DE
PCR purification kit	28104	Qiagen	Hilden, DE
Penicillin-Streptomicin100x	P4333	Merck	Darmstadt, DE
Phenol	A0889.0100	AppliChem	Darmstadt, DE
Polyethyleneglycol	P5413	Merck	Darmstadt, DE
Plasmidial DNA isolation	Maxiprep Pure Link K210017	Thermo Fischer Scientific	Darmstadt, DE
Progesterone	P-3972	Merck	Darmstadt, DE
Ribonucleic acid, transfer, from Bakers Yeast	R5636	Merck	Darmstadt, DE
RIPA buffer	R0278	Merck	Darmstadt, DE
Rnase inhibitor	13398800	Roche	Penzberg, DE
Sarcosyl	L9150	Merck	Darmstadt, DE
Sodium azide	S2002	Merck	Darmstadt, DE
Sucrose	27480.360	Merck	Darmstadt, DE
Tamoxifen	T5648	Merck	Darmstadt, DE
Taq DNA polymerase recombinant	10342-020	Thermo Fischer Scientific	Darmstadt, DE
Tert-Butanol	19460-2.5L	VWR	Darmstadt, DE
Tetramisole hydrochloride	L9756	Merck	Darmstadt, DE
ThermoClean	25220100	Bioanalytic	Freiburg, DE
Tissue Tek O.C.T.	4583	Sakura	Alphen aan den Rijn, NL
Triethanolamine	28746290	VWR	Darmstadt, DE
Tris-HCl	108219.1000	Merck	Darmstadt, DE
TritonX100	1.08603.1000	Merck	Darmstadt, DE
Tween20	28829.183	VWR	Darmstadt, DE

UltraPure LMP Agarose	15517-022	Thermo Fischer Scientific	Darmstadt, DE

3.1.5. Antibodies

3.1.5.1. Table 5: Primary antibodies

Primary Antibody	Cat. No.	Manufacturer	Registered Office
Anti-DIG-AP Fab fragments	11093274910	Roche	Penzberg, DE
Goat anti-OTX2	GT15095	Neuromics	Herford, DE
Goat anti-Reelin	AF3820	R & D Systems	Wiesbaden, DE
Mouse anti-TH	MAB318	Merck	Darmstadt, DE
Mouse anti-αTubulin	T5168	Merck	Darmstadt, DE
Mouse anti-αTubulin, acetylated	T6793	Merck	Darmstadt, DE
Rabbit anti-Calbindin	C9848	Swant	Herford, DE
Rabbit anti-CDH2	ab18203	Abcam	Berlin, DE
Rabbit anti-Cofilin	Gurniak et al. 2005	Kindly provided by Prof. Dr. Walter Witke	
Rabbit anti-DAB1	Howell et al. 1997	Kindly provided by Dr. Brian Howell	
Rabbit anti-EB3	ab53360	Abcam	Berlin, DE
Rabbit anti-GFP	A11122	Thermo Fischer Scientific	Darmstadt, DE
Rabbit anti-HRP	#7074	Cell Signaling Technology	Frankfurt am Main, DE
Rabbit anti-LIMK1 (Thr508)	#3842	Cell Signaling Technology	Frankfurt am Main, DE
Rabbit anti-p-Cofilin	Gurniak et al. 2005	Kindly provided by Prof. Dr. Walter Witke	
Rabbit anti-p-LIMK1 (Thr508)	#3841	Cell Signaling Technology	Frankfurt am Main, DE
Rabbit anti-SOX6	ab30455	Abcam	Berlin, DE
Rabbit anti-TH	AB152	Merck	Darmstadt, DE
Rat anti-GFP	04404-84	Nalacai	Heidelberg, DE

3.1.5.2. Table 6: Secondary antibodies

Secondary Antibody (made in donkey)	Cat. No.	Manufacturer	Registered Office
Anti-goat Alexa 488	705-545-147	Jackson ImmunoResearch	Suffolk, UK
Anti-goat Cy3	705-165-147	Jackson ImmunoResearch	Suffolk, UK
Anti-mouse Alexa 488	A21202	Thermo Fischer Scientific	Darmstadt, DE

Anti-mouse Cy3	715-165-150	Jackson ImmunoResearch	Suffolk, UK
Anti-rabbit Alexa 350	A10039	Thermo Fischer Scientific	Darmstadt, DE
Anti-rabbit Alexa 488	A21206	Thermo Fischer Scientific	Darmstadt, DE
Anti-rabbit Alexa 546	A10040	Thermo Fischer Scientific	Darmstadt, DE
Anti-rabbit Cy3	711-165-152	Jackson ImmunoResearch	Suffolk, UK
Biotinylated anti-rabbit	711-065-152	Jackson ImmunoResearch	Suffolk, UK

3.1.6. Table 7: Enzymes

General enzyme	**Cat. No.**	**Manufacturer**	**Registered Office**
Deoxyribinucleas e (DNAse)	M610A	Promega Corp	Mannheim, DE
Proteinase K	03115879001	Roche	Penzburg, DE
Ribonuclease (RNAse) A	12091-021 PureLink	Thermo Fischer Scientific	Darmstadt, DE
Restriction enzyme	**Cat. No.**	**Manufacturer**	**Registered Office**
NotI	RO189S	New England Biolabs	Frankfurt am Main, DE
EcoRI	RO0101S	New England Biolabs	Frankfurt am Main, DE

3.1.7. Table 8: RNA and DNA Polymerases

Polymerase	**Cat. No.**	**Manufacturer**	**Registered Office**
Taq RNA SP6 Polymerase	10810274001	Roche	Penzburg, DE
Taq RNA T7 Polymerase	10881767001	Roche	Penzburg, DE

3.1.8. Table 9: RNA *in situ* probes

RNA probe	**Gene name**	**Description**	**Restriction Enzyme**	**RNA Polymerase**	**Provided by**
RELN	Reelin	pCRII-Topo vector, 0.64 kb(cDNA) RELN inserted fragment	NotI	Sp6	Mengqing Xiang lab, Rutgers, USA
LMO3	LIM Domain Only 3	pCMV-SPORT6 vector, 3kb(partial cDNA) inserted fragment Image clone 4913098 accession #BC034128	EcoRI	T7	Source Bioscience, Berlin, DE

3.1.9. Table 10: PCR primers for genotyping mice

Primer	Sequence 5'-3'
ADF	#145 Lac-3' GAT TAA GTT GGG TAA CGC C #106 ADF-150-3' GAA GAA GGC AAA GAG ATC TT #403 ADF-INT2-5' CTA CCT AAA GGG CAT CCT TTC
Cre	F: TAAAFATATCTCACGTACTGACGGTG R: TCTCTGACCAGAGTCATCCTTAGC
Cofilin 1	#347: Coinsma-3' CGC TGG ACC AGA GCA CGC GGC ATC #348: Coin2-5'a CTG GAA GGG TTG TTA CAA CCC TGG #349: cofNTS-3'a CAT GAA GGT TCG CAA GTC CTC AAC
Dab1	WT F: GGTTCAGTGCCTATCATGTATC WT R: GAGCCAGTGAGCGGTTCC MT R: CCTATACTTTCTAGAGAATAGGAAC
R26	RR1: AAAGTCGCTCTGAGTTGTTAT RR2: GCGAAGAGTTTGTCCTCAACC RR3: GGAGCGGGAGAAATGGATATG

3.1.10. Table 11: Buffers and solutions

Buffers /Solutions	Content
Solutions for genotyping	
Lysis Buffer (for genotyping)	333 µL 1.5 M Tris, pH 8.8 (50 mM), 20 µL 0.5 M EDTA (1 mM), 500 µL 10% Tween, 9.1 mL dH_2O
Solutions for RNA *in situ* hybridization	
Triethanolamine (TEA)-HCl 0.1M	650 µL TAE in 50 mL Ampuwa H_2O, 130 µL 12M HCl
RNAse A	100 mg RNAse A, 100 µl Tris-HCL (pH 7.5), 30 µl 5 M NaCl (15 mM), 9.8 mL
SSC 20X	88.2 g NaCitrate (C_6 H_5 Na_3 O_7), 174 g NaCL in 1 L Ampuwa H_2O (pH 7.0)
RNase Buffer	100 mL 5 M NaCl (0.5 M), 10 mL 1 M Tris-HCl (pH 7.5, 10 mM), 10 mL 0.5 M EDTA (pH 8, 5 mM), 880 mL dH_2O
NTMT	2 mL 5 M NaCl (100 mM) 10 mL 1 M Tris-HCl, pH 9.5 (100 mM) 5 mL 1 M $MgCl_2$ (50 mM) 0.1 mL Tween 20 (0.1%) 82.9 mL dH_2O
Hybridization solution	50 mL Formamide (deionized), 20 mL 50% Dextran sulfate, 2 mL 50x Denhardt's, 2.5 mL yeast tRNA (10 mg/mL), 6 mL 5 M NaCl, 2 mL 1 M Tris-HCl (pH 8.0), 1 mL 0.5 M EDTA, 1 mL 1 M $NaPO_4$ (pH 8.0), 5 mL 20% Sarcosyl, 11.5 mL Ampuwa H_2O
TE buffer pH8.0	1mL 1M Tris-HCl pH8, 200µL 0.5M EDTA; up to 100mL with dH_2O
Solutions for Organotypic slice culture preparation	
Culture medium	48.73% DMEM high glucose, 25% Horse serum, heat inactivated, 25% HBSS 1X, 1.27%Glucose, Penicillin/Streptomycin1x, filtered sterile and stored at 4°C for 2-3 months.
Krebs buffer 10X	252 mL NaCl 5M, 25mL KCl 1M, 12mL NaH_2PO_4 1M, 12mL $MgCl_2$ 1M and 3,68 g $CaCl_2$ up to 1L with dH_2O, stored at 4°C up to 3 months

Krebs (1X)	100mL Krebs buffer (10x), 50mL $NaHCO_3$ 0.5M, 1,98 g Glucose, up to 1L with dH_2O, prepared fresh
LMP-Agarose (4%)	4 g LMP agarose in 100 mL dH_2O, melted in a microwave and kept at 45°C in a water bath.
Solutions for immunohistochemistry	
PBS (5X)	40 g NaCl (137 mM) 1 g KCl (2,7 mM) 7.1 g Na2HPO4 (10 mM) 1.36 g KH2P4 (2 mM) in 1 L dH2O
PBS-NaAzide (0.1%)	0.1% sodium-azide in PBS
20% Paraformaldehyde (PFA)	500 g PFA 2.0 L ddH2O 8.0 mL NaOH, filtered through 0.4 µm filter and stored at -20°C
Fixation solution (4% PFA)	10 mL 20% PFA in 50mL PBS
PBT (0.1%)	10 mL 10% Triton-X (0.1 %), 990 mL PBS (1x)
PBT (0.2%)	20 mL 10% Triton-X (0.1 %), 990 mL PBS (1x)
Blocking solution	10% normal donkey serum (NDS) in PBT
Antigen retrieval: Citrate buffer 10mM	1.92 g Citric acid (anhydrous), 0.05%Tween 20 in 1 L dH_2O
Antigen retrieval: 0.1M EDTA (pH 8.0)	200mL 0.5M EDTA. pH adjusted with NaOH. Volume made up to 1L with dH_2O
Solutions for gel electrophoreses	
50X Tris-acetate-buffer (TAE)	242g Tris-base, 100mL 0.5M EDTA (pH 8.0), 57.1mL glacial acetic acid in 1L H_2O, stored at room temperature
1X TAE	50 x TAE was diluted 1:50 with H_2O, stored at room temperature
10X Loading buffer	50%Glycerol, 0.4%; Bromphenol blue 0.4%; Xylene Cyanol, Mixed and stored at 4°C
Solutions for immunoblotting	
Blocking solution	10% milk in 1X TBST
Tris Buffer Saline (10X)	12.114g Tris base, 43.83g NaCl, make up to 500mL with dH_2O (pH 7.2-7.4)
TBST – 1X (Washing solution)	200mL 10X TBS, 1mL Tween-20 in 2L dH_2O
Stripping buffer	2% SDS, 60.02mM Tris (pH 6.8), 100mM ß-mercaptoehanol in 1L dH_2O

3.2. Mice

3.2.1. Table 12: List of mouse lines

Symbol	Details	Allele type	Provided by/ purchased from	Reference
ADF^{del}	Insertion of lacZ-casette (ß-galactosidase) into exon 2 of the ADF gene	Targeted (knockout)	Walter Witke lab, University of Bonn	Bellenchi et al. 2007
Cofilin1^{fl}	Exon 2 of *Cofilin1*gene flanked by *loxP* sequences at 5' and 3' regions.	Targeted (knockout)	Walter Witke lab, University of Bonn	Gurniak et al. 2005
Dab1^{fl}	Exon 2 of *Dab1* gene flanked by *loxP* sequences inserted into 5' and 3' regions.	Targeted (knockout)	Amparo Acker-Palmer lab, University of Frankfurt	Franco et al. 2011

Dab1^{del}	Generated by crossing *Dab1*$^{fl/fl}$ mice with mice expressing Cre in the germline	Targeted (knockout)	Amparo Acker-Palmer lab, University of Frankfurt	Franco et al. 2011
DAT^{Cre}	*Cre* gene was inserted into the *DAT* locus	Targeted (knockout)	Nils-Görran Larsson, Max Planck Institute for Biology of Aging, Köln	Ekstrand et al. 2007
R26^{YFP}	*YFP* gene preceded by a stop sequence flanked by loxP sites was inserted into the *R26* locus	Targeted (knockout)	Frank Constantini lab, Columbia University	Srinivas et al. 2001
Shh^{CreER}	CreER cassette was inserted into the *SHH* locus	Targeted (knockout)	Clifford Tabin Lab, Harvard University	Harfe et al. 2004

3.2.2. Transgenic mouse lines

3.2.2.1. Conditional and complete inactivation of Reelin signaling pathway

DAT^{Cre} mice were generated by inserting a *Cre* casette into the *DAT* locus (Ekstrand et al. 2007). The line was kindly provided by Nils-Görran Larrson, Max Planck Institue for Biology of Aging. *Dab1*^{flox} allele was generated by inserting *loxP* sequences into sites flanking exon2 of the *Dab1* allele (Franco et al. 2011). Cre-mediated recombination results in the excision of exon 2, which encodes for the first few amino acids of the protein interacting (PI/PTB) domain of DAB1 (Howell et al. 1997). *Dab1*$^{del/+}$ *(Dab1*$^{-/+}$*)* mice were generated by the Cre-medidate excision of exon 2 of *Dab1* in the germline of parents with the *Dab1*^{flox} allele (Howell et al. 1997; Franco et al. 2011). *Dab1*^{flox} and *Dab1*^{del} mouse lines were kindly provided by Dr. Ulrich Müller, Johns Hopkins University, Baltimore and obtained from Dr. Amparo Acker-Palmer, University of Frankfurt. To inactivate *Dab1* specifically in differentiated dopaminergic neurons, *DAT*$^{Cre/+}$*, Dab1*$^{flox-/+}$ mice were crossed with *Dab1*$^{flox/flox}$ mice. *DAT-Dab1* CKO mice (*DAT*$^{Cre/+}$, *Dab1*$^{-/flox}$ or *DAT*$^{Cre/+}$*, Dab1*$^{flox/flox}$) were compared to littermate controls (*DAT*$^{Cre/+}$, *Dab1*$^{flox/+}$ or *DAT*$^{Cre/+}$*, Dab1*$^{-/+}$). Heterozygous *Dab1*^{del} *(Dab1*$^{-/+}$*)* mice were mated to generate complete knockouts of *Dab1* (*Dab1*$^{-/-}$*)*.

To inactivate *Cofilin 1* specifically in mDA neurons, *Cofilin 1*$^{flox/flox}$ mice (Gurniak et al. 2005) were crossed with the *DAT*$^{Cre/+}$*, Cofilin 1*$^{flox/+}$ mice. To rule out phenotypic rescue in *DAT-Cofilin 1* CKO mice (*DAT*$^{Cre/+}$*, Cofilin1*$^{flox/flox}$*)* by actin depolymerizing factor (ADF) (Hotulainen et al. 2005), *DAT-Cofilin 1* CKO mice were also generated on a *ADF*$^{-/-}$ background (Bellenchi et al. 2007). *ADF*$^{-/-}$, *Cofilin 1*$^{flox/flox}$ mouse lines were kindly provided by Dr. Walter Witke, Institute of Genetics, University of Bonn.

3.2.2.2. Mosaic labeling of SN-mDA neurons

The *Shh*^{CreER} knock-in mouse line, previously described (Harfe et al. 2004), was generated by knocking *CreER* into the *Shh* locus. CreER (Cre Estrogen Receptor) is a fusion protein of Cre and a modified human estrogen receptor. This CreER fusion protein can only enter the nucleus upon binding with tamoxifen (TM). Hence, Cre-mediated recombination is only possible after an injection of TM at the desired time-point. *ROSA*$^{loxP\text{-}STOP\text{-}loxP\text{-}YFP}$ (*R26YFP*) mouse line was used as a yellow fluorescent protein (YFP) expressing reporter line. This line was generated by inserting a *loxP-STOP-loxP-YFP* cassette into *Rosa26* locus (Srinivas et al. 2001). Upon Cre- mediated recombination, the *STOP* sequence is excised resulting in YFP expression in Cre-expressing cells and their progeny. Both these lines were maintained in house. *Shh*^{CreER}, *R26*^{YFP}, *Dab1*$^{del/+}$ mice were crossed with *R26*^{YFP}, *Dab1*$^{del/+}$ mice. Day of the vaginal plug was recorded as embryonic day (E) 0.5. Tamoxifen (TM) was administered to pregnant dams at E8.5 to mosaically label SN-mDA neurons in *Dab1*$^{-/-}$ and control embryos (Bodea et al. 2014). TM (Sigma Aldrich) was prepared as a 20 mg/mL solution in corn oil, with progesterone (5 mg/mL) added to the solution to help reduce miscarriages. Fluorescent *Shh*^{CreER}, *R26*^{YFP}, *Dab1*$^{-/-}$ embryos (expected frequency of 1 in 8 embryos) were compared to fluorescent controls (*Shh*^{CreER}, *R26*^{YFP}, *Dab1*$^{del/+}$ or *Shh*^{CreER}, *R26*^{YFP}).

3.2.2.3. Mouse breeding and maintenance

Dab1^{flox} and *Dab1*$^{del/+}$ *(Dab1-)* mice were obtained on a C57BL/6 background. They were subsequently crossed with CD1 mice, as females from mixed or outbred backgrounds have larger litter sizes and fewer abortions. All other mouse lines were maintained on a CD1 background. All transgenic lines were outbred every two generations with outbred CD1 mice to prevent inbreeding and genetic drift. The mice were housed in a controlled environment, with 12 hour light/night cycles and *ad libidum* availability of food and water. All experiments were performed in compliance with the guidelines for the welfare of animals issued by the Federal Government of Germany and the guidelines of the University of Bonn. Genehmigung: 84-02.04.2014.A019; 84-02.04.2014.A436.

3.2.3. Mouse genotyping

3.2.3.1. Tissue Lysis

Tail or ear biopsies from postnatal mice or embryonic mice were used to identify the transgenic alleles described above. Tail and ear tips were digested in 100 µL of lysis buffer and 1 µL of proteinase K at 60°C overnight. Embryonic tissue was digested for 3-4 hrs at 60°C. Digestion was followed by heat inactivation of proteinase K for 10 min at 95°C. Polymerase chain reaction (PCR) was carried out on 1 µL of digest supernatant.

3.2.3.2. PCR protocols

The following PCR protocols were performed to determine mouse genotype.

Table 13: List of PCR protocols:

ADF			
Amount of reaction component	**Thermocycler program**		
1.00µL sample 2.00µL PCR rxn buffer (1x)	Steps	Temp.°C	Time min.
0.16µL dNTPs (25 nM)	1) 1st Denaturing	94	2:00
2.00 µL Primer #106 (5 µM)	2) Denaturing	94	0:30
1.00 µL Primer #145 (5 µM)	3) Annealing	58	0:30
1.50 µL Primer #403 (5 µM)	4) Extension	68	0:40
0.6 µL $MgCl_2$ (1.5mM)	5) Last Extension	68	5:00
11.54 µL dH_2O	6) Incubation	8	hold
0.2 µL Taq Polymerase (1 U) 20 µL volume (total)	Repeat steps 2-4 for 30 cycles		
Gel electrophoresis – 1.5% agarose, Wild-type band: 420 bp; mutant band: 180 bp			

Cofilin1			
Amount of reaction component	**Thermocycler program**		
1.00µL sample 2.00µL PCR rxn buffer (1x)	Steps	Temp.°C	Time min.
0.16µL dNTPs (25 nM)	1) 1st Denaturing	94	2:00
1.50 µL Primer #348 (5 µM)	2) Denaturing	94	0:30
0.50 µL Primer #347 (5 µM)	3) Annealing	58	0:30
0.50 µL Primer #349 (5 µM)	4) Extension	68	0:40
0.6 µL $MgCl_2$ (1.5mM)	5) Last Extension	68	5:00
13.54 µL dH_2O	6) Incubation	8	hold
0.2 µL Taq Polymerase (1 U) 20 µL volume (total)	Repeat steps 2-4 for 30 cycles		
Gel electrophoresis – 1.5% agarose, Wild-type band: 380 bp; floxed band: 420 bp; deleted band: 170 bp			

Cre			
Amount of reaction component	**Thermocycler program**		
1.00µL sample 2.00µL PCR rxn buffer (1x)	Steps	Temp.°C	Time min.
0.16µL dNTPs (25 nM)	1) 1st Denaturing	95	2:00
1.00 µL FW Primer (5 µM)	2) Denaturing	95	0:40
1.00 µL RW Primer (5 µM)	3) Annealing	59	1:00
0.6 µL $MgCl_2$ (1.5mM)	4) Extension	72	0:50
13.54 µL dH_2O	5) Last Extension	72	10:00
0.2 µL Taq Polymerase (1 U)	6) Incubation	8	hold
20 µL volume (total)	Repeat steps 2-4 for 30 cycles		
Gel electrophoresis – 1.5% agarose, mutant band: 300 bp			

Dab1-flox			
Amount of reaction component	**Thermocycler program**		
1.00µL sample 2.00µL PCR rxn buffer (1x)	Steps	Temp.°C	Time min.
0.16µL dNTPs (25 nM)	1) 1st Denaturing	94	3:00

1.00 µL FW Primer (5 µM)	2) Denaturing	94	0:30
1.00 µL RW Primer (5 µM)	3) Annealing	57	0:45
0.6 µL $MgCl_2$ (1.5mM)	4) Extension	72	0:45
13.54 µL dH_2O	5) Last Extension	72	5:00
0.2 µL Taq Polymerase (1 U)	6) Incubation	8	hold
20 µL volume (total)	Repeat steps 2-4 for 30 cycles		
Gel electrophoresis – 3% agarose, Wild-type band: 491 bp; floxed band: 542 bp			

Dab1-del			
Amount of reaction component	**Thermocycler program**		
1.00µL sample 2.00µL PCR rxn buffer (1x)	Steps	Temp.°C	Time min.
0.16µL dNTPs (25 nM)	1) 1st Denaturing	95	3:00
1.00 µL FW Primer (5 µM)	2) Denaturing	95	1:00
1.00 µL RW Primer (5 µM)	3) Annealing	54	1:00
0.6 µL $MgCl_2$ (1.5mM)	4) Extension	72	1:00
13.54 µL dH_2O	5) Last Extension	72	10:00
0.2 µL Taq Polymerase (1 U)	6) Incubation	8	hold
20 µL volume (total)	Repeat steps 2-4 for 30 cycles		
Gel electrophoresis – 2% agarose, Wild-type band: 1000 bp; mutant band: 331 bp			

R26			
Amount of reaction component	**Thermocycler program**		
1.00µL sample 2.00µL PCR rxn buffer (1x)	Steps	Temp.°C	Time min.
0.16µL dNTPs (25 nM)	1) 1st Denaturing	94	2:00
1.00 µL R26-RR1 Primer (5 µM)	2) Denaturing	94	1:00
1.00 µL R26-RR2 Primer (5 µM)	3) Annealing	61	1:00
1.00 µL R26-RR3 Primer (5 µM)	4) Extension	72	1:00
0.6 µL $MgCl_2$ (1.5mM)	5) Last Extension	72	10:00
13.54 µL dH_2O	6) Incubation	8	hold
0.2 µL Taq Polymerase (1 U) 20 µL volume (total)	Repeat steps 2-4 for 30 cycles		
Gel electrophoresis – 1.5% agarose, Wild-type band: 500 bp; mutant band: 220 bp			

3.3. Organotypic slice culture experiments

Organotypic slice cultures were prepared as described previously (Bodea and Blaess 2012). As we were interested in the tangential migration of SN-mDA neurons, we prepared horizontal slice cultures at E13.5 (Bodea et al. 2014).

3.3.1. Dissection of embryonic brains

Pregnant dams were anaesthetized with isofluorane and sacrificed by cervical dislocation. Embryos were dissected out of the uterus and immediately decapitated in ice-cold Krebs buffer. Embryonic heads were then transferred to a previously cooled 12-well plate with Krebs buffer. Tail tips or limb buds were collected from each embryo during decapitation and were placed in correspondingly numbered tubes and a digestion protocol was started. Embryonic

heads were screened for YFP fluorescence at an Axioobserver Z1 (Zeiss) microscope with 5X magnification. Fluorescent embryonic brains were freed from the skull and surrounding tissue with fine forceps under a stereomicroscope (MZ10F, Leica). Dissected embryonic brains were transferred to a new 12-well plate, kept on ice, and numbered as before. 4% low melting point (LMP) agarose was melted and preheated in a water bath to 40°C. Brains were embedded in LMP agarose on a hotplate maintained at 40°C. Care was taken to ensure a horizontal orientation of brains in the embedding dish. Each brain was embedded in a numbered petri dish and then placed on ice for 5 min.

3.3.2. Vibratome sectioning and slice culture

LMP agarose from each numbered petri dish was trimmed to a block, and glued to the specimen stage of the vibratome (HM650V, Microm), with the dorsal side of the brain placed parallel to the stage. The stage was placed at 4°C, in a cooled chamber containing Krebs buffer. Vibratome blade amplitude was set to 1.1 mm, blade frequency was set to 50 Hz, and sectioning speed to 25 mm/sec. Blocks were sectioned at 300 µm thickness. Slices at all the dorsoventral levels containing the midbrain were collected with the help of a fine brush and perforated spoon. Slices were placed on semi-porous membrane inserts (0.4 µm pore size) and cultured overnight in 1 mL of slice culture medium at 37°C, 5% CO_2 (**Figure 5**).

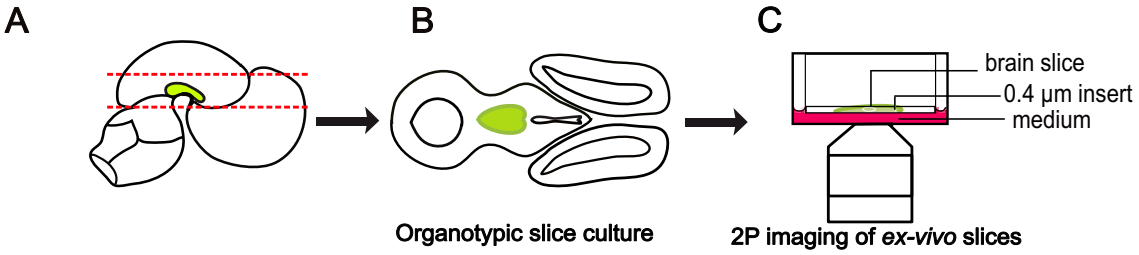

Figure 5. (A) Schematic representing dorsoventral level (red dashed lines) of horizontal organotypic slices. (B) Organotypic slice with mDA domain in green. (C) Schematic representing imaging of organotypic slices with two photon excitation microscopy. Figure adapted from (Bodea and Blaess 2012)

3.4. Tissue clearing and whole mount imaging of embryonic brains

To visualize morphology of mDA neurons during their development in 3D, we carried out tissue clearing and whole mount imaging of embryonic brains at E12.5 and E13.5.

3.4.1. Tissue clearing

Tissue clearing was carried out as described previously (Schwarz et al. 2015). The procedure was modified for embryonic tissue as described here: Embryonic brains were carefully dissected out and fixed in 4% PFA for 4 hours at room temperature, or overnight at 4°C. Immunostaining was carried out for TH and/or YFP as described in section 6.4. After

immunostaining, brains were incubated in increasing concentrations (30%, 50%, 70%) of tert-butanol (pH 9.5) for 4 hours at room temperature. Brains were then incubated in 96% and 100% tert-butanol (pH 9.5) for 4 hours at 33°C. Brains were incubated overnight in a triethylamine pH-adjusted 1:1 mixture of benzyl alcohol/benzyl benzoate (BABB, pH 9.5) at 33°C. Brains were stored in clearing solution at 4°C and imaged within 1 week of clearing.

3.5. Histology

3.5.1. Tissue fixation

Pregnant dams were anesthetized with isofluoran and sacrificed by cervical dislocation. Embryos were dissected out of the uterus as described in section 3.1, in ice cold PBS. Embryo heads (E13.5-15.5) or brains (E16.6-E18.5) were fixed in 4% paraformaldehyde (PFA) for 2-3 hrs at room temperature (RT). Adult mice were perfused transcardially with 50 mL of PBS, followed by 50 mL of 4% PFA. Brains were dissected out and post-fixed overnight in 4%PFA at 4°C with shaking.

3.5.2. Cryopreservation

Fixed brains were briefly washed with PBS before sucrose dehydration. Brains were allowed to sink, first in 15% and then in 30% sucrose solutions prepared in PBS. Brains were oriented and embedded in cryo-molds containing OCT Tissue Tek, frozen on dry ice and stored at -80°C.

3.5.3. Tissue sectioning

Embryonic tissue was cryosectioned at 14 µm thickness and collected on superfrost ultra plus adhesion slides. Slides were stored at -20°C. Adult brains were sectioned at 40 µm thickness, collected as free-floating sections, and stored at 4°C in 0.01% sodium azide solution in PBS. Cryosectioning was carried out at an object temperature of -20 to -22°C and knife temperature of -21 to -23°C at a Leica Cryostat (CM 3050S).

3.6 Immunostaining

3.6.1. Immunostaining on frozen embryonic sections

Slides were thawed in PBS and briefly fixed in 4% PFA for 5 min. Slides washed successively in PBS (5 min) and 0.1% PBT (1 in PBS), and transferred to a humid chamber. Sections were incubated for 1 hour in 10% normal donkey serum (NDS) in 0.1% PBT. Primary antibodies were prepared in 3% NDS in 0.1% PBT. Slides were incubated overnight at 4°C in primary antibody solution. The following antibody concentrations were used: rabbit anti-TH (1: 500), mouse anti-TH (1: 500), rabbit anti-GIRK2 (1:400), rabbit anti-Calbindin (1: 5000), rabbit anti-GFP (1: 400), rat anti-GFP (1: 1500), goat anti-Reelin (1: 200), rabbit anti-DAB1 (1: 50),

goat anti-OTX2 (1: 5000), rabbit anti-SOX6 (1: 500), rabbit anti-CDH2 (1: 250). After primary antibody incubation, sections were washed 3X in 0.1% PBT before incubating with secondary antibody solution for 2 hours at RT. Secondary antibodies were prepared in 3% NDS in 0.1% PBT at the following concentrations: Donkey anti-rabbit Alexa 488 (1: 500), donkey anti-rabbit Alexa 350 (1: 500), donkey anti-mouse Alexa 488 (1: 500), donkey anti-rat Alexa 488 (1: 500), donkey anti-goat Alexa 488 (1: 500), donkey anti-rabbit Cy3 (1: 200), donkey anti-mouse Cy3 (1: 200), donkey anti-goat Cy3 (1: 200). Hoechst solution (1: 10000) was added to the secondary antibody solution, when counterstaining of nuclei was desired. After secondary antibody incubation, sections were washed in 0.1% PBT 3X for 5 min. Sections were air-dried for 2 min before mounting with Aqua Polymount. All washes were carried out in 50 mL Coplin jars.

3.6.1.1. Antigen retrieval and signal amplification

To improve detection of transcription factors Otx2 and Sox6, sections were incubated in 0.1M EDTA buffer (pH 8.5) at 65°C for 30 min before blocking. To improve detection of Dab1 protein with rabbit anti-DAB1 antibody in E15.5 embryonic sections, a tyramide signal amplification (TSA) was carried out with the TSA kit from Perkin Elmer as follows: Sections were incubated in blocking solution from Perkin Elmer for 1 hour before primary antibody incubation. Sections were incubated with rabbit anti-Dab1 (Howell et al. 1997) at 1:5000 concentration, in 0.1% TBST overnight at 4°C. Slides were washed in TBST before biotinylation. Sections were incubated for 2 hours at RT with donkey anti-rabbit Biotin (1: 200) in TBST. Sections were washed 3X in TBST and incubated with HRP conjugated Streptavidin (1: 1000) in TBST for 1 hour at RT. Sections were washed 3X in TBST and incubated for 10 min with TSA detection reagent. Sections were washed with TBST, and then with 0.1% PBT for 5 min before co-staining for TH with regular immunohistochemistry procedure (described above).

3.6.2. Immunostaining on adult free-floating sections

Free floating sections were washed briefly in PBS and 0.2% PBT before blocking for 1 hour in 10% NDS in 0.2% PBT at RT. Sections were incubated overnight in primary antibody solution at 4°C. Rabbit anti-TH (1: 500), mouse anti-TH (1: 500), rabbit anti-GIRK2 (1:400), rabbit anti-Calbindin (1: 5000) were used. Sections were washed 3X with 0.2% PBT before secondary antibody incubation in 0.2% PBT for 2 hours. Donkey anti-rabbit Alexa 488 (1: 500), donkey anti-mouse Alexa 488 (1: 500), donkey anti-rabbit Cy3 (1: 200), donkey anti-mouse Cy3 (1: 200) were used. All steps were carried out in a 12 well plate, and with shaking.

3.6.3. Immunostaining on organotypic slices

Organotypic slice cultures were fixed in 4% PFA for 1 hour at RT, then rinsed in PBS and 0.3 % PBT for 10 min. Slices were incubated in blocking solution (10% NDS in 0.3% PBT) at RT for 2 hours, or overnight at 4°C. After blocking, slices were incubated with primary antibody solution for 24-48 hours at 4°C. The following primary antibodies and dilutions were used: rabbit anti-TH (1:500), rat anti-GFP (1:1000). Slices were washed and then incubated in secondary antibody solution, at RT for 4 hours, or overnight at 4°C. Secondary antibodies donkey anti-rabbit Cy3 (1:200) and donkey anti-rat Alexa 488 (1:500) were used. All washing and incubation steps were performed using 0.3% PBT. All steps were carried out in a 6 well plate.

3.6.4. Immunostaining on whole mount embryonic brains

Brains from E13.5 embryos were fixed in 4% PFA for 4 hours at room temperature, or overnight at 4°C. Brains were washed with PBS, 0.3% PBT, and incubated with blocking solution (10%NDS in 0.3% PBT) overnight at 4°C. The brains were incubated with primary antibodies: rabbit anti-TH (1:500) and rat anti-GFP (1:1000) at 4°C for 2 days. Next, the primary antibody solution was removed and the brains were washed three times with 0.3% PBT at RT for 15 min. The tissue was incubated with secondary antibodies: donkey anti-rat IgG-DyLight 647 (1:100) and donkey anti-rabbit Cy3 (1:200) at RT for 1 day. Subsequently, the tissue was washed three times with 0.3% PBT and three times with PBS for 20 min. All washing steps and antibody solutions preparation were performed using 0.3 % PBT. All steps were carried out in 24 well plates.

3.7. *In situ* hybridization

3.7.1. RNA probe preparation

Single stranded, anti-sense DIG-labeled RNA probes were made from plasmids containing complete or partial cDNA sequences of genes of interest.

3.7.1.1. Plasmid extraction

Purchased cDNA clones were used to inoculate 3 mL of LB medium supplemented with the appropriate antibiotic. The bacterial culture was grown for 8 hours at 37°C and 225 rpm. 200 µL of this culture was used to inoculate 200 mL of LB medium supplemented with the appropriate antibiotic. Cells were grown at 37°C and 225 rpm overnight. The following day, bacterial cells were centrifuged at 4000 rpm. Pelleted cells were resuspended and lysed, and DNA was extracted and purified using the PureLink HiPure Plasmid Maxiprep kit according to the manufacturer's protocol. DNA concentration was determined by measuring optical density (OD) at a wavelength of 260nm (peak absorption wavelength fo nucleic acids). A measurement

of OD at a wavelength of 280 nm was carried out to determine protein contamination, and an OD ratio of 260/280 > 1.80 was regarded as pure.

3.7.1.2. Plasmid linearization

Plasmids were linearized with the appropriate restriction enzymes (2 to 5 units of enzyme were used for 1 µg DNA. All reactions were performed in appropriate buffers supplemented for 2 hours at 37°C. Purification of linearized plasmids was carried out with the PCR purification kit, according to the manufacturer's protocol.

3.7.1.3. *In vitro* transcription to generate anti-sense RNA probes

RNA probes were transcribed from the linearized DNA templates using DNA-dependent RNA polymerases from the bacteriophages SP6, T3 or T7. DIG-labeled nucleotide tri-phosphate (NTP) mix was used as a substrate.

Table 14: *In vitro* transcription protocol

***In vitro* transcription mix**		**Protocol**
1.5 µL	Purified DNA (1-2 µg)	- incubate 3 hours at 37°C - add 1 µL DNase I - incubate 15 min., 37°C - add 2 µL EDTA (4mM), 2.5 µL LiCl (100mM) and 75 µL 100% EtOH to precipitate RNA - incubate 15 min, -80°C - centrifuge max. speed, 15 min - air-dry 3-5 min at RT - add 50 µL ddH_2O with 1% RNase inhibitor - measure concentration and store at -20°C
2 µL	Transcription buffer (10x)	
2 µL	DIG-NTP labeling mix (10x)	
0.5 µL	RNase inhibitor (10U)	
0.5 µL	RNA polymerase (30U)	
12.5 µL	ddH_2O	
20 µL volume final		

3.7.2. Hybridization

Sections were post-fixed in 4% PFA for 10 min, rinsed in PBS and acetylated in 50 mL 0.1 M TEA-HCl with 125 µL acetic anhydride for 5 min with stirring. Sections were washed in PBS and briefly dehydrated in 70%, 95% and 100% ethanol (EtOH). 1 µg of RNA probe was added to 1 mL hybridization buffer and incubated for 2 min at 80°C. Sections were air-dried and transferred to a humidified hybridization cassette. A 1: 1 mixture of formamide and H_2O was used as humidifying solution. 300 µL hybridization solution containing RNA probe was added to each slide, slides were covered with RNAse-free coverslips and incubated at 55°C overnight. On the following day, coverslips were removed in prewarmed 5X SSC. To reduce unspecific hybridization, sections were incubated in a 1:1 solution of formamide and 2X SSC (high stringency wash solution) for 30 min at 65°C. Sections were then washed with RNAse buffer, containing 0.1% RNAse A at 37°C for 10 min to remove non-hybridized RNA. Sections were washed twice with high stringency solution for 20 min at 65°C, once with 2X SSC and once with 0.1X SSC for 15 min at 37°C. Sections were placed in a humidified chamber and

incubated with 10 % normal goat serum in 0.1% PBS-Tween (blocking solution) for 1 hour at RT. Sections were incubated with anti-DIG-AP Fab fragments (diluted 1:5000 in 1% goat serum in 0.1% PBS-Tween) for 3 hrs at RT, or overnight at 4°C. Sections were washed several times 0.1% PBS-Tween, followed by two washes in NTMT buffer (containing 1 mg/mL levamisole to reduce background of endogenous alkaline phosphatase activity) for 10 min at RT. Sections were incubated in BM purple, a substrate for alkaline phosphatase (with 0.5 mg/mL levamisole) at RT until signal was observed. The chromogenic reaction was stopped by a 10 min incubation in TE buffer at RT. Sections were then washed in PBS, and immunostained for TH.

3.8. Image acquisition

3.8.1. Two photon time lapse imaging of organotypic slices

Slices were briefly examined at a Zeiss Axioobserver microscope with conventional epifluorescence. Healthy slices, with well defined, strongly fluorescent cells, were chosen for two photon imaging. Two photon imaging allows for deeper light penetration into the dense 300µm thick organotypic slices, while minimizing out of plane excitation of fluorophores. Chosen slices were transferred, along with their membrane inserts, to prewarmed, specialized imaging dishes containing 750 µL of fresh culture medium. Slices were imaged at 320X magnification with an inverted, two-photon Zeiss LSM 710 NLO microscope equipped with temperature and CO_2 control (Light microscopy facility, DZNE, Bonn). The microscope setup and the 32X water immersion objective were preheated for 8 hours before time lapse experiments. Images were acquired once every 10 min, for durations of 3-4.33 hours, at 920 nm wavelength, and 5-10% laser power. Tiles were stitched with Zen black software. A total of 13 control and 9 *Dab1*$^{-/-}$ slices, across 4 litters, were imaged as described. 3 control and 3 *Dab1*$^{-/-}$ slices with comparable dorsoventral level, fluorescence intensity and negligible drift were chosen for further analysis. After imaging, slices were fixed and post-stained as described in section 6.3.

3.8.2. Whole mount imaging of embryonic brains

Whole mount brains were imaged in clearing solution with a 20X BABB dipping objective (Olympus) at a Leica SP8 upright microscope (Microscope Core Facility, Universitätsklinikum Bonn). Multi-channel image acquisition of the whole brain (4-6 tiles, 150-200 z-steps, 1 z-step = 1.5 µm) took 30-70 hours, and resulted in multichannel datasets of large sizes (20-80 GB). Voxel size of thus acquired images was 0.432 µm X 0.432 µm X 1.5 µm. Individual tiles at each z-step were stitched together with the Leica SP8 PC suite.

3.8.3. Imaging of frozen sections

Embryonic and adult sections were imaged at an inverted Zeiss AxioObserver Z1 microscope equipped with an ApoTome. At 10X and 20X magnifications, tile images were acquired with conventional epifluorescence. ApoTome function was used to acquire tile images and z-stacks at 40X and 63X magnifications. *In situ* hybridized sections were imaged with transillumination at the AxioObserver Z1 setup. Images were stitched with Zen blue software (Zeiss, 2012). Sections stained with Alexa 649 secondary antibody were imaged at a Leica SP8 confocal microscope and stitched with Leica PC suite (Leica, 2014).

3.9. Data analysis

3.9.1. Soma tracking of mDA neurons in organtoypic slices

3.9.1.1. Soma detection

To track mDA neurons in our two photon time lapse datasets, we used the semi-automatic plugin TrackMate in Fiji (Tinevez et al. 2017). Before soma detection, a 3X3 median filter was applied by the TrackMate plugin, to reduce salt and pepper background noise. Soma detection was carried out using the Laplacian of Gaussian (LoG) detector in TrackMate. This detector applies a Laplacian of Gaussian filter, of a radius decided by the user, to segment the image. This detector is one of three offered by the plugin and is optimal for the detection of spots (soma) that range from 5-20 pixels in size. Cell radii in our acquired datasets were estimated to range between 2.5-7 µm (measurements performed on randomly chosen cells in ImageJ), and voxel size of the datasets was 0.421 µm X 0.421 µm X 1.17 µm. Hence, cell radii in the datasets was roughly estimated vary between 6-17 pixels, making LoG detector the optimal choice for soma segmentation. The LoG detector was set to detect spots (soma) of 6 µm radius. Spot radius was estimated by trial and error. To curtail spurious spot detection, a threshold of 3 (numerical value, estimated by trial and error by eye) was set on the quality of detected spots. To improve the accuracy of detected spot positions, the position of each spot was recalculated with a simple parabolic interpolation scheme {Lowe:kp}. In this first spot detection step of the analysis, spots were detected at all time points individually. These spots were further filtered based on their locations in the dataset, and thus soma detections in the midline were excluded from analysis.

3.9.1.2. Tracking soma over time

The soma detected by the TrackMate plugin were automatically linked across time, in 3D, by using the linear assignment problem (LAP) tracker in TrackMate. The LAP tracker, assumes that every spot in time frame 1 (t1) could be linked to every spot in time frame 2 (t2). However, based on the LAP framework, there is a cost penalty for every hypothetical spot–spot linkage, proportional to the square of the distance between the two spots (Jaqaman 2008; Tinevez et

al. 2017). The LAP tracker builds a cost matrix of all possible spot–spot linkages between consecutive time frames and then solves for the linkage with minimum cost (Tinevez et al. 2017). The LAP tracker can also assign cost penalties based on other spot features. We assigned a cost penalty of 3 on the mean intensity of linked spots and their z distance. After automatic tracking, the track scheme view in TrackMate was used to check the accuracy of each track by eye. Spurious tracks were deleted and missed detections were added using the manual tracking mode in TrackMate. Only cells for which the soma were detected at all time points of imaging were included in the analysis. Using this approach, we tracked 811 control cells and 892 *Dab1*$^{-/-}$ cells, across 3 slices and acquired their speed and trajectory profiles. Each cell (and track) had a unique ID assigned by the TrackMate plugin. These cell IDs were used to identify and locate individual cells in the slice for further analysis (section 9.3).

3.9.2. Analysis of speed and trajectory profiles of tracked mDA neurons

Tracks from the TrackMate plugin were imported into MatLab. Soma velocity was obtained at every time point (in units of μm/hr) of the analysis (starting t = 10 min) as the change in soma position vector between the previous frame and the current frame, divided by the time duration (0.167 hr) between frames (Wu, Giri and Wirtz 2015). This data was used to generate probability histograms for average soma speed (average soma speed of a cell over all observed time-frames), maximum soma speed (maximum observed soma speed of a neuron measured between two consecutive time-frames), time spent at rest (defined as soma speed < 10 μm/ hr), time spent in slow migration (soma speed between 10 and 60 μm/ hr) and time spent in fast migration (soma speed > 60 μm/ hr). Cells with soma speed > 60 μm/ hr in at least one timepoint of analysis were defined as fast migrating cells.

Cell trajectory angles were measured in 2D as the angle between midline (negative y-axis in the image) and the line joining the first and final soma positions. Cells that moved less than 10 μm during the entire duration of imaging were excluded from the trajectory analysis. Angles of individual migratory movements were measured as the angle made by the line joining the current soma position and the soma position at the previous time-frame to the midline. These angles of individual migratory movements were then separated into slow, moderate and fast groups based on the magnitude of speed of the movements. As the distributions of trajectory angles and angles of individual migratory movements consisted of circular variables (angle of 0° is equivalent to the angle of 360°), they were tested for statistical difference by the Kuiper's test designed for circular variables.

3.9.3. Morphological analysis of migrating mDA neurons

Cells selected for morphology analysis were located in the slice by using the Cell IDs in the track scheme view in TrackMate. Morphology was analysed only for the first 18 frames of

imaging as even slight deterioration in image quality affected the sensitivity towards small protrusions and processes. Analysis was manually done, by rendering individual neurons in 4D (3D projection over all time frames) in ImageJ, and recording the number of primary processes (arising from the soma) and secondary processes at each time point. Counting of processes and their branches was done by eye. A cell was defined as bipolar when fewer than two primary processes were observed arising directly from the soma. Soma was defined as the 6 µm spot detected by the TrackMate plugin. The appearance/ disappearance of any branch was regarded as a branch transition. At each time point, the morphology of the cell, and the number of branch transitions, was manually annotated to the spot position data of the cell in excel sheets exported from TrackMate. All fast-moving cells were analyzed in this fashion, cells whose morphology could not be analysed due to their location in a dense cluster of cells were excluded from the analysis. In addition to these cells, 20 slow moving cells each, from control and *Dab1*$^{-/-}$ slices were analyzed.

3.9.4. Tracing mDA neuronal morphology in organotypic slices

20 control and *Dab1*$^{-/-}$ cells were randomly chosen for tracing in 3D. These neurons were traced manually in simple neurite tracer (SNT) plugin of Fiji. Tracings were carried out, at each time point individually, for the first 18 frames of imaging. Fills of traced neurons were generated semi-automatically in the SNT plugin. Fill thickness was decided by eye but was maintained across all time points for a cell. Maximum intensity projections were also generated for the 3D segmentation fills and the lookup table (LUT) 'Physics' was applied to these images by which different colors were assigned to the cell based on the volume and intensity of filled regions. SNT traces were also used to measure length of the leading process in 3D.

3.9.5. Tracing mDA neuronal morphology in whole mount embryonic brains

To analyze mDA morphology in fixed tissue in 3D, whole mount datasets were rendered in Imaris (Bitplane). The semi-automatic tracing module in Imaris was used to trace neurons in 3D. Traces were exported as csv files from Imaris and analyzed for process length and dendrite straightness.

3.9.6. mDA distribution in *DAT-Dab1* CKO and *Dab1*$^{-/-}$ brains

We examined the mediolateral distribution of TH+ mDA neurons in coronal midbrain sections of control, *Dab1* CKO and *Dab1*$^{-/-}$ (complete knockouts for *Dab1)* mice at postnatal (P30) and embryonic time points (E18.5, E15.5). To account for variances in brain size, we constructed normalized mediolateral bins as follows: We observed that in both, *Dab1* CKO and *Dab1*$^{-/-}$ mice, a few cells of the lateral most SN were always present. Hence, we defined the mediolateral bins by quadrisecting a line, perpendicular to the midline, extending from the

midline to the lateral most TH^+ cell (**Figure 9C)**. We then evaluated the fraction of the total number of TH^+ cells in each mediolateral bin for control, *Dab1* CKO and *Dab1*$^{-/-}$ brains by manually counting the cells.

3.10. Statistical analysis

Mediolateral distributions of TH^+ mDA neurons in control, *Dab1* CKO and *Dab1*$^{-/-}$ adult and embryonic brains were analyzed for using two-way ANOVA with Tukey's correction for multiple comparisons (n = 6 animals/genotype at P30 and n = 4 animals/genotype at E18.5). Mediolateral distributions of TH^+ mDA neurons at E15.5, and mediolateral distribution of P30 TH^+ $GIRK2^+$ neurons in control and *Dab1* CKO brains were assessed for statistically significant differences using Student's t-test (n = 3 animals/genotype).

Average soma speeds and max. soma speeds (measured by tracking as described in section **3.9.2, Figure 16**) of individual cells from across 3 control slices were pooled together, as were average and maximum soma speeds of neurons from the 3 *Dab1*$^{-/-}$ slices. Distributions of average and maximum soma speeds thus obtained for control and *Dab1*$^{-/-}$ populations were non-parametric, non-gaussian and long-tailed (**Figure 18**). These non-parametric distributions of control and *Dab1*$^{-/-}$ populations were compared and analyzed with Mann-Whitney's non-parametric rank test or a two-sample Kolmogorov-Smirnov test (mentioned in the figure legends) using Prism7/MatLab. The Mann-Whitney's rank test is a non-parametric counterpart to the student's t-test. It examines whether a random value chosen from one distribution will be less than or greater than a randomly selected value from a second distribution (Gaddis and Gaddis 1990). In this study, this test was used to determine whether two independent samples (selected from control and *Dab1*$^{-/-}$ populations) were selected from populations having the same distribution. The two-sample Kolmogorov-Smirnov test is also a non-parametric test used to check whether two values come from populations having the same distribution. The two-sample Kolmogorov-Smirnov test compares the cumulative distribution function (CDF) for the two populations being analyzed and measures the 'distance' between the two CDFs (Gaddis and Gaddis 1990).

For the comparison of total 3D displacement and directionality of slow, moderate and fast mDA neurons (separated based on maximum soma speed) within control and *Dab1*$^{-/-}$ populations, the Kruskal-Wallis non-parametric test was used. The Kruskal-Wallis test is used to compare more than two independent populations, and is the non-parametric equivalent of an ANOVA (analysis of variance)(Gaddis and Gaddis 1990).

The circular variables in this study: trajectory angles and angles of individual migratory movements were analyzed with Kuiper's test for circular variables. The Kuiper's test is a Kolmogorov-Smirnov-type test that is invariant in cyclic conditions (such as angular variables). This test compares the angular cumulative distribution functions (CDF) of angular distributions

obtained from two populations to assess whether they are significantly different from each other. The angular CDFs and Kuiper's test were carried out using the CircStat toolbox in MatLab (Berens 2009).

4. RESULTS

4.1. Inactivation of Reelin signaling specifically in tangentially migrating mDA neurons

In mutants lacking functional Reelin or DAB1, SN-mDA neurons fail to migrate laterally and accumulate instead in the lateral VTA (Bodea et al. 2014). To understand whether Reelin is directly involved in this process, the first step was to establish a method to selectively inactivate Reelin signaling by the specific knockout of *Dab1* in tangentially migrating mDA neurons after E13.5 (by this time, radial migration of mDA neurons is essentially complete). For this purpose, a *DAT*$^{Cre/+}$ mouse line was used. In this line, a sequence encoding Cre is knocked into the endogenous *dopamine transporter (Dat)* locus (**Figure 6A**).

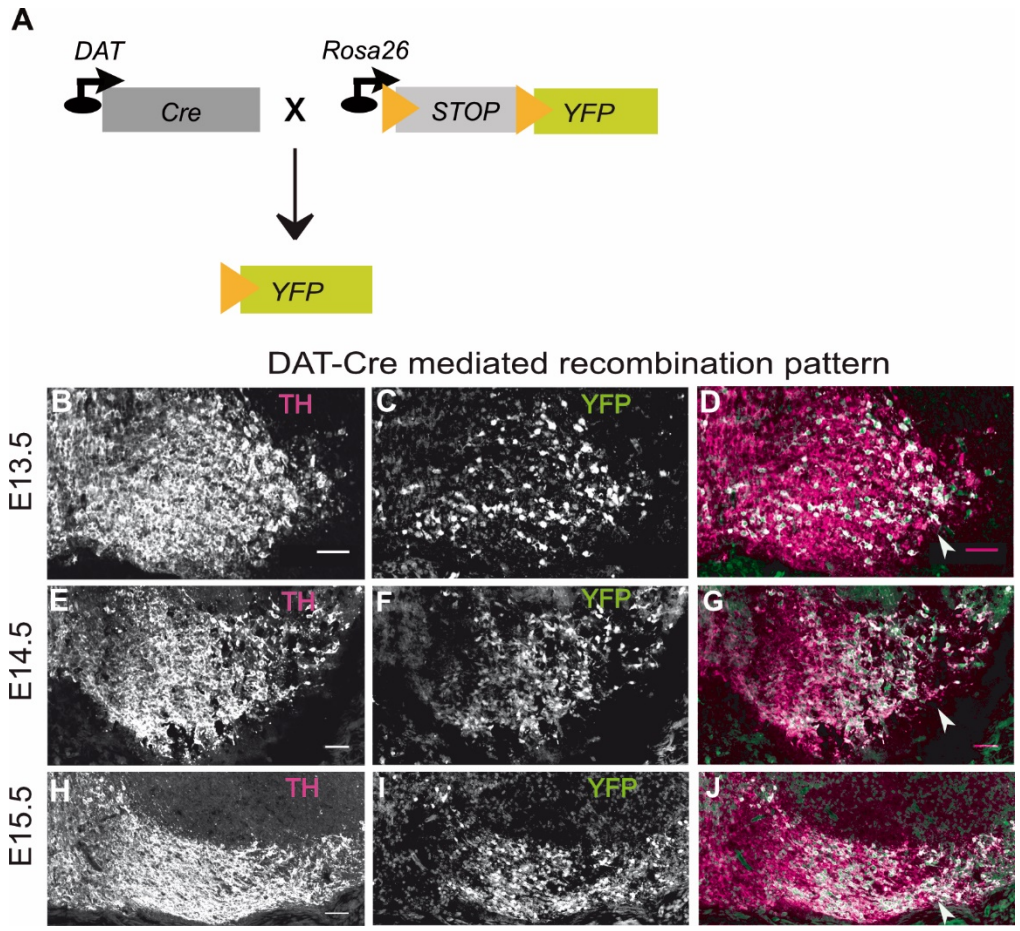

Figure 6. (A) Schematic of transgenic mouse lines used to analyze Cre-mediated recombination under the *Dat* promoter. (B-D) Immunostaining for YFP (yellow fluorescent protein, C) and TH (Tyrosine hydroxylase, B) starting at E13.5. (D) Co-labelling of TH (magenta) and YFP (green) in lateral mDA neurons. (E-F) At E14.5, most lateral mDA neurons (future SN-mDA neurons) are recombined by Cre to express YFP. (H-G) By E15.5, Cre-mediated recombination is found throughout SN and lateral VTA-mDA neurons. White arrowheads in (C, G, J) indicate TH$^+$, YFP$^+$ neurons. Figure modified from (Vaswani et al. 2019).

To confirm whether *Dab1* is inactivated early enough (starting E13.5), and in the right population of mDA neurons, it was necessary to analyze when the onset of Cre-mediated recombination occurs under the *Dat* promoter. For this purpose, $DAT^{Cre/+}$ mice were crossed with a YFP-expressing reporter mouse line ($Rosa26^{lox\text{-}stop\text{-}lox\text{-}YFP}$). The $Rosa26^{lox\text{-}stop\text{-}lox\text{-}YFP}$ reporter mouse line requires Cre-mediated recombination to excise a stop codon preceding the YFP sequence, resulting in YFP labeling of Cre-expressing cells (Srinivas et al. 2001) (**Figure 6A**).

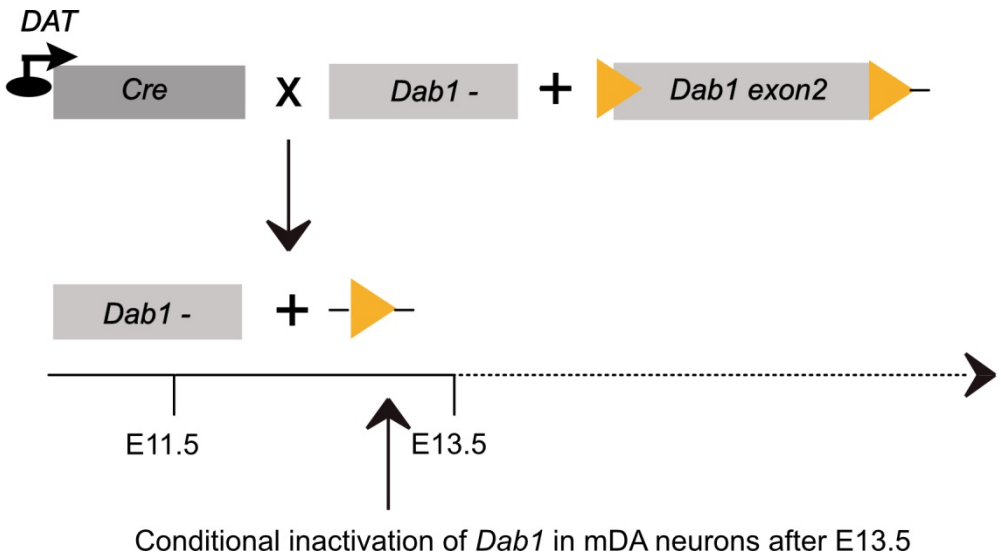

Figure 7. Schematic representing transgenic mouse lines used to inactivate DAB1 specifically in mDA neurons after E13.5, using Cre-mediated recombination under the *Dat* promoter. DAT^{Cre} mice were crossed with mice containing *Dab1* alleles in which exon 2 of was flanked by loxP sites (yellow triangles). In offspring expressing *Cre* under the *Dat* promoter, exon 2 of *Dab1* is floxed out in mDA neurons after E13.5 resulting in the life-long, conditional inactivation of *Dab1* in these neurons. Figure modified from (Vaswani et al. 2019).

In the $DAT^{Cre/+}$, $Rosa26^{lox\text{-}stop\text{-}lox\text{-}YFP}$ mice, strong YFP-expression was observed in TH-expressing (TH^+) cells in the lateral mDA domain starting at E13.5 (**Figure 6B-D**). At E14.5, strong expression of YFP was seen in a majority of cells in the lateral mDA domain (**Figure 6E-G**) and by E15.5 recombination was essentially complete, with almost all SN-mDA cells expressing YFP (**Figure 6H-J**).

Having examined the onset and extent of recombination under the *Dat* promoter in the $DAT^{Cre/+}$ mouse line, $DAT^{Cre/+}$, $Dab1^{-/+}$ mice were crossed with $Dab1^{flox/flox}$ mice to generate *Dab1* CKO mice (genotype: $Dat^{Cre/+}$, $Dab1^{-/flox}$) (**Figure 7**). To confirm the selective inactivation of *Dab1* in mDA neurons, DAB1 protein distribution was analyzed. Immunostaining for DAB1 at E15.5 showed loss of DAB1 expression in the lateral TH^+ domain in *Dab1* CKO mice, but not in a non-dopaminergic area lateral to the SN (**Figure 8A-L**). Because *Dab1* inactivation occurs after mDA radial migration is essentially completed, the *Dab1* CKO model can be used to dissect out the role of Reelin signaling specifically in the tangential migration of mDA

neurons, and defects observed in mDA migration in *Dab1* CKO mice can be attributed to alterations in their tangential migration.

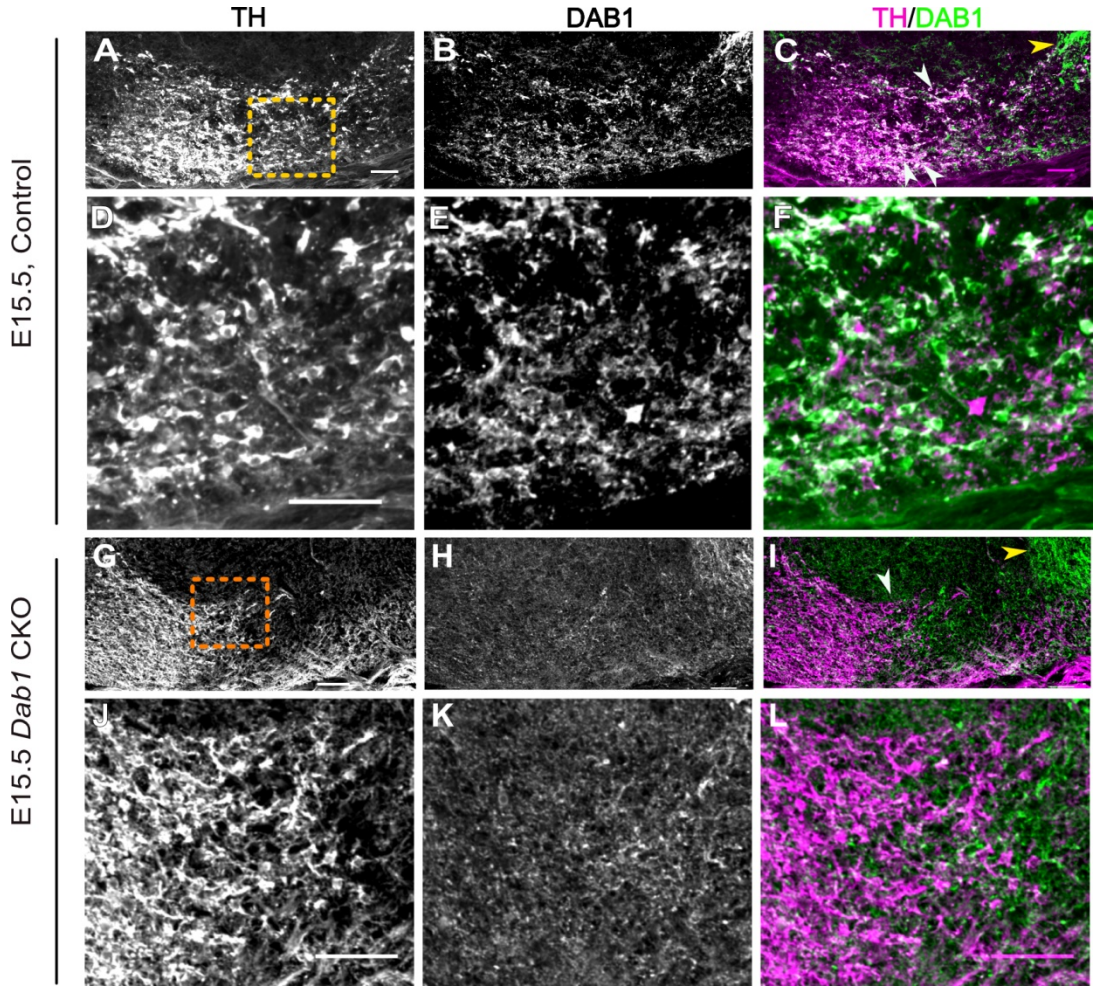

Figure 8. DAB1 expression in mDA neurons. (A-C) DAB1 protein (B) is observed in laterally located TH^+ mDA neurons (A), but not in medial mDA neurons in brains of control mice at E15.5. (C) Co-labelling of TH (magenta) and DAB1 (green). White arrowheads indicate TH^+, $DAB1^+$ mDA neurons, yellow arrowhead points to DAB1 expression outside the mDA domain (TH^- region). (D-F) Higher zoom of cyan box indicated in (A) shows coexpression of TH (D) and DAB1 (E). (G-I) In conditional knockouts of DAB1 (*Dab1* CKO) at E15.5, DAB1 expression (H) is missing from the TH^+ domain (G) as indicated by white arrowheads in (I), but DAB1 expression persists in non-dopaminergic (TH^-) region (yellow arrowhead in I). This persistent DAB1 expression in non-dopaminergic populations demonstrates the specific inactivation of DAB1 in mDA neurons by E15.5. (J-L) Higher zoom of region indicated by orange box in (G) shows lack of co-labeling of TH and DAB1 in *Dab1* CKO mDA neurons. Scale bars: 50µm. Figure modified from (Vaswani et al. 2019).

4.2. Reelin signaling is directly required by mDA neurons for the correct formation of the substantia nigra pars compacta

To test whether Reelin is directly required for mDA neuronal migration, the next step was to analyze and compare the mediolateral distribution of TH^+ mDA neurons in coronal midbrain sections of control, *Dab1* CKO and *Dab1*$^{-/-}$ mice at postnatal (postnatal day (P)21-P30) and embryonic time points (E18.5, E15.5) (**Figure 9**).

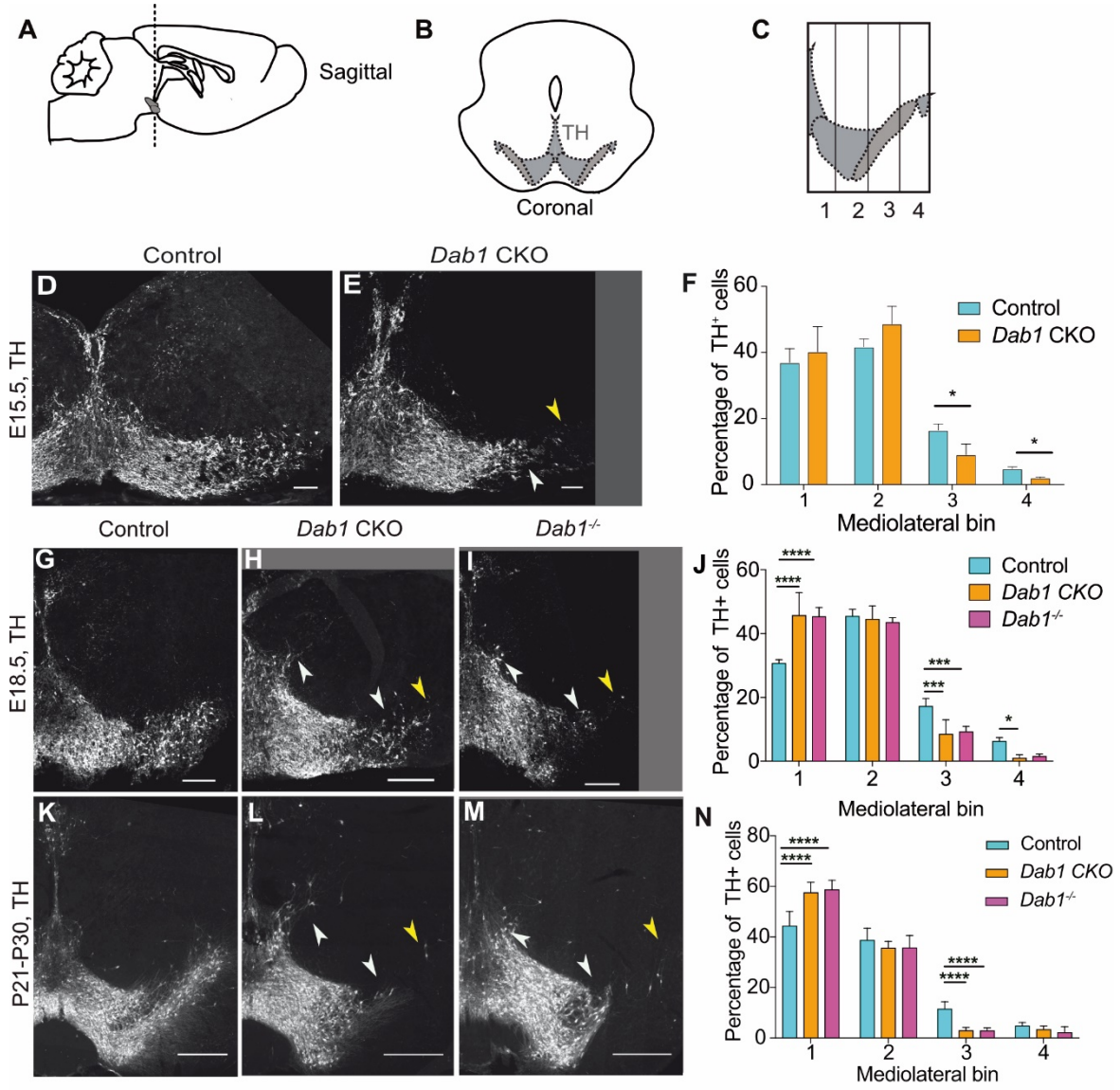

Figure 9. (A) Schematic of the rostrocaudal level of intermediate coronal sections (B) used in this analysis. (C) Mediolateral grid used to quantify distribution of TH$^+$ mDA neurons. (D-F) Immunostaining for TH and quantification of cell distribution for control and *Dab1* CKO mice at E15.5. (G-N) Immunostaining for TH and quantification of cell distribution for control, *Dab1* CKO, and *Dab1*$^{-/-}$ midbrain regions at E18.5 (G-J) and at P21-P30 (K-N). White arrowheads indicate differences in the mediolateral distribution of TH$^+$ cells in *Dab1* CKO, and *Dab1*$^{-/-}$ mice. Yellow arrowheads point to cells in the SN used to determine lateral position edge of the mediolateral grids. (F,J,N) Quantification of mediolateral distribution of TH$^+$ cells for control and *Dab1* CKO brains at E15.5 (F, n = 3 for each genotype); control, *Dab1* CKO and *Dab1*$^{-/-}$ brains at E18.5 (J, n=4 for each genotype) and at P21-P30 (N, n=6 for each genotype). Data are represented as mean + s.e.m. * indicates significant difference $p<0.05$; **** indicates $p<0.0001$ as assessed by Student's t-test in (F); and two-way ANOVA with Tukey's multiple comparison correction in (J,N). Scale bars: (D,E) 50 µm, (G-I) 100 µm, (K-M) 500 µm. Figure modified from (Vaswani et al. 2019).

To analyze mediolateral distribution of mDA neurons, sections at four different rostrocaudal levels were analyzed in each animal (**Figure 10)**. In agreement with previous studies, prominent differences were found in mediolateral distributions of TH$^+$ neurons in *Dab1* CKO and *Dab1*$^{-/-}$ brains in sections at the intermediate rostrocaudal levels of the mDA domain

(Bodea et al. 2014) (**Figure 9A, B;** for schematic of mDA rostrocaudal levels see **Figure 4D** in Introduction**;** for the four levels analyzed in this study refer to **Figure 10J-M** in Results). At intermediate rostrocaudal levels, in both the *Dab1* CKO and *Dab1*$^{-/-}$ mice, mDA neurons failed to reach lateral positions in the SN and settled in more medial locations (**Figure 9D-N**). To precisely quantify the mediolateral distribution of mDA neurons, normalized mediolateral bins were constructed, for each section analyzed, based on the midline and lateral-most TH^{+} neuron in that section. Yellow arrowheads in **Figure 9** indicate the lateral-most cells used for the construction of mediolateral bins (for more details, see materials and methods section 2.9.6). The fraction of TH^{+} mDA neurons in mediolateral bins of controls, *Dab1* CKO and *Dab1*$^{-/-}$ brains was measured and compared at E15.5, E18.5 and P21-30. At E15.5, only control and *Dab1* CKO animals were analyzed and significantly fewer TH^{+} cells were observed in the lateral bins of *Dab1* CKO brains compared to controls (**Figure 9D-F**). At E18.5 and P21-30, control, *Dab1* CKO and *Dab1*$^{-/-}$ animals were analyzed. In both *Dab1* CKO and *Dab1*$^{-/-}$ animals, a significant decrease in the fraction of TH^{+} cells in lateral bins and a corresponding increase in the fraction of cells in medial bins was detected. Interestingly, in both *Dab1* CKO and *Dab1*$^{-/-}$ brains at adult and embryonic stages, a few aberrantly located mDA neurons were found dorsal to the VTA, in the region of the red nucleus (**Figure 9H,I,L,M**).

A significant medial shift was observed in the distribution of TH^{+} neurons in *Dab1* CKO and *Dab1*$^{-/-}$ brains compared to controls (**Figure 9D-N**). This medial shift was in agreement with the previously reported data on *reeler, scrambler*, and *Dab1*$^{-/-}$ mice (Nishikawa et al. 2003; Kang et al. 2010; Bodea et al. 2014). The similarity in the mediolateral distribution of mDA neurons in *Dab1* CKO and *Dab1*$^{-/-}$ brains demonstrates that complete inactivation of *Dab1*, and the specific inactivation of *Dab1* in mDA neurons after E13.5, have a comparable effect on mDA neuron migration. These data imply that Reelin acts directly on SN-mDA neurons to regulate their lateral movement.

The analysis above describes mediolateral distribution of mDA neurons irrespective of anatomical definitions of SN and VTA, and was carried out for the intermediate rostrocaudal level, where the phenotype in the absence of DAB1 was the most severe. An additional quantification was carried out to assess the net reduction in the fraction of SN-mDA neurons and the corresponding net gain in the fraction of VTA-mDA neurons in *Dab1* CKO and *Dab1*$^{-/-}$ brains. In this analysis, anterior, intermediate and posterior rostrocaudal levels containing the SN and VTA subpopulations were analyzed at P30 (**Figure 10J-M**). The most rostral

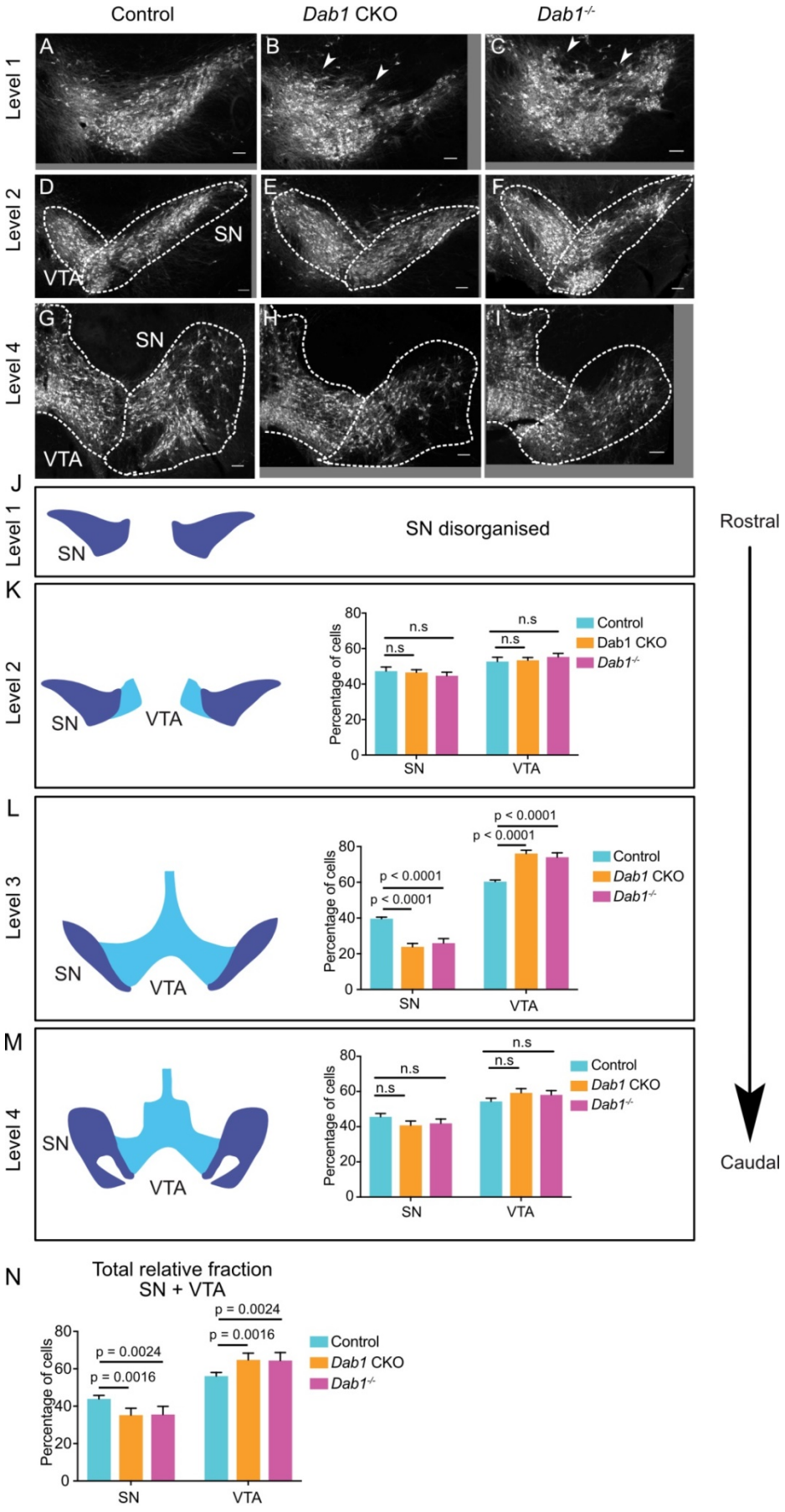

Figure legend on next page.

Figure 10. Characterization of mDA neuron distribution along the rostrocaudal axis in *Dab1* CKO and *Dab1*$^{-/-}$ brains. Immunostaining for TH. (A-C) Rostral sections (Level 1) in *Dab1* CKO and *Dab1*$^{-/-}$ brains, containing only SN-mDA neurons, show disorganization (arrowheads) compared to controls at P21-30. (D-F) Rostral sections (Level 2) containing SN and VTA-mDA neurons were analyzed in control (D), *Dab1* CKO (E) and *Dab1*$^{-/-}$ (F) brains but no significant difference was observed in the relative fractions of mDA neurons located in the SN or the VTA (K). (G-I, M) No significant difference was observed, in caudal sections (Level 4), in the relative fractions of mDA neurons located in the SN or the VTA. (J-M) Schematic representing the rostrocaudal levels analyzed, and results of the quantification of relative SN and VTA fractions at these levels. (L) Quantification of the relative fractions of mDA neurons located in the SN or the VTA at intermediate rostrocaudal levels (TH immunostaining shown in **Figure 9**) revealed a significant decrease in the SN and a corresponding increase in the region of the VTA ($p < 0.0001$, student's t-test) in both *Dab1* CKO and *Dab1*$^{-/-}$ brains compared to controls. (N) Even when all analyzed rostrocaudal levels were included and compared, *Dab1* CKO and *Dab1*$^{-/-}$ animals still showed a significant reduction in the relative fraction of mDA neurons located in the SN compared to controls (student's t-test, n = 5 animals/genotype for all levels). Scale bars: 100 µm. Figure modified from (Vaswani et al. 2019).

levels contained only the SN and were not analyzed in a quantitave manner, but it was noted that the SN seemed disorganized in *Dab1* CKO and *Dab1*$^{-/-}$ brains (**Figure 10A-C,J**). No difference was found in the relative fraction of SN and VTA-mDA neurons at anterior and posterior levels (**Figure 10D-K**). However, as described previously, intermediate rostrocaudal levels showed a significant decrease in mDA neurons in the SN, and their corresponding accumulation in the VTA, resulting in a net increase in VTA-mDA neurons at this level (**Figure 10L**). When all rostrocaudal levels analyzed were pooled and the total relative fraction of SN and VTA-mDA neurons was analyzed for the four levels combined, significant increase in the number of mDA neurons was observed in the VTA region and a corresponding decrease was measured in the SN region of *Dab1* CKO and *Dab1*$^{-/-}$ brains (**Figure 10N).**

Next, the number of TH^{+} neurons in the intermediate rostro-caudal sections analyzed from control, *Dab1* CKO and *Dab1*$^{-/-}$ brains was compared at E15.5, E18.5 and P21-30 (**Figure 11A-C**). As has been previously reported, no significant differences were found in the total number of TH^{+} cells in *Dab1* CKO and *Dab1*$^{-/-}$ brains at prenatal stages (E15.5 and E18.5) (Nishikawa et al. 2003) (**Figure 11A,B**). However, a significant decrease was observed in the total number of mDA neurons in *Dab1*$^{-/-}$ and *Dab1* CKO brains at P21-30 compared to their control counterparts suggesting that Reelin signaling or Dab1 might have additional functions in the maintenance and survival of mDA neurons during postnatal stages (**Figure 11C**).

Interestingly, this decrease in mDA neurons was even more severe in *Dab1*$^{-/-}$ brains at this stage than in *Dab1* CKO animals indicating that this effect might be partially indirect. However, as this is the first study to investigate the number of mDA neurons in the absence of Reelin signaling at adult stages (not only in *Dab1* CKO animals but also in *Dab1*$^{-/-}$ animals), further studies with inducible inactivation of Reelin signaling at later stages will be necessary to delineate the role of this pathway in postnatal mDA neuronal survival.

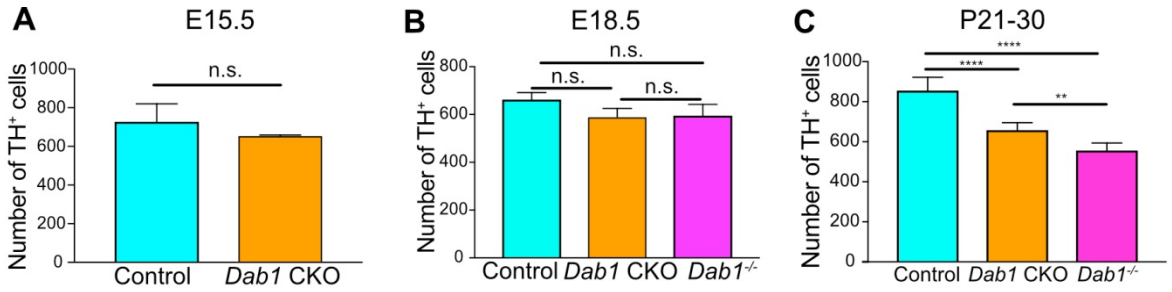

Figure 11. Quantification of total number of TH$^+$ mDA neurons in *Dab1* CKO and *Dab1*$^{-/-}$ mice. (A) No significant difference in total number of TH+ cells in control vs. *Dab1* CKO brains at E15.5 for n = 3 brains. (B) No significant difference in total number of TH+ cells in control, *Dab1* CKO and *Dab1 -/-* brains at E18.5 for n = 4 brains. (C) Control, *Dab1* CKO and *Dab1 -/-* brains (n = 6) are significantly different from each other in total number of TH+cells at P30. All data are represented as mean + s.e.m. **** $p < 0.0001$, ** $p < 0.01$ as assessed by one-way ANOVA.

4.3. Reelin protein is localized to the region of the developing ventrolateral midbrain at E13.5 and E14.5

Having established the direct role of Reelin signaling in the formation of the SN, the next question was where Reelin protein was distributed relative to mDA neurons during their tangential migration. Previous studies have shown localization of Reelin protein within the mDA domain, but only at E16 and later, by which time tangential migration is already complete (Sharaf et al. 2014). *Reelin* mRNA expression in the red nucleus has been previously shown in the ventral midbrain at E13.5, but Reelin protein distribution has not been investigated during the time window of tangential migration (before E15.5) (Nishikawa et al. 2003; Sharaf et al. 2014; Bodea et al. 2014). The distribution of Reelin protein relative to SN-mDA neurons would provide an important clue as to whether Reelin might function as a chemoattractant, chemorepellant or permissive factor in mDA lateral migration. Hence, the distribution of *Reelin* mRNA and Reelin protein was examined at E13.5 and E14.5. Immunostaining for Reelin and *in situ* hybridization for *Reelin* mRNA in the ventral midbrain revealed Reelin$^+$ cells in the red nucleus region dorsomedial to SN-mDA neurons (**Figure 11**). However, Reelin protein, but not *Reelin mRNA* was localized to lateral mDA domains in the E13.5 and E14.5 ventral midbrain (**Figure 12**), demonstrating that while mDA neurons do not themselves produce *Reelin* mRNA or protein, Reelin protein is localized extracellularly in lateral mDA domains.

Hence, secreted Reelin protein is appropriately distributed around DAB1$^+$ mDA neurons. This distribution is consistent with the direct role of Reelin in SN-mDA tangential migration. Furthermore, these data point to a permissive or promotive function of Reelin in SN-mDA tangential migration as the complex spatial relationship between possible Reelin sources and lateral mDA domains may preclude a simple chemoattractive/repulsive action.

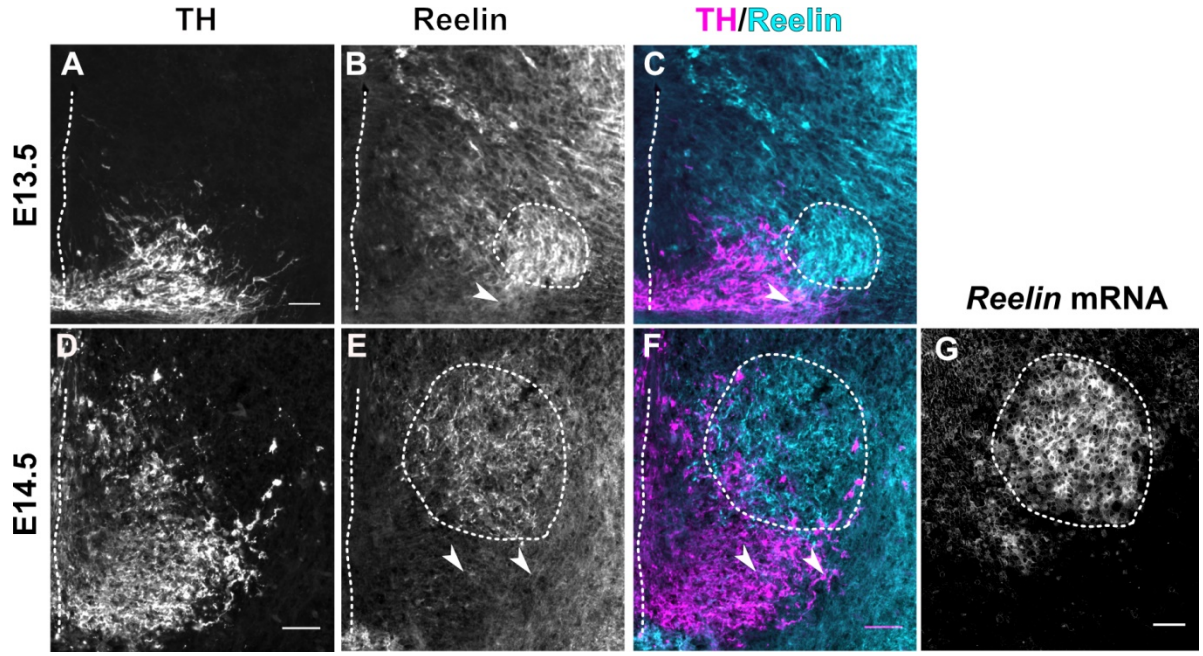

Figure 12. Localization of Reelin protein in the mDA domain at E13.4 and E14.5. (A-C) Immunostaining for TH (A) and Reelin (B) shows Reelin protein in the region of the red nucleus (RN, white dashed outline) and in the lateral TH$^+$ mDA domain (white arrowhead) at E13.5. (D-G) Double immunolabeling for TH (D) and Reelin (F) and RNA in situ hybridization for *Reelin* mRNA (G) at E14.5 show that *Reelin* mRNA and Reelin protein are strongly expressed in the RN. Reelin protein is also localized ventral and lateral to the RN, overlapping with the lateral mDA domain (white arrowheads). The brightfield image of *Reelin* mRNA was inverted and false colored to obtain the image shown in (G). Dashed lines indicate the ventral midline. Scale bar: 50 µm. Figure modified from (Vaswani et al. 2019).

4.4. Reelin signaling aids in the segregation of SN-mDA neurons from VTA-mDA neurons

Given that DAB1$^+$ SN-mDA neurons directly respond to extracellular Reelin to take up lateral positions, the next question was whether Reelin signaling is important for the segregation of SN- and VTA-mDA neurons into separate clusters. To answer this question, several established markers preferentially expressed in SN-mDA or VTA-mDA neurons were used, and the extent of separation or segregation between these subpopulations was analyzed in controls and *Dab1* CKO brains.

SN-mDA neurons preferentially express the transcription factor SOX6 (sex determining region Y-box6), the potassium channel GIRK2 (G-protein-regulated inward-rectifier potassium channel 2) and the Lim domain protein LMO3 (LIM domain only protein 3) (La Manno et al. 2016; Bifsha, Balsalobre, and Drouin 2017). VTA-mDA neurons preferentially express the transcription factor OTX2 (Orthodenticle homeobox 2) and Calbindin (Panman et al. 2014; Poulin et al. 2014; Di Salvio et al. 2010).

It has been previously shown that mDA neurons expressing the potassium channel GIRK2 are shifted medially in *Dab1*$^{-/-}$ mice, while VTA-mDA neurons expressing Calbindin are correctly localized (Bodea et al. 2014). Comparison of the mediolateral position of TH$^+$, GIRK2$^+$

cells in control and *Dab1* CKO brains at P30 showed that, similar to studies analyzing *Dab1*$^{-/-}$ mice, the GIRK2^{+} SN-mDA subpopulation showed a significant shift to more medial positions in the *Dab1* CKO mice (**Figure 13**). These results further confirm that the *Dab1* CKO phenotype recapitulates the *Dab1*$^{-/-}$ phenotype, not just in the distribution of TH^{+} neurons, but also in the distribution of the TH^{+}, GIRK2^{+} subpopulation of mDA neurons.

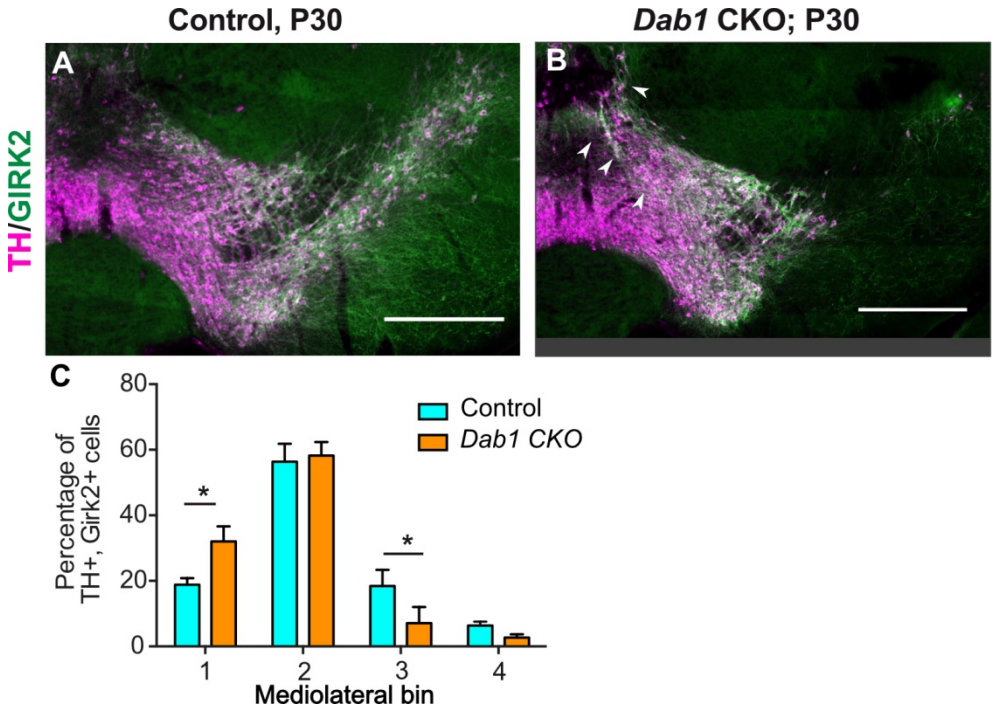

Figure 13. (A-C) Immunostaining for TH and GIRK2 in P30 *Dab1* CKO mice. White arrowheads show increased medial accumulation of TH^{+}, Girk2^{+} cells in *Dab1* CKO (B) compared to control littermates (A). (C) Quantification of mediolateral distribution of TH^{+}, Girk2^{+} cells reveals that these cells are shifted medially in *Dab1* CKO brains compared to controls. * indicates $p<0.05$ as assessed by student's t-test corrected for multiple comparisons (Holm-Sidak method) for n=3 brains/genotype. Scale bars: 200 µm. Figure modified from (Vaswani et al. 2019).

While GIRK2 and Calbindin are established markers known to be predominantly expressed by SN and VTA-mDA neurons respectively, recent studies have reported additional, more specific SN- and VTA markers (described above, and in Introduction section 1.5.2). Hence, the analysis was extended to include mediolateral distribution of TH^{+} cells expressing either SOX6 or LMO3 (SN-mDA neuronal markers) and TH^{+} cells expressing OTX2 (as a marker for VTA-mDA neurons). In E18.5 control brains, TH^{+}, OTX2^{+} cells and TH^{+}, SOX6^{+} cells were clearly separated at the SN/lateral VTA boundary (**Figure 14A,C**). However, in *Dab1* CKO mice, TH^{+}, SOX6^{+} cells were intermingled with TH^{+}, OTX2^{+} cells, and a clear demarcation of SN and VTA domains based on these two markers was not observed (**Figure 14B,D**).

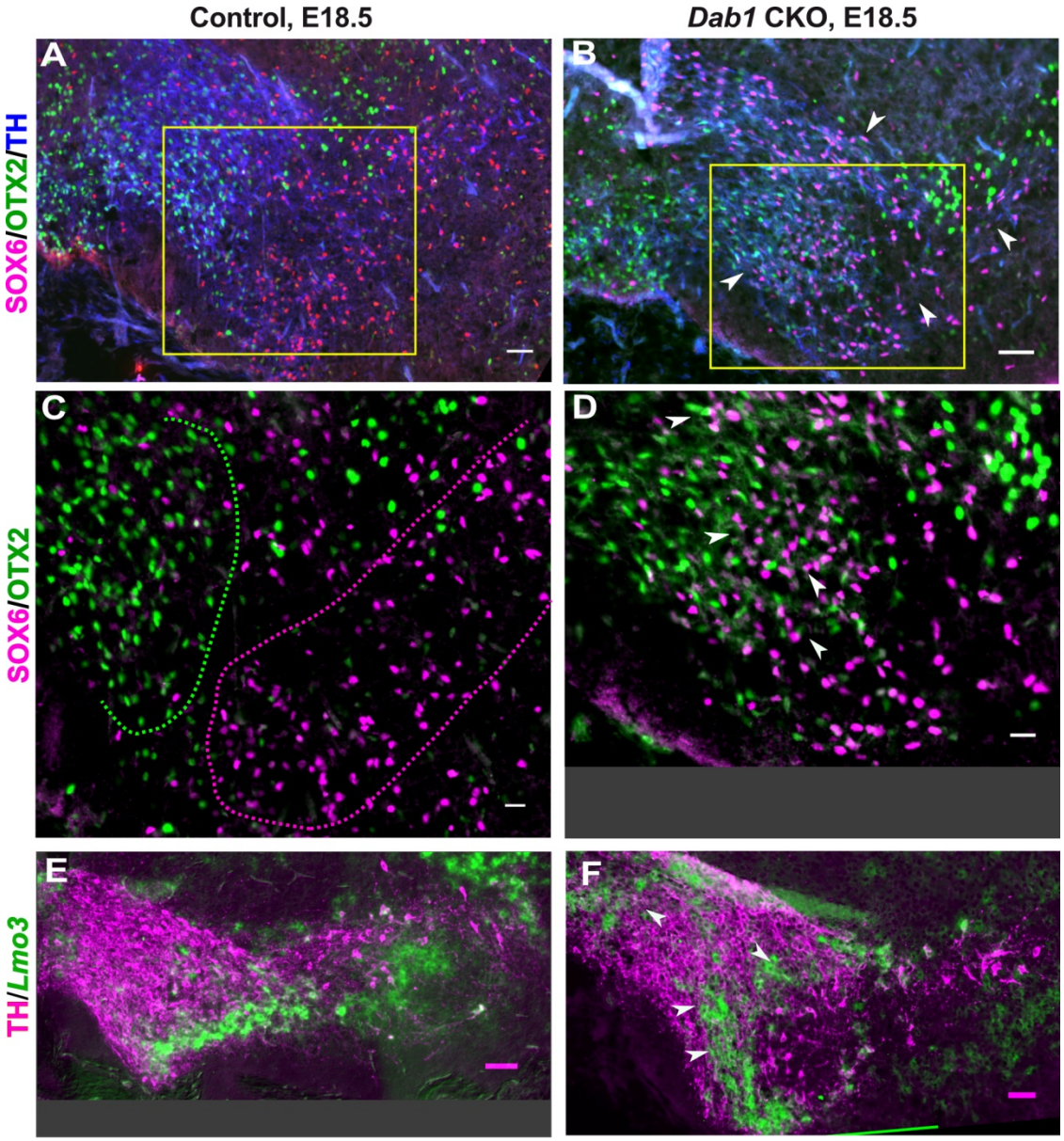

Figure 14. (A,B) Triple immunostaining for SOX6 (magenta), OTX2 (green) and TH (blue) on control and *Dab1* CKO brains at E18.5 reveals altered distribution of TH$^+$, SOX6$^+$ cells in *Dab1* CKO mice (White arrowheads in B). (C,D) Higher zoom of TH$^+$ lateral VTA region indicated by yellow boxes in D and E. In controls, SOX6$^+$ cells (dashed magenta line) and OTX2$^+$ cells (dashed green line) are largely localized to separate regions (C). In *Dab1* CKO mice, SOX6$^+$ cells accumulate medially and are partially intermingled with OTX2$^+$ cells (white arrowheads) (D). (E,F) Immunostaining for TH and RNA in situ hybridyzation for *Lmo3* shows ectopic medial localization of TH$^+$, *Lmo3*$^+$ cells in *Dab1* CKO mice (white arrowheads in I). Brighfield image of *in situ* hybridization signal for *Lmo3* mRNA was inverted and then false-colored in green. Cells in which *Lmo3* was detected show weak TH immunostaining as the strong RNA in situ hybridization signal interferes with antibody binding. Scale bars:, (A,B,E,F) 50 µm, (C,D) 25 µm. Figure modified from (Vaswani et al. 2019).

Similar to TH$^+$, SOX6$^+$ cells, the TH$^+$, *Lmo3*$^+$ subpopulation was shifted towards medial regions in *Dab1* CKO compared to controls and was partially intermingled with non-*Lmo3* TH$^+$ neurons (**Figure 14E,F)**. Based on these results, Reelin signaling seems to aid in the segregation of SN-mDA neurons from VTA-mDA neurons. Inactivation of Reelin signaling in mDA neurons results in an ectopic medial location of SN-mDA neurons, and an intermingling

of SN-mDA neurons with VTA-mDA neurons as assessed by OTX2, SOX6 and *Lmo3* markers. Thus, the direct role of Reelin in SN formation, extracellular Reelin localization in the SN, and the contribution of Reelin to the separation of SN-mDA neurons from VTA-mDA neurons have been clarified by these results. The next few sections focus on the question of how Reelin regulates the cell behavior of tangentially migrating SN-mDA neurons during development.

4.5. Visualizing and tracking mDA neuronal migration with 3D time-lapse, two-photon excitation microscopy

To understand Reelin regulation of mDA migratory behavior and accompanying morphology, it was essential to visualize mDA tangential migration and the underlying morphological changes in the presence and absence of Reelin signaling. The first step in this process was to mosaically (or sparsely) label tangentially migrating SN-mDA neurons so that their migratory and morphological characteristics could be visualized. For this purpose, a previously established genetic inducible fate-mapping system under the control of the *Shh* promoter was used.

A brief explanation of the fate-mapping system used in this study is given here (more details in Introduction section 1.5.2): Mice with the *CreER* (Cre- estrogen receptor) sequence inserted into the *Shh* locus ($Shh^{CreER/+}$) (Harfe et al. 2004) were crossed with the YFP-expressing reporter mouse line described in section 3.1 ($Rosa26^{lox\text{-}stop\text{-}lox\text{-}YFP}$) (Srinivas et al. 2001)(**Figure 15A**). The CreER fusion protein can bind tamoxifen (TM), translocate to the nucleus and excise the STOP codon to induce YFP expression. In the neurogenic ventral midbrain floor plate, SHH is expressed by mDA progenitors starting at E8.5. Furthermore, using the same inducible Cre-LoxP system described here, it has been shown that the *Shh*-expressing progenitor domain at E8.5 gives rise predominantly to SN-mDA neurons (Blaess et al. 2011; Bodea et al. 2014). Hence, by administering TM at E8.5, mosaic labeling of predominantly SN-mDA neurons can be achieved (**Figure 15A**). At E13.5, 70% of YFP-expressing cells in the lateral mDA domain are TH^+, by E14.5, almost 90% of YFP-expressing cells of the lateral mDA domain are TH^+ neurons (Bodea et al. 2014).

In this study, this method of preferentially labeling SN-mDA neurons was used either on a control background ($Shh^{CreER/+}$, $Rosa26^{lox\text{-}stop\text{-}lox\text{-}YFP/+}$, $Dab^{+/+}$ or $Shh^{CreER/+}$, $Rosa26^{lox\text{-}stop\text{-}lox\text{-}YFP/+}$, $Dab1^{-/+}$) or on a $Dab1^{-/-}$ background ($Shh^{CreER/+}$, $Rosa26^{lox\text{-}stop\text{-}lox\text{-}YFP/+}$, $Dab1^{-/-}$) to visualize mDA migration in presence and absence of Reelin signaling (**Figure 15A,B**). Next, as the migratory behavior of mDA neurons has not yet been characterized in detail on a wildtype background, an imaging and semi-automated analysis pipeline was established to observe and characterize migrating mDA neurons with high spatial resolution. Organotypic slice cultures of E13.5

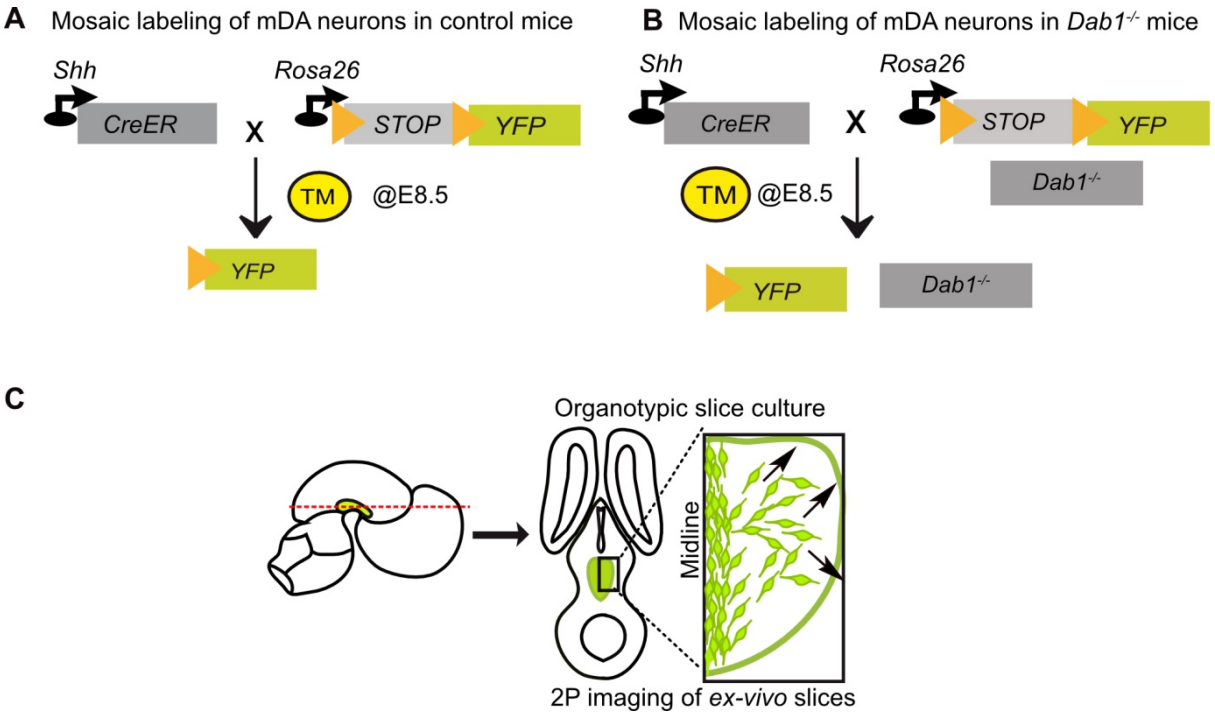

Figure 15. Visualizing mDA neuronal migration in the presence and absence of Reelin signaling. (A,B) Schematic of the inducible genetic fate mapping system used to mosaically label mDA neurons by administering tamoxifen (TM) at E8.5 in control (A) and *Dab1*$^{-/-}$ mice (B). Shh: Sonic Hedgehog; YFP: yellow fluorescent protein. CreER: gene encoding a CRE-Estrogen Receptor fusion protein. (C) Schematic of horizontal organotypic slice culture preparations in mosaically labelled E13.5 control and *Dab1*$^{-/-}$ brains. Green regions represent location of mDA neurons in the embryonic brains (left) and in horizontal slices (right). Red dashed line indicates dorsoventral level of slices. Black arrows indicate direction of tangential mDA migration. Figure modified from (Vaswani et al. 2019).

embryonic brains with sparsely labeled mDA neurons were prepared (Bodea and Blaess 2012; Bodea et al. 2014) and a two-photon imaging system was used to acquire 3D volume images of slices every 10 minutes (**Figure 15C**).

4.6. Speed profiles of migrating mDA neurons reveal large variations in migratory behavior of individual neurons over time, and significant differences across neurons in the population

The experiment and analysis described here was carried out on control and *Dab1*$^{-/-}$ embryonic slices. To characterize the whole range of migratory behaviors observed within a limited interval of imaging (2.6-4.33 hrs), soma positions of a large number of neurons (806 neurons from 3 control slices, 844 neurons from 3 *Dab1*$^{-/-}$ slices) were tracked semi-automatically. Differences in soma positions in consecutive volume images were used to calculate speed and trajectories of these neurons at every time-point of the analysis (**Figure 16A-C**). For every tracked mDA neuron, the following speed parameters were determined: (1) the instantaneous speed of the neuron, defined as the speed at a given time-point of imaging (obtained by measuring the change in position of the soma from the previous time-point). (2) The average speed of the neuron, defined as the arithmetic mean of instantaneous speed over

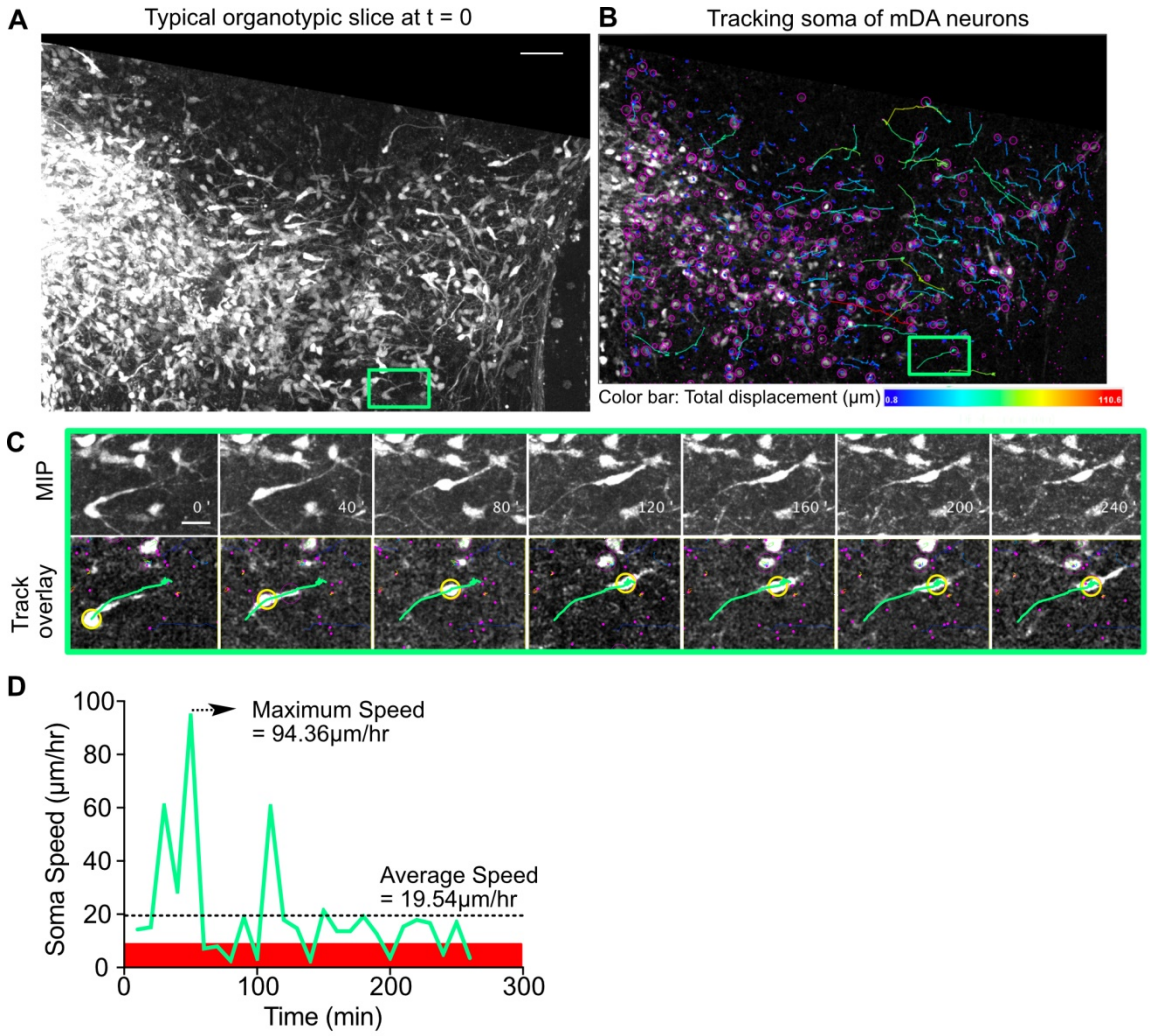

Figure 16. Speed and trajectory analysis of tangentially migrating mDA neurons. (A) Maximum intensity projection of image of a control slice at t = 0. Bright green rectangle indicates location of cell shown in (C). (B) Trajectories of tracked neurons in slice shown in (A) after imaging for 270 min. Trajectory in bright green represents trajectory of neuron in (C). (C) Maximum intensity projection frames at various time-points of imaging show soma and processes of a tangentially migrating cell. Track overlay frames show the position of the soma (yellow circle) and trajectory of the cell (green line) analyzed with the semi-automated tracking plugin TrackMate in Fiji. Magenta dots and circles indicate soma positions of neighboring tracked cells at different z-levels. (D) Speed profile of cell marked by orange circle in (C) shows large variations in speed over time, with a maximum speed (dashed arrow) that is much higher than the average speed (dashed horizontal line). Rest phase (soma speed less than 10 µm/hr) is indicated in red. Scale bars: (A) 50 µm, (C) 20 µm. Figure modified from (Vaswani et al. 2019).

all time-points of imaging. (3) Maximum (max.) speed of the neuron, defined as the maximum observed instantaneous speed during the imaging time window (**Figure 16D**).To confirm that migratory behavior was not significantly different across individual slices of the same genotype (control or *Dab1*$^{-/-}$), the average speed of all cells from each slice were separately plotted. Comparing these distributions across individual control and *Dab1*$^{-/-}$ slices, the distribution of average speeds was not significantly different between slices of the same genotype (**Figure 17A,B**).

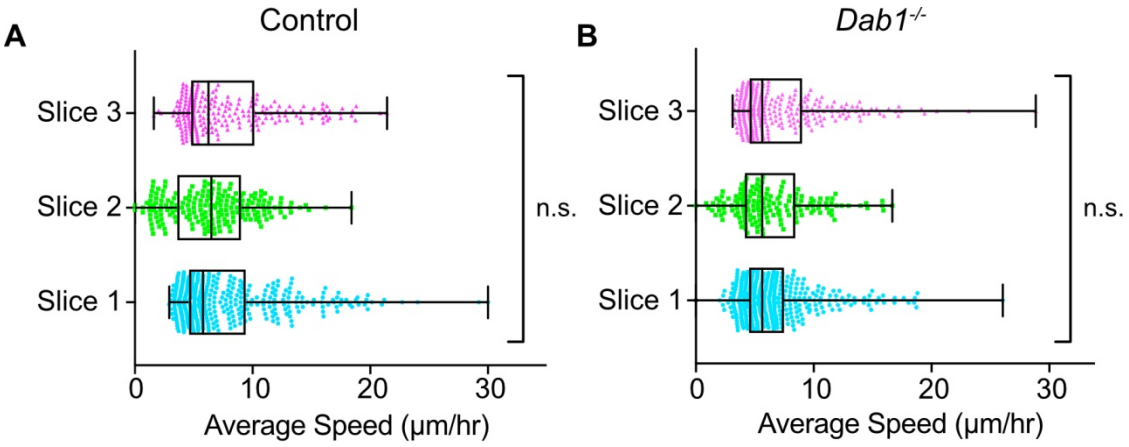

Figure 17. Average speed distributions of SN-mDA neurons. (A) Average speed distributions across 3 control slices are not significantly different (p = 0.1065, Kruskal-Wallis test for non-parametric distributions). Each dot represents an individual tracked mDA neuron's average speed. Box plots represent distribution of average speeds in each slice (C) Average speed distributions across the 3 *Dab1*$^{-/-}$ slices analyzed are not significantly different (p = 0.2279, Kruskal-Wallis test for non-parametric distributions). Figure modified from (Vaswani et al. 2019).

However, individual cells' soma speeds varied considerably over time, and the maximum observed soma speed (henceforth max. speed) of a cell could be several times greater than its average speed. The variation in instantaneous soma speed was not reflected always by the average speed of a neuron, as high speeds when attained in only a few frames did not significantly raise the average speed. Hence, **Figure 18** ranks all control (**Figure 18A**) and *Dab1*$^{-/-}$ (**Figure 18B**) cells by their max. speeds, and reveals great diversity in max. speeds, average speeds and standard deviation of instantaneous speed around the average speed in the two populations.

4.7. Absence of Reelin signaling results in a decrease in the maximum observed speed of mDA neurons

Due to the diversity in migratory behavior within the large control and *Dab1*$^{-/-}$ populations, both average and max. speed distributions of the two populations were compared. The average speeds' distribution for the *Dab1*$^{-/-}$ mDA neurons was not significantly different from the average speed distribution of the control neurons (**Figure 19A**).

However, comparing the max. speed distributions of the two populations revealed a significant shift in the *Dab1*$^{-/-}$ population towards lower max. speeds (**Figure 19B**). Control max. speeds ranged from 0 to 183 μm/hr, with a median max. speed of 23.6 μm/hr (25th percentile = 12.4 μm/hr, 75th percentile = 48.1 μm/hr, n = 806 control cells). In the *Dab1*$^{-/-}$ population, max. speeds varied from 0 to 133.7 μm/hr, with a median max. speed of 15 μm/hr (25th percentile = 10.1 μm/hr, 75th percentile = 29.8 μm/hr, n = 844 *Dab1*$^{-/-}$ cells) (**Figure 19B**). Based on this data, Reelin signaling promotes higher max. speeds in migrating mDA neurons. In the absence

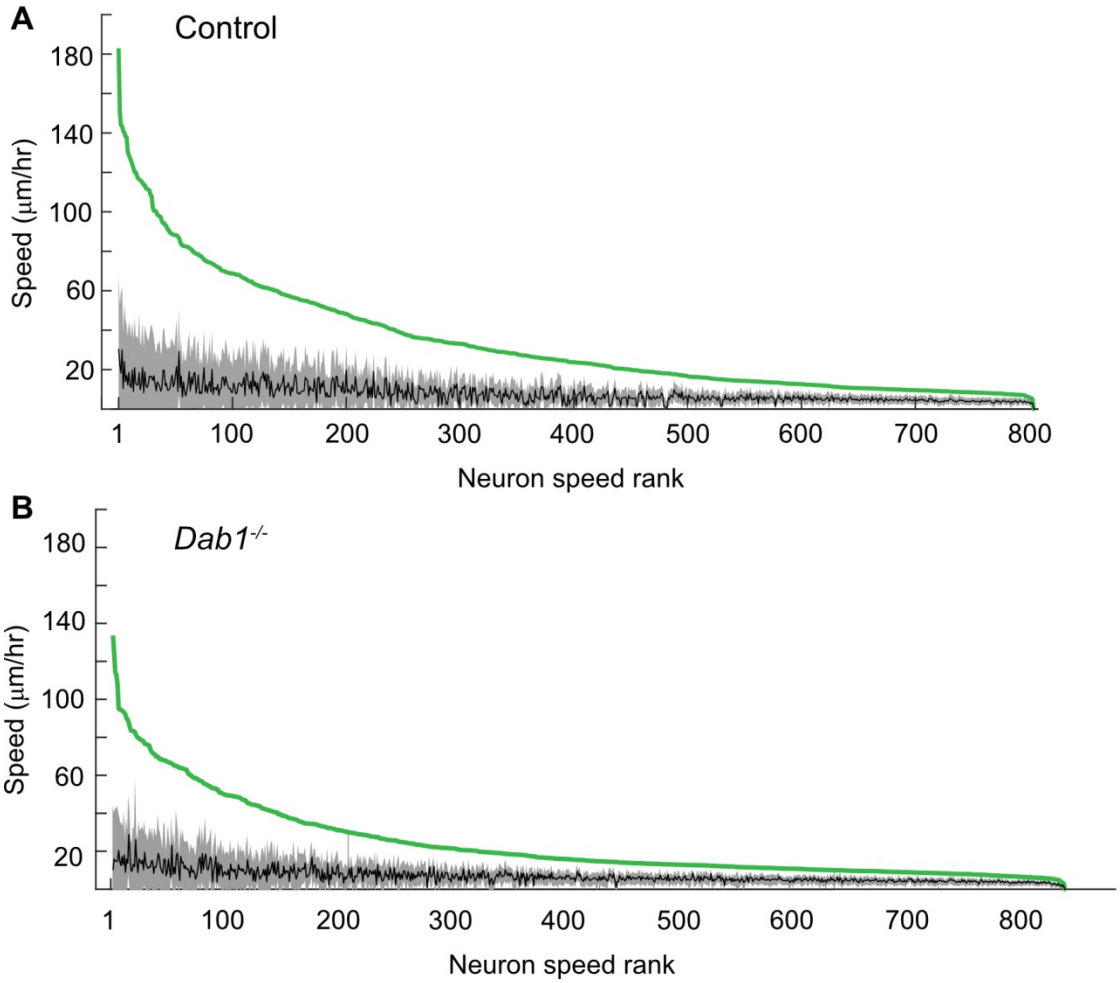

Figure 18. Variation in speed profiles across mDA neurons. (A,B) To demonstrate the extent of max. speed variation in control and *Dab1*$^{-/-}$ mDA neurons from their average speeds, each neuron in the dataset was ranked by its max. speed (green curve for the population; each neuron forms one point on the curve, rank of each neuron according to max. speed is shown on the x-axis). For each neuron, the average and standard deviation around the mean were also plotted. Grey and black curves represent variation of soma speed (grey) around average soma speed (black) for each mDA neuron in the dataset ranked according to their max. speeds. Figure modified from (Vaswani et al. 2019).

of Reelin signaling, max. speeds of mDA neurons are, at the population level, lower than the max. speeds observed in control mDA neurons. To understand how exactly the absence of Reelin signaling affects mDA migration, it was necessary to understand whether the shift towards lower max. speeds in *Dab1*$^{-/-}$ SN-mDA neurons was accompanied by other changes in migratory behavior or cell morphology. The alternative would be that *Dab1*$^{-/-}$ neurons simply displayed lower max. speeds while maintaining the same migratory, directional and morphological characteristics as control mDA neurons. Because max. speeds varied considerably within and between control and *Dab1*$^{-/-}$ populations, mDA neurons were grouped based on their max. speeds. Instantaneous migratory speed, direction and cell morphology of control and *Dab1*$^{-/-}$ mDA neurons with similar max-speeds were then compared.

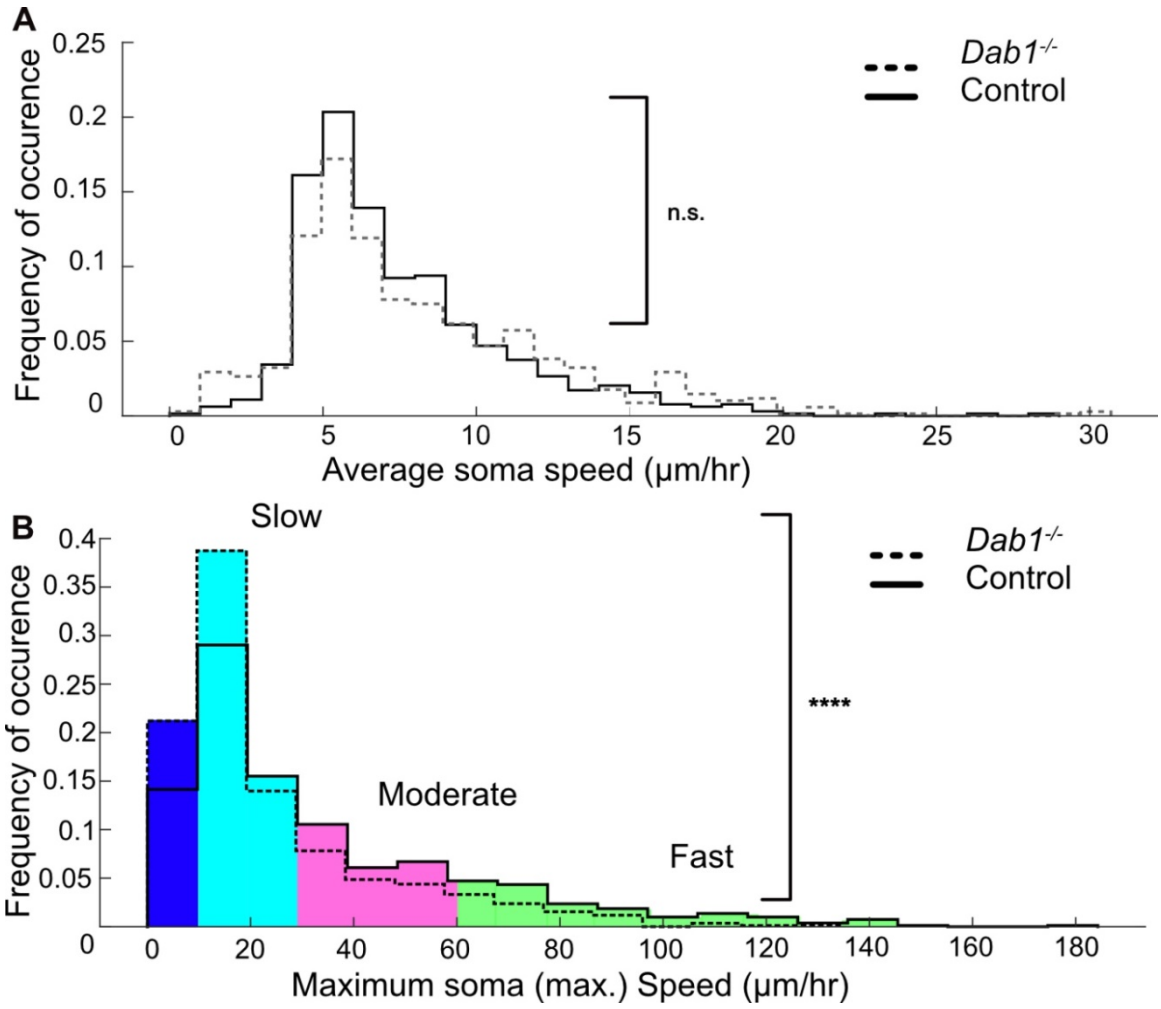

Figure 19. Comparison of average and max. speeds of control and *Dab1*$^{-/-}$ populations. (A) The frequency distribution of average speeds for the entire population of tracked control and *Dab1*$^{-/-}$ mDA neurons. The frequency of occurrence of average speeds of mDA neurons is plotted against the range of observed average speeds. Meidan of the frequency distribution of average soma speeds of mDA neurons is not significantly altered in *Dab1*$^{-/-}$ slices compared to controls. Note that distributions of control (solid black line) and *Dab1*$^{-/-}$ mDA neurons (dashed black line) were compared ($p = 0.0657$, Mann-Whitney's test, n = 806 control, 844 *Dab1*$^{-/-}$ mDA neurons). (B) The same analysis as shown (A) was carried out for the frequency of occurence of max. speeds in the two populations. At the population level (distributions were compared), *Dab1*$^{-/-}$ mDA neurons' max-speeds are shifted significantly towards slower max. speeds compared to controls ($p < 0.0001$, Mann-Whitney's test, n = 806 control, 844 *Dab1*$^{-/-}$ mDA neurons). Non-migratory (max-speed 0-10 μm/hr), slow (30-10 μm/hr), moderate (60-30 μm/hr) and fast cells (> 60μm/hr) are indicated by dark blue, bright blue, magneta and bright green background colors, respectively. Figure modified from (Vaswani et al. 2019).

To divide control and *Dab1*$^{-/-}$ populations, we defined four groups based on the lower (10 μm/hr) and upper quartiles (30 μm/hr) of the *Dab1*$^{-/-}$ max. speed distribution. Based on this arbitrary but helpful criterion, control and *Dab1*$^{-/-}$ neurons were divided into four groups based on their max. speeds as: non-migratory cells with max. speeds of less than 10 μm/hr (control = 126/806, *Dab1*$^{-/-}$ = 205/844), 'slow' cells with max. speeds from 10-30 μm/hr (control = 355/806, *Dab1*$^{-/-}$ = 430/844), 'moderate' cells with max. speeds from 30-60 μm/hr (control = 186/806, *Dab1*$^{-/-}$ = 139/844) and 'fast' cells with max. speeds > 60 μm/hr, control = 139/806,

Dab1$^{-/-}$ = 70/844) (**Figure 19B**). Non-migratory cells (max. speed < 10 µm/hr), were those cells that failed to move more than 1.7 µm in any two consecutive frames of analysis and hence were not included into the further analysis. Based on this division, in the absence of Reelin signaling, the predominance of non-migratory and slow groups of cells was increased in *Dab1*$^{-/-}$ slices, while the proportion of moderate and fast cells was decreased (**Figure 19B**).

4.8. mDA neurons display two distinct migratory modes: a default slow, non-directed mode and an infrequent, fast, directed mode promoted by Reelin signaling

The observation that the proportion of mDA neurons displaying fast max. speeds was decreased in *Dab1*$^{-/-}$ population, while average speeds of mDA neurons in control and *Dab1*$^{-/-}$ populations were not significantly different suggested that max. speeds were only attained by cells during a small fraction of the total imaging time and hence did not contribute heavily to the average speed over all time-points. **Figure 20** displays, in the form of a heat map, instantaneous soma speeds of 20 fast, moderate and slow control mDA neurons, and further suggests that low soma speeds are more likely than high soma speeds.

To confirm this hypothesis, it was necessary to measure the fraction of overall imaging time spent by cells of control and *Dab1*$^{-/-}$ populations in fast or slow migratory modes. The same criterion used to define max. speed groups in the previous section was applied to the instantaneous soma speed of individual mDA neurons. Based on their instantaneous soma speeds at any given point of time, mDA neurons were defined as being in ‘rest’ (< 10 µm/hr) ‘slow’ (10-30 µm/hr), ‘moderate’ (30-60 µm/hr) or ‘fast’ (> 60 µm/hr) migratory phases.

In control and *Dab1*$^{-/-}$ slices, ‘fast’ and ‘moderate’ migratory phases were achieved by ‘fast’ and ‘moderate’ cells in only a few frames (**Figure 21A,B**). In control and *Dab1*$^{-/-}$ ‘fast’, ‘moderate’ and ‘slow’ mDA neurons, a predominant fraction of time was spent in ‘rest’ and ‘slow’ migratory phase and these two phases accounted for more than 80% of all measured soma speeds (**Figure 21A-C**).

Furthermore, the amount of time spent by SN-mDA neurons of the same max. speed group in the rest phase or in the respective migratory phases was comparable between individual cells in control and *Dab1*$^{-/-}$ slices. These results demonstrate that migratory phases of mDA neurons are rare and interrupt longer periods of rest (**Figure 20**).

Hence SN-mDA tangential migration occurs in distinct migratory modes: a frequent, slow phase, seen in all migrating SN-mDA neurons, and an infrequent moderate-to-fast phase that is observed only in a subset of SN-mDA neurons. The data also show that Reelin signaling increases the proportion of migratory mDA neurons displaying moderate and fast migratory behaviors. As moderate and fast migratory phases are only attained in very few frames in our experiments, the average speed distribution of SN-mDA neurons are not changed in *Dab1*$^{-/-}$ compared to control slices.

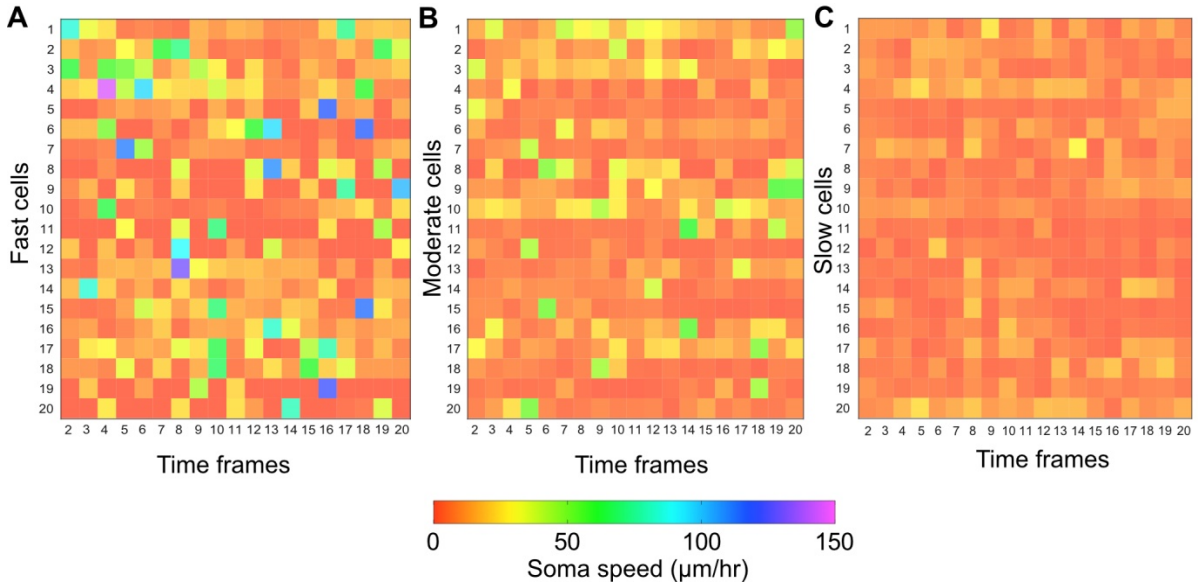

Figure 20. Variation in instantaneous soma speed of mDA neurons. (A-C) Instantaneous soma speeds of 20 fast, moderate or slow cells in control slices depicted as a heat map across 20 consecutive time frames. Each row represents one cell in the heat-map, each column is a time frame. Soma speeds range from 0 – 150 µm/hr for the 60 mDA neurons in this dataset. Figure modified from (Vaswani et al. 2018).

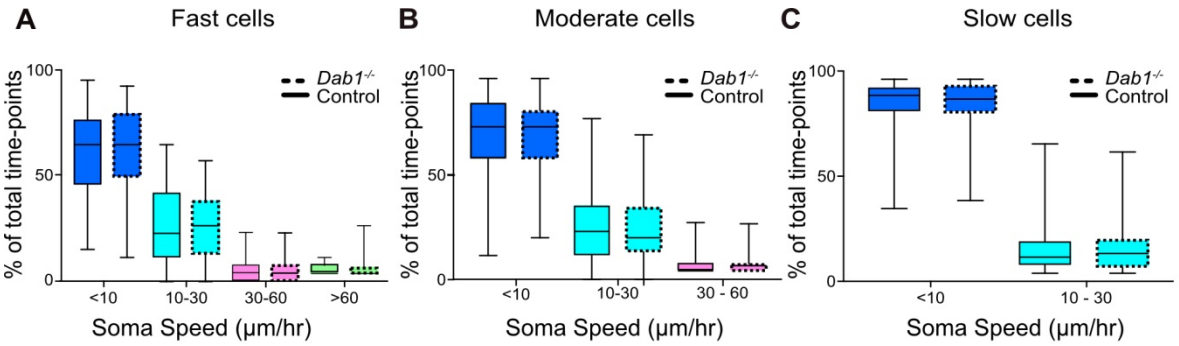

Figure 21. mDA neurons spend a majority of time frames at rest or in slow migration. (A) Fast cells in both control and *Dab1*$^{-/-}$ slices spend more than 60% of observed time-points at rest, but only 5% in fast migration. (B) Moderate cells also spend most of their time at rest or in slow migration. (C) Slow cells spend most of their time at rest. Importantly, the percentage of total observed time-points in rest (dark-blue), slow (cyan), moderate (magenta) and fast (green) soma-speeds are similar for fast (A), moderate (B) and slow (C) cells in control and *Dab1*$^{-/-}$ slices. Figure modified from (Vaswani et al. 2019).

Given that fast and moderate phases were only observed infrequently and in a subset of mDA neurons, it was necessary to assess the contribution of these rare migratory events to their net migratory displacement and directionality. For this purpose, the total displacements of slow, moderate and fast mDA neurons from control and *Dab1*$^{-/-}$ slices were measured. Total displacement was defined as the 3D displacement between the initial and final positions of a neuron. In control and *Dab1*$^{-/-}$ slices, total displacement increased with increasing max. speeds (**Figure 22A,B**). When grouped into slow, moderate and fast cell groups, average total

displacement was greatest in fast cells, and moderate cells had greater total displacement than slow cells, which showed the least average total displacement (**Figure 22C,D**). This result was true in both control and *Dab1*$^{-/-}$ populations (**Figure 22A-D**). These data indicate that infrequent moderate and fast phases of migration significantly increase the total migratory displacement of mDA neurons.

Next, we assessed the correlation between max. speed and directionality of mDA neurons. Directionality is defined as the ratio of total displacement to path length (the sum of the distance travelled by a neuron over all time-points) and measures the frequency of direction change during migration (Petrie, Doyle, and Yamada 2009). A high value of directionality (maximum value = 1) indicates almost no change in migratory direction while low values indicate frequent changes in direction. Similar to total displacement, in both control and *Dab1*$^{-/-}$ mDA neurons, directionality increased with increasing max. speeds.

The average directionality of fast cells was significantly higher than that of moderate and slow cells (**Figure 23A-D**). Slow cells showed the least directionality, demonstrating that they were more likely to make frequent changes in direction. Having demonstrated that infrequent, fast, directed migratory phases are promoted by Reelin, the next question was to analyze the extent to which these directed movements contributed to the lateral, tangential migration required for SN formation.

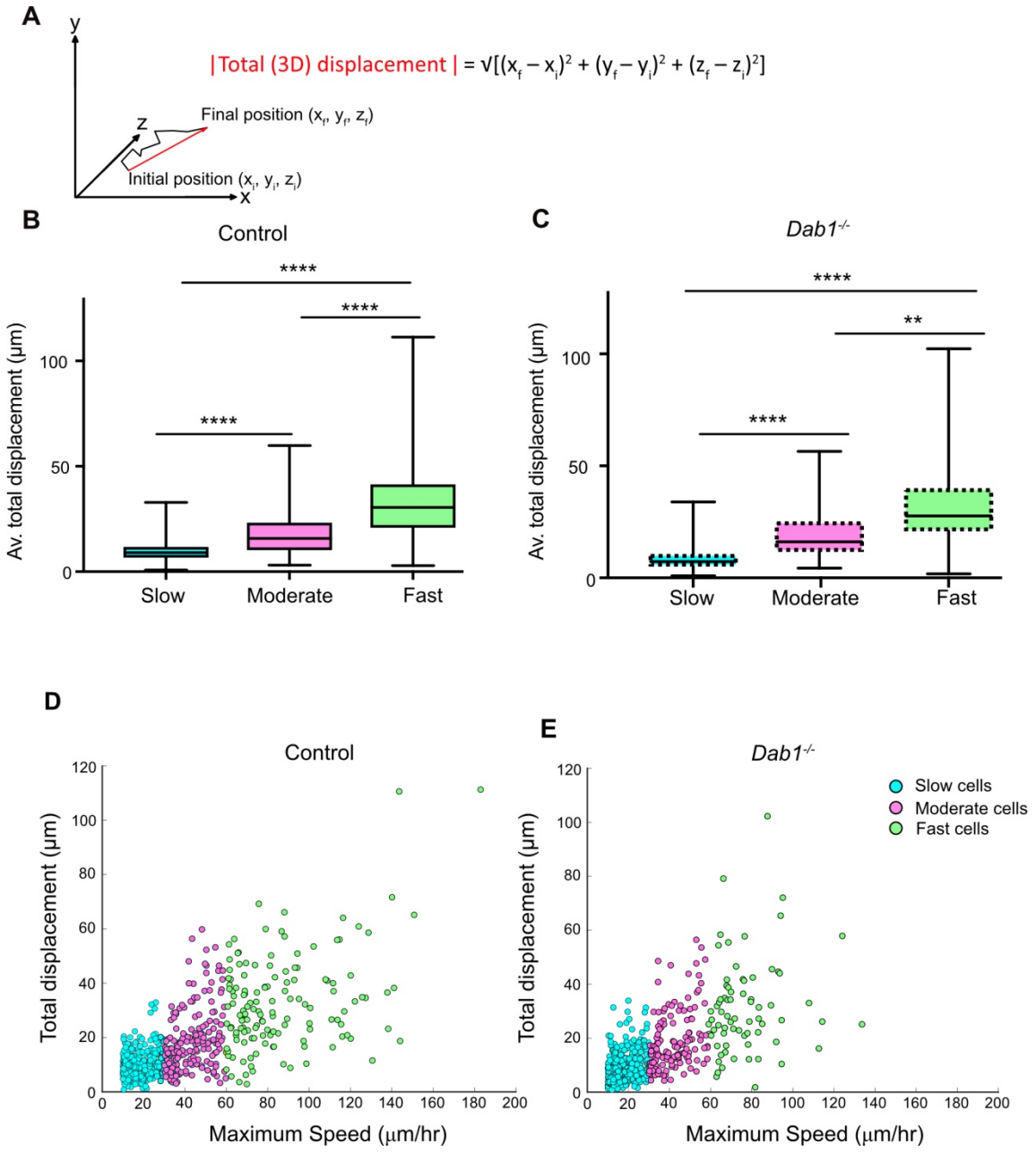

Figure 22. Total displacement is correlated to max. speeds of mDA neurons. (A) Schematic explaining the definition of total (3D) displacement of a neuron (arrow in red). (B,C) Average total displacement (in 3D) of mDA neurons displaying slow migration only (Slow cells, cyan) is significantly lesser than that of moderate cells (magenta) in both control (B) and *Dab1*$^{-/-}$ slices (C). Similarly, fast cells (green) display the greatest average total displacement in both control (B) and *Dab1*$^{-/-}$ slices (C). **** indicates $p < 0.0001$, ** indicates $p < 0.01$ as measured by Kruskal Walis test. (D,E) Total displacement of individual cells plotted against their max. speeds. Each circle represents an mDA neuron belonging to slow (cyan), moderate (magenta) or fast (green) groups. Figure modified from (Vaswani et al. 2019).

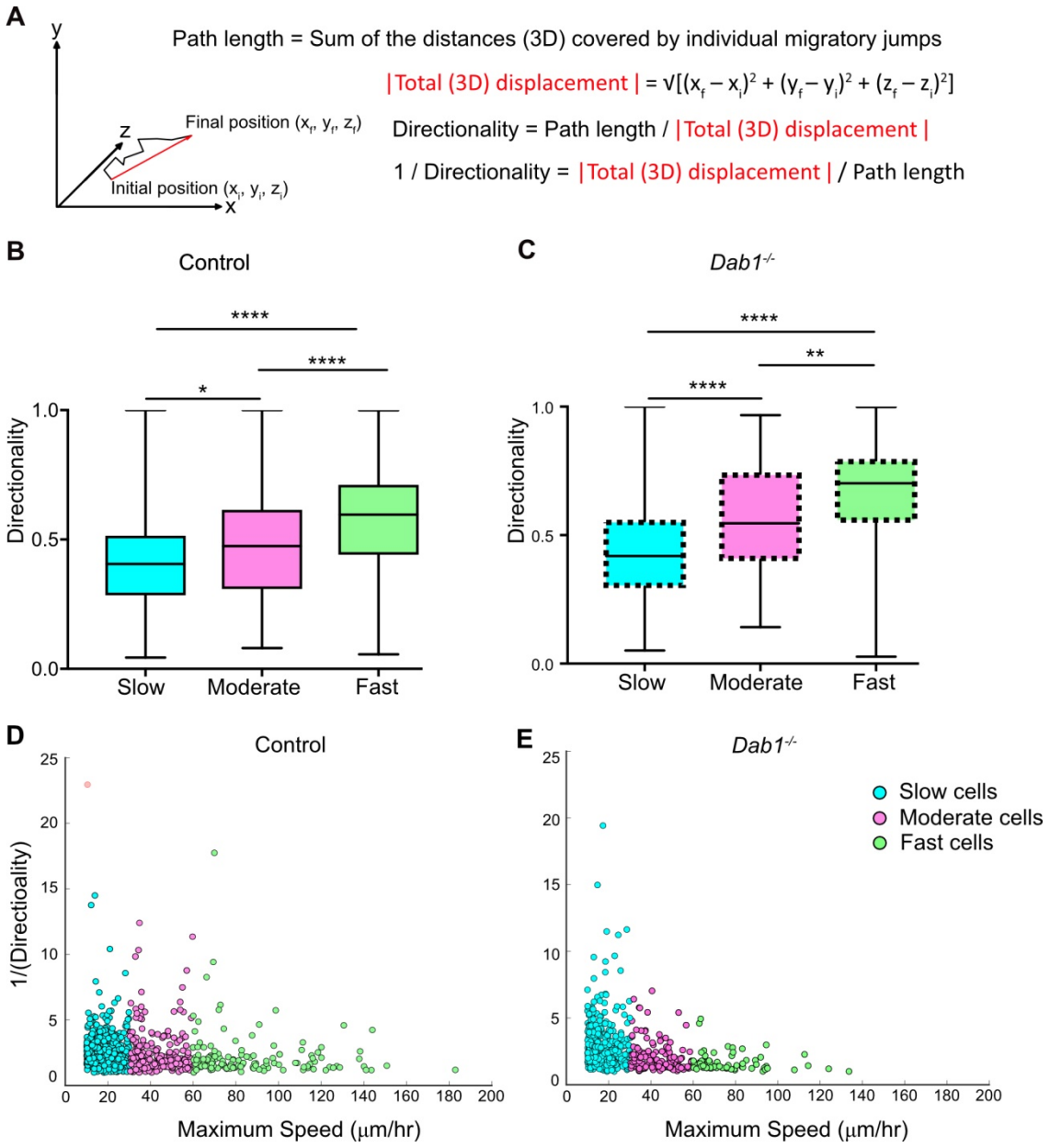

Figure 23. Individual fast, moderate and slow mDA neurons from *Dab1*$^{-/-}$ slices have similar directionality profiles to mDA neurons in control slices. (A) Schematic describes the definition of directionality. (B,C) Average directionality of slow mDA neurons (cyan bars) is lower than the average directionality of moderate mDA neurons (magenta bars), which in turn is lower than fast mDA neurons (green bars) in both control (B) and *Dab1*$^{-/-}$ (C) slices. **** indicates $p < 0.0001$, ** $p < 0.01$, * $p < 0.05$ as measured by Kruskal Walis test. (D,E) Directionality of individual slow (cyan dots), moderate (magenta dots) and fast mDA neurons (green dots) increases with increasing max-speed in both control (C) and *Dab1*$^{-/-}$ (D) slices. Note that inverse values of directionality are plotted against the max-speeds of migratory mDA neurons. Figure modified from (Vaswani et al. 2019).

4.9. Reelin signaling promotes a preference for lateral migratory directions in mDA neurons

In order for correct lateral localization to occur, SN-mDA neurons must migrate away from the midline towards lateral regions of the slice. To understand how Reelin influences migratory direction, the trajectories of migratory SN-mDA neurons were analyzed in the presence and absence of Reelin signaling. A "trajectory angle" was defined for each cell as the angle between the midline (y-axis in live-images) and the cell's total displacement vector(in 2D, z-axis was ignored in this analysis) (**Figure 24A**). **Figure 24B** shows all trajectories from a *Dab1*$^{-/-}$ slice (red) superimposed on trajectories from a control slice (green).

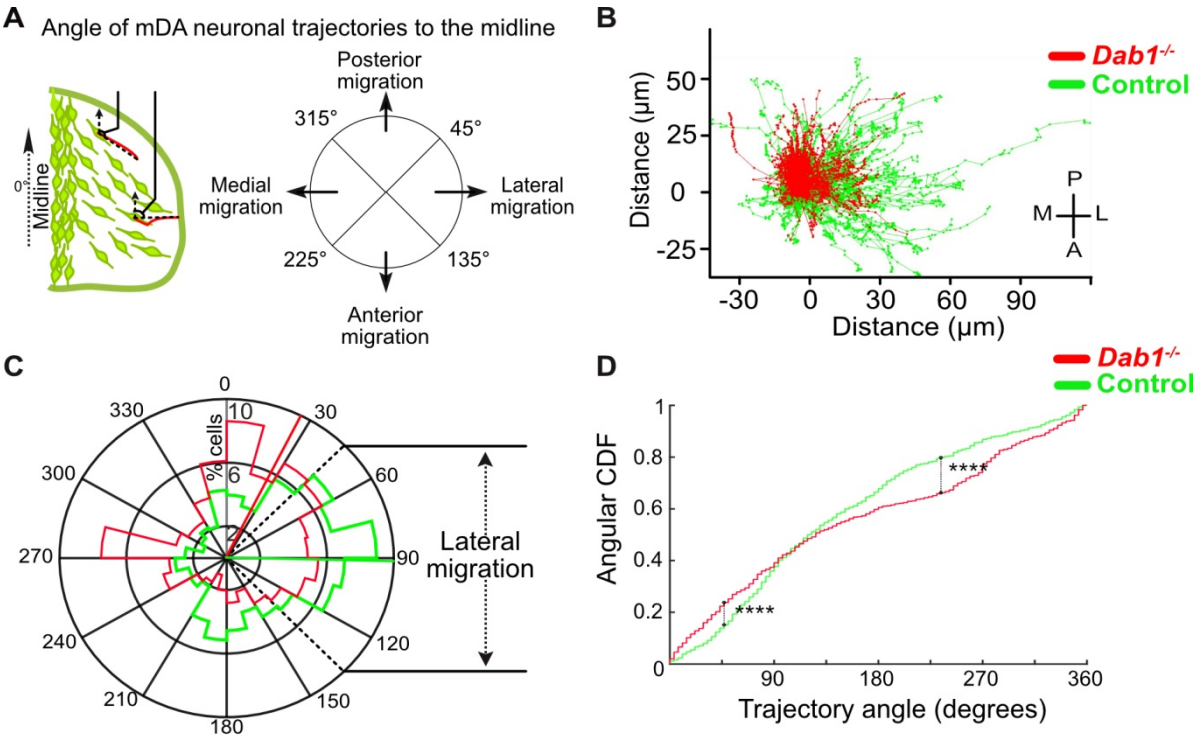

Figure 24. mDA neurons' lateral migration is reduced in the absence of Reelin signaling. (A) Schematic representing trajectory angle measurement. (B) Trajectories of control (green) and *Dab1*$^{-/-}$ (red) mDA neurons (from 1 control and 1 *Dab1*$^{-/-}$ slice imaged over the same duration), plotted relative to their starting point show loss of lateral directionality in *Dab1*$^{-/-}$ mDA neurons. (C) Polar histogram of the mDA trajectory angles to the midline (0°) for all control (green) and *Dab1*$^{-/-}$ (red) mDA neurons analyzed shows a decrease in lateral anisotropy for *Dab1*$^{-/-}$ slices. Lateral migration corresponds to migratory angles between 45 – 135°. (D) Angular CDF (angular cumulative distribution function) for angular distributions in (C) of control (green) and *Dab1*$^{-/-}$ (red) mDA neurons were used to run a Kuiper's test. The test confirmed a significant difference in the angular distributions of control (green) and *Dab1*$^{-/-}$ (red) mDA neurons (**** $p < 0.0001$, Kuiper's test for circular variables; n = 680 control, n = 639 *Dab1*$^{-/-}$ mDA neurons, from 3 slices/genotype). Figure modified from (Vaswani et al. 2019).

As angles were measured from the midline in a clockwise direction, trajectory angles of 45-135° indicated lateral migration, 135-225° represented anterior migration, while 225-315° indicated migration towards the midline and 315-45° referred to posterior migration (**Figure 24A**). By this definition, a trajectory angle of 90° indicates a cell whose total migratory displacement is precisely aligned to the lateral axis (x-axis in live-images). The angular mean

and standard deviation (σ_{ang}) of trajectory angles across the population of SN-mDA neurons, in control and *Dab1*$^{-/-}$ slices were then evaluated using a previously published toolbox for circular statistics (Berens 2009).

While SN-mDA neurons in control and *Dab1*$^{-/-}$ slices showed a diverse range of trajectories, with trajectory angles covering all quadrants, the average trajectory angle, and the preferred trajectory angles of these two populations was very different. Control SN-mDA neurons displayed a high preference towards lateral migratory directions and 36.5% of all control mDA neurons displayed laterally-directed trajectories (population angular mean 92.5°, σ_{ang} 68.4). In contrast, *Dab1*$^{-/-}$ SN-mDA neurons showed a significantly reduced preference for lateral migration and only 28.4% of the trajectories were laterally directed (population angular mean 27.5°, σ_{ang} 70.4) (see materials and methods section **3.9.2** and section **3.10**) (**Figure 24C,D**).
Next, to evaluate whether cells with low max. speeds showed differences in their preference for lateral migration compared to cells displaying high max. speeds, 'fast', 'moderate' and 'slow' cell populations of control and *Dab1*$^{-/-}$ slices were analyzed separately. While lateral migratory directions were preferred in all migratory control SN-mDA groups, the fraction of cells undergoing lateral migration in the 'slow' control group was greater in fast and moderate cells than in slow cells **(Figure 25A,C,E).** In the absence of Reelin signaling, slow but not moderate or fast *Dab1*$^{-/-}$ mDA neurons showed a reduced preference for lateral migration (**Figure 25E,F**). In contrast, moderate and fast *Dab1*$^{-/-}$ cells displayed nearly identical trajectory angles compared to their control counterparts (**Figure 25A-D**).

While the above described analysis reveals differences in trajectory angles of neurons that display low or high max. speeds, it does not provide information about the direction of individual migratory movements. Hence to understand whether fast migratory movements were more laterally directed than slow migratory movements, angles of individual migratory movements to the midline were measured and analyzed **(Figure 26**). This analysis was very similar to the trajectory angle analysis of various cell groups, which measured the angle made by the cells' total displacement vector (based on the first and last recorded position of the cell). However, in the analysis of angles of individual migratory movements, the angle of every instantaneous speed vector of a cell (based on the current position and the soma position at the previous time-point) was measured, and categorized into slow, moderate or fast migratory phase based on the magnitude of speed (described in section **3.9.2**).
Interestingly, the trends observed in the slow, moderate and fast cell groups (**Figure 25**), were recapitulated by angles of slow, moderate and fast migratory phases. Slow migratory phases were weakly laterally directed in controls, but in the absence of Reelin signaling, individual slow migratory movements lost their slight lateral preference (**Figure 26E,F**).

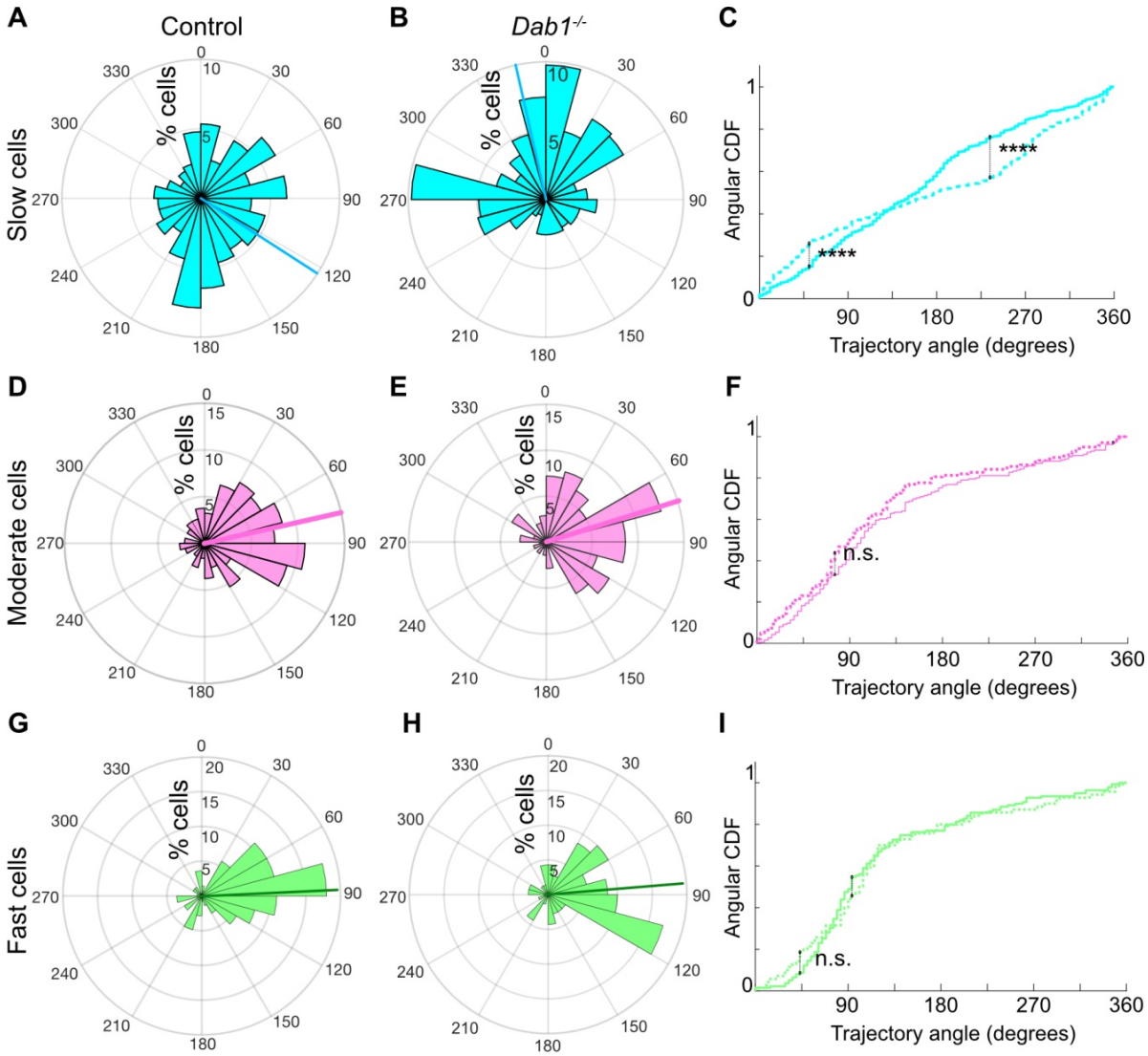

Figure 25: Reelin promotes preference for lateral migration in slow mDA neurons. Data from Table 17 are presented as polar histograms for the angle of mDA trajectories to the midline. Radial axes represent the percentage of cells that migrate with various angles to the midline. (A,B) shows that slow cells have the least preference for lateral migratory direction in both control (A) and *Dab1*$^{-/-}$ (B) slices. (C) Circular statistical analysis for angular distributions of slow mDA neurons shows significant loss of preference for lateral migration in slow *Dab1*$^{-/-}$ mDA neurons compared to controls (**** $p < 0.0001$, Kuiper's test for circular variables; n = 355 control, 480 *Dab1*$^{-/-}$ mDA neurons). (D-I) Moderate (D,E) and fast mDA neurons (G,H) show high preference for lateral migration. Moderate (F) (n = 186 control, n = 139 *Dab1*$^{-/-}$ mDA neurons) and fast mDA neurons (I) (n = 139 control, n = 70 *Dab1*$^{-/-}$ mDA neurons) are laterally directed and their angular distributions are comparable in control and *Dab1*$^{-/-}$ slices. Cyan (A,B), magenta (C,D) and green (G,H) lines represent mean angular direction for slow, moderate and fast populations, respectively. Angular CDF: angular cumulative distribution function. Figure modified from (Vaswani et al. 2019).

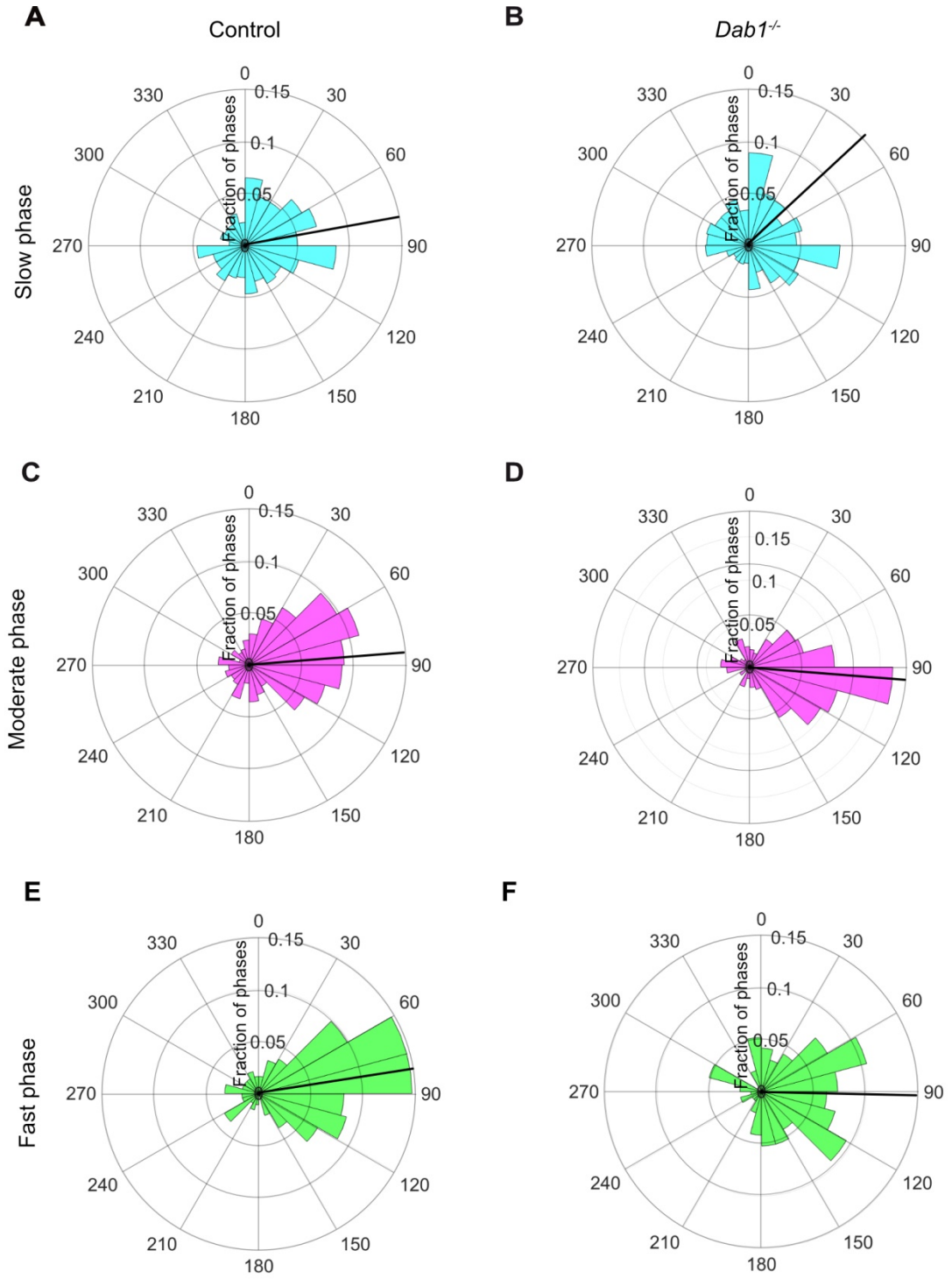

Figure 26. Lateral migration occurs predominantly during moderate and fast migratory phases of mDA neurons. (A,B) Polar histogram for angle of slow mDA trajectories to the midline shows that slow migratory movements have the least preference for lateral migratory direction in both control (A) and *Dab1*$^{-/-}$ (B) slices (n = 3506 movements in control, n = 2622 movements in *Dab1*$^{-/-}$ mDA neurons). (C-F) Moderate (C,D; n = 506 movements in control, n = 298 movements in *Dab1*$^{-/-}$ mDA neurons) and fast movements (E,F; n = 184 movements in control, n = 96 movements in *Dab1*$^{-/-}$ mDA neurons) are laterally directed and comparable in control and *Dab*$^{-/-}$ slices. Thick black lines represent mean angular direction. Figure modified from (Vaswani et al. 2019).

Similar to moderate and fast cell groups, individual moderate and fast migratory movements were nearly identical in the presence and absence of Reelin signaling. The analyses described so far reveal a complex role for Reelin signaling in mDA migratory speeds and trajectories. Firstly, slow movements in *Dab1*$^{-/-}$ mDA neurons lose the preference for lateral directions seen in control mDA neurons. Hence Reelin promotes a preference for laterally directed small migratory movements. Secondly, Reelin promotes tangential (lateral) mDA migration by increasing the fraction of neurons undergoing moderate-to-fast movements. Individual moderate and fast movements are predominantly laterally directed, even in the absence of Reelin signaling, suggesting that factors other than Reelin signaling are responsible for their lateral migratory behavior.

4.10. mDA neurons display bipolar and multipolar morphologies, but are predominantly bipolar during moderate or fast migratory behaviors

The above described experiments resulted in a large dataset of migratory mDA neurons with recorded migratory speed and trajectories. Furthermore, these mDA neurons were imaged with a resolution that permitted the investigation of the cellular morphologies that were associated with their tangential migration. Hence, the next objective of the study was to examine correlations between migratory behavior and cell morphology. Because not much was previously known about morphology of migrating mDA neurons, the first step was to define and describe specific types of morphology displayed by these neurons. Three morphological classes were defined based on previous studies of dynamic morphologies of migrating cortical pyramidal neurons and interneurons (Nadarajah et al. 2001; Tanaka et al. 2009).

A neuron was defined as ‘bipolar-unbranched’ if a maximum of two processes arose directly from the soma (bipolar neurons) and the leading process (LP) was unbranched (**Figure 27A**). Bipolar cells that extended a branched LP were defined as 'bipolar-branched’ (**Figure 27B**). Neurons with more than two processes arising from the soma were defined as ‘multipolar’ (**Figure 27C**). Some cells transitioned between ‘bipolar’ (refers to ‘bipolar-unbranched’ and ‘bipolar branched groups’) and multipolar morphology. These were defined as ‘transitionary’ cells (**Figure 27D**).

Next, cell morphologies of control and *Dab1*$^{-/-}$ mDA neurons were manually investigated and classified into the categories described above. As cell morphology was dynamic, every neuron had to be examined at every time-point of analysis. Only cells with clearly defined processes during all time-points of imaging were included. In total, 150 control and 129 *Dab1*$^{-/-}$ mDA neurons were analyzed for the first 19 time-points of imaging.

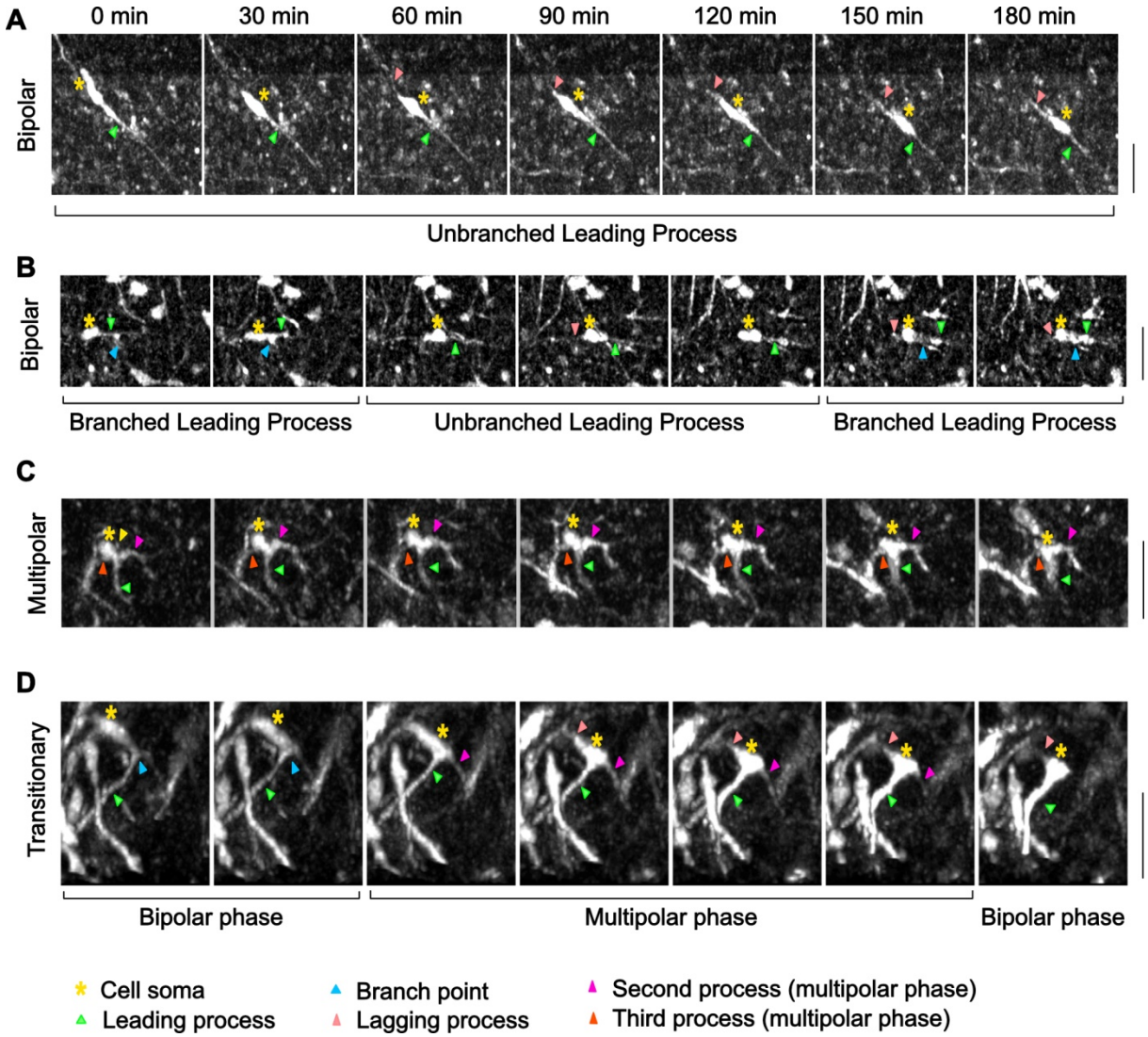

Figure 27. Morphological characterization of mDA neurons. (A) Control bipolar mDA neuron displaying bipolar-unbranched morphology at all analyzed time-points. (B) Bipolar mDA neuron that switches between a branched and unbranched leading process. (C) Transitionary mDA neuron that switches between bipolar and multipolar phases twice in the duration of analysis. (D) mDA neuron that remains multipolar during the entire duration of analysis. Figure modified from (Vaswani et al. 2019).

As the objective was to investigate cell morphology in relation to slow, moderate and fast migratory phases, 70 'fast', 40 'moderate' and 40 'slow' control cells were compared to 49 'fast', 40 'moderate' and 40 'slow' *Dab1*$^{-/-}$ cells (**Table 15**) for details of morphological analysis see materials and methods section **3.9.3**). Then, the morphology of these cells, whether bipolar- unbranched, bipolar branched or multipolar, was comparred with their soma speed (as calculated by change in soma position between the current and the subsequent time point) (**Figure 28A,B)**. In both control and *Dab1*$^{-/-}$ SN-mDA neurons, fast and moderate migratory phases were strongly associated with bipolar morphology (96.7% of all fast phases, 85.4% of all moderate phases in control cells; 84% in *Dab1*$^{-/-}$ fast phases, 94.4% in *Dab1*$^{-/-}$ moderate phases) (**Figure 28C,D**). Correspondingly, multipolar morphology was rare in fast (3.2% control; 16.2% *Dab1*$^{-/-}$ fast phases) and moderate migratory phases (13.3 % control; 12.6% in

Dab1$^{-/-}$ moderate phases (**Figure 28C,D**). In contrast, slow migratory phases and rest phases were more likely to be associated with multipolar morphology (26% slow phases in control; 28.6% slow phases in *Dab1*$^{-/-}$; 28.7% rest phases in control, 33.8% rest phases in *Dab1*$^{-/-}$).

Hence, while rest or slow migratory phases can occur in either bipolar or multipolar morphology, fast and moderate migration events are predominantly associated with bipolar morphology (**Figure 28C,D**). Consistent with these results, almost half of the 'slow' control mDA neurons were multipolar at all time-points (17/40), while constant multipolarity was very rare in 'fast' and 'moderate' cells (1/70 and 1/40, respectively). 'Fast' and 'moderate' cells were either bipolar (35/70 'fast', 17/40 'moderate') throughout the entire imaging period or transitioned between bipolar and multipolar morphologies (transitionary cells; 34/70 'fast', 22/40 'moderate'). The fraction of 'fast' multipolar cells but not 'moderate' multipolar cells was increased in *Dab1*$^{-/-}$ slices (**Table 15**).

		Control			***Dab1-/-***		
Cell type	Morphology	**Slice 1**	**Slice 2**	**Slice 3**	**Slice 1**	**Slice 2**	**Slice 3**
Fast	# Analyzed	27	26	17	16	15	18
	% Bipolar	55.56	46.15	41.18	31.25	40	27.78
	% Transitionary	44.45	50	58.82	56.25	53.33	66.67
	% Multipolar	0	3.85	0	12.5	6.67	5.56
Moderate	# Analyzed	16	10	14	13	19	8
	% Bipolar	50	40	28.57	30.77	26.32	62.5
	% Transitionary	43.75	60	71.43	69.23	73.68	37.5
	% Multipolar	6.25	0	0	0	0	0
Slow	# Analyzed	11	12	17	14	15	11
	% Bipolar	27.27	7/12	41.18	35.71	33.33	18.18
	% Transitionary	18.18	1/12	17.65	35.71	33.33	45.45
	% Multipolar	54.55	4/12	41.18	28.57	33.33	36.36

Table 15. In the absence of Reelin signaling, moderate and fast mDA neurons are less strongly associated with bipolar morphology. Table shows the percentage of constantly bipolar, transitionary and multipolar cells across 3 control and *Dab1*$^{-/-}$ slices belonging to fast, moderate and slow max. speed groups. The number of cells evaluated in each group is provided in the rows labelled '# Analyzed'. Bar plot of this data is shown in (Figure 29). Data clearly indicate a decrease in fast mDA neurons that maintain bipolar constant morphology in the absence of Reelin signalling.

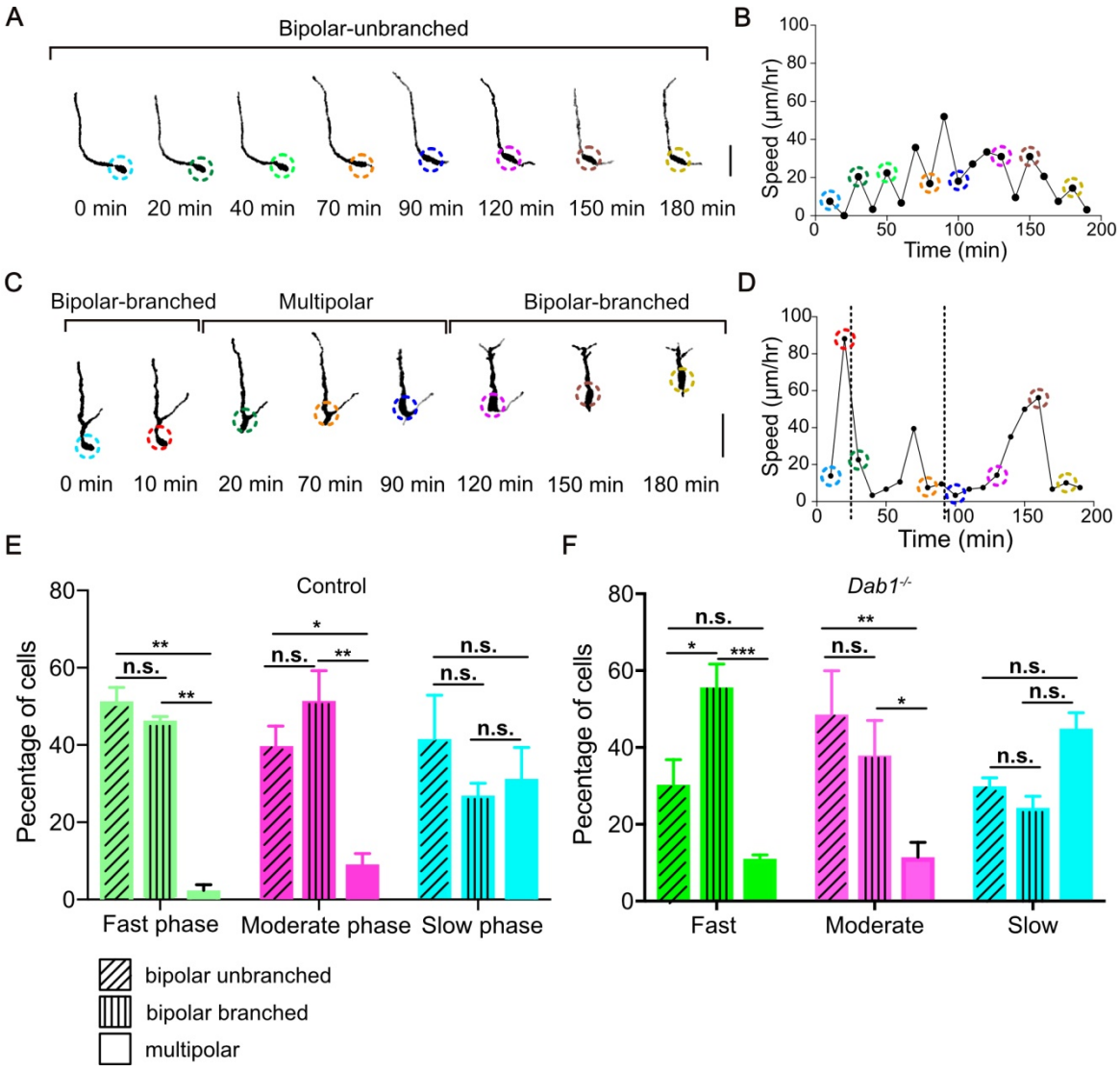

Figure 28. Reelin promotes unbranched morphology of migrating SN-mDA neurons. (A) Control mDA neuron displaying a 'bipolar-unbranched' morphology at all analyzed time-points. (B) Soma speed profile of mDA neuron shown in (A). (C) Control mDA neuron transitioning between bipolar and multipolar morphology. At t = 0 min, the cell has a branched leading process (LP), the cell soma moves along the LP to reach the branch-point and takes up a multipolar morphology (t = 20 min). The cell remains multipolar until t =90 min, after which one process is retracted (t = 120 min) and the cell resumes a bipolar morphology (t=150 min). Bipolar phase: one or two processes arise directly from the soma. Multipolar phase: more than two processes arise directly from the soma. (A,C) Colored circles: soma as defined by the tracking process. Scale bar: 25 µm. (D) Soma speed for the neuron in (C) is higher during its bipolar phase. Figure modified from (Vaswani et al. 2018). (E,F) Proportion of bipolar unbranched and bipolar branched morphology in control mDA neurons (E) is significantly higher than multipolar morphology during fast and moderate phases of migration than in the slow phase. In *Dab1*$^{-/-}$ fast and moderate mDA neurons (F), a higher proportion of multipolar cells is seen compared to bipolar (branched and unbranched) morphology (* $p < 0.05$, ** $p < 0.005$, *** $p < 0.001$, **** $p < 0.0001$; two-way ANOVA). Total number of datapoints in fast phase (A,B): Control: 126, *Dab1*$^{-/-}$: 81 data-points. Total number of datapoints in moderate phase (C,D): Control: 156, *Dab1*$^{-/-}$: 99 data-points. Total number of datapoints in slow phase (E,F): Control: 408, *Dab1*$^{-/-}$: 626 data-points. Figure modified from (Vaswani et al. 2019).

4.11. Reelin signaling stabilizes the leading process (LP) of migrating mDA neurons, and is important for the regulation of LP length

As mentioned above, some mDA neurons transitioned between bipolar and multipolar morphology. In migrating interneurons, branching and selective stabilization of LPs has been shown to be important for guiding the direction of their migration (Martini et al. 2008). Hence, to examine whether Reelin played a role in stabilizing cell morphology of mDA neurons, proportions of migrating SN-mDA neurons that displayed a constantly bipolar (branched and unbranched), constantly multipolar or transitionary morphology were plotted for control and *Dab1*$^{-/-}$ populations (**Figure 29A**). In controls, transitionary cells made up 42.8+/-2.7% of the examined population, while in the *Dab1*$^{-/-}$ population, the fraction of transitionary cells was significantly increased to 54.2+/-0.5 (**Figure 29A, Table 15**). Correspondingly, the proportion of constantly bipolar cells was significantly decreased in the *Dab1*$^{-/-}$ population (44.5+/-3.5% in controls; 32.5+/-0.1% in *Dab1*$^{-/-}$) (**Figure 29A, Table 15**).

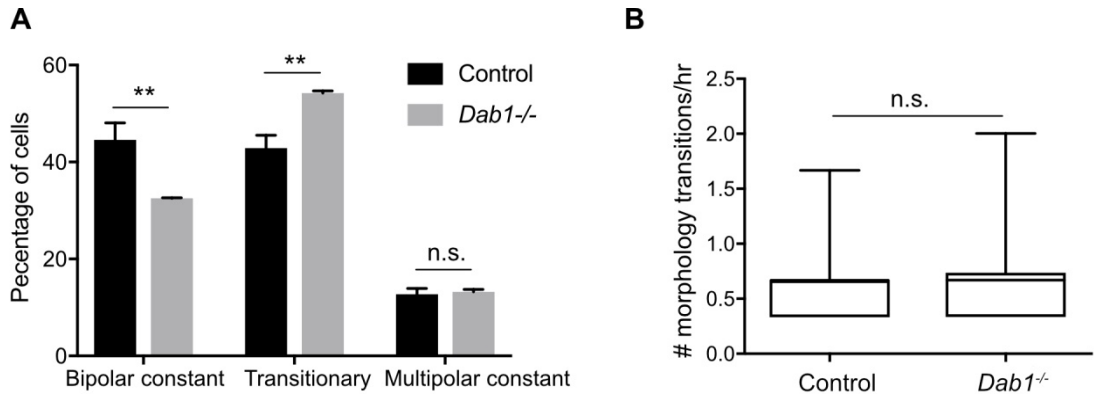

Figure 29. In the absence of Reelin signaling, moderate and fast mDA cells are less strongly associated with bipolar morphology. (A) Relative proportion of constantly bipolar mDA neurons are decreased, while transitionary mDA neurons are increased in *Dab1*$^{-/-}$ slices. (B) Frequency of transitions from multipolar to bipolar phase (and vice versa) are not significantly altered in the absence of Reelin signalling (p = 0.6922; Mann-Whitney's test). Tabular form of data in (A) is presented in Table 15. Figure modified from (Vaswani et al. 2019).

Next, the frequency with which mDA neurons transitioned between bipolar and multipolar morphology was analyzed in control and *Dab1*$^{-/-}$ populations. Interestingly, while the fraction of transitionary cells was increased in the absence of Reelin signaling, individual *Dab1*$^{-/-}$ mDA neurons transitioned between bipolar and multipolar morphology with similar frequencies as their control counterparts (**Figure 29B**). Thus, Reelin signaling promotes transitions in cell morphologies at the population level, but does not regulate the frequency at which individual mDA neurons make these transitions.

During the manual annotation and classification of mDA cell morphology, it was observed that small protrusions frequently appeared on the leading process of *Dab1*$^{-/-}$ neurons. The

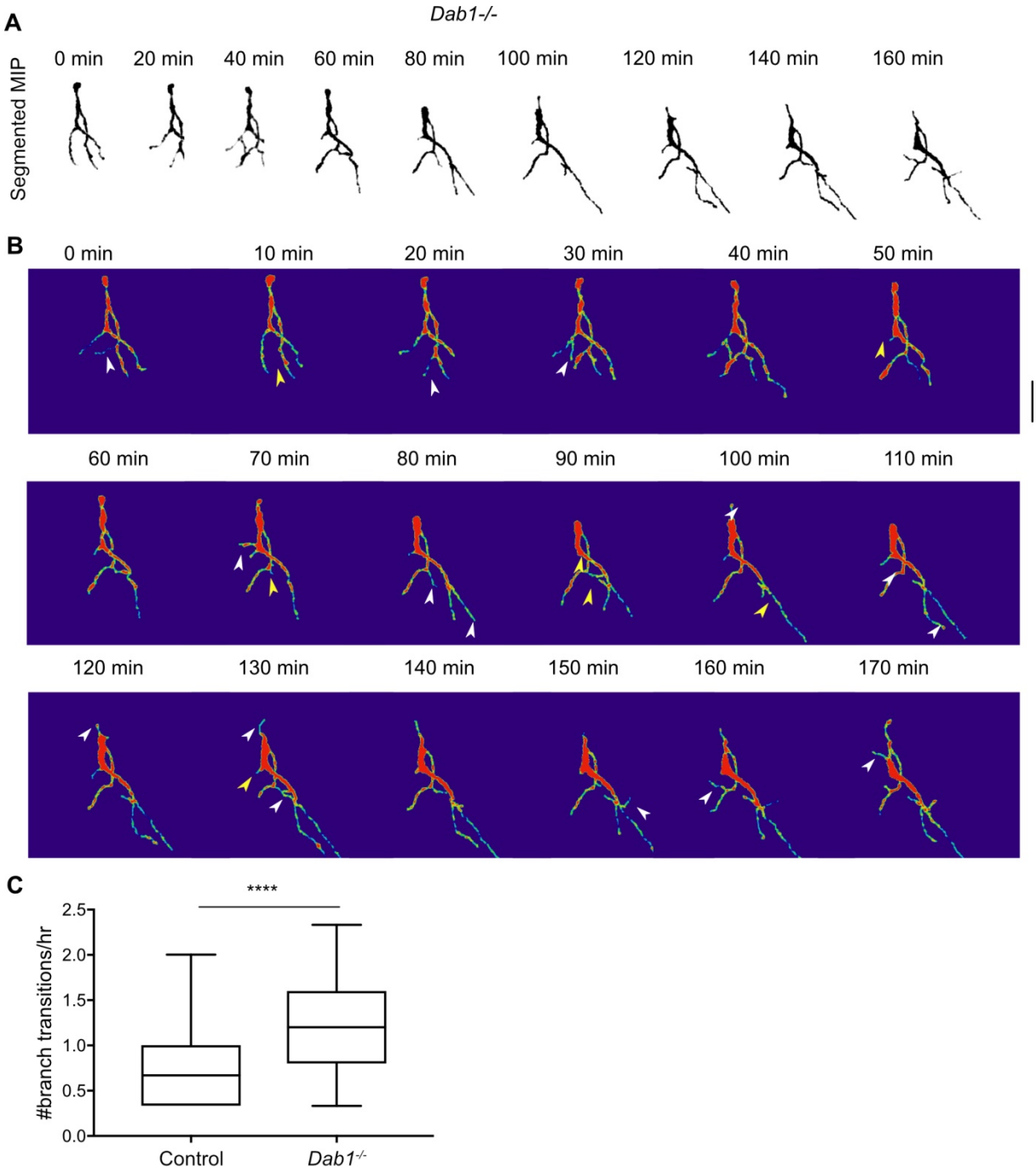

Figure 30. Absence of Reelin signaling results in the formation of unstable protrusions on the leading process of mDA neurons. (A) Bipolar and multipolar phase of a *Dab1*$^{-/-}$ transitionary mDA neuron. In this example, the bipolar phase lasts from t=0 min to t =60 min. In the multipolar phase (starting at t = 80 min) many, unstable protrusions form. Scale bar: 25 µm. (B) Cell in (A) is color-coded for the intensity of YFP in images (Physics LUT in Fiji). Red represents bright structures, green-blue represents weakly labelled structures. White arrowheads indicate appearance of a branch/protrusion, yellow arrowheads indicate disappearance. Scale bar: 25µm. (C) Quantification of appearance and disappearance of branches (defined as branch transitions per hour) in control and *Dab1*$^{-/-}$ mDA transitionary neurons shows a significant increase in branch transitions in mDA neurons in *Dab1*$^{-/-}$ slices (**** $p < 0.0001$; Mann-Whitney's test). Figure modified from (Vaswani et al. 2019).

appearance and disappearance of these protrusions, on the LP of transitionary neurons (n = 64 in control, n = 70 in *Dab1*$^{-/-}$), was examined in further detail **(Figure 30A,B)**. Each appearance or disappearance was defined as a branch transition event, and the number of branch transition events per hour was measured for every transitionary control and *Dab1*$^{-/-}$ neuron **(Figure 30B)**. Branch transitions were significantly more frequent in *Dab1*$^{-/-}$ SN-mDA transitionary neurons (**Figure 30C**), and *Dab1*$^{-/-}$ neurons often displayed short protrusions that transiently appeared on the LP **(Figure 30B**).

Next, to investigate whether other subtle differences could be observed in *Dab1*$^{-/-}$ mDA neurons, the cell morphologies of 20 control and 20 *Dab1*$^{-/-}$ mDA neurons were manually traced in 3D for the first 19 imaging time-points (**Figure 31**). Through this analysis, it was observed that mDA neurons in *Dab1*$^{-/-}$ slices displayed a broader distribution of LP length with very long and very short LPs **(Figure 31C**)**.** Hence, in the absence of Reelin signaling, SN-mDA neurons display abnormal morphology. On a population level, their aberrant morphology profiles result in an increased proportion of transitionary neurons. On a cellular level, *Dab1*$^{-/-}$mDA neurons exhibit unstable protrusions on their leading processes and a greater variation in LP length.

Since morphology of mDA neurons during tangential migration (E13.5) was not characterized previously, it was necessary to validate whether mDA morphologies observed with YFP labeling during the live-imaging of organotypic slices could also be observed with TH immunostaining *in* vivo. To this end, embryonic brains labeled with the inducible fate-mapping system used in this study (described in detail in section **3.2.2.2**) were dissected at E13.5. Then by modifying an existing, passive, tissue-clearing method (Schwarz et al. 2015), whole-mount YFP-labeled brains were immunostained for TH and YFP, cleared and imaged in 3D with a confocal microscope (details on tissue clearing: sections 3.4.1; 3.6.4; 3.8.2). Morphology of SN-mDA neurons labeled with YFP was similar to their morphology as assessed by TH-immunostaining in cleared whole-mount brains at E13.5 (n=116 neurons) (**Figure 32A-C**). mDA neurons were manually segmented in 3D whole-mount brain images and bipolar unbranched, bipolar branched and multipolar morphology were all observed in fixed embryonic brains (**Figure 32D,E**).

Furthermore, a preliminary analysis of TH^{+} projections in whole-mount control and *Dab1*$^{-/-}$ embryonic brains (n=1) show no gross differences in morphology, indicating that Reelin signaling might not be important for TH^{+} projections to reach the forebrain (**Figure 33A-D**). This hypothesis is supported by the observation that the intensity of TH immunostaining in the striatum of adult *Dab1* CKO mice is not significantly reduced compared to their control counterparts (**Figure 33E-G**). However, further detailed analysis of mDA projections to target areas, using viral injections in control, *Dab1* CKO and *Dab1*$^{-/-}$ brains will be required to comprehensively understand the consequences of altered migration on axonal connectivity.

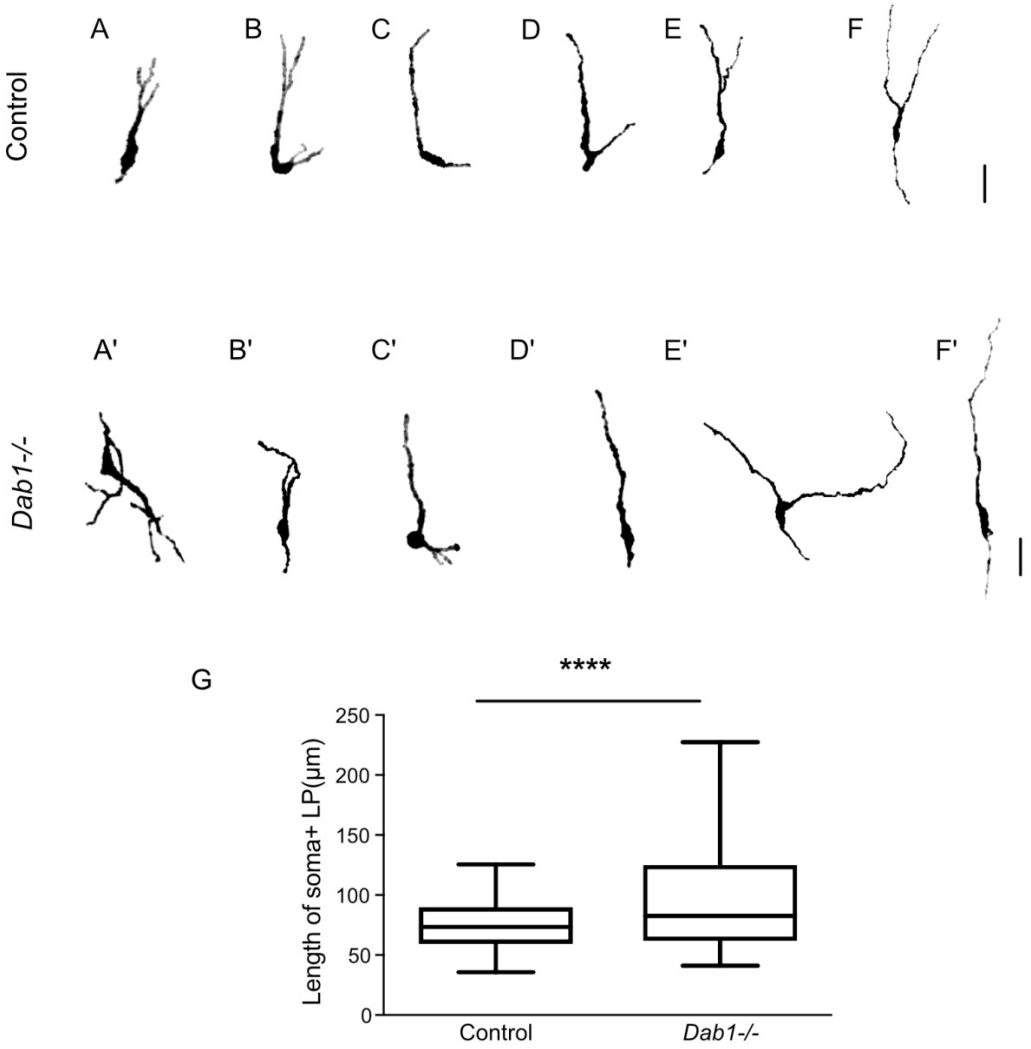

Figure 31. Greater spread in length of leading process in Dab1$^{/-}$ mDA neurons. (A-F) 6 of 20 manually segmented control mDA neurons. (A'F') 6 of 20 manually segmented Dab1$^{/-}$ mDA neurons. (G) Length of cell soma and leading process shows a wider spread in the absence of Reelin signalling. **** $p < 0.001$ as assessed by Mann-Whitney's test. Figure modified from (Vaswani et al. 2019).

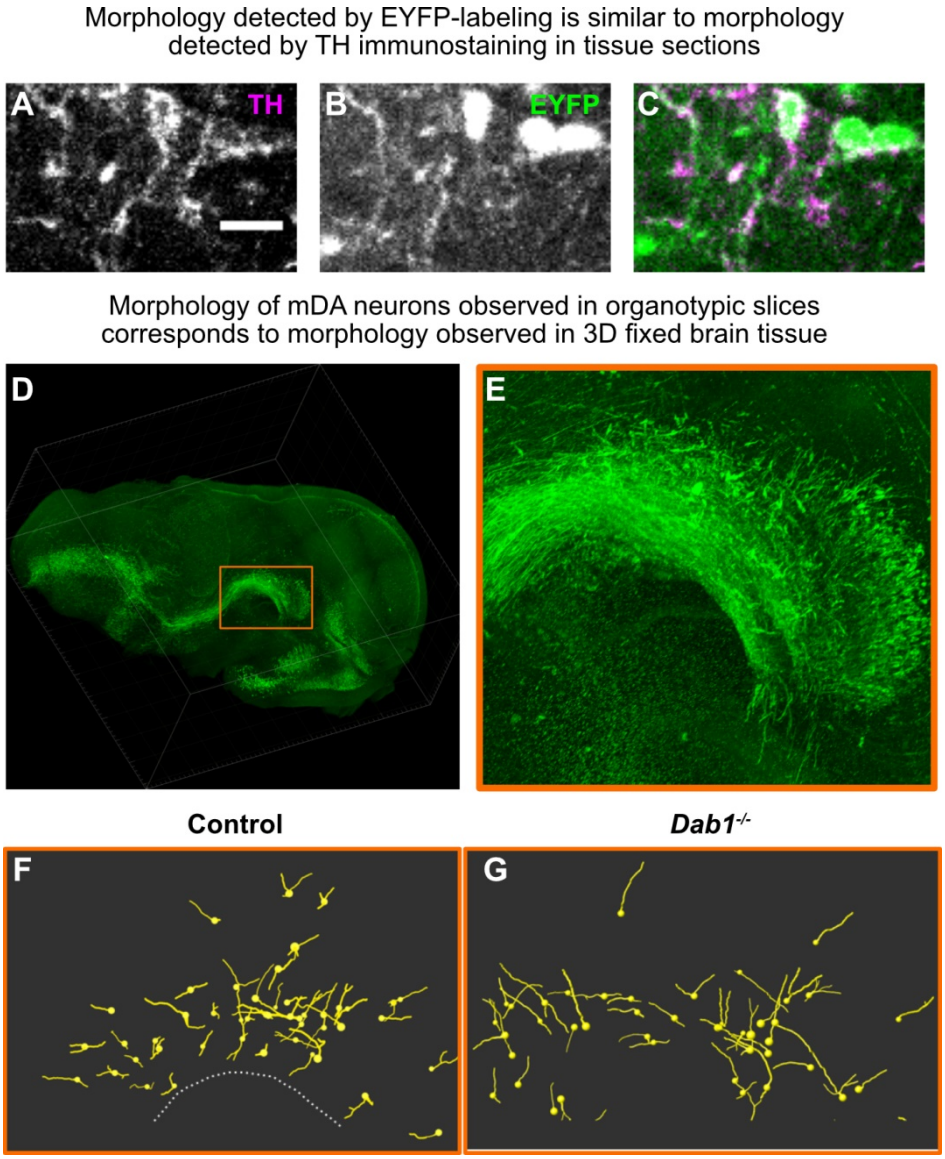

Figure 32. Morphology of mDA neurons in fixed preparations, and their projections to forebrain target areas during development. (A-C) Morphology as assessed by TH (A) immunostaining is similar to morphology observed with YFP labeling (B) in fixed mDA neurons, thereby validating our approach that uses YFP labeling to analyze mDA morphology. (D-G) Morphology of mDA neurons observed in 3D whole-mount fixed brains is similar to their morphology observed in *ex vivo* slices. (D,E) show the region of mDA neurons in wole-mount embryonic used for the analysis. (F,G) Morphology of 100 mDA neurons (TH^+) traced manually in IMARIS in control (F) and *Dab1*$^{-/-}$ brains show similar morphology to those observed *ex vivo* in slices. Scale bar: 10µm

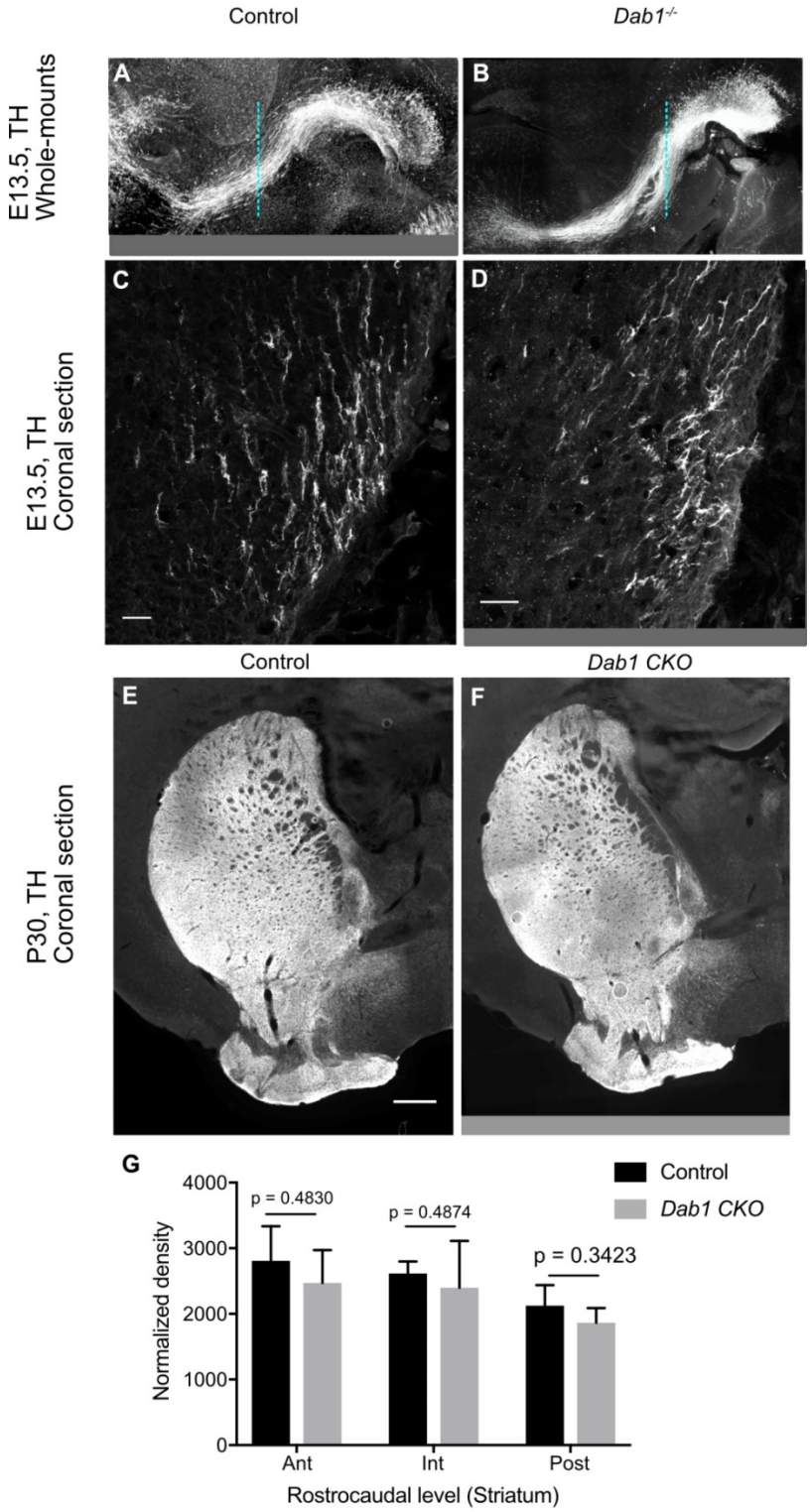

Figure 33. (A-F) Immunostaining for TH. (A,B) Even in the absence of Reelin signaling, gross projections of *Dab1*$^{-/-}$ neurons remain unaltered (I) compared to controls (H). (C,D) Higher zoom coronal images at the level indicated by dashed cyan line in (A) show similar morphology of TH projections. (E-G) Normalized density of TH^{+} innervation to the striatum is similar in controls (E) and *Dab1*$^{-/-}$ brains (F) as assessed by student's t-test, n = 6 animals/genotype (G). Scale bars: (C,D) 25 μm; (E,F) 500 μm. Figure modified from (Vaswani et al. 2019)

4.12. Investigating the role and regulation of Cofilin 1 and Cadherin 2 (CDH2) downstream of Reelin in mDA tangential migration.

It is not known which downstream components of the Reelin signaling pathway regulate SN-mDA tangential migration (downstream components of the Reelin pathway are described in section **1.4**). In this study, Cofilin 1 and CDH2 were investigated because they were previously shown to influence orientation of neurons and LP stability in other populations of migrating neurons (Franco et al. 2011; Krüger et al. 2010; Chai et al. 2009). Reelin-mediated inactivation of Cofilin 1 ultimately leads to the stabilization of the actin cytoskeleton and has been implicated in stabilizing LPs of radially migrating cortical neurons as well as in preventing the aberrant tangential migration of neurons of the autonomous nervous system in the spinal cord (Krüger et al. 2010; Chai et al. 2009; Frotscher et al. 2017) (described in detail in section 1.4).

Cofilin 1 is an actin depolymerizing protein of the ADF/Cofilin family (Chai et al. 2009) (Frotscher et al. 2017) (Maciver and Hussey 2002). To investigate whether Cofilin 1 was involved downstream of DAB1 in mDA neurons, conditional knockouts of Cofilin 1 were generated by inactivating *Cofilin 1* under the *Dat* promoter (**Figure 34A**). Similar to the *Dab1* CKO animals (Section **3.1**), Cofilin 1 was specifically inactivated in mDA neurons by combining the *Cofilin-1^{flox}* allele (Bellenchi et al. 2007) with the *DAT$^{Cre/+}$* mouse line (Ekstrand et al. 2007). It has been shown that actin depolymerizing protein (ADF) can compensate for the loss of Cofilin-1 as the phenotypic effects of Cofilin 1 protein knockdown can be rescued by the overexpression of ADF and vice-versa (Hotulainen et al. 2005). Hence, in addition to specific inactivation of *Cofilin 1* in mDA neurons, the crosses to generate *Cofilin* CKO mice were also carried out on a *ADF* null background (*ADF$^{-/-}$*).

The mediolateral distribution of TH$^+$ neurons in the *DAT$^{Cre/+}$; Cofilin 1$^{flox/flox}$; ADF$^{-/-}$* mutants (refered to as *ADF$^{-/-}$; Cofilin 1* CKO mice) was compared to control littermates. In contrast to *Dab1* CKO mice that clearly displayed altered mediolateral TH$^+$ cell distributions compared to control littermates (**Figure 9**), no difference could be observed in the TH mediolateral distribution in *ADF$^{-/-}$; Cofilin 1* CKO mice at P30 (**Figure 34C-E**) or E18.5 (data not shown). However, as an immunostaining protocol for Cofilin 1 could not be established, the absence of Cofilin 1 in mDA neurons of *ADF$^{-/-}$; Cofilin 1* CKO mice during tangential migration (E13.5-E15.5) could not be demonstrated. It has been previously shown that Cofilin 1 protein is detected in brain tissue lysates for more than two days after the onset of Cre-mediated recombination (Bellenchi et al. 2007). In *ADF$^{-/-}$; Cofilin 1* CKO mice, Cre-mediated inactivation of Cofilin 1 begins at E13.5 under the *Dat* promoter (**Figure 6**). Hence, it is possible that the *ADF$^{-/-}$; Cofilin 1* CKO mice show no changes in mDA mediolateral distribution as some Cofilin 1 is present in their mDA neurons until their tangential migration ends at E15.5. Future experiments would need to rule out the presence of Cofilin 1 in *ADF$^{-/-}$; Cofilin* CKO brains

between E13.5-E15.5 before any conclusion can be drawn about the role of Cofilin 1 in mDA tangential migration.

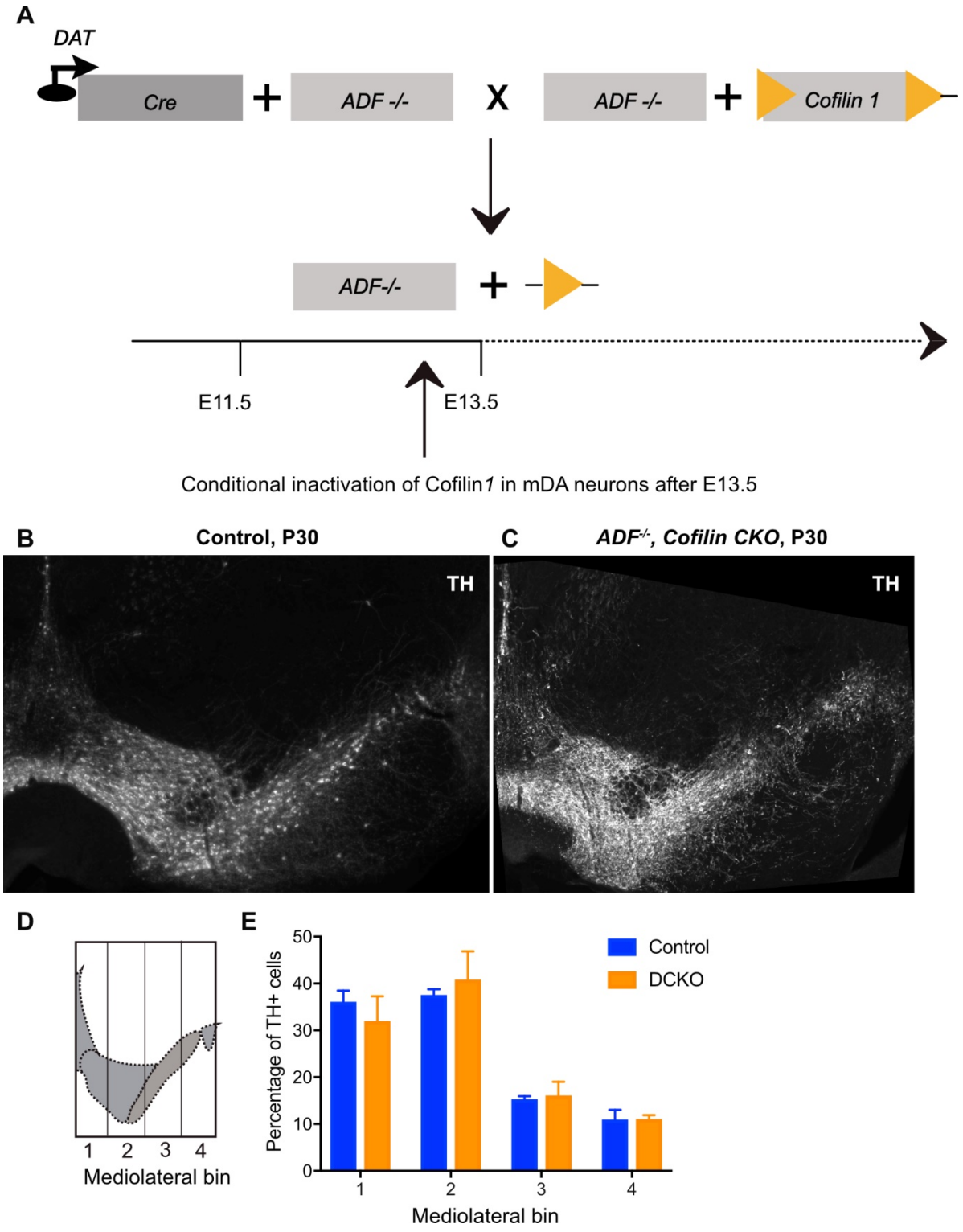

Figure 34. No change in the mediolateral distribution of TH⁺ mDA neurons in *ADF$^{-/-}$; Cofilin 1* CKO mice compared to control littermates. (A) Schematic representing transgenic mice used to generate *ADF$^{-/-}$; Cofilin 1* CKO mice. (B,C) TH⁺ domain in control (B) and *ADF$^{-/-}$; Cofilin 1* CKO littermates (C) at P(30). (D) Schematic indicating grids used for analysis of mediolateral distribution of TH⁺ mDA neurons. (F) Quantification of mediolateral distribution of TH⁺ mDA neurons shows no significant differences between the two groups as assessed by student's t-test (n=3 brains/genotype).

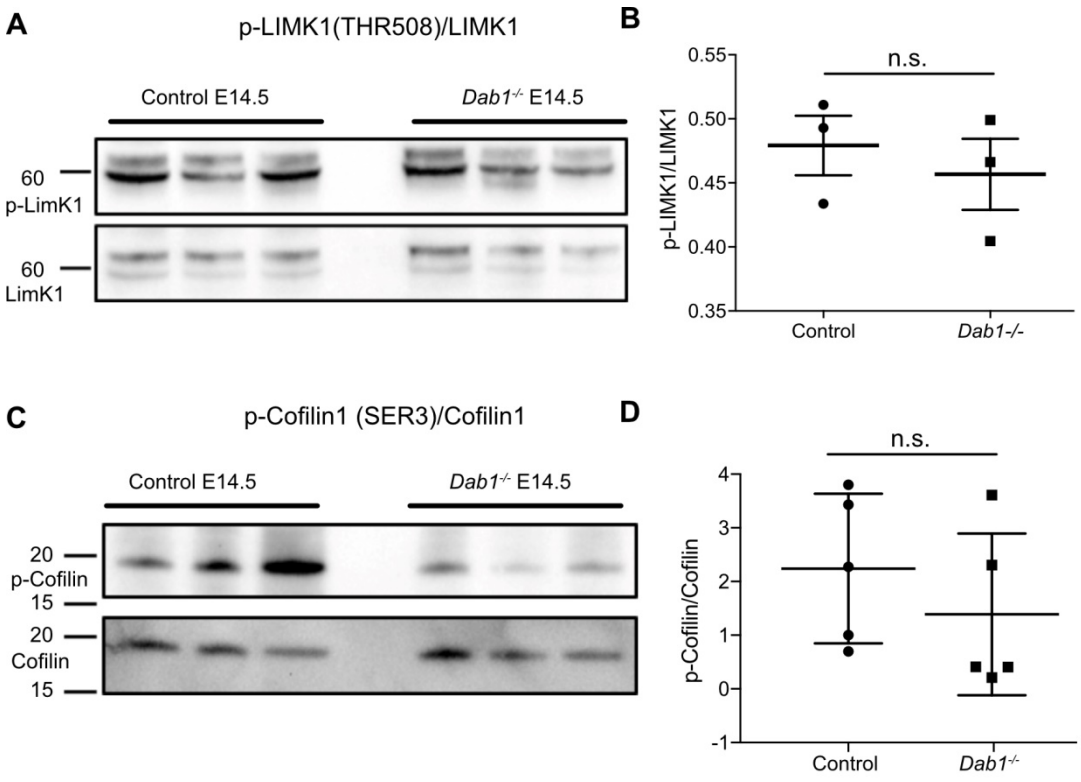

Figure 35. Phosphorylation levels of proteins in the canonical Reelin signaling pathway are not altered in *Dab1*$^{-/-}$ ventral midbrain at E14.5. (A,B) No significant changes in the absence of Reelin signalling in the relative phosphorylation levels of LIMK1 in *Dab1*$^{-/-}$ ventral midbrains. p-value = 0.5682, Student's t-test (n = 5 brains/ genotype). (C,D) Phosphorylation levels of Cofilin 1 are not significantly changed in *Dab1*$^{-/-}$ ventral midbrains. p-value = 0.854, Student's t-test (n = 5 brains/ genotype). Western blot experiments carried out in collaboration with Beatrice Weykopf, Institute of Reconstructive Neurobiology, Bonn.

An alternative approach to investigating the role of Cofilin 1 in mDA migration was to detect a misregulation of downstream events that are involved in Cofilin 1 phosphorylation (see Introduction section **1.4.2**, **Figure 3**). Hence, to detect a misregulation fo Cofilin 1 downstream of Reelin, the relative levels of phosphorylation of p-LIMK1/LIMK1 and p-Cofilin 1/Cofilin 1 were assessed by western blots in control and *Dab1*$^{-/-}$ ventral midbrain tissue at E14.5. Due to a high inter-sample variability, no significant differences in protein levels or in relative expression of p-LIMK1/LIMK1 or p-Cofilin 1/Cofilin 1 could be detected (**Figure 35A-D**). These data suggest that the regulation of Cofilin 1 via LimK1 is probably not involved in regulating cytoskeletal stability of migrating mDA neurons downstream of Reelin signaling.

Next, to investigate whether CDH2 facilitates the migratory and morphology regulation of mDA neurons downstream of Reelin, the membrane localization of CDH2 was examined in control and *Dab1*$^{-/-}$ mDA neurons by immunostaining at E14.5 (for the role of CDH2 downstream of Reelin in cortical pyramidal neurons, refer to Introduction section **1.4.2-1.4.3**). Whether levels of CDH2 are altered at the membrane of mDA neurons in *Dab1*$^{-/-}$ mice compared to controls could not be assessed as the immunostaining for CDH2 on sections was

not of sufficient quality (**Figure 36A-F**). However, it is possible that subtle differences in membrane localization were not detected in these experiments due to the low signal to noise ratio in the immunostaining with the CDH2 antibody.

Next, relative protein levels of CDH2 in tissue lysates from control and *Dab1*$^{-/-}$ E14.5 ventral midbrains were measured by western blotting (**Figure 36G,H**). A high inter-sample variability was observed in CDH2 relative protein levels and no significant difference could be detected between the two groups by this method (**Figure 36H**).

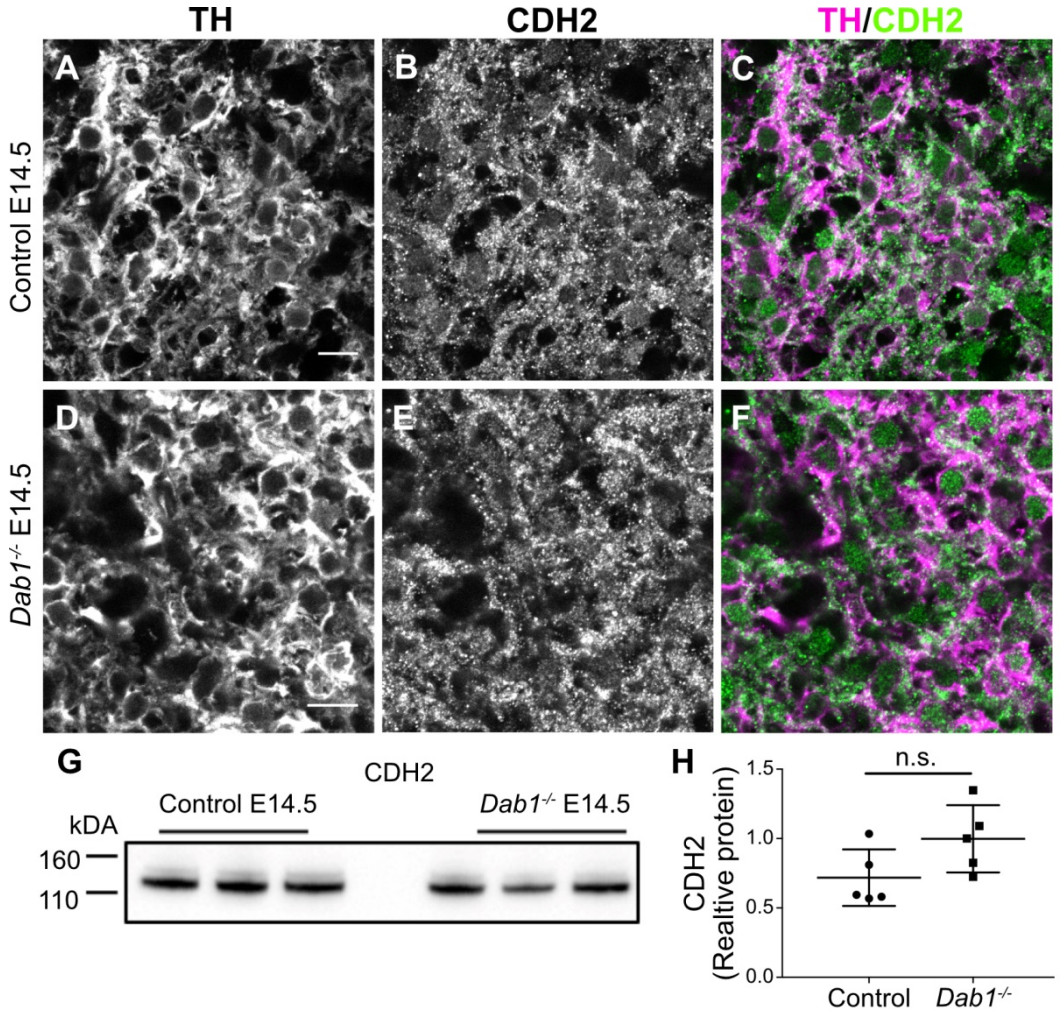

Figure 36. CDH2 membrane localization and expression levels (as measured by western blot) in the ventral midbrain of control and *Dab1*$^{-/-}$ brains at E14.5. (A-C) Double immunolabeling for TH (magenta) and CDH2 (green) in E14.5 control midbrain shows CDH2 expression around the edges of mDA neurons. (D-F) The localization of CDH2 to the edges of TH^{+} cells in the absence of Reelin signalling. (G,H) Western blots for ventral midbrain tissue from control and *Dab1*$^{-/-}$ brains (G) show no changes in relative protein levels of CDH2 in *Dab1*$^{-/-}$ tissue compared to controls (H). p-value 0.08 as assessed by Student's t-test (n= 5 brains/ genotype). Western blot experiments carried out in collaboration with Beatrice Weykopf, Institute of Reconstructive Neurobiology, Bonn.

4.13. Assessment of microtubule assembly in migrating mDA neurons in the presence and absence of Reelin signaling.

Reelin has been shown to promote mictrobule assembly by facilitating microtubule plus end dynamics in neurons of the neocortex and hippocampus (Meseka, Cavus and Förster 2013). To ascertain whether microtubule assembly, stability and dynamics are affected in mDA neurons in the presence and absence of Reelin signaling, immunostaining in E13.5 control and *Dab1*$^{-/-}$ ventral midbrain sections was performed with the microtubule markers α-Tubulin, acetylated α-Tubulin and End-binding protein (EB3).

Heterodimers of α- and ß-Tubulin polymerize to form microtubules. In this study, an antibody against α-Tubulin was used that intensely marks α-Tubulin when in polymerized form (in microtubules), but is relatively weak in intensity when binding to disorganized α-Tubulin (Meseka, Cavus and Förster 2013). Thus the intensity of α-Tubulin immunostaining was compared in control and *Dab*$^{-/-}$ ventral midbrain sections to evaluate the extent of microtubule organization in the presence and absence of Reelin signaling (**Figure 37**). While sections of the *Dab*$^{-/-}$ neocortex showed a disorganization in α-Tubulin staining as previously reported (Meseka, Cavus and Förster 2013), a high variability was observed in intensity and quality of staining in both control and *Dab*$^{-/-}$ midbrain sections (**Figure 37**) and no obvious differences could be identified between the two genotypes.

A similar experiment to that described above was carried out with an antibody against acetylated α-Tubulin. Acetylation of α-Tubulin is a posttranslational modification that is relatively enriched in stabilized microtubules (Fernández-Barrera and Alonso 2018). As in the case of α-Tubulin, no obvious defferences could be detected between control and *Dab1*$^{-/-}$ TH^{+} mDA neurons in this experiment (**Figure 38**). These data suggest that organization and stabilization of microtubules is likely unaffected by the absence of Reelin signaling, or is too subtle to identify by the experiments performed in this study.

Lastly, to investigate extent of microtubule dynamics, an antibody against EB3 was used. EB3 is part of a large protein complex that is localized at the growing end of microtubules (Stepanova et al. 2003). No significant differences were observed in the intensity and distribution of EB3 signal in TH^{+} control and *Dab*$^{-/-}$ mDA neurons at E13.5 (**Figure 39**). Hence, Reelin signaling does not seem to affect mictrotubule stability and dynamics in E13.5 mDA neurons.

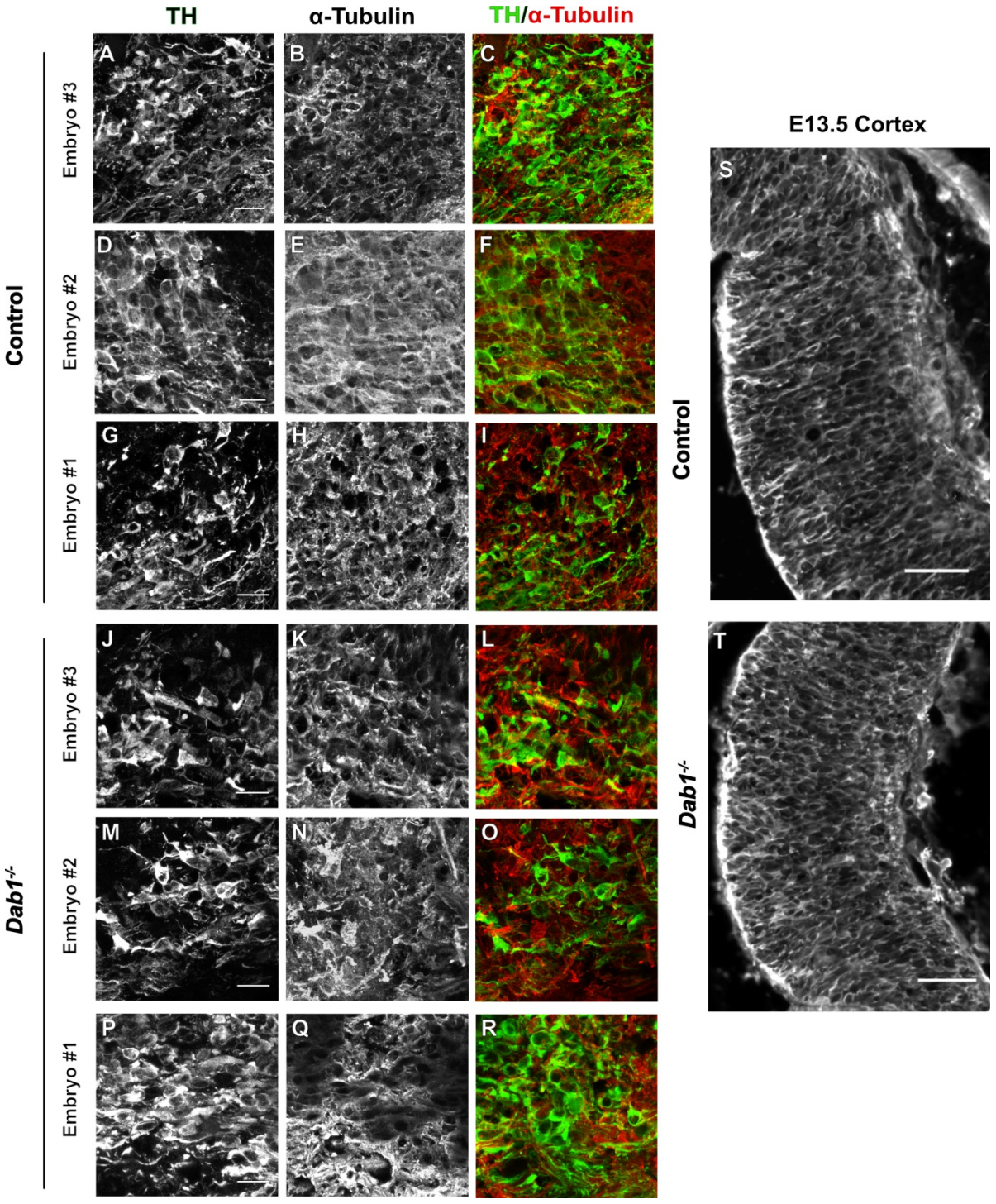

Figure 37. α-Tubulin in control and *Dab1*$^{-/-}$ E13.5 brains. (A-I) Immunostaining for TH (A,D,G), α-Tubulin (B,E,H) and their overlap (C,F,I) in the developing lateral mDA domain of control embryos (n = 3, from 2 litters). (J-R) Immunostaining for TH (J,M,P), α-Tubulin (K,N,Q) and their overlap (L,O,R) in the developing lateral mDA domains of *Dab1*$^{-/-}$ embryos (n = 3, across 2 litters). Due to high variability in stainings of individual animals, and due to low signal-to-noise ratio in the α-Tubulin immunostainings, no definite conclusions could be drawn from the data. (T) Panel of α-Tubulin staining in the cortex is provided to demonstrate specificity of the antibody used. In this example, subtle differences in the organization of α-Tubulin can be clearly seen in *Dab1*$^{-/-}$ embryonic cortical section compared to the control.

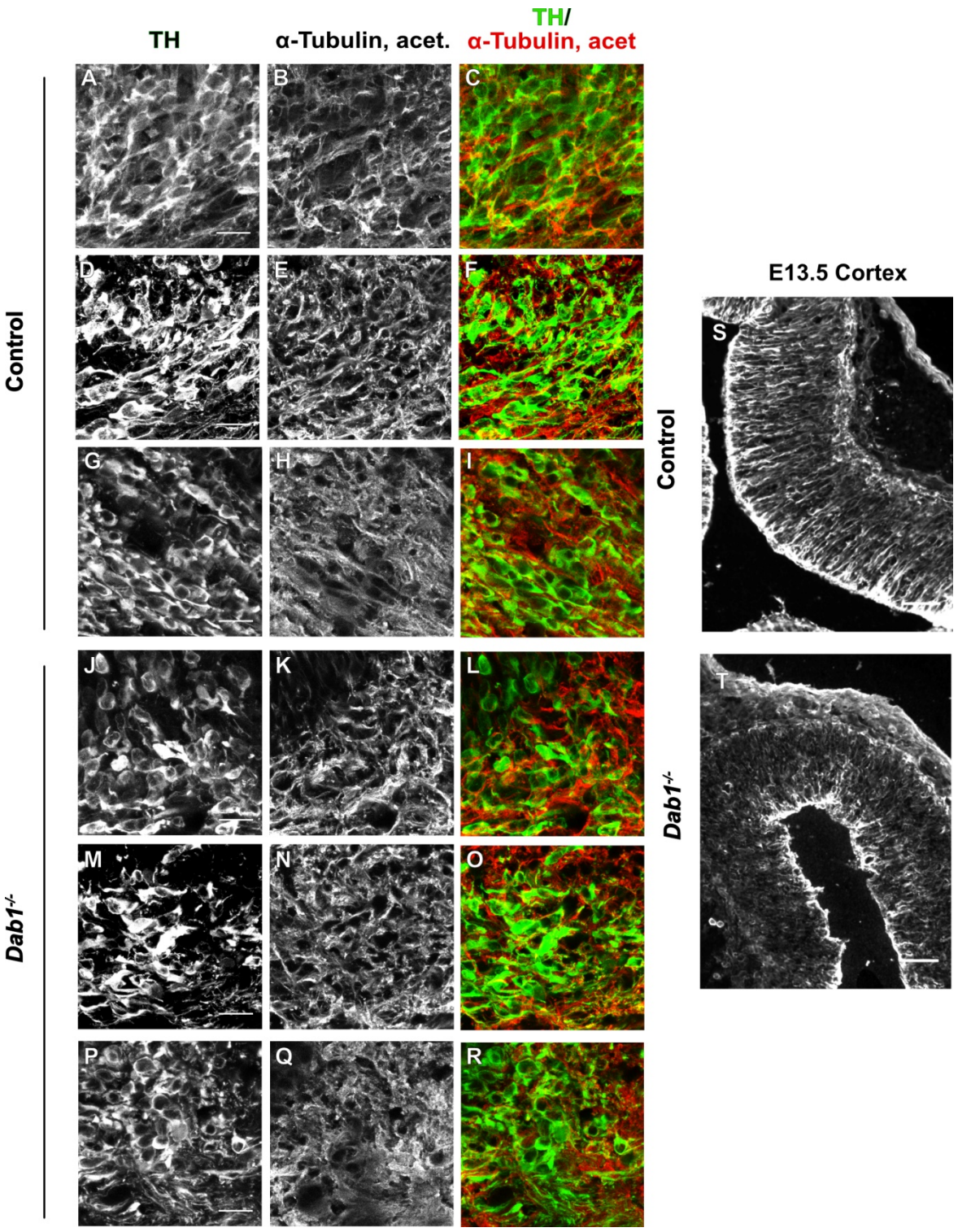

Figure 38. Acetylated α-Tubulin in control and *Dab1*$^{-/-}$ E13.5 brains. (A-I) Immunostaining for TH (A,D,G), acetylated α-Tubulin (B,E,H) and their overlap (C,F,I) in the developing lateral mDA domain of control embryos (n = 3, from 2 litters). (J-R) Immunostaining for TH (J,M,P), acetylated α-Tubulin (K,N,Q) and their overlap (L,O,R) in the developing lateral mDA domains of *Dab1*$^{-/-}$ embryos (n = 3, across 2 litters). Due to high variability in stainings of individual animals, and due to low signal-to-noise ratio in the acetylated α-Tubulin immunostainings, no definite conclusions could be drawn from the data. (T) Panel of α-Tubulin staining in the cortex is provided to demonstrate specificity of the antibody used. In this example, subtle differences in the organization of acetylated α-Tubulin can be clearly seen in *Dab1*$^{-/-}$ embryonic cortical section compared to the control.

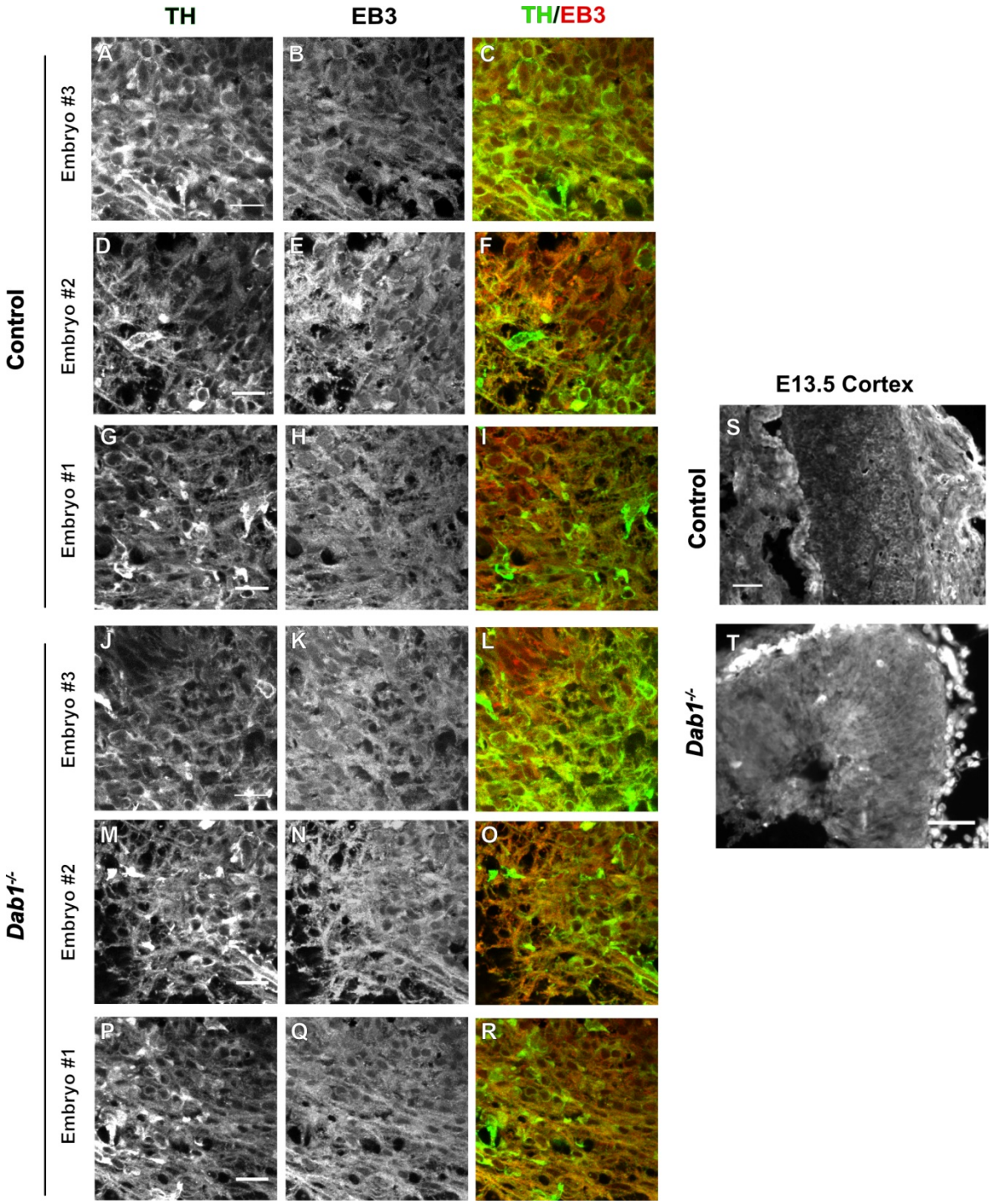

Figure 39. EB3 in control and *Dab1*$^{-/-}$ E13.5 brains. (A-I) Immunostaining for TH (A,D,G), EB3 (B,E,H) and their overlap (C,F,I) in the developing lateral mDA domain of control embryos (n = 3, from 2 litters). (J-R) Immunostaining for TH (J,M,P), EB3 (K,N,Q) and their overlap (L,O,R) in the developing lateral mDA domains of *Dab1*$^{-/-}$ embryos (n = 3, across 2 litters). Due to low signal-to-noise ratio in the EB3 immunostainings, no definite conclusions could be drawn from the data. (T) Panel of EB3 immunostaining in the cortex is provided to demonstrate specificity of the antibody used.

5. DISCUSSION

Proper tangential migration of SN-mDA neurons is essential for the anatomical separation of SN-mDA neurons from VTA-mDA neurons. To achieve this positional segregation, SN-mDA neurons must recognize specific extracellular cues and carry out the appropriate cellular maneuvers to undergo tangential migration. This study focusses on the extracellular ligand Reelin and the mechanisms by which it regulates SN-mDA tangential migration.

This study makes the following contributions:

(1) Reelin acts directly on SN-mDA neurons to regulate their tangential migration. This means that the aberrant medial location of SN-mDA neurons previously observed in mouse mutants in which components of the Reelin signaling pathway are absent.

(2) Establishes a set of live-imaging and data analysis techniques that can be used to study migration and cell morphology in the developing dopaminergic, and other neuronal populations.

(3) Provides the first comprehensive insight into speed, trajectory and morphology profiles of tangentially migrating mDA neurons, and thus furthers the understanding of the complex relationship between cell motility and cell shape during dopaminergic migration.

(4) Careful comparison of migratory and morphological behavior of mDA neurons in the presence and absence of Reelin uncovers the alterations of tangential migratory behavior that result in aberrant SN formation in the absence of Reelin signaling (**Figure 40**).

5.1. Reelin acts directly on mDA neurons and regulates correct SN formation

As described in section 1.4, Reelin acts directly on cortical projection neurons to stabilize their leading process and for their correct orientation. However, Reelin also indirectly affects cortical radial migration by regulating radial glia morphology and maturation (Hartfuss et al. 2003; Keilani and Sugaya 2008). While these diverse roles of Reelin are well established in the context of radial migration, Reelin regulation of tangential migration is less well understood. Furthermore, the effect of Reelin on tangential migration is often indirect, as seen in cortical interneurons that are mislocalized in *reeler* and *Dab1*$^{-/-}$ cortices due to improper layering caused by defective radial migration of cortical projection neurons (Yabut et al. 2007). Hence, until a recent study showed the direct role of Reelin as a stop signal in the tangential migration of sympathetic preganglionic neurons of the spinal cord, Reelin was thought to be a regulator of radial migration, with only indirect effects on tangential migration (Krüger et al. 2010).

In this study, *Dab1* was inactivated in mDA neurons at E13.5. At this embryonic age, *Dab1* mRNA is expressed in lateral regions of the mDA domain and radial migration of SN-mDA neurons is complete (Bodea et al. 2014). Hence in the *Dab1* CKO model, Reelin signaling is

inactivated only in tangentially migrating SN-mDA neurons without affecting radial migration or surrounding fibers or radial glia that could potentially act as scaffolds for mDA migration. Both *Dab1* CKO and *Dab1*$^{-/-}$ brains show a medial accumulation of SN-mDA neurons in the region of the medial VTA (**Figure 9D-N**). This similarity in the distribution of mDA neurons means that the loss of Reelin signaling specifically in tangentially migrating SN-mDA neurons has the same effect on their mediolateral positioning as the lack of Reelin signaling in the whole brain. Hence, Reelin signaling, acting directly on SN-mDA neurons, results in the correct, laterally directed migration of these neurons important for the formation of the SN.

In both *Dab1* CKO and *Dab1*$^{-/-}$ brains, medial accumulation of SN-mDA neurons is most prominent at intermediate rostrocaudal levels. While mDA neurons at anterior and posterior levels are disorganized in *Dab1* CKO and *Dab1*$^{-/-}$ brains, their mediolateral distribution is not significantly different from control littermates. Hence, while the overall decrease in mDA neurons located in the SN is roughly equal to the net gain in mDA neurons located in the VTA, this difference mainly arises due to the altered distributions at intermediate rostrocaudal levels. Why this phenotype is so restricted to a specific level on the rostrocaudal axis remains to be investigated. One reason could be that the quantitative techniques used here, whether the mediolateral grids (**Figure 9**) or the anatomical demarcation of SN and VTA (**Figure 10**) are not sensitive to subtle disorganization within these nuclei but only detect large differences in mediolateral distribution. Furthermore, as anterior regions of the dopaminergic system predominantly consist of the SN, it is not possible to quantify the relative fraction of SN and VTA-mDA neurons at these levels. At posterior levels, the SN is located ventro-lateral to the VTA resulting in a larger fraction of SN and VTA neurons being located in the same mediolateral grid. At the intermediate rostrcaudal level there is a clearer demarcation between SN and VTA-mDA neurons with most VTA neurons occupying the medial grids and SN mDA neurons occupying more lateral position allowing for an easy identification of ectopic medially-localized SN-mDA neurons. These subtle differences might be better analyzed by stereological quantifications along the rostro-caudal axis on serial sections obtained from control and *Dab1*$^{-/-}$ brains, or by comparing mDA distribution in whole-mount, cleared brains in 3D.

A few ectopic mDA neurons were also observed dorsal to the VTA, in the region of the red nucleus, not only in *Dab1*$^{-/-}$ mice but also in *Dab1* CKO (**Figure 9H,I,L,M**). This phenotype seems to suggest a radial migration defect due to some late, radial migration events. One explanation lies in the observation that a few mDA neurons, located in the dorsomedial part of the mDA domain also express DAB1 at E15.5 (**Figure 8B,C**). It is possible that the loss of *Dab1* in these neurons results in an aberrant migration into the Reelin^{+} red nucleus area. A similar effect has been reported in sympathetic preganglionic neurons of the spinal cord, where in the absence of Reelin signaling, these neurons do not stop at their final position in the intermediolateral column and migrate aberrantly instead towards the central canal (Phelps et

al. 2002). Interestingly, the number of ectopic mDA neurons in the region of the red nucleus seems to be higher at E18.5 and P21-30 than at E15.5 (**Figure 9E,H,I,L,M**) suggesting that this aberrant migration might partially occur between E13.5 to E18.5.

5.2. Reelin protein is localized to the lateral ventral midbrain during the time-window of SN-mDA tangential migration

While *Reelin* mRNA was previously reported to be expressed by the cells of the red nucleus at E13.5 and E14.5 (Bodea et al. 2014) (**Figure 12**), Reelin protein expression had not been analyzed at these time points. This study analyzes the distribution of Reelin protein and shows strong expression in the red nucleus and in regions just lateral to migrating SN-mDA neurons, while weaker staining is observed in the area where SN-mDA neurons are localized. This Reelin protein distribution is consistent with a direct role of Reelin in regulating SN-mDA tangential migration.

However, the exact source of Reelin protein, in the midbrain, remains to be uncovered. Early studies in the field posited that striatonigral axonal projections from the striatum at E16.5 were a source of Reelin in the midbrain (Nishikawa et al. 2003). However, in view of the findings of this study and previous studies, this seems unlikely as tangential migration of SN-mDA neurons is complete by E15.5 (Bodea et al. 2014) and the striatonigral system develops after E15.5 (Fishell and van der Kooy 1987). In addition, *Reelin* mRNA expression has also been reported in the hypothalamus, located anterior to migrating SN-mDA neurons, and in the ventral thalamus (Alcántara et al. 1998). While the red nucleus seems to be the most likely source of Reelin in the ventral midbrain, mouse mutants with only a partially formed red nucleus do not show any obvious defects in the positioning of SN-mDA neurons (at least not up to E18.5), suggesting that other Reelin sources could be important for mDA neuronal migration (Prakash et al. 2006). Interestingly, in horizontal orgaonotypic slices used in this study, the dorsal red nucleus is absent. This suggests that if Reelin is released by the red nucleus, the process happens before the embryonic age at which the brains were sliced (E13.5).

One way to test for the source of Reelin in organotypic slice cultures would be to treat horizontal and sagittal slices of the ventral midbrain (between E11.5-13.5) with Brefeldin A. This compound blocks the secretion of Reelin, causing the cells releasing Reelin to swell up with excess Reelin that can be detected by immunostaining (Kubasak et al. 2004). Hence, embryonic slices at ages between E11.5-E13.5 cultured with Brefeldin A could be stained for Reelin along with controls cultured with saline. Reelin-rich areas in Brefeldin A-cultured slices would then indicate possible sources for Reelin in ventral midbrain slices.

5.3. Reelin signaling is involved in the separation of SN-mDA neurons from VTA-mDA neurons

It was previously reported that medially located SN-mDA neurons continue to express GIRK2 (a marker preferentially expressed by SN-mDA neurons) in the absence of Reelin signaling. Furthermore, these GIRK2^{+} SN-mDA neurons formed a cluster separate from Calbindin^{+} VTA-mDA neurons and did not intermingle in the absence of Reelin signaling, suggesting that the ectopic location these cells, and the absence of Reelin signaling are not important for their segregation (Bodea et al. 2014). However, GIRK2 and Calbindin are not strictly specific to the SN and VTA respectively. This study confirmed that the GIRK2 mDA population, which consists of lateral VTA- and SN-mDA neurons, was clustered separate from the Calbindin population in *Dab1*$^{-/-}$ and *Dab1* CKO mice (**Figure 13**).

However, a clearer understanding was obtained when more specific markers such as *Lmo3* and SOX6 that label SN-mDA neurons, and OTX2 that labels VTA-mDA neurons, were examined. In *Dab1* CKO mice, medially misplaced SN-mDA neurons were partially intermingled with VTA-mDA neurons (**Figure 14**). Hence some subpopulations of SN-mDA neurons require Reelin signaling for their correct lateral localization, and to fully separate from their VTA counterparts.

5.4. mDA tangential migration consists of two migratory modes: slow, frequent, less-directed and fast, infrequent, highly-directed modes

Mosaic-labeling of mDA neurons in organotypic slice culture of the dopaminergic system at E13.5, combined with 2P-excitation time-lapse imaging techniques used in this study allow for the visualization of migrating mDA neurons (**Figure 15**). Most studies analyzing neuronal migration in live images have considered average soma speeds or displacements over a long duration of time as a read-out of migratory behavior (Tanaka et al. 2009; Britto et al. 2010; Watanabe and Murakami 2009; Chai et al. 2016). However, these averages ignore instantaneous changes in soma speed and their possible connections to cell shape. In this study, cell-position tracking of a large fraction of mDA neurons was used to obtain instantaneous, average and maximum soma speeds (max. speed) during the imaging interval (**Figure 16**).

In this study, no difference was found in average soma speeds of control and *Dab1*$^{-/-}$ mDA neurons. Using the same labeling and slice culture system, Bodea et al. 2014 showed a statistically significant difference in average speeds between controls and slices treated with Reelin inhibitor. This difference could be due to the duration of imaging employed in the two studies: Bodea et al. 2014 imaged slices every 10 min for 8-15 hours, while in this study, due to the severe photobleaching effects observed after 4.5-5 hours of 2P imaging, slices were imaged at 10 min intervals for 2.5-4.33 hours. Inactivating DAB1 might result in different effects

in mDA neurons compared to adding Reelin inhibitor to slices, and any one of these factors or both might be responsibe for the different results obtained by these two studies. One way to test the reason for this difference would be to image *Dab1*$^{-/-}$ slices with the imaging setup used by Bodea et al. 2014 and compare the average speed of *Dab1*$^{-/-}$ mDA neurons with control slices and slices treated with Reelin inhibitor from the Bodea et al. 2014 study. Examining the max. speed of all tracked neurons revealed a large variation among neurons. However, low max. speeds were much more commonly observed, while high max. speeds were rare (**Figure 18, 19**).

Categorizing the instantaneous soma speed of individual mDA neurons into slow, moderate and fast phases revealed that irrespective of their max-speed, mDA neurons spent a majority of their time at rest and a correspondingly small fraction of time in migration (**Figure 20; Figure 21; Table 15**). Furthermore, during their migratory phase, mDA neurons move mostly at slow speed, while fast migratory spurts that result in large soma displacements are infrequent and occur in only a subset of mDA neurons during the imaging interval (**Figure 21**). A recent study of cortical interneuron migration revealed comparable choreography of slow and fast migration, with similar relative rest and migration frequencies (Silva et al. 2018). In these neurons, periods of rest seem to be important for correct cortical invasion. Variation in instantaneous soma speeds interspersed by periods of rest, as seen in mDA neurons in this study, has also been reported for newly generated granule cells in the dentate gyrus and for cortical projection neurons (Simó, Jossin and Cooper 2010; Wang et al. 2018).

Assessing the contribution of slow, moderate and fast migratory phases to the total migratory displacement and directionality of mDA neurons showed that fast and moderate phases were directed, and resulted in large migratory displacements (**Figure 22; Figure 23**). In comparison, slow phases were less directed, resulting in frequent directional changes and a low net displacement. Correspondingly, mDA neurons that displayed only slow phases of migration, covered shorter migratory distances, and were less directed in their migration than mDA neurons that displayed moderate or fast phases. Thus, mDA tangential migration consists of two modes: a frequent, less-directed, slow mode and an infrequent, highly-directed, fast mode. Due to photobleaching effects, it was not possible to visualize individual mDA neurons in this study for the entire time-window of tangential migration (E13.5-E15.5). Hence, whether all mDA neurons are capable of the fast, directed mode of migration or whether this is a property of a subpopulation could not be answered and remains to be elucidated. This question might be answered if all labeled mDA neurons in slices could be tracked between E13.5-E15.5, but with current methods of slice culture and microscopy, this is not possible.

5.5. Reelin promotes directed migration by increasing the fraction of mDA neurons that display moderate and fast migratory modes

When speed profiles of mDA neurons in the presence and absence of Reelin signaling were compared, average speed distribution was similar between control and *Dab1*$^{-/-}$ slices (**Figure 17**). However, fewer mDA neurons in *Dab1*$^{-/-}$ slices displayed moderate or fast migratory movements compared to controls, and correspondingly, a higher fraction of *Dab1*$^{-/-}$ mDA neurons spent the entire imaging interval at rest (**Figure 18**). As moderate and fast movements are more directed than slow movements, directed migration and the net migratory displacement on the population level are also significantly decreased in *Dab1*$^{-/-}$ slices (**Figure 22; Figure 23**). These data show that Reelin promotes directed migration in mDA neurons by increasing the proportion of cells that display moderate or fast migratory behaviors.

However, the time spent by individual moderate or fast mDA neurons in rest, slow, moderate and fast migratory phases is very similar in control and *Dab1*$^{-/-}$ slices (**Figure 21**). This suggests that while Reelin promotes fast, directed migration at the population level, the migratory rhythm of moderate and fast mDA neurons is unaffected by Reelin signaling and is regulated by other signaling pathways. A recent study showed that cytosolic carboxypeptidase 1 (CC1), an enzyme involved in post-translational deglutamylation, regulates rest and migratory duration in tangentially migrating cortical interneurons without affecting their average speeds (Silva et al. 2018). Whether similar mechanisms play a role in mDA tangential migration downstream of Reelin signaling could be tested by imaging *Dab1*$^{-/-}$ slices for a longer duration (8-15 hours) using the imaging setup of Bodea et al. 2014. If the average speed of mDA neurons in *Dab1*$^{-/-}$ slices thus obtained is similar to controls, this would suggest that DAB1 promotes the frequency of fast migration without affecting the migratory rhythm of mDA neurons.

Interestingly, Reelin signaling can regulate duration of rest and migration in radially migrating cortical projection neurons: in the absence of the E3 ubiquitin Ligase Cullin-5, reduced ubiquitination and degradation increases levels of activated DAB1 in these neurons. As a result, periods of rest are decreased, and average as well as instantaneous speed, and net migratory distance are increased during late stages of cortical migration (E16.5) (Simó, Jossin and Cooper 2010). While rest and migratory duration in mDA neurons is unaffected by Reelin signaling, the results of the aforementioned study are consistent with the effect of Reelin on the net migratory distance, and higher max. speeds of mDA neurons observed in this study.

In contrast to the study by Simó, Jossin and Cooper 2010, a recent study showed that the average speed of cortical neurons of *reeler* mutants is not significantly altered compared to controls of the same age (Chai et al. 2016). Yet another examination of cortical projection neurons as they transition from multipolar to bipolar phase at E15.5, suggested that cortical neurons migrate faster in the absence of Reelin signaling (Britto et al. 2010), while addition of

exogenous Reelin slowed down migrating neurons, but only within the subventricular zone (Britto et al. 2013). Thus, even in the same neuronal population, Reelin signaling might have diverse effects on the speed of neuronal migration at different stages of migration, based on the genetic models used and the exact anatomical location of neurons being studied.

5.6. Reelin promotes the inherent preference for lateral direction in tangentially migrating mDA neurons during their slow migratory phase

Analysis of trajectories of control mDA neurons reveals that independent of their max. or instantaneous speeds, all mDA neurons have a slight preference for laterally-directed movements (**Figure 25A,D,G; Figure 26A,C,E**). However, highly-directed, moderate and fast migratory movements are predominantly lateral in direction (**Figure 26C,E**). Hence, the mDA neurons that display moderate and fast movements also have laterally-directed trajectories (**Figure 25D,G**). In *Dab1*$^{-/-}$ slices, slow migratory movements, and hence mDA neurons that only undergo slow phase of migration, lose their slight lateral preference and are significantly more isotropic compared to controls (**Figure 25A,B; Figure 26A,B**). It is possible that the loss of the laterally-directed slow movements interferes with the ability of mDA neurons to initiate moderate and fast, laterally-directed spurts, thereby decreasing the fraction of cells displaying these behaviors in *Dab1*$^{-/-}$ slices. Laterally-directed slow movements might also be important for mDA neurons to make small changes in position that allow them to adopt the correct lateral orientation before they make fast, laterally-directed jumps. This hypothesis would be consistent with previous findings that reported an aberrant orientation of mDA neurons, where mDA neurons were oriented parallel to the midline or even towards the midline at E13.5 in *reeler* brains (Bodea et al. 2014).

Interestingly, while moderate and fast migratory events are less likely in the overall *Dab1*$^{-/-}$ mDA population, individual moderate and fast movements are equally laterally-directed in *Dab1*$^{-/-}$ mDA neurons as in controls (**Figure 25F,I; Figure 26C-F,** data not shown). This means that while Reelin promotes anisotropy towards lateral directions in slow movements, some other mechanism(s) unaffected by Reelin signaling ensures that moderate and fast movements are predominantly laterally directed or that only laterally directed movements can reach higher speeds.

Many lines of evidence have established Reelin as a regulator of cell orientation, migratory direction and polarity: Reelin is important for the directionality of cortical projection neurons in their early phase of migration. In the absence of Reelin signaling, as well as in the presence of exogenous Reelin, these neurons deviate from radial migratory trajectories (Britto et al. 2010; Britto et al. 2013; Chai et al. 2016). Reelin regulates cell polarity of multipolar cortical projection neurons in the intermediate zone and thus facilitates their switch to bipolar, glia-dependent migration (Jossin and Cooper 2011; Gärtner et al. 2012; Gil-Sanz et al. 2013). In

the developing hippocampus, Reelin promotes directionality during the radial migration of dentate gyrus cells (Wang et al. 2018). Interestingly, a recent study reports a disruption in directed migratory behavior, in neurosphere assays, of mDA neurons derived from induced pluripotent stem cells that are homozygous or heterozygous for a *Reelin* deletion. Hence, in the absence of any organized tissue structure, Reelin signaling appears to modulate mDA neurons' directed migration independent of a specific pattern of Reelin protein deposition in the surrounding tissue (Arioka et al. 2018). These findings might suggest that Reelin signaling in mDA neurons does not guide their migration but encourages directed migration in slow movements thereby promoting the likelihood of moderate and fast, laterally-directed spurts. Other cues that ensure lateral direction of these moderate and fast spurts remain to be identified. Finally, on the population level, increased isotropy of slow movements in *Dab1*$^{-/-}$ slices is associated with an increased fraction of mDA neurons that only undergo slow migration mode. Together, these two factors significantly reduce lateral anisotropy in the *Dab1*$^{-/-}$ mDA population (**Figure 24**).

5.7. Reelin stabilizes SN-mDA cell morphology

Detailed examination of cellular morphologies underlying the migration of cortical projection neurons and interneurons has provided a deeper understanding of distinct molecular and developmental mechanisms that regulate cell movements of diverse populations (Nadarajah et al. 2001; Noctor et al. 2004; Martini et al. 2008). This study provides the first insight into cell morphology underlying mDA tangential migration.

mDA neurons transition between multipolar and bipolar morphologies (**Figure 27B, Figure 28C**). While mDA bipolar morphology is much more prevalent than multipolar morphology, moderate and fast movements of mDA neurons are almost always associated with bipolar morphologies (**Figure 28**). In contrast, about 30% of slow phases are associated with multipolar morphology. This result is true for both control and *Dab1*$^{-/-}$ slices.

However, in control slices, more than 50% of the observed mDA neurons maintain a bipolar morphology throughout the imaging period, about 40% transition between multipolar and bipolar morphologies and only 10% of cells stay multipolar throughout the imaging interval (**Figure 29A**). In absence of Reelin signaling, the percentage of transitionary cells is significantly increased, and correspondingly, the proportion of stable bipolar cells is decreased. Interestingly, the increase in the proportion of transitionary cells in *Dab1*$^{-/-}$ slices is particularly pronounced in the mDA population that displays isotropic, slow movements suggesting a correlation between loss of anisotropy in these cells and increased transitioning between bipolar and multipolar morphology (**Table 15**).

Furthermore, a significantly higher number of small protrusions are observed along the LP of transitionary cells of *Dab1*$^{-/-}$ slices compared to controls, indicating decreased branch

stability (**Figure 30**). The length of the LP is significantly more variable in *Dab1*$^{-/-}$ than in control neurons (**Figure 31**). Thus, Reelin signaling appears to promote stability of morphologies. Whether this is due to the direct action of Reelin or whether aberrant morphologies are observed due to ectopic, relatively medial positions of mDA neurons in *Dab1*$^{-/-}$ slices is not completely clear.

Reelin is an established regulator of cell morphology. Cortical projection neurons in organotypic slices display increased multipolar morphology when exposed to exogenous Reelin. Moreoever, the increase in multipolarity in these neurons is accompanied by reduced migratory speeds (Britto et al. 2013). In dissociated cortical neuronal cultures, Reelin signaling, via activation of CDC42, causes an increase in filopodia formation (Leemhuis et al. 2010). Reelin signaling is also required to maintain a stable LP during the final somal translocation step of cortical neurons (Franco et al. 2011; Chai et al. 2016). Finally, a recent study has reported an increase in multipolar neurons in the subventricular zone of the cortex in the absence of DAB1 phosphorylation via the Netrin-DCC pathway (Zhang et al. 2018).

An indirect regulation of morphology by Reelin signaling has also been reported in tangentially-migrating cortical interneurons. Branching of LPs in these neurons is important for their precise sensing of the extracellular environment during chemotaxis (Martini et al. 2008). In the *reeler* cortex, interneurons that are in the wrong layer of the cortex due to mislayering, display a significantly higher number of branch nodes and higher length of LPs than interneurons in control brains (Yabut et al. 2007). Since interneurons do not directly require Reelin signaling for their migration, it is likely that their aberrant morphology in the *reeler* cortex is an indirect effect of their altered position. As similar effects on cell morphology are observed in *Dab1*$^{-/-}$ mDA neurons, it is tempting to suggest that the aberrant mDA neuronal morphology may be a consequence of an increased scanning of the environment for guidance cues in ectopic medial positions. This could be tested by establishing a method to transplant lateral SN-mDA neurons into medial regions of E13.5 horizontal slices to observe their morphology.

5.8. Downstream of the Reelin signaling pathway in SN-mDA neurons

To understand which molecules are downstream of Reelin in mDA neurons, generation of conditional knockouts, immunostainings for candidate proteins and western blot to detect differences in phosphorylation levels of potential downstream targets were carried out (**Figure 34, 35**).

Cofilin 1 has been shown to stabilize the LPs of migrating cortical neurons downstream of Reelin signaling through activated LIMK1 (Chai et al. 2009; Chai et al. 2016). To examine the role of Cofilin 1, downstream of Reelin in mDA neurons' tangential migration, conditional knockouts were generated for Cofilin 1 under the *Dat* promoter on an *ADF* null background, similar to the conditional knockouts generated for DAB1. Unlike the *Dab1* CKO conditional

knockouts, no difference was seen in the mediolateral positioning of mDA neurons in the *ADF$^{-/-}$; Cofilin 1* CKO mice (**Figure 34)**.

While it is tempting to assume that this result rules out Cofilin 1 as a potential downstream target of Reelin in mDA neurons, such a conclusion cannot be drawn unless the absence of Cofilin 1 protein is confirmed in mDA domains by E15.5. This is important as it has been previously reported that Cofilin 1 has a long half-life and residual Cofilin 1 protein could still be detected in brain tissue upto 4 days after Cre-mediated deletion of *Cofilin 1* (Bellenchi et al. 2007). Hence, it is possible that *DAT^{Cre}* mediated deletion of *Cofilin 1*, which starts at E13.5, does not result in a timely inactivation of Cofilin 1 protein by E15.5. To investigate whether Cofilin 1 is indeed inactivated in mDA neurons of *ADF$^{-/-}$; Cofilin 1* CKO mice by E15.5, FACS (fluorescence-assisted cell sorting) to determine cells in which Cre-mediated recombination has occurred will be required, followed by sensitive western-blot analysis to detect Cofilin 1 protein levels in recombined cells. These experiments are outside the scope of the current study and hence no conclusion can be drawn from the experiments carried out on *ADF$^{-/-}$; Cofilin 1* CKO mice.

As an alternative approach to investigating the role of Cofilin 1 in mDA migration and to detect a misregulation for Cofilin 1 downstream of Reelin, the relative levels of phosphorylation of p-LIMK1/LIMK1 and p-Cofilin 1/Cofilin 1 were assessed by western blots in control and *Dab1$^{-/-}$* ventral midbrain tissue at E14.5. No significant differences in protein levels or in relative phosphorylation levels were detected by this method, suggesting that the LIMK1-Cofilin 1 branch of the Reelin signaling downstream pathway might not be involved in mDA migration (**Figure 35**).

It has previously been demonstrated that the regulation of membrane localization of CDH2 via the Crk/CrkL-C3G-Rap1 pathway at the cell surface is important for the effect of Reelin on the polarity of cortical projection neurons during their migration (Franco et al. 2011; Sekine et al. 2012; Park and Curran 2008; Voss et al. 2008). No obvious differences were detected in the overall expression levels by westen blots on control and *Dab1$^{-/-}$* tissue, or by immunostainings carried out for CDH2 on E14.5 control and *Dab1$^{-/-}$* brains to investigate any abnormalities in membrane localization of CDH2 (**Figure 36**). However, it is possible that subtle differences in CDH2 membrane localization may have been missed due to the low signal-to-noise ratio of the immunostainings. More sensitive immunostaining methods might shed further light on this question.

It was also surprising that no obvious differences were detected by immunostaining experiments for microtublule dynamics and stability factors Tubulin, acetylated Tubulin and EB3 (**Figure 37-39**). One factor common to these and the CDH2 immunostaining experiments is the dense, clustered arrangement of mDA neurons *in vivo* at E13.5-14.5 (stage at which these experiments were carried out). In laminar brain structures, the layered organization of

migrating neurons allows for easier detection of neuronal disorganization. Furtheremore, layered arrangement of cells makes it easer to identify changes in subcellular localization of proteins. Hence the lack of an obvious spatial organization in clustered mDA nuclei, make the detection of disorganization in subcellular membrane and microtubule-protein localization harder. *In vitro* experiments in migration assays carried out on primary mDA neurons in culture will be needed to shed more light on the question of disruption of CDH2, or changes in microtubule dynamics and stability in mDA neurons in the absence of Reelin signaling. Migration assays of primary *Dab1*$^{-/-}$ mDA neurons, wildtype mDA neurons treated with Reelin inhibitor, and wildtype mDA neurons treated with saline (control) could be immunostained for CDH2, Tubulin, acetylated Tubulin and EB3. In this way, differences that might have been missed in dense mDA neuronal clusters in fixed sections might be detected in a monolayer of cultured mDA neruons.

5.9. Potential signaling pathways in SN-mDA neurons

Other potential signaling events that could influence mDA migration are those that have been shown to influence cortical migration downstream or in parallel to Reelin signaling: Integrin α5ß1 or the Netrin1-DCC pathway are possible candidates. The knockdown of integrin α5ß1 in cortical neurons affects apical process stability during terminal translocation suggesting that additional adhesion molecules may be recruited by Reelin signaling (Sekine et al. 2012). In the cortex, both CDH2 and integrin α5ß1 act downstream of Reelin: integrin α5ß1 anchors the leading tip of terminally translocating neurons in the marginal zone, while CDH2 regulates subsequent cell movements (Sekine et al. 2014). Interestingly, integrin α5ß1 is important for stabilizing neurite extensions of mDA neurons in vitro. Whether it plays a general role in stabilizing neuronal processes in mDA neurons, including LPs, and in mDA migration has not been explored (Izumi et al. 2017). Recently, Netrin1-DCC and Reelin–DAB1 pathways have been shown to cross-regulate each other in migration of cortical projection neurons (Zhang et al. 2018). The Netrin1–DCC pathway is also important for proper localization of SN-mDA neurons during development (Xu et al. 2010; Li et al. 2014). Though the effect on mDA distribution induced by *Dcc* inactivation differs from the effect caused by *Dab1* inactivation, it is possible that effectors downstream of the Netrin1-DCC pathway, such as focal adhesion kinase may play a role in mediating Reelin signal in mDA neurons (Zhang et al. 2018). A comprehensive and sensitive screen, for differences in expression and activation levels of the abovementioned potential candidiates will have to be carried out before the downstream targets of Reelin signaling in mDA neurons can be delineated. This screening process could involve examining the expression levels (upregulation or downregulation) of potential candidates in *Dab1*$^{-/-}$ mDA neurons compared to controls, to identify which genes are differently expressed in the absence of Reelin signaling.

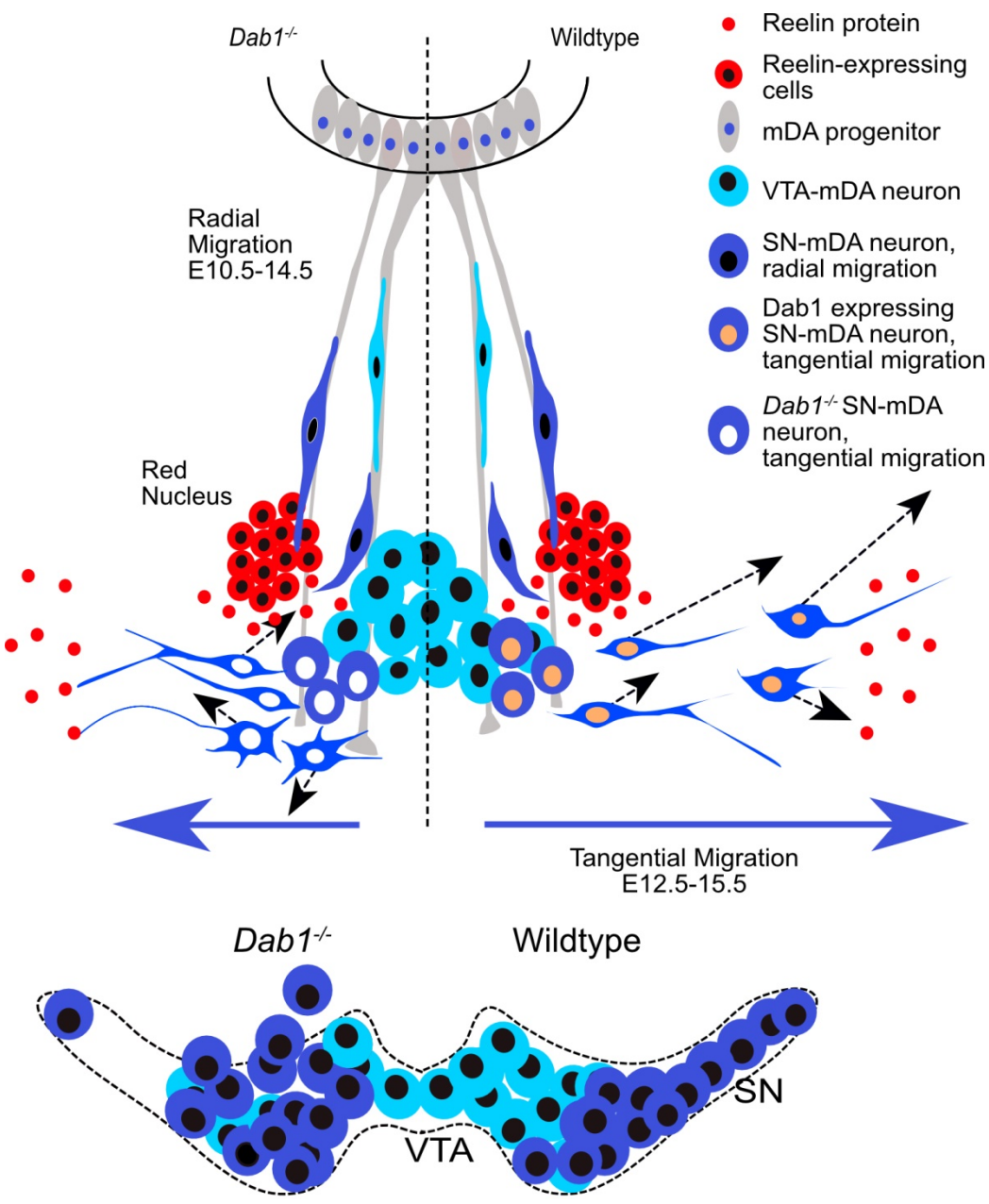

Figure 40. Reelin regulation in mDA tangential migration. Reelin directly regulates lateral, tangential migration of mDA neurons. It promotes fast, laterally directed mode of migration by promoting a preference for small lateral movements and stabilizing morphology of mDA neurons. In absence of Reelin signaling, slow movements in mDA neurons lose their lateral anisotropy, morphologies are less stable during migration and the fraction of neurons undergoing fast, laterally directed migration is significantly reduced. This results in a medial clustering of SN-mDA neurons at late embryonic and postnatal stages. Figure modified from (Vaswani et al. 2019).

6. CONCLUSION

This study provides evidence for the direct involvement of Reelin in the lateral migration of SN-mDA neurons and delineates the migratory speeds, trajectories and cellular morphologies that underlie this process. Data presented here demonstrate complex regulation of tangential mDA neuronal migration by Reelin signaling: Reelin promotes lateral anisotropy in small migratory movements, increases the frequency of fast lateral movements and stabilizes the leading process morphology of migrating mDA neurons. In the absence of Reelin signaling, slow migratory movements are no longer predominantly lateral in direction and fewer mDA neurons make moderate-to fast lateral jumps. This results in reduced tangential displacement and an ectopic medial location of mDA neurons. The model for Reelin action presented in this study (**Figure 40**), while similar to the mechanism observed in the formation of laminar structures, differs in several essential ways. Hence this study provides novel insight into how Reelin might regulate tangential migration in the formation of neuronal clusters.

By establishing an imaging and data analysis pipeline that allows for detailed characterization of mDA migration, this study paves the way for further identification of molecules that regulate mDA migration downstream of Reelin. The experimental setup used in this study can also be used to dissect other signaling pathways, such as the Netrin-DCC pathway, that regulate mDA neuronal migration.

7. REFERENCES

Albin, R. L., Young, A. B., & Penney, J. B. (1989). The functional anatomy of basal ganglia disorders. *Trends in neurosciences*, *12*(10), 366-375. doi: 10.1016/0166-2236(89)90074-X

Alcántara, S., Ruiz, M., D'Arcangelo, G., Ezan, F., de Lecea, L., Curran, T., ... & Soriano, E. (1998). Regional and cellular patterns of reelin mRNA expression in the forebrain of the developing and adult mouse. *Journal of Neuroscience*, *18*(19), 7779-7799.

Allard, J., & Mogilner, A. (2013). Traveling waves in actin dynamics and cell motility. *Current opinion in cell biology*, *25*(1), 107-115. doi:10.1016/j.ceb.2012.08.012.

Anderegg, A., Poulin, J. F., & Awatramani, R. (2015). Molecular heterogeneity of midbrain dopaminergic neurons–Moving toward single cell resolution. *FEBS letters*, *589*(24PartA), 3714-3726. doi:10.1016/j.febslet.2015.10.022.

Anderson, S. A., Eisenstat, D. D., Shi, L., & Rubenstein, J. L. R. (1997). Interneuron migration from basal forebrain to neocortex: dependence on Dlx genes. *Science*, *278*(5337), 474-476. doi:10.1126/science.278.5337.474.

Andersson, E., Tryggvason, U., Deng, Q., Friling, S., Alekseenko, Z., Robert, B., ... & Ericson, J. (2006). Identification of intrinsic determinants of midbrain dopamine neurons. *Cell*, *124*(2), 393-405. doi: 10.1016/j.cell.2005.10.037.

Andrianantoandro, E., & Pollard, T. D. (2006). Mechanism of actin filament turnover by severing and nucleation at different concentrations of ADF/cofilin. *Molecular cell*, *24*(1), 13-23. doi: 10.1016/j.molcel.2006.08.006.

Ang, S. L. (2006). Transcriptional control of midbrain dopaminergic neuron development. *Development*, *133*(18), 3499-3506. doi:10.1242/dev.02501.

Anthony, T. E., Klein, C., Fishell, G., & Heintz, N. (2004). Radial glia serve as neuronal progenitors in all regions of the central nervous system. *Neuron*, *41*(6), 881-890. doi: 10.1016/S0896-6273(04)00140-0. doi: 10.1016/S0896-6273(04)00140-0.

Arenas, E. (2014). Wnt signaling in midbrain dopaminergic neuron development and regenerative medicine for Parkinson's disease. *Journal of molecular cell biology*, *6*(1), 42-53.

Arioka, Y., Shishido, E., Kubo, H., Kushima, I., Yoshimi, A., Kimura, H., ... & Kuzumaki, N. (2018). Single-cell trajectory analysis of human homogenous neurons carrying a rare RELN variant. *Translational psychiatry*, *8*(1), 129.

Austin, C. P., & Cepko, C. L. (1990). Cellular migration patterns in the developing mouse cerebral cortex. *Development*, *110*(3), 713-732.

Ayala, R., Shu, T., & Tsai, L. H. (2007). Trekking across the brain: the journey of neuronal migration. *Cell*, *128*(1), 29-43. doi:10.1016/j.cell.2006.12.021.

Bagri, A., Gurney, T., He, X., Zou, Y. R., Littman, D. R., Tessier-Lavigne, M., & Pleasure, S. J. (2002). The chemokine SDF1 regulates migration of dentate granule cells. *Development*, *129*(18), 4249-4260.

Ballif, B. A., Arnaud, L., & Cooper, J. A. (2003). Tyrosine phosphorylation of Disabled-1 is essential for Reelin-stimulated activation of Akt and Src family kinases. *Molecular brain research*, *117*(2), 152-159. doi:10.1016/S0169-328X(03)00295-X.

Bartolini, G., Ciceri, G., & Marín, O. (2013). Integration of GABAergic interneurons into cortical cell assemblies: lessons from embryos and adults. *Neuron*, *79*(5), 849-864. doi:10.1016/j.neuron.2013.08.014.

Baudoin, J. P., Alvarez, C., Gaspar, P., & Metin, C. (2008). Nocodazole-induced changes in microtubule dynamics impair the morphology and directionality of migrating medial ganglionic eminence cells. *Developmental neuroscience*, *30*(1-3), 132-143. doi:10.1159/000109858.

Baudoin, J. P., Viou, L., Launay, P. S., Luccardini, C., Gil, S. E., Kiyasova, V., ... & Lechaire, J. P. (2012). Tangentially migrating neurons assemble a primary cilium that promotes their reorientation to the cortical plate. *Neuron*, *76*(6), 1108-1122. doi:10.1016/j.neuron.2012.10.027.

Bayer, S. A., Wills, K. V., Triarhou, L. C., & Ghetti, B. (1995). Time of neuron origin and gradients of neurogenesis in midbrain dopaminergic neurons in the mouse. *Experimental brain research*, *105*(2), 191-199.

Beier, K. T., Steinberg, E. E., DeLoach, K. E., Xie, S., Miyamichi, K., Schwarz, L., ... & Luo, L. (2015). Circuit architecture of VTA dopamine neurons revealed by systematic input-output mapping. *Cell*, *162*(3), 622-634. doi:10.1016/j.cell.2015.07.015.

Bellenchi, G. C., Gurniak, C. B., Perlas, E., Middei, S., Ammassari-Teule, M., & Witke, W. (2007). N-cofilin is associated with neuronal migration disorders and cell cycle control in the cerebral cortex. *Genes & development*, *21*(18), 2347-2357. doi:10.1101/gad.434307.

Bellion, A., Baudoin, J. P., Alvarez, C., Bornens, M., & Métin, C. (2005). Nucleokinesis in tangentially migrating neurons comprises two alternating phases: forward migration of the Golgi/centrosome

associated with centrosome splitting and myosin contraction at the rear. *Journal of Neuroscience*, *25*(24), 5691-5699. doi:10.1523/JNEUROSCI.1030-05.2005.

Bentivoglio, M., & Mazzarello, P. (1999). The history of radial glia. *Brain research bulletin*, *49*(5), 305-315. doi:10.1016/S0361-9230(99)00065-9

Berens, P. (2009). CircStat: a MATLAB toolbox for circular statistics. *J Stat Softw*, *31*(10), 1-21. doi:10.18637/jss.v031.i10.

Bifsha, P., Balsalobre, A., & Drouin, J. (2017). Specificity of pitx3-dependent gene regulatory networks in subsets of midbrain dopamine neurons. *Molecular neurobiology*, *54*(7), 4921-4935. doi:10.1007/s12035-016-0040-y.

Björklund, A., & Dunnett, S. B. (2007a). Dopamine neuron systems in the brain: an update. *Trends in neurosciences*, *30*(5), 194-202. doi:10.1016/j.tins.2007.03.006.

Björklund, A., & Dunnett, S. B. (2007b). Fifty years of dopamine research. *Trends in neurosciences*, *30*(5), 185-187. doi:10.1016/j.tins.2007.03.004.

Blaess, S., & Ang, S. L. (2015). Genetic control of midbrain dopaminergic neuron development. *Wiley Interdisciplinary Reviews: Developmental Biology*, *4*(2), 113-134. doi:10.1002/wdev.169.

Blaess, S., Bodea, G. O., Kabanova, A., Chanet, S., Mugniery, E., Derouiche, A., ... & Joyner, A. L. (2011). Temporal-spatial changes in Sonic Hedgehog expression and signaling reveal different potentials of ventral mesencephalic progenitors to populate distinct ventral midbrain nuclei. *Neural development*, *6*(1), 29. doi:10.1186/1749-8104-6-29.

Blaess, S., Corrales, J. D., & Joyner, A. L. (2006). Sonic hedgehog regulates Gli activator and repressor functions with spatial and temporal precision in the mid/hindbrain region. *Development*, *133*(9), 1799-1809. doi:10.1242/dev.02339.

Bodea, G. O., & Blaess, S. (2012). Organotypic slice cultures of embryonic ventral midbrain: a system to study dopaminergic neuronal development in vitro. *JoVE (Journal of Visualized Experiments)*, (59), e3350. doi:10.3791/3350.

Bodea, G. O., Spille, J. H., Abe, P., Andersson, A. S., Acker-Palmer, A., Stumm, R., ... & Blaess, S. (2014). Reelin and CXCL12 regulate distinct migratory behaviors during the development of the dopaminergic system. *Development*, *141*(3), 661-673. doi:10.1242/dev.099937.

Bravo-Cordero, J. J., Magalhaes, M. A., Eddy, R. J., Hodgson, L., & Condeelis, J. (2013). Functions of cofilin in cell locomotion and invasion. *Nature reviews Molecular cell biology*, *14*(7), 405. doi:10.1038/nrm3609.

Britto, J. M., Tait, K. J., Johnston, L. A., Hammond, V. E., Kalloniatis, M., & Tan, S. S. (2010). Altered speeds and trajectories of neurons migrating in the ventricular and subventricular zones of the reeler neocortex. *Cerebral cortex*, *21*(5), 1018-1027.

Britto, J. M., Tait, K. J., Lee, E. P., Gamble, R. S., Hattori, M., & Tan, S. S. (2013). Exogenous Reelin modifies the migratory behavior of neurons depending on cortical location. *Cerebral Cortex*, *24*(11), 2835-2847.

Bromberg-Martin, E. S., Matsumoto, M., & Hikosaka, O. (2010). Dopamine in motivational control: rewarding, aversive, and alerting. *Neuron*, *68*(5), 815-834. doi:10.1016/j.neuron.2010.11.022.

Butt, S. J., Fuccillo, M., Nery, S., Noctor, S., Kriegstein, A., Corbin, J. G., & Fishell, G. (2005). The temporal and spatial origins of cortical interneurons predict their physiological subtype. *Neuron*, *48*(4), 591-604. doi: 10.1016/j.neuron.2005.09.034.

Bye, C. R., Thompson, L. H., & Parish, C. L. (2012). Birth dating of midbrain dopamine neurons identifies A9 enriched tissue for transplantation into Parkinsonian mice. *Experimental neurology*, *236*(1), 58-68.

Chai, X., Zhao, S., Fan, L., Zhang, W., Lu, X., Shao, H., ... & Mannherz, H. G. (2016). Reelin and cofilin cooperate during the migration of cortical neurons: a quantitative morphological analysis. *Development*, *143*(6), 1029-1040. doi:10.1242/dev.134163.

Chai, X., Förster, E., Zhao, S., Bock, H. H., & Frotscher, M. (2009). Reelin stabilizes the actin cytoskeleton of neuronal processes by inducing n-cofilin phosphorylation at serine3. *Journal of Neuroscience*, *29*(1), 288-299. doi:10.1523/JNEUROSCI.2934-08.2009.

Chai, X., Münzner, G., Zhao, S., Tinnes, S., Kowalski, J., Häussler, U., ... & Frotscher, M. (2013). Epilepsy-induced motility of differentiated neurons. *Cerebral cortex*, *24*(8), 2130-2140. doi:10.1093/cercor/bht067.

Chédotal, A., & Rijli, F. M. (2009). Transcriptional regulation of tangential neuronal migration in the developing forebrain. *Current opinion in neurobiology*, *19*(2), 139-145. doi:10.1016/j.conb.2009.04.005.

Cohen, J. Y., Haesler, S., Vong, L., Lowell, B. B., & Uchida, N. (2012). Neuron-type-specific signals for reward and punishment in the ventral tegmental area. *nature*, *482*(7383), 85.

Cooper, J. A. (2008). A mechanism for inside-out lamination in the neocortex. *Trends in neurosciences*, *31*(3), 113-119. doi:10.1016/j.tins.2007.12.003.

Cooper, J. A. (2014). Molecules and mechanisms that regulate multipolar migration in the intermediate

zone. *Frontiers in cellular neuroscience*, *8*, 386. doi:10.3389/fncel.2014.00386.
Corbin, J. G., & Butt, S. J. (2011). Developmental mechanisms for the generation of telencephalic interneurons. *Developmental neurobiology*, *71*(8), 710-732. doi:10.1002/dneu.20890.
D'Arcangelo, G. (2014). Reelin in the years: controlling neuronal migration and maturation in the mammalian brain. *Advances in Neuroscience*, *2014*. doi:10.1155/2014/597395.
D'arcangelo, G., Miao, G. G., Chen, S. C., Scares, H. D., Morgan, J. I., & Curran, T. (1995). A protein related to extracellular matrix proteins deleted in the mouse mutant reeler. *Nature*, *374*(6524), 719. doi:10.1038/374719a0.
Da Silva, J. S., & Dotti, C. G. (2002). Breaking the neuronal sphere: regulation of the actin cytoskeleton in neuritogenesis. *Nature Reviews Neuroscience*, *3*(9), 694. doi:10.1038/nrn918.
Dahlström, A., & Fuxe, K. (1964). Localization of monoamines in the lower brain stem. *Cellular and Molecular Life Sciences*, *20*(7), 398-399. doi:10.1007/BF02147990.
Danielian, P. S., & McMahon, A. P. (1996). Engrailed-1 as a target of the Wnt-1 signalling pathway in vertebrate midbrain development. *Nature*, *383*(6598), 332. doi:10.1038/383332a0.
de Anda, F. C., Meletis, K., Ge, X., Rei, D., & Tsai, L. H. (2010). Centrosome motility is essential for initial axon formation in the neocortex. *Journal of Neuroscience*, *30*(31), 10391-10406. doi:10.1523/JNEUROSCI.0381-10.2010.
Dent, E. W., Gupton, S. L., & Gertler, F. B. (2011). The growth cone cytoskeleton in axon outgrowth and guidance. *Cold Spring Harbor perspectives in biology*, *3*(3), a001800. doi:10.1101/cshperspect.a001800.
Devreotes, P., & Horwitz, A. R. (2015). Signaling networks that regulate cell migration. *Cold Spring Harbor perspectives in biology*, *7*(8), a005959. doi:10.1101/cshperspect.a005959.
Di Salvio, M., Di Giovannantonio, L. G., Omodei, D., Acampora, D., & Simeone, A. (2009). Otx2 expression is restricted to dopaminergic neurons of the ventral tegmental area in the adult brain. *International Journal of Developmental Biology*, *54*(5), 939-945. doi:10.1387/ijdb.092974ms.
Drakew, A., Deller, T., Heimrich, B., Gebhardt, C., Del Turco, D., Tielsch, A., ... & Frotscher, M. (2002). Dentate granule cells in reeler mutants and VLDLR and ApoER2 knockout mice. *Experimental neurology*, *176*(1), 12-24. doi:10.1006/exnr.2002.7918.
Dulabon, L., Olson, E. C., Taglienti, M. G., Eisenhuth, S., McGrath, B., Walsh, C. A., ... & Anton, E. S. (2000). Reelin binds α3β1 integrin and inhibits neuronal migration. *Neuron*, *27*(1), 33-44. doi:10.1016/S0896-6273(00)00007-6.
Edmondson, J. C., Liem, R. K., Kuster, J. E., & Hatten, M. E. (1988). Astrotactin: a novel neuronal cell surface antigen that mediates neuron-astroglial interactions in cerebellar microcultures. *The Journal of cell biology*, *106*(2), 505-517.
Ekstrand, M. I., Terzioglu, M., Galter, D., Zhu, S., Hofstetter, C., Lindqvist, E., ... & Hoffer, B. (2007). Progressive parkinsonism in mice with respiratory-chain-deficient dopamine neurons. *Proceedings of the National Academy of Sciences*, *104*(4), 1325-1330. doi:10.1073/pnas.0605208103.
Elias, L. A., Turmaine, M., Parnavelas, J. G., & Kriegstein, A. R. (2010). Connexin 43 mediates the tangential to radial migratory switch in ventrally derived cortical interneurons. *Journal of Neuroscience*, *30*(20), 7072-7077. doi:10.1523/JNEUROSCI.5728-09.2010.
Elias, L. A., Wang, D. D., & Kriegstein, A. R. (2007). Gap junction adhesion is necessary for radial migration in the neocortex. *Nature*, *448*(7156), 901. doi:10.1038/nature06063.
Evsyukova, I., Plestant, C., & Anton, E. S. (2013). Integrative mechanisms of oriented neuronal migration in the developing brain. *Annual review of cell and developmental biology*, *29*, 299-353. doi:10.1146/annurev-cellbio-101512-122400.
Falck, B., Hillarp, N. Å., Thieme, G., & Torp, A. A. (1962). Fluorescence of catechol amines and related compounds condensed with formaldehyde. *Journal of histochemistry & cytochemistry*, *10*(3), 348-354. doi:10.1177/10.3.348.
Falconer, D. S. (1951). Two new mutants,'trembler'and 'reeler', with neurological actions in the house mouse (Mus musculus L.). *Journal of genetics*, *50*(2), 192-205.
Fernández-Barrera, J., & Alonso, M. A. (2018). Coordination of microtubule acetylation and the actin cytoskeleton by formins. *Cellular and molecular life sciences*, *75*(17), 3181-3191.
Fishell, G., & van der Kooy, D. (1987). Pattern formation in the striatum: developmental changes in the distribution of striatonigral neurons. *Journal of Neuroscience*, *7*(7), 1969-1978.
Flynn, K. C., Hellal, F., Neukirchen, D., Jacob, S., Tahirovic, S., Dupraz, S., ... & Meyn, L. (2012). ADF/cofilin-mediated actin retrograde flow directs neurite formation in the developing brain. *Neuron*, *76*(6), 1091-1107. doi: 10.1016/j.neuron.2012.09.038.
Flynn, K. C. (2013). The cytoskeleton and neurite initiation. *Bioarchitecture*, *3*(4), 86-109. doi:10.4161/bioa.26259.
Fogarty, M., Grist, M., Gelman, D., Marín, O., Pachnis, V., & Kessaris, N. (2007). Spatial genetic patterning of the embryonic neuroepithelium generates GABAergic interneuron diversity in the adult cortex. *Journal of Neuroscience*, *27*(41), 10935-10946. doi:10.1523/JNEUROSCI.1629-07.2007

Förster, E., Zhao, S., & Frotscher, M. (2006). Laminating the hippocampus. *Nature reviews neuroscience*, *7*(4), 259. doi:10.1038/nrn1882.

Förster, E. (2014). Reelin, neuronal polarity and process orientation of cortical neurons. *Neuroscience*, *269*, 102-111. doi: 10.1016/j.neuroscience.2014.03.004.

Franco, S. J., Martinez-Garay, I., Gil-Sanz, C., Harkins-Perry, S. R., & Müller, U. (2011). Reelin regulates cadherin function via Dab1/Rap1 to control neuronal migration and lamination in the neocortex. *Neuron*, *69*(3), 482-497. doi:10.1016/j.neuron.2011.01.003.

Friedl, P., & Bröcker, E. B. (2000). The biology of cell locomotion within three-dimensional extracellular matrix. *Cellular and molecular life sciences CMLS*, *57*(1), 41-64. doi:10.1007/s000180050498.

Friedl, P., & Wolf, K. (2009). Proteolytic interstitial cell migration: a five-step process. *Cancer and Metastasis Reviews*, *28*(1-2), 129-135. doi:10.1007/s10555-008-9174-3.

Frotscher, M., Zhao, S., Wang, S., & Chai, X. (2017). Reelin signaling inactivates cofilin to stabilize the cytoskeleton of migrating cortical neurons. *Frontiers in cellular neuroscience*, *11*, 148. doi:10.3389/fncel.2017.00148.

Gaddis, G. M., & Gaddis, M. L. (1990). Introduction to biostatistics: Part 5, Statistical inference techniques for hypothesis testing with nonparametric data. *Annals of emergency medicine*, *19*(9), 1054-1059.

García-Marín, V., García-López, P., & Freire, M. (2007). Cajal's contributions to glia research. *Trends in neurosciences*, *30*(9), 479-487. doi:10.1016/j.tins.2007.06.008.

Gärtner, A., Fornasiero, E. F., Munck, S., Vennekens, K. L., Seuntjens, E., Huttner, W. B., ... & Dotti, C. G. (2012). N-cadherin specifies first asymmetry in developing neurons. *The EMBO journal*, *31*(8), 1893-1903.

Gelman, D. M., Martini, F. J., Nóbrega-Pereira, S., Pierani, A., Kessaris, N., & Marín, O. (2009). The embryonic preoptic area is a novel source of cortical GABAergic interneurons. *Journal of Neuroscience*, *29*(29), 9380-9389. doi: 10.1523/JNEUROSCI.0604-09.2009.

Gelman, D. M., & Marín, O. (2010). Generation of interneuron diversity in the mouse cerebral cortex. *European Journal of Neuroscience*, *31*(12), 2136-2141. doi:10.1111/j.1460-9568.2010.07267.x.

Gerfen, C. R. (1985). The neostriatal mosaic. I. Compartmental organization of projections from the striatum to the substantia nigra in the rat. *Journal of Comparative Neurology*, *236*(4), 454-476. doi:10.1002/cne.902360404.

Ghashghaei, H. T., Lai, C., & Anton, E. S. (2007). Neuronal migration in the adult brain: are we there yet?. *Nature Reviews Neuroscience*, *8*(2), 141. doi:10.1038/nrn2074.

Gilmore, E. C., & Herrup, K. (2000). Cortical development: receiving reelin. *Current Biology*, *10*(4), R162-R166. doi: 10.1016/S0960-9822(00)00332-8.

Gil-Sanz, C., Franco, S. J., Martinez-Garay, I., Espinosa, A., Harkins-Perry, S., & Müller, U. (2013). Cajal-Retzius cells instruct neuronal migration by coincidence signaling between secreted and contact-dependent guidance cues. *Neuron*, *79*(3), 461-477. doi:10.1016/j.neuron.2013.06.040.

Graziano, B. R., & Weiner, O. D. (2014). Self-organization of protrusions and polarity during eukaryotic chemotaxis. *Current opinion in cell biology*, *30*, 60-67. doi:10.1016/j.ceb.2014.06.007.

Guo, J., & Anton, E. S. (2014). Decision making during interneuron migration in the developing cerebral cortex. *Trends in cell biology*, *24*(6), 342-351. doi:10.1016/j.tcb.2013.12.001.

Gurniak, C. B., Perlas, E., & Witke, W. (2005). The actin depolymerizing factor n-cofilin is essential for neural tube morphogenesis and neural crest cell migration. *Developmental biology*, *278*(1), 231-241. doi: 10.1016/j.ydbio.2004.11.010.

Hanaway, J., McConnell, J. A., & Netsky, M. G. (1971). Histogenesis of the substantia nigra, ventral tegmental area of Tsai and interpeduncular nucleus: an autoradiographic study of the mesencephalon in the rat. *Journal of Comparative Neurology*, *142*(1), 59-73. doi:10.1002/cne.901420105.

Hansen, A. H., Duellberg, C., Mieck, C., Loose, M., & Hippenmeyer, S. (2017). Cell polarity in cerebral cortex development—cellular architecture shaped by biochemical networks. *Frontiers in cellular neuroscience*, *11*, 176. doi: 10.3389/fncel.2017.00176.

Harfe, B. D., Scherz, P. J., Nissim, S., Tian, H., McMahon, A. P., & Tabin, C. J. (2004). Evidence for an expansion-based temporal Shh gradient in specifying vertebrate digit identities. *Cell*, *118*(4), 517-528. doi:10.1016/j.cell.2004.07.024.

Hartfuss, E., Förster, E., Bock, H. H., Hack, M. A., Leprince, P., Luque, J. M., ... & Götz, M. (2003). Reelin signaling directly affects radial glia morphology and biochemical Hatanaka, Y., & Murakami, F. (2002). In vitro analysis of the origin, migratory behavior, and maturation of cortical pyramidal cells. *Journal of Comparative Neurology*, *454*(1), 1-14. doi:10.1002/cne.10421.

Hatanaka, Y., & Murakami, F. (2002). In vitro analysis of the origin, migratory behavior, and maturation of cortical pyramidal cells. *Journal of Comparative Neurology*, *454*(1), 1-14. doi:10.1093/cercor/bhr383.

Hatanaka, Y., & Yamauchi, K. (2012). Excitatory cortical neurons with multipolar shape establish neuronal polarity by forming a tangentially oriented axon in the intermediate zone. *Cerebral cortex*, *23*(1), 105-113. doi: 10.1093/cercor/bhr383.

Hatanaka, Y., Zhu, Y., Torigoe, M., Kita, Y., & Murakami, F. (2016). From migration to settlement: the pathways, migration modes and dynamics of neurons in the developing brain. *Proceedings of the Japan Academy, Series B*, *92*(1), 1-19. doi:10.2183/pjab.92.1.

Hayes, L., Zhang, Z., Albert, P., Zervas, M., & Ahn, S. (2011). Timing of Sonic hedgehog and Gli1 expression segregates midbrain dopamine neurons. *Journal of Comparative Neurology*, *519*(15), 3001-3018.

He, M., Zhang, Z. H., Guan, C. B., Xia, D., & Yuan, X. B. (2010). Leading tip drives soma translocation via forward F-actin flow during neuronal migration. *Journal of Neuroscience*, *30*(32), 10885-10898. doi:10.1523/JNEUROSCI.0240-10.2010.

He, S., Li, Z., Ge, S., Yu, Y. C., & Shi, S. H. (2015). Inside-out radial migration facilitates lineage-dependent neocortical microcircuit assembly. *Neuron*, *86*(5), 1159-1166. doi: 10.1016/j.neuron.2015.05.002

Hiesberger, T., Trommsdorff, M., Howell, B. W., Goffinet, A., Mumby, M. C., Cooper, J. A., & Herz, J. (1999). Direct binding of Reelin to VLDL receptor and ApoE receptor 2 induces tyrosine phosphorylation of disabled-1 and modulates tau phosphorylation. *Neuron*, *24*(2), 481-489. doi:10.1016/s0896-6273(00)80861-2.

Higginbotham, H. R., & Gleeson, J. G. (2007). The centrosome in neuronal development. *Trends in neurosciences*, *30*(6), 276-283. doi: 10.1016/j.tins.2007.04.001.

Hotulainen, P., Paunola, E., Vartiainen, M. K., & Lappalainen, P. (2005). Actin-depolymerizing factor and cofilin-1 play overlapping roles in promoting rapid F-actin depolymerization in mammalian nonmuscle cells. *Molecular biology of the cell*, *16*(2), 649-664. doi:10.1091/mbc.e04-07-0555.

Howell, B. W., Hawkes, R., Soriano, P., & Cooper, J. A. (1997). Neuronal position in the developing brain is regulated by mouse disabled-1. *Nature*, *389*(6652), 733. doi:10.1038/39607.

Howell, B. W., Herrick, T. M., & Cooper, J. A. (1999). Reelin-induced tryosine phosphorylation of disabled 1 during neuronal positioning. *Genes & development*, *13*(6), 643-648. doi:10.1101/gad.13.6.643.

Huang, C. H., Tang, M., Shi, C., Iglesias, P. A., & Devreotes, P. N. (2013). An excitable signal integrator couples to an idling cytoskeletal oscillator to drive cell migration. *Nature cell biology*, *15*(11), 1307. doi:10.1038/ncb2859.

Ichetovkin, I., Han, J., Pang, K. M., Knecht, D. A., & Condeelis, J. S. (2000). Actin filaments are severed by both native and recombinant dictyostelium cofilin but to different extents. *Cell motility and the cytoskeleton*, *45*(4), 293-306.

Ikemoto, S. (2007). Dopamine reward circuitry: two projection systems from the ventral midbrain to the nucleus accumbens–olfactory tubercle complex. *Brain research reviews*, *56*(1), 27-78. doi: 10.1016/j.brainresrev.2007.05.004.

Izumi, Y., Wakita, S., Kanbara, C., Nakai, T., Akaike, A., & Kume, T. (2017). Integrin α5β1 expression on dopaminergic neurons is involved in dopaminergic neurite outgrowth on striatal neurons. *Scientific reports*, *7*, 42111.

Jaqaman, K., Loerke, D., Mettlen, M., Kuwata, H., Grinstein, S., Schmid, S. L., & Danuser, G. (2008). Robust single-particle tracking in live-cell time-lapse sequences. *Nature methods*, *5*(8), 695.

Jessell, T. M., & Sanes, J. R. (2000). Development: The decade of the developing brain. *Current opinion in neurobiology*, *10*(5), 599-611. doi:10.1016/S0959-4388(00)00136-7.

Jiang, J., Zhang, Z. H., Yuan, X. B., & Poo, M. M. (2015). Spatiotemporal dynamics of traction forces show three contraction centers in migratory neurons. *J Cell Biol*, *209*(5), 759-774. doi: 10.1083/jcb.201410068.

Joksimovic, M., Yun, B. A., Kittappa, R., Anderegg, A. M., Chang, W. W., Taketo, M. M., ... & Awatramani, R. B. (2009). Wnt antagonism of Shh facilitates midbrain floor plate neurogenesis. *Nature neuroscience*, *12*(2), 125.

Jossin, Y., Ignatova, N., Hiesberger, T., Herz, J., de Rouvroit, C. L., & Goffinet, A. M. (2004). The central fragment of Reelin, generated by proteolytic processing in vivo, is critical to its function during cortical plate development. *Journal of Neuroscience*, *24*(2), 514-521. doi:10.1523/JNEUROSCI.3408-03.2004.

Jossin, Y., & Goffinet, A. M. (2007). Reelin signals through phosphatidylinositol 3-kinase and Akt to control cortical development and through mTor to regulate dendritic growth. *Molecular and cellular biology*, *27*(20), 7113-7124. doi:10.1128/MCB.00928-07.

Jossin, Y., & Cooper, J. A. (2011). Reelin, Rap1 and N-cadherin orient the migration of multipolar neurons in the developing neocortex. *Nature neuroscience*, *14*(6), 697. doi:10.1038/nn.2816.

Joyner, A. L., Liu, A., & Millet, S. (2000). Otx2, Gbx2 and Fgf8 interact to position and maintain a mid–hindbrain organizer. *Current opinion in cell biology*, *12*(6), 736-741. doi:10.1016/S0955-

0674(00)00161-7.
Kanellos, G., Zhou, J., Patel, H., Ridgway, R. A., Huels, D., Gurniak, C. B., ... & Brunton, V. G. (2015). ADF and Cofilin1 control actin stress fibers, nuclear integrity, and cell survival. *Cell reports*, *13*(9), 1949-1964. doi: 10.1016/j.celrep.2015.10.056.
Kang, W. Y., Kim, S. S., Cho, S. K., Kim, S., Suh-Kim, H., & Lee, Y. D. (2010). Migratory defect of mesencephalic dopaminergic neurons in developing reeler mice. *Anatomy & cell biology*, *43*(3), 241-251. doi:10.5115/acb.2010.43.3.241.
Kawano, H., Ohyama, K., Kawamura, K., & Nagatsu, I. (1995). Migration of dopaminergic neurons in the embryonic mesencephalon of mice. *Developmental brain research*, *86*(1-2), 101-113. doi: 10.1016/0165-3806(95)00018-9
Kawauchi, T., Sekine, K., Shikanai, M., Chihama, K., Tomita, K., Kubo, K. I., ... & Hoshino, M. (2010). Rab GTPases-dependent endocytic pathways regulate neuronal migration and maturation through N-cadherin trafficking. *Neuron*, *67*(4), 588-602. doi:10.1016/j.neuron.2010.07.007.
Kawauchi, T. (2015). Cellullar insights into cerebral cortical development: focusing on the locomotion mode of neuronal migration. *Frontiers in cellular neuroscience*, *9*, 394. doi: 10.3389/fncel.2015.00394.
Keilani, S., & Sugaya, K. (2008). Reelin induces a radial glial phenotype in human neural progenitor cells by activation of Notch-1. *BMC developmental biology*, *8*(1), 69. doi:10.1186/1471-213X-8-69.
Kele, J., Simplicio, N., Ferri, A. L., Mira, H., Guillemot, F., Arenas, E., & Ang, S. L. (2006). Neurogenin 2 is required for the development of ventral midbrain dopaminergic neurons. *Development*, *133*(3), 495-505. doi: 10.1242/dev.02223.
Komuro, H., & Rakic, P. (1998). Distinct modes of neuronal migration in different domains of developing cerebellar cortex. *Journal of Neuroscience*, *18*(4), 1478-1490. doi:10.1523/JNEUROSCI.18-04-01478.1998.
Komuro, H., Yacubova, E., Yacubova, E., & Rakic, P. (2001). Mode and tempo of tangential cell migration in the cerebellar external granular layer. *Journal of Neuroscience*, *21*(2), 527-540.
Kratochwil, C. F., Maheshwari, U., & Rijli, F. M. (2017). The long journey of pontine nuclei neurons: from rhombic lip to cortico-ponto-cerebellar circuitry. *Frontiers in neural circuits*, *11*, 33. doi:10.3389/fncir.2017.00033.
Krüger, M. T., Zhao, S., Chai, X., Brunne, B., Bouché, E., Bock, H. H., & Frotscher, M. (2010). Role for Reelin-induced cofilin phosphorylation in the assembly of sympathetic preganglionic neurons in the murine intermediolateral column. *European Journal of Neuroscience*, *32*(10), 1611-1617. doi:10.1111/j.1460-9568.2010.07433.x.
Kubasak, M. D., Brooks, R., Chen, S., Villeda, S. A., & Phelps, P. E. (2004). Developmental distribution of reelin-positive cells and their secreted product in the rodent spinal cord. *Journal of Comparative Neurology*, *468*(2), 165-178.
La Manno, G., Gyllborg, D., Codeluppi, S., Nishimura, K., Salto, C., Zeisel, A., ... & Lönnerberg, P. (2016). Molecular diversity of midbrain development in mouse, human, and stem cells. *Cell*, *167*(2), 566-580. doi:10.1016/j.cell.2016.09.027.
Lammel, S., Hetzel, A., Häckel, O., Jones, I., Liss, B., & Roeper, J. (2008). Unique properties of mesoprefrontal neurons within a dual mesocorticolimbic dopamine system. *Neuron*, *57*(5), 760-773. doi:10.1016/j.neuron.2008.01.022.
Lammel, S., Lim, B. K., Ran, C., Huang, K. W., Betley, M. J., Tye, K. M., ... & Malenka, R. C. (2012). Input-specific control of reward and aversion in the ventral tegmental area. *Nature*, *491*(7423), 212.
Lammel, S., Lim, B. K., & Malenka, R. C. (2014). Reward and aversion in a heterogeneous midbrain dopamine system. *Neuropharmacology*, *76*, 351-359. doi:10.1016/j.neuropharm.2013.03.019.
Lappalainen, P., & Drubin, D. G. (1997). Cofilin promotes rapid actin filament turnover in vivo. *Nature*, *388*(6637), 78. doi:10.1038/40418.
Lavdas, A. A., Grigoriou, M., Pachnis, V., & Parnavelas, J. G. (1999). The medial ganglionic eminence gives rise to a population of early neurons in the developing cerebral cortex. *Journal of Neuroscience*, *19*(18), 7881-7888. doi: 10.1523/JNEUROSCI.19-18-07881.1999.
Leemhuis, J., Bouché, E., Frotscher, M., Henle, F., Hein, L., Herz, J., ... & Bock, H. H. (2010). Reelin signals through apolipoprotein E receptor 2 and Cdc42 to increase growth cone motility and filopodia formation. *Journal of Neuroscience*, *30*(44), 14759-14772. doi:10.1523/JNEUROSCI.4036-10.2010.
Lerner, T. N., Shilyansky, C., Davidson, T. J., Evans, K. E., Beier, K. T., Zalocusky, K. A., ... & Deisseroth, K. (2015). Intact-brain analyses reveal distinct information carried by SNc dopamine subcircuits. *Cell*, *162*(3), 635-647. doi:10.1016/j.cell.2015.07.014.
Levitt, P., & Rakic, P. (1980). Immunoperoxidase localization of glial fibrillary acidic protein in radial glial cells and astrocytes of the developing rhesus monkey brain. *Journal of Comparative Neurology*, *193*(3), 815-840. doi:10.1002/cne.901930316.
Li, J., Duarte, T., Kocabas, A., Works, M., McConnell, S. K., & Hynes, M. A. (2014). Evidence for

topographic guidance of dopaminergic axons by differential Netrin-1 expression in the striatum. *Molecular and Cellular Neuroscience*, *61*, 85-96. doi:10.1016/j.mcn.2014.05.003.

Liu, A., & Joyner, A. L. (2001). EN and GBX2 play essential roles downstream of FGF8 in patterning the mouse mid/hindbrain region. *Development*, *128*(2), 181-191.

Lodato, S., Rouaux, C., Quast, K. B., Jantrachotechatchawan, C., Studer, M., Hensch, T. K., & Arlotta, P. (2011). Excitatory projection neuron subtypes control the distribution of local inhibitory interneurons in the cerebral cortex. *Neuron*, *69*(4), 763-779. doi:10.1016/j.neuron.2011.01.015.

Lourenço, M. R., Garcez, P. P., Lent, R., & Uziel, D. (2012). Temporal and spatial regulation of interneuron distribution in the developing cerebral cortex—an in vitro study. *Neuroscience*, *201*, 357-365. doi:10.1016/j.neuroscience.2011.10.041.

Lysko, D. E., Putt, M., & Golden, J. A. (2011). SDF1 regulates leading process branching and speed of migrating interneurons. *Journal of Neuroscience*, *31*(5), 1739-1745. doi:10.1523/JNEUROSCI.3118-10.2011.

Lysko, D. E., Putt, M., & Golden, J. A. (2014). SDF1 reduces interneuron leading process branching through dual regulation of actin and microtubules. *Journal of Neuroscience*, *34*(14), 4941-4962. doi: 10.1523/JNEUROSCI.4351-12.2014.

Maciver, S. K., & Hussey, P. J. (2002). The ADF/cofilin family: actin-remodeling proteins. *Genome biology*, *3*(5), reviews3007-1. doi:10.1186/gb-2002-3-5-reviews3007.

Magdaleno, S., Keshvara, L., & Curran, T. (2002). Rescue of ataxia and preplate splitting by ectopic expression of Reelin in reeler mice. *Neuron*, *33*(4), 573-586. doi:10.1016/S0896-6273(02)00582-2.

Malatesta, P., Hartfuss, E., & Gotz, M. (2000). Isolation of radial glial cells by fluorescent-activated cell sorting reveals a neuronal lineage. *Development*, *127*(24), 5253-5263.

Mann, D. M. A., & Yates, P. O. (1974). Lipoprotein pigments—their relationship to ageing in the human nervous system: I. The lipofuscin content of nerve cells. *Brain*, *97*(3), 481-488.

Marín, O., Yaron, A., Bagri, A., Tessier-Lavigne, M., & Rubenstein, J. L. (2001). Sorting of striatal and cortical interneurons regulated by semaphorin-neuropilin interactions. *Science*, *293*(5531), 872-875. doi:10.1126/science.1061891.

Marín, O., & Rubenstein, J. L. (2003). Cell migration in the forebrain. *Annual review of neuroscience*, *26*(1), 441-483. doi:10.1146/annurev.neuro.26.041002.131058.

Marín, O., Valiente, M., Ge, X., & Tsai, L. H. (2010). Guiding neuronal cell migrations. *Cold Spring Harbor perspectives in biology*, *2*(2), a001834. doi:10.1101/cshperspect.a001834.

Marín, O. (2013). Cellular and molecular mechanisms controlling the migration of neocortical interneurons. *European Journal of Neuroscience*, *38*(1), 2019-2029. doi:10.1111/ejn.12225.

Martini, F. J., Valiente, M., Bendito, G. L., Szabó, G., Moya, F., Valdeolmillos, M., & Marín, O. (2009). Biased selection of leading process branches mediates chemotaxis during tangential neuronal migration. *Development*, *136*(1), 41-50. doi:10.1242/dev.025502.

Meseke, M., Cavus, E., & Förster, E. (2013). Reelin promotes microtubule dynamics in processes of developing neurons. *Histochemistry and cell biology*, *139*(2), 283-297.

Matsuda, W., Furuta, T., Nakamura, K. C., Hioki, H., Fujiyama, F., Arai, R., & Kaneko, T. (2009). Single nigrostriatal dopaminergic neurons form widely spread and highly dense axonal arborizations in the neostriatum. *Journal of Neuroscience*, *29*(2), 444-453. doi:10.1523/JNEUROSCI.4029-08.2009.

Matsumoto, M., & Hikosaka, O. (2009). Two types of dopamine neuron distinctly convey positive and negative motivational signals. *Nature*, *459*(7248), 837.

Matsunaga, Y., Noda, M., Murakawa, H., Hayashi, K., Nagasaka, A., Inoue, S., ... & Nakajima, K. (2017). Reelin transiently promotes N-cadherin–dependent neuronal adhesion during mouse cortical development. *Proceedings of the National Academy of Sciences*, *114*(8), 2048-2053. doi:10.1073/pnas.1615215114.

Mavromatakis, Y. E., Lin, W., Metzakopian, E., Ferri, A. L., Yan, C. H., Sasaki, H., ... & Ang, S. L. (2011). Foxa1 and Foxa2 positively and negatively regulate Shh signalling to specify ventral midbrain progenitor identity. *Mechanisms of development*, *128*(1-2), 90-103. doi:10.1016/j.mod.2010.11.002.

McMahon, A. P., & Bradley, A. (1990). The Wnt-1 (int-1) proto-oncogene is required for development of a large region of the mouse brain. *Cell*, *62*(6), 1073-1085. doi:10.1016/0092-8674(90)90385-r.

Menegas, W., Bergan, J. F., Ogawa, S. K., Isogai, Y., Venkataraju, K. U., Osten, P., ... & Watabe-Uchida, M. (2015). Dopamine neurons projecting to the posterior striatum form an anatomically distinct subclass. *Elife*, *4*, e10032. doi:10.7554/eLife.10032.001.

Miyata, T., Kawaguchi, A., Okano, H., & Ogawa, M. (2001). Asymmetric inheritance of radial glial fibers by cortical neurons. *Neuron*, *31*(5), 727-741. doi: 10.1016/S0896-6273(01)00420-2

Miyata, T., & Ogawa, M. (2007). Twisting of neocortical progenitor cells underlies a spring-like mechanism for daughter-cell migration. *Current biology*, *17*(2), 146-151. doi:10.1016/j.cub.2006.11.023.

Miyata, T., Ono, Y., Okamoto, M., Masaoka, M., Sakakibara, A., Kawaguchi, A., ... & Ogawa, M. (2010).

Migration, early axonogenesis, and Reelin-dependent layer-forming behavior of early/posterior-born Purkinje cells in the developing mouse lateral cerebellum. *Neural development*, *5*(1), 23. doi:10.1186/1749-8104-5-23.

Morales, M., & Margolis, E. B. (2017). Ventral tegmental area: cellular heterogeneity, connectivity and behaviour. *Nature Reviews Neuroscience*, *18*(2), 73. doi:10.1038/nrn.2016.165.

Nadarajah, B., Brunstrom, J. E., Grutzendler, J., Wong, R. O., & Pearlman, A. L. (2001). Two modes of radial migration in early development of the cerebral cortex. *Nature neuroscience*, *4*(2), 143. doi:10.1038/83967.

Nadarajah, B., Alifragis, P., Wong, R. O., & Parnavelas, J. G. (2002). Ventricle-directed migration in the developing cerebral cortex. *Nature neuroscience*, *5*(3), 218. doi:10.1038/nn813.

Nakatani, T., Kumai, M., Mizuhara, E., Minaki, Y., & Ono, Y. (2010). Lmx1a and Lmx1b cooperate with Foxa2 to coordinate the specification of dopaminergic neurons and control of floor plate cell differentiation in the developing mesencephalon. *Developmental biology*, *339*(1), 101-113. doi:10.1016/j.ydbio.2009.12.017.

Namba, T., Kibe, Y., Funahashi, Y., Nakamuta, S., Takano, T., Ueno, T., ... & Oda, K. (2014). Pioneering axons regulate neuronal polarization in the developing cerebral cortex. *Neuron*, *81*(4), 814-829. doi: 10.1016/j.neuron.2013.12.015.

Nery, S., Fishell, G., & Corbin, J. G. (2002). The caudal ganglionic eminence is a source of distinct cortical and subcortical cell populations. *Nature neuroscience*, *5*(12), 1279. doi:10.1038/nn971.

Nichols, A. J., & Olson, E. C. (2010). Reelin promotes neuronal orientation and dendritogenesis during preplate splitting. *Cerebral cortex*, *20*(9), 2213-2223. doi:10.1093/cercor/bhp303.

Nishikawa, S., Goto, S., Yamada, K., Hamasaki, T., & Ushio, Y. (2003). Lack of Reelin causes malpositioning of nigral dopaminergic neurons: evidence from comparison of normal and Relnrl mutant mice. *Journal of Comparative Neurology*, *461*(2), 166-173. doi:10.1002/cne.10610.

Nóbrega-Pereira, S., Kessaris, N., Du, T., Kimura, S., Anderson, S. A., & Marín, O. (2008). Postmitotic Nkx2-1 controls the migration of telencephalic interneurons by direct repression of guidance receptors. *Neuron*, *59*(5), 733-745. doi:10.1016/j.neuron.2008.07.024.

Nóbrega-Pereira, S., & Marín, O. (2009). Transcriptional control of neuronal migration in the developing mouse brain. *Cerebral Cortex*, *19*(suppl_1), i107-i113. doi:10.1093/cercor/bhp044.

Noctor, S. C., Flint, A. C., Weissman, T. A., Dammerman, R. S., & Kriegstein, A. R. (2001). Neurons derived from radial glial cells establish radial units in neocortex. *Nature*, *409*(6821), 714. doi:10.1038/35055553.

Noctor, S. C., Flint, A. C., Weissman, T. A., Wong, W. S., Clinton, B. K., & Kriegstein, A. R. (2002). Dividing precursor cells of the embryonic cortical ventricular zone have morphological and molecular characteristics of radial glia. *Journal of Neuroscience*, *22*(8), 3161-3173.

Noctor, S. C., Martínez-Cerdeño, V., & Kriegstein, A. R. (2008). Distinct behaviors of neural stem and progenitor cells underlie cortical neurogenesis. *Journal of Comparative Neurology*, *508*(1), 28-44. doi:10.1002/cne.21669.

Noctor, S. C., Martínez-Cerdeño, V., Ivic, L., & Kriegstein, A. R. (2004). Cortical neurons arise in symmetric and asymmetric division zones and migrate through specific phases. *Nature neuroscience*, *7*(2), 136. doi:10.1038/nn1172.

Ogawa, M., Miyata, T., Nakajimat, K., Yagyu, K., Seike, M., Ikenaka, K., ... & Mikoshibat, K. (1995). The reeler gene-associated antigen on Cajal-Retzius neurons is a crucial molecule for laminar organization of cortical neurons. *Neuron*, *14*(5), 899-912. doi:10.1016/0896-6273(95)90329-1.

Panman, L., Papathanou, M., Laguna, A., Oosterveen, T., Volakakis, N., Acampora, D., ... & Muhr, J. (2014). Sox6 and Otx2 control the specification of substantia nigra and ventral tegmental area dopamine neurons. *Cell reports*, *8*(4), 1018-1025. doi:10.1016/j.celrep.2014.07.016.

Park, T. J., & Curran, T. (2008). Crk and Crk-like play essential overlapping roles downstream of disabled-1 in the Reelin pathway. *Journal of Neuroscience*, *28*(50), 13551-13562. doi:10.1523/JNEUROSCI.4323-08.2008.

Petrie, R. J., Doyle, A. D., & Yamada, K. M. (2009). Random versus directionally persistent cell migration. *Nature reviews Molecular cell biology*, *10*(8), 538. doi:10.1038/nrm2729.

Phelps, P. E., Barber, R. P., & Vaughn, J. E. (1991). Embryonic development of choline acetyltransferase in thoracic spinal motor neurons: somatic and autonomic neurons may be derived from a common cellular group. *Journal of Comparative Neurology*, *307*(1), 77-86. doi:10.1002/cne.903070108.

Phelps, P. E., Rich, R., Dupuy-Davies, S., Ríos, Y., & Wong, T. (2002). Evidence for a cell-specific action of Reelin in the spinal cord. *Developmental biology*, *244*(1), 180-198.

Pohlkamp, T., Xiao, L., Sultana, R., Bepari, A., Bock, H. H., Henkemeyer, M., & Herz, J. (2016). Ephrin Bs and canonical Reelin signalling. *Nature*, *539*(7630), E4. doi:10.1038/nature20129.

des Portes, V., Pinard, J. M., Billuart, P., Vinet, M. C., Koulakoff, A., Carrié, A., ... & Catala, M. (1998). A novel CNS gene required for neuronal migration and involved in X-linked subcortical laminar

heterotopia and lissencephaly syndrome. *Cell*, *92*(1), 51-61. doi:10.1523/ENEURO.0350-17.2018.
Poulin, J. F., Zou, J., Drouin-Ouellet, J., Kim, K. Y. A., Cicchetti, F., & Awatramani, R. B. (2014). Defining midbrain dopaminergic neuron diversity by single-cell gene expression profiling. *Cell reports*, *9*(3), 930-943. doi:10.1016/j.celrep.2014.10.008.
Prakash, N., Brodski, C., Naserke, T., Puelles, E., Gogoi, R., Hall, A., ... & Martinez, S. (2006). A Wnt1-regulated genetic network controls the identity and fate of midbrain-dopaminergic progenitors in vivo. *Development*, *133*(1), 89-98.
Przedborski, S. (2017). The two-century journey of Parkinson disease research. *Nature Reviews Neuroscience*, *18*(4), 251.
Rakic, P. (1971). Neuron-glia relationship during granule cell migration in developing cerebellar cortex. A Golgi and electonmicroscopic study in Macacus rhesus. *Journal of Comparative Neurology*, *141*(3), 283-312. doi:10.1002/cne.901410303.
Reiner, O., & Sapir, T. (2009). Polarity regulation in migrating neurons in the cortex. *Molecular neurobiology*, *40*(1), 1-14.
Rivas, R. J., & Hatten, M. E. (1995). Motility and cytoskeletal organization of migrating cerebellar granule neurons. *Journal of Neuroscience*, *15*(2), 981-989.
Roeper, J. (2013). Dissecting the diversity of midbrain dopamine neurons. *Trends in neurosciences*, *36*(6), 336-342. doi:10.1016/j.tins.2013.03.003.
Ruiz-Reig, N., & Studer, M. (2017). Rostro-Caudal and Caudo-Rostral Migrations in the Telencephalon: Going Forward or Backward?. *Frontiers in neuroscience*, *11*, 692. doi:10.3389/fnins.2017.00692.
Sanada, K., Gupta, A., & Tsai, L. H. (2004). Disabled-1-regulated adhesion of migrating neurons to radial glial fiber contributes to neuronal positioning during early corticogenesis. *Neuron*, *42*(2), 197-211. doi: 10.1016/S0896-6273(04)00222-3.
Sanchez, A. D., & Feldman, J. L. (2017). Microtubule-organizing centers: from the centrosome to non-centrosomal sites. *Current opinion in cell biology*, *44*, 93-101. doi:10.1016/j.ceb.2016.09.003.
Schaar, B. T., & McConnell, S. K. (2005). Cytoskeletal coordination during neuronal migration. *Proceedings of the National Academy of Sciences*, *102*(38), 13652-13657. doi:10.1073/pnas.0506008102.
Scherer, H. J. (1939). Melanin pigmentation of the substantia nigra in primates. *Journal of Comparative Neurology*, *71*(1), 91-98. doi:10.1002/cne.900710106.
Schelski, M., & Bradke, F. (2017). Neuronal polarization: From spatiotemporal signaling to cytoskeletal dynamics. *Molecular and Cellular Neuroscience*, *84*, 11-28. doi:10.1016/j.mcn.2017.03.008
Schilling, K. (2018). Moving into shape: cell migration during the development and histogenesis of the cerebellum. *Histochemistry and cell biology*, *150*(1), 13-36.
Schultz, W. (1997). Dopamine neurons and their role in reward mechanisms. *Current opinion in neurobiology*, *7*(2), 191-197. doi: 10.1016/S0959-4388(97)80007-4.
Schwarz, M. K., Scherbarth, A., Sprengel, R., Engelhardt, J., Theer, P., & Giese, G. (2015). Fluorescent-protein stabilization and high-resolution imaging of cleared, intact mouse brains. *PloS one*, *10*(5), e0124650. doi:10.1371/journal.pone.0124650.
Sekine, K., Kawauchi, T., Kubo, K. I., Honda, T., Herz, J., Hattori, M., ... & Nakajima, K. (2012). Reelin controls neuronal positioning by promoting cell-matrix adhesion via inside-out activation of integrin α5β1. *Neuron*, *76*(2), 353-369. doi:10.1016/j.neuron.2012.07.020.
Sekine, K., Kubo, K. I., & Nakajima, K. (2014). How does Reelin control neuronal migration and layer formation in the developing mammalian neocortex?. *Neuroscience research*, *86*, 50-58. doi:10.1016/j.neures.2014.06.004.
Sentürk, A., Pfennig, S., Weiss, A., Burk, K., & Acker-Palmer, A. (2011). Ephrin Bs are essential components of the Reelin pathway to regulate neuronal migration. *Nature*, *472*(7343), 356. doi:10.1038/nature09874.
Sharaf, A., Bock, H. H., Spittau, B., Bouche, E., & Krieglstein, K. (2013). ApoER2 and VLDLr are required for mediating reelin signalling pathway for normal migration and positioning of mesencephalic dopaminergic neurons. *PloS one*, *8*(8), e71091. doi:10.1371/journal.pone.0071091.
Sharaf, A., Rahhal, B., Spittau, B., & Roussa, E. (2015). Localization of reelin signaling pathway components in murine midbrain and striatum. *Cell and tissue research*, *359*(2), 393-407. doi:10.1007/s00441-014-2022-6.
Sheen, V. L., Ferland, R. J., Harney, M., Hill, R. S., Neal, J., Banham, A. H., ... & Folkerth, R. (2006). Impaired proliferation and migration in human Miller-Dieker neural precursors. *Annals of neurology*, *60*(1), 137-144. doi:10.1002/ana.20843.
Shim, S. Y., Wang, J., Asada, N., Neumayer, G., Tran, H. C., Ishiguro, K. I., ... & Nguyen, M. D. (2008). Protein 600 is a microtubule/endoplasmic reticulum-associated protein in CNS neurons. *Journal of Neuroscience*, *28*(14), 3604-3614. doi:10.1523/JNEUROSCI.5278-07.2008.
Shults, C. W., Hashimoto, R., Brady, R. M., & Gage, F. H. (1990). Dopaminergic cells align along radial

glia in the developing mesencephalon of the rat. *Neuroscience*, *38*(2), 427-436. doi:10.1016/0306-4522(90)90039-7.

Silva, C. G., Peyre, E., Adhikari, M. H., Tielens, S., Tanco, S., Van Damme, P., ... & Kessaris, N. (2018). Cell-intrinsic control of interneuron migration drives cortical morphogenesis. *Cell*, *172*(5), 1063-1078. doi: 10.1016/j.cell.2018.01.031.

Simó, S., Jossin, Y., & Cooper, J. A. (2010). Cullin 5 regulates cortical layering by modulating the speed and duration of Dab1-dependent neuronal migration. *Journal of Neuroscience*, *30*(16), 5668-5676. doi: 10.1523/JNEUROSCI.0035-10.2010.

Smidt, M. P., & Burbach, J. P. H. (2007). How to make a mesodiencephalic dopaminergic neuron. *Nature Reviews Neuroscience*, *8*(1), 21. doi:10.1038/nrn2039.

Solecki, D. J., Model, L., Gaetz, J., Kapoor, T. M., & Hatten, M. E. (2004). Par6α signaling controls glial-guided neuronal migration. *Nature neuroscience*, *7*(11), 1195. doi:10.1038/nn1332.

Solecki, D. J., Trivedi, N., Govek, E. E., Kerekes, R. A., Gleason, S. S., & Hatten, M. E. (2009). Myosin II motors and F-actin dynamics drive the coordinated movement of the centrosome and soma during CNS glial-guided neuronal migration. *Neuron*, *63*(1), 63-80. doi:10.1016/j.neuron.2009.05.028.

Srinivas, S., Watanabe, T., Lin, C. S., William, C. M., Tanabe, Y., Jessell, T. M., & Costantini, F. (2001). Cre reporter strains produced by targeted insertion of YFP and ECFP into the ROSA26 locus. *BMC developmental biology*, *1*(1), 4. doi:10.1186/1471-213X-1-4.

Steffen, A., Rottner, K., Ehinger, J., Innocenti, M., Scita, G., Wehland, J., & Stradal, T. E. (2004). Sra-1 and Nap1 link Rac to actin assembly driving lamellipodia formation. *The EMBO journal*, *23*(4), 749-759. doi:10.1038/sj.emboj.7600084.

Stepanova, T., Slemmer, J., Hoogenraad, C. C., Lansbergen, G., Dortland, B., De Zeeuw, C. I., ... & Galjart, N. (2003). Visualization of microtubule growth in cultured neurons via the use of EB3-GFP (end-binding protein 3-green fluorescent protein). *Journal of Neuroscience*, *23*(7), 2655-2664.

Sultan, K. T., & Shi, S. H. (2018). Generation of diverse cortical inhibitory interneurons. *Wiley Interdisciplinary Reviews: Developmental Biology*, *7*(2), e306. doi:10.1002/wdev.306.

Sussel, L., Marin, O., Kimura, S., & Rubenstein, J. L. (1999). Loss of Nkx2. 1 homeobox gene function results in a ventral to dorsal molecular respecification within the basal telencephalon: evidence for a transformation of the pallidum into the striatum. *Development*, *126*(15), 3359-3370.

Tabata, H., & Nakajima, K. (2003). Multipolar migration: the third mode of radial neuronal migration in the developing cerebral cortex. *Journal of Neuroscience*, *23*(31), 9996-10001.

Tanaka, D. H., Maekawa, K., Yanagawa, Y., Obata, K., & Murakami, F. (2006). Multidirectional and multizonal tangential migration of GABAergic interneurons in the developing cerebral cortex. *Development*, *133*(11), 2167-2176. doi:10.1242/dev.02382.

Tanaka, D. H., Yanagida, M., Zhu, Y., Mikami, S., Nagasawa, T., Miyazaki, J. I., ... & Murakami, F. (2009). Random walk behavior of migrating cortical interneurons in the marginal zone: time-lapse analysis in flat-mount cortex. *Journal of Neuroscience*, *29*(5), 1300-1311. doi:10.1523/JNEUROSCI.5446-08.2009.

Tinevez, J. Y., Perry, N., Schindelin, J., Hoopes, G. M., Reynolds, G. D., Laplantine, E., ... & Eliceiri, K. W. (2017). TrackMate: An open and extensible platform for single-particle tracking. *Methods*, *115*, 80-90. doi:10.1016/j.ymeth.2016.09.016.

Tissir, F., & Goffinet, A. M. (2003). Reelin and brain development. *Nature Reviews Neuroscience*, *4*(6), 496.

Trivedi, N., & Solecki, D. J. (2011). Neuronal migration illuminated: a look under the hood of the living neuron. *Cell adhesion & migration*, *5*(1), 42-47. doi:10.4161/cam.5.1.13609

Trivedi, N., Ramahi, J. S., Karakaya, M., Howell, D., Kerekes, R. A., & Solecki, D. J. (2014). Leading-process actomyosin coordinates organelle positioning and adhesion receptor dynamics in radially migrating cerebellar granule neurons. *Neural development*, *9*(1), 26. doi: 10.1186/1749-8104-9-26.

Tsai, J. W., Bremner, K. H., & Vallee, R. B. (2007). Dual subcellular roles for LIS1 and dynein in radial neuronal migration in live brain tissue. *Nature neuroscience*, *10*(8), 970. doi:10.1038/nn1934.

Tsai, L. H., & Gleeson, J. G. (2005). Nucleokinesis in neuronal migration. *Neuron*, *46*(3), 383-388. doi:10.1016/j.neuron.2005.04.013.

Tsujita, K., Takenawa, T., & Itoh, T. (2015). Feedback regulation between plasma membrane tension and membrane-bending proteins organizes cell polarity during leading edge formation. *Nature cell biology*, *17*(6), 749. doi:10.1038/ncb3162.

Uchida, T., Baba, A., Pérez-Martínez, F. J., Hibi, T., Miyata, T., Luque, J. M., ... & Hattori, M. (2009). Downregulation of Functional Reelin Receptors in Projection Neurons Implies That Primary Reelin Action Occurs atEarly/Premigratory Stages. *Journal of Neuroscience*, *29*(34), 10653-10662. doi:10.1523/JNEUROSCI.0345-09.2009.

Umeshima, H., Hirano, T., & Kengaku, M. (2007). Microtubule-based nuclear movement occurs independently of centrosome positioning in migrating neurons. *Proceedings of the National Academy of Sciences*, *104*(41), 16182-16187. doi:10.1073/pnas.0708047104.

Valiente, M., & Marín, O. (2010). Neuronal migration mechanisms in development and disease. *Current opinion in neurobiology*, *20*(1), 68-78. doi:10.1016/j.conb.2009.12.003.

Vaswani, A. R., & Blaess, S. (2016). Reelin signaling in the migration of ventral brain stem and spinal cord neurons. *Frontiers in cellular neuroscience*, *10*, 62. doi:10.3389/fncel.2016.00062.

Vaswani, A. R., Weykopf, B., Hagemann, C., Fried, H. U., Brüstle, O., & Blaess, S. (2019). Correct setup of the substantia nigra requires Reelin-mediated fast, laterally-directed migration of dopaminergic neurons. *eLife*, *8*, e41623. doi:10.1101/413708.

Veenvliet, J. V., dos Santos, M. T. A., Kouwenhoven, W. M., von Oerthel, L., Lim, J. L., van der Linden, A. J., ... & Smidt, M. P. (2013). Specification of dopaminergic subsets involves interplay of En1 and Pitx3. *Development*, *140*(16), 3373-3384. doi:10.1242/dev.094565.

Walsh, C., & Cepko, C. L. (1988). Clonally related cortical cells show several migration patterns. *Science*, *241*(4871), 1342-1345.

Wang, S., Brunne, B., Zhao, S., Chai, X., Li, J., Lau, J., ... & Lutz, D. (2018). Trajectory analysis unveils reelin's Role in the Directed Migration of Granule Cells in the Dentate Gyrus. *Journal of Neuroscience*, *38*(1), 137-148. doi:10.1523/JNEUROSCI.0988-17.2017.

Watanabe, H., & Murakami, F. (2009). Real time analysis of pontine neurons during initial stages of nucleogenesis. *Neuroscience research*, *64*(1), 20-29. doi:10.1016/j.neures.2009.01.007.

Weiner, O. D., Marganski, W. A., Wu, L. F., Altschuler, S. J., & Kirschner, M. W. (2007). An actin-based wave generator organizes cell motility. *PLoS biology*, *5*(9), e221. doi:10.1371/journal.pbio.0050221.

Wu, P. H., Giri, A., & Wirtz, D. (2015). Statistical analysis of cell migration in 3D using the anisotropic persistent random walk model. *Nature protocols*, *10*(3), 517.

Vogt Weisenhorn, D. M., Giesert, F., & Wurst, W. (2016). Diversity matters–heterogeneity of dopaminergic neurons in the ventral mesencephalon and its relation to Parkinson's Disease. *Journal of neurochemistry*, *139*, 8-26. doi:10.1111/jnc.13670.

Wichterle, H., Garcia-Verdugo, J. M., Herrera, D. G., & Alvarez-Buylla, A. (1999). Young neurons from medial ganglionic eminence disperse in adult and embryonic brain. *Nature neuroscience*, *2*(5), 461.

Wichterle, H., Turnbull, D. H., Nery, S., Fishell, G., & Alvarez-Buylla, A. (2001). In utero fate mapping reveals distinct migratory pathways and fates of neurons born in the mammalian basal forebrain. *Development*, *128*(19), 3759-3771.

Wise, R. A. (2004). Dopamine, learning and motivation. *Nature reviews neuroscience*, *5*(6), 483. doi:10.1038/nrn1406.

Xu, B., Goldman, J. S., Rymar, V. V., Forget, C., Lo, P. S., Bull, S. J., ... & Kennedy, T. E. (2010). Critical roles for the netrin receptor deleted in colorectal cancer in dopaminergic neuronal precursor migration, axon guidance, and axon arborization. *Neuroscience*, *169*(2), 932-949. doi: 10.1016/j.neuroscience.2010.05.025.

Yabut, O., Renfro, A., Niu, S., Swann, J. W., Marín, O., & D'Arcangelo, G. (2007). Abnormal laminar position and dendrite development of interneurons in the reeler forebrain. *Brain research*, *1140*, 75-83. doi: 10.1016/j.brainres.2005.09.070.

Yan, C. H., Levesque, M., Claxton, S., Johnson, R. L., & Ang, S. L. (2011). Lmx1a and lmx1b function cooperatively to regulate proliferation, specification, and differentiation of midbrain dopaminergic progenitors. *Journal of Neuroscience*, *31*(35), 12413-12425. doi:10.1523/JNEUROSCI.1077-11.2011.

Yanagida, M., Miyoshi, R., Toyokuni, R., Zhu, Y., & Murakami, F. (2012). Dynamics of the leading process, nucleus, and Golgi apparatus of migrating cortical interneurons in living mouse embryos. *Proceedings of the National Academy of Sciences*, *109*(41), 16737-16742. doi:10.1073/pnas.1209166109.

Yang, S., Edman, L. C., Sánchez-Alcañiz, J. A., Fritz, N., Bonilla, S., Hecht, J., ... & Arenas, E. (2013). Cxcl12/Cxcr4 signaling controls the migration and process orientation of A9-A10 dopaminergic neurons. *Development*, *140*(22), 4554-4564. doi:10.1242/dev.098145.

Ye, W., Shimamura, K., Rubenstein, J. L., Hynes, M. A., & Rosenthal, A. (1998). FGF and Shh signals control dopaminergic and serotonergic cell fate in the anterior neural plate. *Cell*, *93*(5), 755-766. doi:10.1016/S0092-8674(00)81437-3.

Yip, Y. P., Capriotti, C., & Yip, J. W. (2003). Migratory pathway of sympathetic preganglionic neurons in normal and reeler mutant mice. *Journal of Comparative Neurology*, *460*(1), 94-105. doi:10.1002/cne.10634.

Yokota, Y., Ghashghaei, H. T., Han, C., Watson, H., Campbell, K. J., & Anton, E. S. (2007). Radial glial dependent and independent dynamics of interneuronal migration in the developing cerebral cortex. *PloS one*, *2*(8), e794. doi:10.1371/journal.pone.0000794.

Yozu, M., Tabata, H., & Nakajima, K. (2005). The caudal migratory stream: a novel migratory stream of interneurons derived from the caudal ganglionic eminence in the developing mouse forebrain. *Journal of Neuroscience*, *25*(31), 7268-7277.doi:10.1523/JNEUROSCI.2072-05.2005.

Zhang, J. H., Zhao, Y. F., He, X. X., Zhao, Y., He, Z. X., Zhang, L., ... & Yu, H. L. (2018). DCC-Mediated Dab1 phosphorylation participates in the Multipolar-to-Bipolar transition of migrating neurons. *Cell reports*, *22*(13), 3598-3611. doi: 10.1016/j.celrep.2018.03.005.

Zhang, S. X., Duan, L. H., Qian, H., & Yu, X. (2016). Actin aggregations mark the sites of neurite initiation. *Neuroscience bulletin*, *32*(1), 1-15. doi:10.1007/s12264-016-0012-2.

Zechel, S., Nakagawa, Y., & Ibáñez, C. F. (2016). Thalamo-cortical axons regulate the radial dispersion of neocortical GABAergic interneurons. *Elife*, *5*, e20770. doi:10.7554/eLife.20770.001.

Zimmer, G., Rudolph, J., Landmann, J., Gerstmann, K., Steinecke, A., Gampe, C., & Bolz, J. (2011). Bidirectional ephrinB3/EphA4 signaling mediates the segregation of medial ganglionic eminence- and preoptic area-derived interneurons in the deep and superficial migratory stream. *Journal of Neuroscience*, *31*(50), 18364-18380. doi:10.1523/JNEUROSCI.4690-11.2011

8. ACKNOWLEDGEMENTS

I would like to thank Prof. Dr. Sandra Blaess for the opportunity to carry out my doctoral thesis at her lab. I am deeply grateful for her guidance and support throughout the duration of my work. Her intellectual involvement in my work and training has gone a long way in ensuring the scientific quality of this study. The encouragement and independence she gave me to explore ideas and establish methods while working with her on this project, have helped me to grow as a scientist. Her understanding and welcoming nature has helped me through the challenging times during my thesis work. I also thank her for the patient and thorough evaluation of my thesis.

I thank Prof. Dr. Oliver Brüstle for his guidance, collaborative effort and for providing a stimulating and pleasant work environment at the Institute of Reconstructive Neurobiology. I thank Prof. Dr. Walter Witke for agreeing to act as the second referee for this thesis. I am also deeply grateful to him for his collaborative support and scientific inputs on the *ADF$^{-/-}$; Cofilin 1* CKO experiments presented in this study, and for providing the *ADF$^{-/-}$; Cofilin1^{flox}* mouse lines and the Cofilin 1 antibody. I thank Prof. Dr. Waldemar Kolanus and Prof. Dr. Ulrich Kubitschek for agreeing to be on my thesis committee. I also thank Prof. Dr. Ulrich Kubitschek for collaborative support and scientific inputs on light sheet microscopy imaging of whole mount embryonic brains.

I gratefully acknowledge the PhD scholarship funding awarded to me by the Deutsche Akademischer Austausch Dienst and the funding awarded by the Rheinische Friedrich-Wilhelms-Universität Bonn (Gradute Student Support; BONFOR).

I am thankful for the collaborative support of Prof. Dr. Martin K. Schwarz and his lab in the clearing of whole-mount embryonic brains. I also thank Prof. Dr. Martin K. Schwarz for guidance and engaging scientific discussions. I thank Prof. Dr. Donato Di Monte, Dr. Michael Helwig, Dr. Hans-Ulrich Fried and the DZNE light microscopy facility for assistance with two-photon imaging. I am deeply grateful to Dr. Wolfgang Hübner for stimulating discussions, helpful suggestions and collaborative effort in pilot experiments in imaging organotypic slices. I thank Dr. Hannes Beckert and the UKB microscopy core facility for support with confocal imaging. I am grateful to Dr. Brian Howell for providing the DAB1 antibody; Prof. Dr. Joachim Herz for providing the *Reelin* in situ probe; Prof. Dr. Ulrich Müller and Prof. Dr. Amparo Acker-Palmer for providing the *Dab1^{del}* and *Dab1^{flox}* mouse lines; Prof. Dr. Nils-Göran Larsson for providing the *DAT^{Cre}* mouse line.

I am grateful to all the former and current members of the Institute of Reconstructive Neurobiology for the pleasant and enriching work environment. I am especially grateful to Jonas Doerr for stimulating discussions on imaging, for assistance with confocal microscopy of whole-mount embryonic brains and for help with the IMARIS software. I specially thank Anke Leinhaas for her excellent technical assistance and warm friendliness. I deeply appreciate the

collaborative efforts of Beatrice Weykopf in performing the western blot experiments presented in this study. Special thanks also go to Mona Matthews, Liviu Bodea, Anahita Sharaz, Shoba Kapoor Gandhi, Ammar Jabali, Frederike Klaus, Kevin Weynans, Jule Fischer, Laura Stappert, Christine Schuy, Laura Osterman, Melanie Bloschies, Matthias Hebisch and Andreas Till for friendly discussions and lending a helping hand when possible.

I deeply appreciate the former and current members of the Blaess lab: Dr. Gabriela Bodea, Viktoria Bosch, Erick Martinez Cavez, Marianna Tolve, Cathleen Hagemann, Petra Mocellin, Alessandro Petese, Ushna Khondker Islam, Adrian Fernandez Lopez, Norissa Meli, Philip Grumwald, Kilian Berendes, Astrid Metani and Franca Fries. I am deeply grateful to Dr. Gabriela Bodea for her mentorship at the beginning of my PhD and for being a great friend ever since. I am very thankful to Viktoria Bosch for her friendship, technical guidance and support. I am deeply grateful to Marianna Tolve for her warmth, friendship and support. Special thanks to Cathleen Hagemann for being a good friend and student.

This work would not have been possible without the love, encouragement and support of my family. They have been a constant source of strength and positivity. I am indebted to my father Ravi Vaswani and mother Vina Vaswani for their patient attention and advice. I am very grateful to my husband David Greenberg for his love and support. I thank David and my brother Aditya Vaswani for critical reading of this thesis.

9. LIST OF PUBLICATIONS AND CONFERENCES

Publications:

Kabanova, A., Pabst, M., Lorkowski, M., Braganza, O., Boehlen, A., Nikbakht, N., et al. (2015). Function and developmental origin of a mesocortical inhibitory circuit. *Nature Neuroscience*, *18*(6), 872–882.

Vaswani, A. R., & Blaess, S. (2016). Reelin Signaling in the Migration of Ventral Brain Stem and Spinal Cord Neurons. *Frontiers in Cellular Neuroscience*, *10*, 579–14.

Vaswani, A. R., Weykopf, B., Hagemann, C., Fried, H. U., Brüstle, O., & Blaess, S. (2019). Correct setup of the substantia nigra requires Reelin-mediated fast, laterally-directed migration of dopaminergic neurons. *eLife*, *8*, e41623.

Conferences and Meetings:

- *Tissue as active matter - Quantitative approaches in Developmental biology* Summer school, Sept. 2015, Göttingen, Germany.
- *The Brain in Focus: New Approaches to Imaging Neurons and Neural Circuits,* FENS Brain Conference, 17-20 April 2016, Rungstedgaard, Denmark. Poster presentation.
- *Bonn Brain 3 Conference*, 15-17 March 2017, Bonn, Germany. Short talk.
- *12th Göttingen Meeting of the German Neuroscience Society*, 22 - 25 March 2017, Göttingen, Germany. Young investigator talk.
- *Bioimage Data Analysis Course* European Molecular Biology Laboratory (EMBL), 14 - 20 May 2017, Heidelberg, Germany.
- *Annual meeting of the Society of Neuroscience 2017,* 11-15 November 2017, Washington DC, USA. Young investigator talk.
- Gene expression laboratory, Salk Insitute, San Diego, USA. 21 November 2017. Invited Doctoral talk.